Structural and functional characterisation of feline calicivirus entry

Michaela Jayne Conley
BSc (Hons), MSc

Submitted in fulfilment of the requirements for the Degree of Doctor of Philosophy

Institute of Infection, Immunity and Inflammation
College of Medical, Veterinary and Life Sciences
University of Glasgow
April 2018

'…by the help of microscopes, there is nothing so small as to escape our enquiry; hence there is a new visible World discovered'

Robert Hooke, 1665
(in the Preface of *Micrographia)*

Acknowledgements

I would like to acknowledge all of the members of the Bhella group, particularly Marion McElwee for all of her help with laboratory experiments and planning. I am grateful to have been part of such a welcoming and friendly research group who are always happy to help and toss ideas around. I would like to thank the remaining group members, Chris Syme, James Streetley, Swetha Vijayakrishnan and in particular Andrew Burns for the many stimulating conversations and for the continual fun and laughter he brings to the lab/office.

I would also like to thank previous members of the group, Saskia Bakker for all of her help while learning to operate the electron microscope and Colin Loney for his tuition and support during the start of my PhD.

Many other principle investigators have contributed to my work including Olwyn Byron and Sharon Kelly, who I would like to thank for their time and patience.

I am also particularly grateful to Ian and Yasmin Goodfellow at the University of Cambridge for providing fJAM-A expressing CHO cells as well as advice on protein purification.

I would like to acknowledge the most important figures during my PhD, my supervisors, Dave Bhella and Brian Willett who provided continued support during my studies, without whom I would not have been able to complete my PhD.

Finally, I would like to thank the BBSRC for providing funding and for seeing my potential.

Author's Declaration

"I declare that, except where explicit reference is made to the contribution of others, that this dissertation is the result of my own work and has not been submitted for any other degree at the University of Glasgow or any other institution."

Printed Name: _____

Signature: _____

Abstract

The *Caliciviridae* are a group of small, non-enveloped viruses with a positive sense, single stranded RNA genome. Caliciviruses include the noroviruses, responsible for winter vomiting disease, as well as several important veterinary pathogens. Feline calicivirus (FCV) is an excellent model for studying calicivirus entry, having a known protein receptor and being readily propagated in cell culture. Here we explore calicivirus entry, using FCV. Virus entry is the critical first step of infection and is therefore an important area of study.

Both alpha 2-6 linked sialic acid and feline junctional adhesion molecule A (fJAM-A) have been identified as receptors for FCV. The attachment of FCV to fJAM-A, is followed by uptake via clathrin mediated endocytosis. Little is known, however, on the viral escape mechanism leading to delivery of the viral RNA into the cytoplasm. We set out to explore the nature of FCV attachment and uncoating using structural, biochemical and biophysical analyses. By cryogenic electron microscopy we have characterized the virus-receptor interaction at high-resolution. Using electron microscopy and an RNA release assay, we have investigated virion uncoating. Finally, we have explored the importance of receptor glycosylation, and oligomerisation.

Our analysis has allowed us to construct an atomic model of the major capsid protein VP1. Upon binding to fJAM-A, FCV undergoes a conformational change (rotation and tilting of the capsomeres). Flexibility in the receptor decorated virion has prevented high-resolution structure analysis of the conformational change or the virus-receptor interaction. We have, however, seen that the structural changes are limited to the capsid spikes. We hypothesised that the conformational change may be a priming step that would prepare the virus for uncoating upon internalisation. We found that upon lowering the pH below 5, receptor decorated virions disassembled, supporting this hypothesis. Disassembly of the virus-receptor complex at low pH presented a tool for estimating the quantity of receptor needed to prime the capsid for uncoating.

Cryo-EM studies reveal that FCV bound fJAM-A is monomeric although the receptor was found to be dimeric in solution as previously described for the human and murine homologues. Furthermore, it is hypothesised that this is the

form found at tight junctions between cells. We propose that disruption of fJAM-A homodimers may be the mechanism by which induction of viral uptake by endocytosis is triggered. Finally, we have confirmed the presence of an N-linked glycosylation on fJAM-A and show that the removal of this carbohydrate moiety does not affect viral binding *in vitro*.

Table of Contents

List of Tables

List of Figures

Publications

Vesivirus 2117 capsids more closely resemble sapovirus and lagovirus particles than other known vesivirus structures. Conley, M., E. Emmott, R. Orton, D. Taylor, D.G. Carneiro, K. Murata, I.G. Goodfellow, G.S. Hansman, and D. Bhella. 2017. *J Gen Virol*. 98:68-76 (see Appendices).

This work was excluded from the thesis as it did not fit the narrative.

Abbreviations

1-Ethyl-3-(3-dimethylaminopropyl) carbodiimide hydrochloride	EDC
Ammonium persulfate	APS
Atypical protein kinase C	aPKC
Baby hamster kidney	BHK
Bcl-2 associated X protein	Bax
Bovine serum albumin	BSA
Calcium dependent serine protein kinase	CASK
Carbon Dioxide	CO_2
Charge coupled device	CCD
Chinese hamster ovary	CHO
Complementary metal oxide semi-conductor	CMOS
Contrast transfer function	CTF
Coxsackie and adenovirus receptor	CAR
Coxsackie group B viruses	CVBs
Crandell Reese feline kidney cells	CrFK
Cryo-electron microscopy	CryoEM
Decay accelerating factor	DAF
Deoxyribonucleic acid	DNA
Direct detection device	DDD
Dissociation Constant	K_D
Electron microscopy	EM
Endoglycosidase H	EndoH
Ethylenediaminetetraacetic acid	EDTA
Eukaryotic translation initiation factor 4 G	eIF4G
European brown hare syndrome virus	EBHSV
Extracellular signal related kinase	ERK
Feline calicivirus	FCV
Feline junctional adhesion molecule A	fJAM-A
Field emission gun	FEG
Foetal bovine serum	FBS
Foot and mouth disease virus	FMDV
Fourier shell correlation	FSC
Glycophosphatidylinositol	GPI
Guanine nucleotide exchange factor	GEF
Hepatitis C virus	HCV
Herpes simplex virus	HSV
High pressure liquid chromatography	HPLC
Hydrochloric acid	HCl
Interferon response factor	IRF
Isothermal calorimetry	iTC
Junctional adhesion molecule A	JAM-A
Leader of the capsid protein	LC
Low melting point agarose	LMA
Lympthocyte function associated antigen 1	LFA-1
Magnesium chloride	$MgCl_2$
Molecular weight	MW
Monolithic active pixel sensors	MAPS
Multi-PDZ domain protein 1	MUPP1
Multiplicity of infection	MOI
N-acetylneuraminic acid	NANA

N-Hydroxysuccinimide	NHS
N,N,N',N'-tetramethylethane-1,2-diamine	TEMED
Non-structural	NS
N-terminal arm	NTA
Open reading frame	ORF
Particle stability thermal release assay	PaSTRy
Penicillin (100 units/ml) and Streptomycin (100µg/ml)	PenStrep
Peptide:N-Glycosidase F	PNGaseF
Phosphatase and tensin homologue	PTEN
Phosphate buffered saline	PBS
Phosphatidylinositol (3,4,5)-trisphosphate	PIP_3
Point spread function	PSF
Polar fourier transform	PFT
Polyacrylamide gel electrophoresis	PAGE
Poly-A binding protein	PABP
Poly-adenylated	PolyA
Polypyrimidine tract binding protein	PTB
Protease activated receptor	Par
Protein interacting with C-kinase	PICK-1
Protein kinase B	Akt
Rabbit haemorrhagic disease virus	RHDV
Ras related protein 1	Rap1
Response units	RU
Revolutions per minute	rpm
Ribonucleic Acid	RNA
RNA dependent RNA polymerase	RdRp
Root mean square deviation	RMSD
Roswell Park Memorial Institute	RPMI
San Miguel sea lion virus	SMSV
Signal to noise ratio	SNR
Small angle x-ray scattering	SAXS
Sodium Chloride	NaCl
Sodium dodecyl sulphate	SDS
Surface plasmon resonance	SPR
Three-dimensional	3D
Tobacco mosaic Virus	TMV
Tomato bushy stunt virus	TBSV
Transmission electron microscopy	TEM
Turnip yellow mosaic virus	TYMV
Two-dimensional	2D
Varicella zoster virus	VZV
Vascular cell adhesion molecule 1	VCAM-1
Vesicular exanthema of swine virus	VESV
Virion protein g	VPg
Zonula occludens	ZO

1 Introduction

1.1 Viruses

Viruses are the smallest class of microorganisms, ranging from 20-400nm in diameter, and have been shown to infect all forms of life on earth i.e.) plants, animals, humans, bacteria etc. They are composed of a nucleic acid genome (ribonucleic acid; RNA or deoxyribonucleic acid; DNA) and a protein coat (capsid) which functions to protect the genome and deliver it into the host cell for viral replication. The genomes of viruses can be single stranded RNA (positive or negative sense), double stranded RNA, single stranded DNA or double stranded DNA. Viruses must bind to a cellular receptor on the surface of a cell which determines not only the host specificity but also the tissue tropism of the microorganism. Viruses may also be enveloped, where the capsid is surrounded by a cell-derived lipid bilayer. The capsid proteins of non-enveloped viruses contain the specific receptor binding sites whereas in enveloped viruses, viral structural proteins containing the receptor binding sites are inserted into the lipid envelope to allow entry of the virus into the host cell, often by membrane fusion at the plasma membrane. Viral genomes encode both structural proteins which make up the progeny viral particles as well as non-structural proteins which function to replicate the viral genome and hijack the cellular protein translation machinery to do so. Some non-structural proteins have also evolved a mechanism/function to evade the host immune response to infection.

The first virus to be discovered was tobacco mosaic virus (TMV) in the late 1800's when Adolf Mayer described a mosaic disease of tobacco plants which could be transmitted to other plants by rubbing them with a filtered extract from the infected plant (in 1879). Martinus Beijerinck, in 1898, described similar findings although went a step further to describe the infectious agent as contagious living fluid ('contagium vivum fluidum'). These contagious living fluids were later described/termed as viruses and this particular disease causing agent was termed tobacco mosaic virus. The second virus to be discovered, and the first animal virus discovered, was foot and mouth disease virus (FMDV) in 1898 by Friedrich Loeffler and Paul Frosch. These were the first to describe the virus as a tiny particle rather than an infectious liquid and even filtered and heated (inactivated) the agent before using it to vaccinate cows and sheep. The

first human virus to be discovered was the causative agent of yellow fever in 1901 by Walter Reed, a US army physician. Helmut Ruska proceeded to visualise several virus structures in the electron microscope throughout the late 1930's including poxviruses, TMV, varicella zoster virus (VZV) and bacteriophages and further proceeded to propose a classification system based on virus structure in 1943 (Kruger et al., 2000; Rybicki and Kightley, 2015).

1.2 Virus Structure

Viruses of different shapes and sizes, regular and irregular have been observed. Generally, non-enveloped viruses adopt a more regular conformation than enveloped viruses although the inner contents or capsid of enveloped viruses often adopt a regular conformation. Some viruses are spherical while others are more rod shaped, most of which exhibit high degrees of symmetry. Crick and Watson suggested that viral capsids must be formed by multiple copies of a set of capsid proteins (Crick and Watson, 1956). This greatly reduces the genome requirement for the virus which is pivotal in small viruses with a limited capsid volume and therefore coding capacity. Some viruses only encode a single capsid protein while some assemble their capsids from more capsid proteins (although this requires a larger genome). For these multiple capsid proteins to form an intact viral capsid, the capsid must exhibit a degree of symmetry, typically an icosahedral shell or a helical tube (Caspar and Klug, 1962; Crick and Watson, 1956).

1.2.1 Symmetry

Caspar was the first to demonstrate that spherical viruses showed icosahedral symmetry (with 5, 3 and 2 fold symmetry axes) (Caspar, 1956). Symmetry axes are present in polyhedra such as tetrahedrons, cubes, octahedrons, icosahedrons and dodecahedrons (see Figure 1). In these structures, each have identical faces, edges and vertices. The line where two faces meet is known as an edge whereas vertices are known as the point at which a number of faces meet (Prasad and Schmid, 2012).

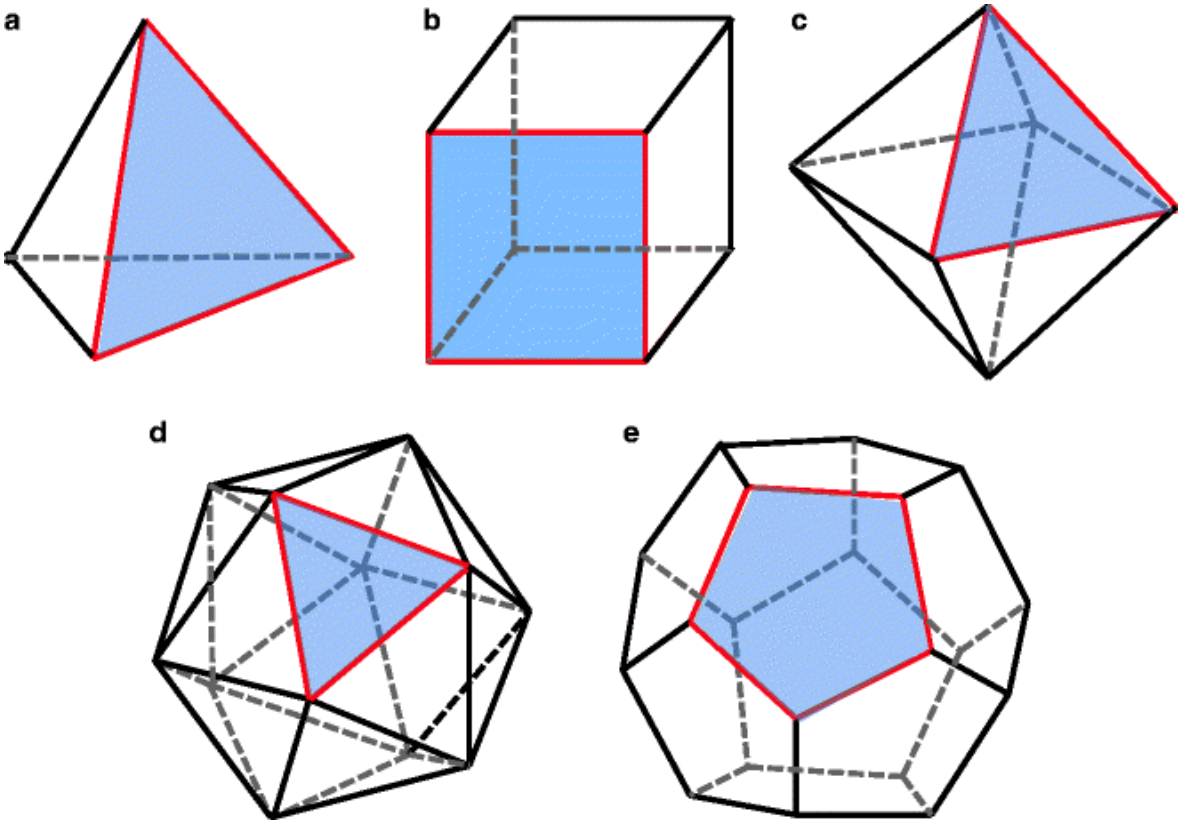

Figure 1- Five polyhedra illustrating aspects of symmetry

Each of the structures in this figure have one of their faces coloured in blue: (a) a tetrahedron, (b) a cube, (c) an octahedron, (d) an icosahedron and (e) a dodecahedron. Solid and dotted lines represent the edges of the structures. Taken from Prasad and Schmid, 2012.

For each of these structures, the number of faces, edges and vertices can be calculated using the formula: $F + V = E + 2$. For example, the tetrahedron has 4 faces, 6 edges and 4 vertices (4 + 4 = 6 + 2) and has both two and three-fold symmetry axes. A cube has 6 faces, 12 edges and 8 vertices and exhibits two, three and four-fold symmetry. An octahedron has 8 faces, 12 edges and 6 vertices with two, three, and four-fold symmetry. An icosahedron contains 20 faces, 30 edges and 12 vertices and exhibits two, three and five-fold symmetry. Finally, a dodecahedron is composed of 12 faces, 30 edges and 20 vertices and also has two, three and five-fold symmetry axes. Caspar was the first to demonstrate icosahedral symmetry in spherical viruses, showing that the characteristic spikes of tomato bushy stunt virus (TBSV) were only present due to the five-fold symmetry of the capsid (Caspar, 1956). This was later supported when icosahedral symmetry was also observed in another plant virus, turnip yellow mosaic virus (TYMV) (Klug et al., 1957).

Icosahedral symmetry allows the assembly of 60 identical proteins while retaining the two, three and five-fold symmetry axes (see Figure 2). As visible in Figure 2, the five-fold symmetry axis passes through the vertices of the icosahedron while the three-fold axes dissect through the centre of the faces and the two-fold axes go through the middle of each edge of the icosahedron.

While 60 subunits can be assembled identically into an icosahedron, many virus particles are composed of more than 60 subunits which cannot form an icosahedron if arranged in identical positions. This can, however, be achieved if minimal distortions are permitted between each subunit where they are arranged in almost identical positions (Caspar and Klug, 1962). The icosahedron is first enlarged and then each face/triangle is further divided into more triangles (triangulation). Due to this division by triangles, only some triangulation numbers can exist: 1, 3, 4, 7 etc as a triangle cannot be divided into 2, 5 or 8 smaller triangles. These are referred to as the *T* numbers of the capsids. If a capsid is composed of 60 subunits, it is said to have *T*=1 icosahedral symmetry.

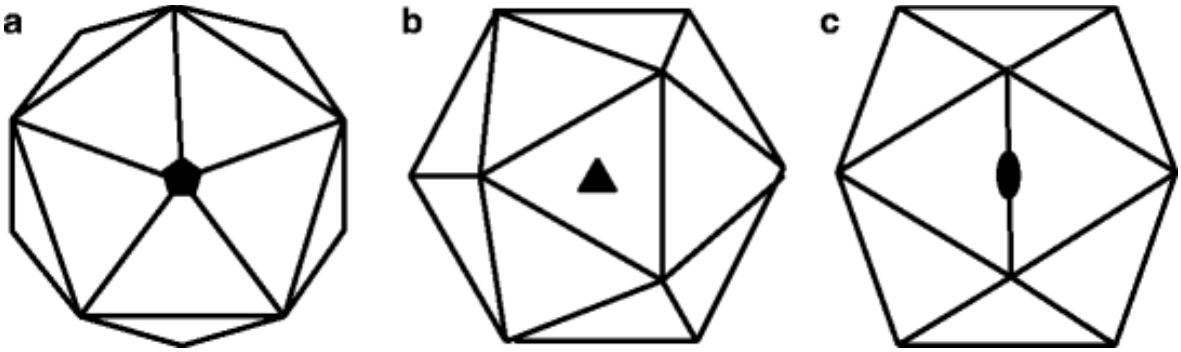

Figure 2- Icosahedral symmetry axes

Icosahedrons displayed looking through the various symmetry axes: (a) five-fold, (b) three-fold and (c) two-fold. Taken from Prasad and Schmid, 2012.

Likewise, if a capsid is composed of 180 subunits, it has *T*=3 icosahedral symmetry and 240 subunits has *T*=4 symmetry and so on. A prolate icosahedron may also exist, like that seen in the bacteriophage phi29, where the icosahedron is stretched in one direction (characterised by *T* number and an elongation number, *Q*: for phi29 *T*=3 and *Q*=5) (Prasad and Schmid, 2012).

As the three-fold symmetry axis passes through each of the faces of the icosahedron, it divides each face into three equal subunits. Each of these subunits is termed an asymmetric unit. Equally, these asymmetric units may consist of multiple proteins for capsids with triangulation numbers of *T*>1. As mentioned previously, the interacting states of capsid subunits with these symmetries cannot be identical/equivalent so they are termed quasi-equivalent. Caspar and Klug proposed that in an icosahedral capsid with quasi-equivalent subunits, these subunits exhibit similar inter-subunit interactions although show some minor distortions to allow for an icosahedral shell to be formed. This quasi-equivalence results in the formation of three-fold locations/axes on the icosahedron as well as the five-fold. Five-fold locations are visible as pentamers while three-fold are visible as hexamers. All icosahedra, independent of *T* number, contain 12 pentamers/five-fold positions. The number of hexamers/three-fold positions, however, varies with *T* number and can be defined as 10(*T* – 1). These arrangements were termed morphological units (Caspar and Klug, 1962).

Some capsid proteins contain ‘flexible’ arms which may act as a switch between different conformations of the same capsid protein. Many small viruses of animals and plants exhibit *T*=3 icosahedral symmetry with 180 copies of one capsid protein. Three quasi-equivalent forms of the capsid protein exist which are generally termed A, B and C and together form one asymmetric unit of the capsid and allow the formation of an icosahedral structure. These subunits form two different types of dimers: A/B and C/C with the A/B dimers located around the five-fold symmetry axes and the C/C dimers located in alternating positions (with A/B dimers) around the three-fold symmetry axes. This results in the capsid comprising 60 A/B dimers and 30 C/C dimers (Prasad and Schmid, 2012). These morphological subunits which comprise the viral capsid may also be formed of trimers (such as in nodaviruses) or even pentamers/hexamers for larger viruses (Ho et al., 2017).

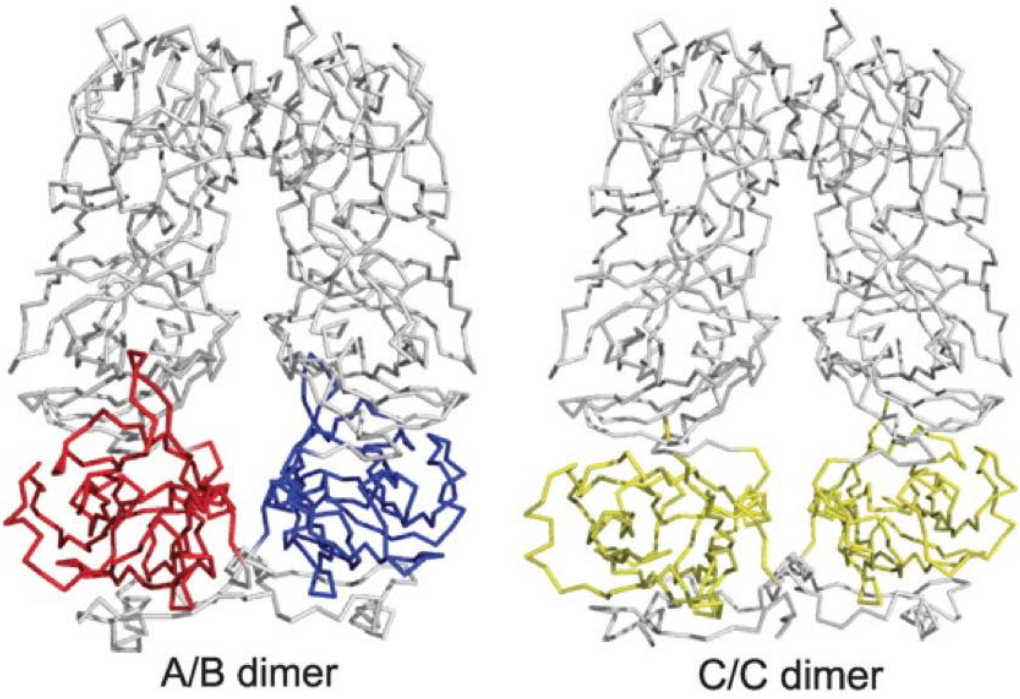

Figure 3- A/B and C/C conformations of Feline Calicivirus VP1 capsid protein

A/B and C/C conformations of the VP1 capsid protein of Feline Calicivirus (FCV) strain 5 illustrating the bent appearance of the A/B dimer and the flat appearance of the C/C dimer enabled by conformational switching induced by the N-terminal arm of the protein. Bending of the capsid proteins at the hinge region between the S domain (coloured) and the P domain (grey) is illustrated by the appearance of a more extended S domain when comparing that of the A/B (red/blue) and C/C (yellow) dimers. Taken from Ossiboff, Zhou et al, 2010. PDB ID: 3M8L.

The N-terminal arm of the capsid protein has been implicated in the switch between these two conformations. Due to the curvature of the icosahedral capsid, the A/B dimers adopt a bent conformation while the C/C dimers adopt a flat conformation (see Figure 3). This conformational switching of capsid proteins is seen in many viruses including FCV, human norovirus and papovaviruses (*T*=7).

Picornaviruses present an interesting variation as they exhibit *T*=3 icosahedral symmetry but rather than the three conformations of the one protein, three different proteins assemble to form the asymmetric unit: VP1, 2 and 3. The VP1, VP3 and VP2 proteins occupy the same coordinates as the A, B and C conformations, respectively, although because the capsid is formed of non-identical subunits, it is termed pseudo *T*=3. Larger, more complex icosahedral viruses often use internal scaffolding proteins as well as other factors including maturation-dependent proteolysis to aid in the formation of their capsid e.g. double stranded DNA bacteriophages, herpes simplex viruses and adenoviruses (Prasad and Schmid, 2012; Rossmann et al., 1986).

1.2.2 Helical symmetry

Many rod-shaped viruses adopt helical symmetry, such as rhabdoviruses, and some use helical symmetry to assemble nucleocapsids. Helical structures are characterised by a number of factors including the location of the subunits in relation to the axis, the rotation of each subunit and the axial rise for each subunit. The best characterised virus with helical symmetry is tobacco mosaic virus (TMV). The genomic RNA of TMV is located within a groove of the surrounding capsid proteins which have been shown to form an alpha helical structure (Caspar and Klug, 1962; Franklin and Klug, 1956; Namba and Stubbs, 1986; Prasad and Schmid, 2012).

1.3 Virus Entry

Viruses have evolved many ways to hijack cellular functions and machinery in order to enter the cell, replicate and release progeny viral particles. Enveloped viruses often fuse with the plasma membrane to release the capsid/nucleoprotein into the cytoplasm of the target cell. This membrane

fusion requires the virus to present a specific type of protein on the viral envelope which can insert into the plasma membrane of a target cell and bring the two membranes into close proximity for fusion. Non-enveloped viruses, however, mostly rely on binding to a specific receptor (or set of receptors) on the cell surface and triggering the cell to internalise the virus where it must then escape the internal organelle (e.g. endosome) to deliver its genome into the cell for replication to occur. Genome release is often associated with a conformational change in the capsid, pore formation and/or membrane lysis. Conformational changes usually result in the exposure of hydrophobic regions, for example, those induced in the FCV capsid upon fJAM-A engagement (Ossiboff et al., 2010). These structural alterations may be triggered by a number of factors including receptor binding or a drop in pH (within the endosome) (Cossart and Helenius, 2014; Lozach et al., 2011; Marsh and Helenius, 2006).

Attachment factors on the cell surface, usually carbohydrates such as heparin sulphate or sialic acid, may act to capture virus particles and concentrate them in an area of the cellular plasma membrane. Unlike receptors, attachment factors cannot promote entry into the cell without an interaction with another molecule/protein. Receptors have the ability to induce conformational changes in some virus particles upon binding, activate specific cellular signalling pathways as well as stimulating endocytosis. As receptors play such a key role in viral internalisation, species and tissue specificity is determined by binding of a virus to a particular receptor(s). It is thought that the affinity of virus particles may be low although binding to multiple receptors on the cell surface likely serves to increase the affinity of the interaction. This is one possible explanation as to why so many viruses use attachment factors to initially capture incoming virus particles and then pass them on to receptors for internalisation. For example, *T*=3 virus particles are composed of 180 capsid proteins and therefore contain up to 180 possible receptor binding sites. Binding of the virus to multiple receptor copies may act to cluster the proteins and trigger a signalling cascade such as entry via endocytosis. Some viruses do this by utilising cell signalling proteins as receptors, such as integrins (Cossart and Helenius, 2014; Marsh and Helenius, 2006).

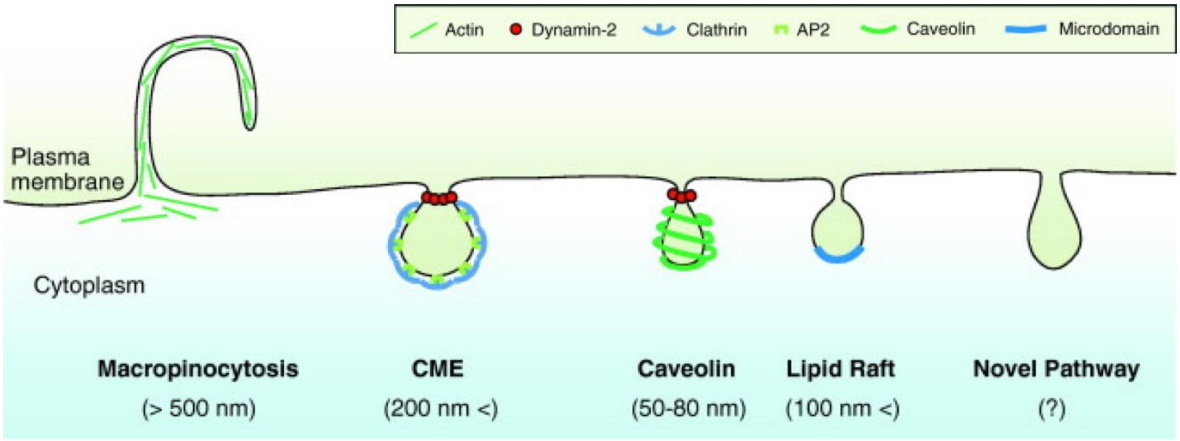

Figure 4- Mechanisms of internalisation utilised by viruses

A schematic showing the different mechanisms utilised by viruses to mediate internalisation and entry into a host cell. Typical 'cargo' sizes for each mechanism are listed along with the different cellular factors involved in the processes. Abbreviations: CME (clathrin mediated endocytosis). Taken from Lozach et al, 2011).

Different viruses have evolved to utilise many different cellular internalisation pathways. For example, herpes simplex virus-1 enters host cells via macropinocytosis, murine polyomavirus utilises lipid rafts and many viruses gain entry into cells via clathrin mediated endocytosis (such as feline calicivirus, human rhinovirus-2 and influenza A virus) (Devadas et al., 2014; Lozach et al., 2011; Snyers et al., 2003; Stuart and Brown, 2006). Simian virus-40 is able to utilise both lipid rafts and caveolin dependent endocytic pathways while other novel entry pathways may still exist for viruses including human papilloma virus-16 (Lozach et al., 2011; Pelkmans, 2005). An overview of the different entry mechanisms utilised by different viruses and the cellular factors involved is presented in Figure 4.

Endocytosis is a general term used to describe the uptake of fluid, macromolecules and plasma membrane components from the surface of the cell for recycling or degradation via the endosome-lysosome acidification pathway. Incredibly, 50-180% of the plasma membrane surface area is recycled into and back out of the cell every hour. The early endosomes are considered a ‘sorting office’ for incoming cargo, with viruses usually targeted to late endosomes which move to the peri-nuclear region where they fuse with lysosomes (Huotari and Helenius, 2011). The reduction in pH from endosomes to lysosomes occurs due to membrane bound protein complexes known as V-ATPases. V-ATPases are proton pumps which form a pore in the organelle (e.g. endosome) membrane to allow the passage of protons into the lumen, thereby lowering the pH (Huotari and Helenius, 2011).

1.3.1 Clathrin dependent endocytosis

The most commonly used method employed by viruses to enter a host cell is clathrin-mediated endocytosis. Clathrin mediated endocytosis internalises both the virus and the receptor(s) into early and late endosomes where a drop in pH may trigger the release of the viral genome. The process is continuous and rapid with the virus particles exposed to low pH within minutes after triggering internalisation. Some viruses may dissociate from their receptors at this point during internalisation although others remain bound within the endocytic pathway. Virus particles must then adopt a mechanism to deliver their genome from the endosome into the cytoplasm of the cell. Some viruses do this by

disrupting the membrane of the endosomes while others form a pore in the capsid and endosomal membrane through which transfer of the genome may occur. The degree of acidification likely acts as a switch/cue for the virus, signalling the appropriate point at which to trigger genome release. This may occur in early endosomes with a pH value of approximately 6.0 to 6.5, in late endosomes with a pH of approximately 5.0 to 6.0 or in lysosomes with a pH value of 4.5 to 5. Differences in pH within the cell have previously been shown to regulate the transport of cargo in endocytic and secretory pathways. A drop in pH, however, may not be enough to trigger the release of the viral genome and another step may be needed such as a conformational change in the capsid induced by receptor/protein binding. (Helenius, 2013; Lozach et al., 2011; Marsh and Helenius, 2006).

During clathrin mediated endocytosis, clathrin is recruited to the cytosolic side of the plasma membrane where it induces curvature and internalisation of a section of plasma membrane to form a vesicle (within approximately 3 minutes). The clathrin is then released from the vesicle (within 5 to 20 seconds) which fuses with an early endosome to begin the gradual lowering of pH and progression towards late endosomes and lysosomes. Many different adaptors, cofactors and tethering proteins are involved in the pinching of the membrane and formation of the initial vesicle/endosome and over ninety kinases have been shown to affect virus internalisation by clathrin mediated endocytosis (Cossart and Helenius, 2014; Marsh and Helenius, 2006).

1.3.2 Clathrin independent endocytosis

The best characterised mechanisms of clathrin independent endocytosis are known as the caveolar/raft pathways. These processes are thought to specialise in the internalisation of lipids, lipid rafts and GPI-anchored proteins. Many proteins are involved in this internalisation pathway including actin, dynamin 2, caveolin-1 and Rho-GTPases. Internalisation may occur independently of caveolin-1 or through caveolae activated for transport across longer distances. Viruses that are internalised via the caveolar/raft pathway are firstly transported to caveosomes which have a neutral pH and following a signalling event, traffic via microtubules in a caveolin independent manner to the endoplasmic reticulum. Viral genome release may then occur following

interaction with specific proteins or due to the different cellular environment. Other clathrin independent pathways do not involve trafficking to the endoplasmic reticulum and may, instead, traffic to endosomes although this pathway is not yet clearly understood. Macropinocytosis is another clathrin independent pathway utilised by viruses to gain entry into a host cell. Macropinocytosis is both actin and cholesterol dependent and involves either caveosomes or endosomes post internalisation (Marsh and Helenius, 2006).

1.4 Junctional Adhesion Molecule A (JAM-A)

1.4.1 JAM-A structure

JAM-A is expressed in a variety of cell types. It is a major component of tight junctions between epithelial and endothelial cells and can also be found on the surface of platelets and leucocytes (including monocytes, neutrophils, B and T cells). JAM-A was the first Ig-like molecule that was identified at tight junctions between both epithelial and endothelial cells and was originally characterised as a platelet receptor (F11) (Ebnet et al., 2004; Prota et al., 2003).

Junctional adhesion molecule A (JAM-A) is a member of the immunoglobulin superfamily. JAM-A is composed of a short cytoplasmic tail, transmembrane domain and an ectodomain present on the surface of the cell which contains two immunoglobulin-like (Ig) motifs. The ectodomain can be divided into two subdomains, D1 and D2 with D1 forming the most outer portion of the protein (furthest away from the plasma membrane) and responsible for dimer formation between JAM proteins. D2 also contains an N-linked glycosylation site which may serve to regulate protein stability.

The recombinant soluble ectodomain of murine JAM-A has been shown to form U-shaped dimers (as well as some tetramers) in solution. At the centre of the dimerisation domain are two stacked salt bridges with a structural motif of R(VIL)E identified in this region. These oligomers, however, have been shown to dissociate into monomers below pH5, possibly due to the disruption of the salt bridges (Kostrewa et al., 2001). The disruption of JAM-A dimers through pH reduction is reversible and may inhibit JAM-A dependent signalling during

Figure 5 has been removed due to copyright restrictions.

Figure 5- Structure of human JAM-A

A ribbon diagram of the human JAM-A dimer is shown with one monomer in orange and another monomer in blue. D1 and D2 domains are labelled with salt bridges shown in green. The plasma membrane (and JAM-A transmembrane domain) would be located at the bottom of the D2 domains in this figure. Taken from Prota et al, 2003. PDB ID: 1NBQ.

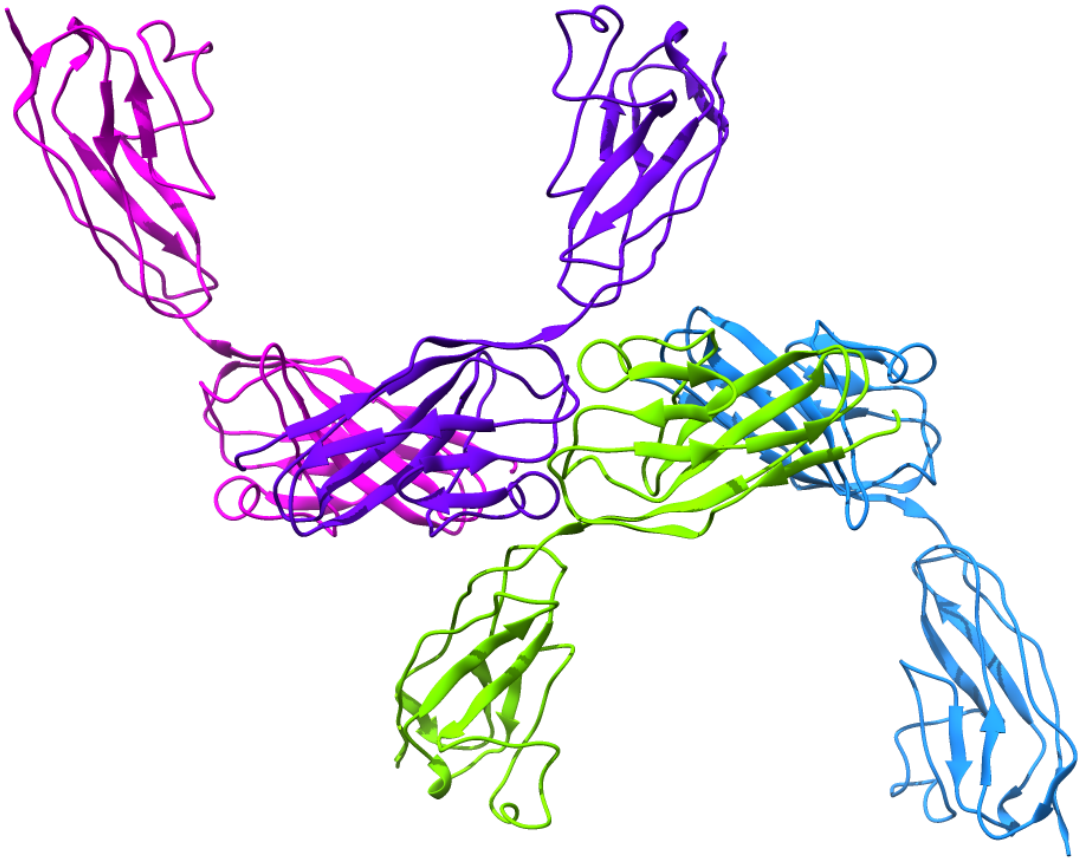

Figure 6- Human JAM-A dimers interacting in *trans*

One U-shaped JAM-A dimer is shown in pink and purple while another is shown in green and blue (hypothesised to be expressed by an adjacent cell from the other dimer shown). PDB ID: 1NBQ.

intracellular trafficking. The assembly into these oligomeric forms is believed to occur during or shortly after movement through the secretory pathway. It is thought that these U-shaped dimers (formed via *cis* interactions) may also interact with other U-shaped dimers on adjacent cells by forming *trans* interactions as illustrated in Figure 6 (Kostrewa et al., 2001; Monteiro et al., 2014).

The human JAM-A ectodomain was predicted to form dimers as seen with murine JAM-A by size exclusion chromatography. Crystallography showed U-shaped dimers similar to murine JAM-A with the D1 and D2 domains bent at an angle of approximately 125° relative to each other within each monomer. This structure revealed the presence of four salt bridges within each dimer between positions Arg-59 and Glu-61 (and vice versa) and between Lys-63 and Glu-121 (and vice versa) as well as surrounding hydrophobic interactions. Prota et al also described a model of *trans* interactions between JAM-A dimers of adjacent cells within tight junctions analogous to that proposed for murine JAM-A. This model proposes a separation of cells by around 85Å which remains in line with predicted distances of 100Å at tight junctions between cells (Prota et al., 2003).

1.4.2 JAM-A in tight junctions and signalling

Tight junctions between adjacent cells serve as a barrier mechanism for the maintenance of internal and external environments such as that needed in the establishment of different tissues. They serve to regulate homeostasis via the diffusion of small molecules and ions and enable signal transduction between the intracellular and extracellular environments through many different proteins. Tight junctions are formed of several types of transmembrane proteins including claudins, occludins, coxsackie-adenovirus receptors and JAMs. Many cellular processes may be regulated via tight junctions and their associated proteins including cell differentiation and proliferation as well as polarity.

E-cadherin and nectin are proposed to provide initial points of contact between neighbouring cells prior to the recruitment of other junctional proteins. After the establishment of these puncta, JAM-A and occludin are thought to be

Figure 7 has been removed due to copyright restrictions.

Figure 7- Stages of contact formation between cells

The four stages of cell-cell contact formation from the formation of lamellipodia (A), adhesion between the lamellipodia of two cells (B), polarisation of the cells (C) and the formation of fully formed tight junctions (TJ) and adherens junctions (AJ) between the cells (D). Taken from Ebnet et al, 2004.

recruited during tight junction formation (see Figure 7). ZO-1 (Zonula occludens-1/tight junction protein-1) or ZO-2 are thought to be sufficient for the recruitment of tight junction components during barrier formation (Bauer et al., 2010; Monteiro and Parkos, 2012).

Many transmembrane proteins are required for tight junction formation and the regulation of paracellular permeability. Although many of these proteins exert different functions, a common factor is their interactions with extracellular proteins on the surface of adjacent cells within tight junctions. These interactions may occur in *cis* (between proteins in the membrane of the same cell) or in *trans* (between proteins in membranes of adjacent cells). Interactions also occur with adaptor proteins on the cytoplasmic side of the cell membrane which may induce signalling pathways involved in many cellular processes.

JAM-A contains PDZ-binding motifs in the C-terminal cytoplasmic tail of the protein which can interact with six adapter proteins in a PDZ-dependent manner (requiring the Phe-Leu-Val motif). JAM-A has the ability to interact with ZO-1, MUPP1, afadin, CASK, PICK-1 and Par-3. Interactions of Par-3 with both Par-6 and aPKC have been suggested to be important in the formation and assembly of tight junctions. Due to the strong interaction between Par-3 and JAM-A, JAM-A has been hypothesised to act as a docking site for the core complex (including Par-3 and aPKC), a step that is crucial for establishing the polarity of cells as well as tight junction formation (Paris et al., 2008). The inhibition of PKC has also been shown to reduce the expression of JAM-A, possibly through phosphorylation as JAM-A in platelets is phosphorylated by PKC. JAM-A phosphorylation at serine-285 by PKC has been shown to affect the assembly of tight junctions and therefore also epithelial barrier functions (Monteiro and Parkos, 2012).

Knock outs of JAM-A act to enhance the permeability between epithelial cells and causes leaky colonic epithelium in JAM-A knock out mice. JAM-A -/- mice also present with an altered pro-inflammatory cytokine profile and an increase in the infiltration of leucocytes among mucosal epithelia (Gonzalez-Mariscal et al., 2014). The addition of the soluble JAM-A ectodomain (herein referred to as JAM-A) in rodents acts to reduce leucocyte transmigration between endothelial cells (Reglero-Real et al., 2016). JAM-A antibodies have been shown to prevent

reassembly of tight junctions and affect the permeability of the junctions. Similar effects were also seen when the JAM-A ectodomain was expressed as a fusion protein with IgG-Fc. Other evidence also suggests that the disruption of the JAM-A dimer interface prevents the clustering of JAM-A within tight junctions showing that the protein is dimeric in its active form (Mandell et al., 2004).

JAM-A has been found to form not only homophilic interactions but also heterophilic through binding to ß1 and 2 integrins as well as LFA-1 within tight junctions (Chiba et al., 2008). It has been suggested that the interaction with JAM-A maintains the stability of ß1 integrin while at the surface of the cell. The interaction between JAM-A and LFA-1 likely mediates transendothelial migration of leucocytes during an immune response. Cytokines such as interferon-γ and tumour necrosis factor-α have the ability to induce the internalisation of JAM-A and therefore enhance the permeability of epithelial and endothelial cell barriers (in a clathrin dependent manner in some cases, also affecting other proteins with the tight junctions). JAM-A also has the ability to affect cell migration through its interaction with afadin and PDZ-GEF2 (guanine nucleotide exchange factor) which results in the activation of Rap1a and stabilisation of ß1 integrins, which in turn enhances migration of the cell. Interestingly, Rap1a also plays a role in the *trans*-dimerisation of E-cadherin and its organisation within tight junctions. It has been proposed that PDZ-containing scaffold proteins such as ZO-1, afadin and PDZ-GEFs may interact with tight junctional proteins containing PDZ binding motifs to direct the maturation of the junctions and maintain barrier function (as well as some containing the ability to interact with actin and possibly influence cytoskeletal arrangement and barrier integrity) (Ebnet et al., 2004; Monteiro and Parkos, 2012).

A known interacting partner of JAM-A is ZO-1 which, together with ZO-2, can associate with a large array of proteins which have regulatory functions in cellular processes including transcriptional regulation and cellular proliferation such as Jun, Fos and Cyclin D1. JAM-A has been shown to affect the migration of cells with JAM-A silencing resulting in reduced migration due to the inability of growth factors to activate the ERK pathway (extracellular signal regulated kinase) (Gonzalez-Mariscal et al., 2008). Reduced migration in epithelial cells

can be observed following reduced expression of JAM-A and decreased Rap1 activity resulting in reduced levels of β1 integrin. Afadin expression and interaction with JAM-A is necessary for the Rap1 interaction and promotion of cellular migration (Severson and Parkos, 2009).

JAM-A dimerisation has been show to regulate cellular proliferation through the Akt/β-catenin pathway. A loss of JAM-A results in an increase in PIP_3 levels (via PI3K activation and PTEN inactivation) resulting in the recruitment of Akt to the membrane. Akt is phosphorylated and can in turn phosphorylate β-catenin resulting in its nuclear translocation and activity as a transcription factor promoting cellular proliferation. It was therefore concluded that JAM-A *cis* dimerisation decreases proliferation by reducing transcriptional activation via the Akt/β-catenin pathway (Nava et al., 2011).

JAM-A also localises to the basolateral membrane, localisation of which may be controlled by either JAM-A phosphorylation or dimerisation. A model has been proposed where the interactions between dimers may control the localisation of JAM-A and its effect on cell migration. *Cis*-interactions (but not *trans*) are expected in sub-confluent or spreading cells and may favour proliferation, however, *trans*-interactions would be seen in confluent cells with established tight junctional barriers and may even play a role in cellular senescence. While salt bridges form between two JAM-A proteins interacting in *cis*, it is thought that van der waals forces are responsible for *trans* interactions. The phosphorylation of the cytoplasmic tail of JAM-A at serine-285 results in the re-localisation to tight junctions rather than the basolateral membrane (Monteiro et al., 2014; Monteiro and Parkos, 2012).

1.4.3 Glycosylation of JAM-A

Protein glycosylation can affect conformation, stability, protection from degradation, intracellular trafficking as well as protein secretion. Glycosylation may be N or O-linked. O-glycans are attached to a hydroxyl group of a serine or threonine residue although no consensus sequence has been identified for this type of glycosylation. In N-linked glycosylation, the oligosaccharide is attached to the amine group of an asparagine residue of a protein with the consensus motif of NXS/T (with X representing any amino acid except proline). N-linked

glycosylation only occurs on proteins that are transported via the secretory pathway. The oligosaccharide begins to assemble on the cytoplasmic side of the endoplasmic reticulum and is then flipped into the lumen where it is fully assembled and added to a protein. Once the protein has folded correctly, it passes through the golgi apparatus of the cell where the oligosaccharide may be processed further involving the possible addition and removal of glycans. The protein folding requirement of N-linked glycans was first demonstrated for the glycoproteins of influenza virus (HA) and vesicular stomatitis virus (G) (Roth et al., 2012; Schwarz and Aebi, 2011; Xu and Ng, 2015).

N-linked glycosylation of proteins is initiated within the endoplasmic reticulum of mammalian cells where a diverse array of glycans can be added to a newly synthesised protein. Glycans can be high mannose, hybrid or complex (see Figure 8). A terminal N-acetylneuraminic acid (NANA) has been linked to protein half-life although Chinese hamster ovary (CHO) cells lack the ability to produce α2,6 linked sialic acid so produce α2,3 linked NANA instead. It has also been demonstrated that low temperatures (30°C) result in a decrease in sialic acid incorporation into proteins. CHO and baby hamster kidney (BHK) cells have been shown to process glycoproteins in a similar manner to humans and so are often used in the production of recombinant glycoproteins for therapeutics (Hossler et al., 2009).

N-linked glycosylation at position 185 has been shown to regulate human JAM-A dimerisation and protein stability/half-life although this glycosylation is not required for the transport of JAM-A. The glycosylation of JAM-A, however, controls cellular migration and is involved in LFA-1 binding. Among cell lines tested, JAM-A glycosylation always contains sialic acid whereas the presence of fucose is only observed in epithelial cells. N-glycosylation of D2 of the JAM-A ectodomain has been shown to stabilise JAM-A dimers despite the dimerisation interface being present only within D1. Glycosylation has previously been shown to regulate homodimerisation of E and N-cadherin (Scott et al., 2015).

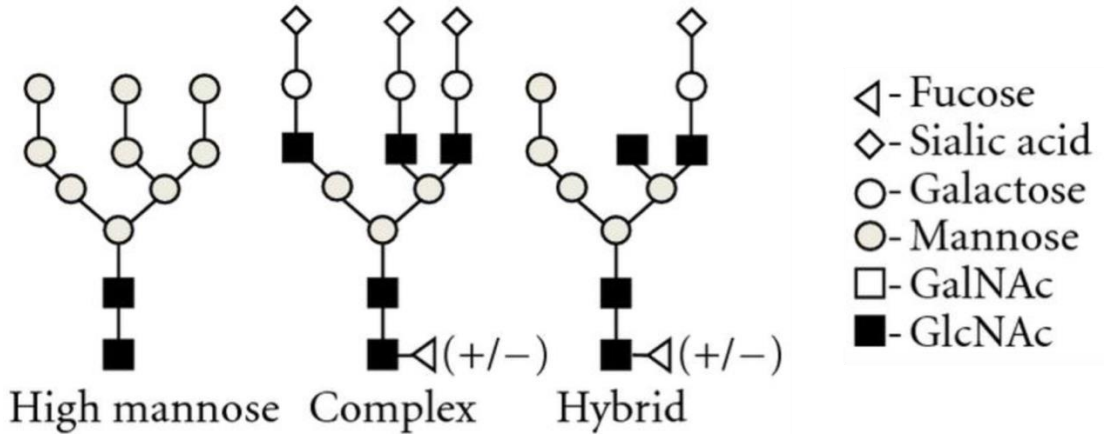

Figure 8- N-glycosylation structures

The three basic core structures of N-linked glycans: high mannose, complex and hybrid. Glycans are linked to proteins via their initial GlcNAc (shown as black squares). Taken from Roth et al, 2012.

1.4.4 JAM-A as a receptor for Reovirus and Hom-1

JAM-A is the cellular receptor for reovirus which has been shown to bind to JAM-A at the top of the dimer interface via residues Glu61, Lys63 and Leu72. The σ1 head of reovirus has the ability to bind to monomeric JAM-A as well as disrupt JAM-A dimers. Residues Glu61 and Lys63 participate in the stabilisation of JAM-A dimers via the salt bridges which illustrates how engagement of JAM-A by reovirus σ1 results in the destabilisation and monomerisation of JAM-A. Low affinity interactions with carbohydrate moieties are hypothesised to localise reovirus to the cellular membrane where it can then laterally move within the membrane until the virus is able to bind to JAM-A via a much higher affinity interaction (a K_D of approximately 2.4nM) (Guglielmi et al., 2007). Two σ1 trimers have been observed bound to three D1 JAM-A ectodomain monomers although this complex is unstable below pH5. Interestingly, the K_D of the JAM-A D1-D1 interaction was 11μM compared to 2.4nM for σ1-D1 interaction which suggests that the higher affinity for σ1 than other JAM-A monomers may be involved in reovirus binding and disruption of JAM-A dimers (Kirchner et al., 2008).

Hom-1 was the first calicivirus found to replicate in human cells and was isolated following the accidental infection of a laboratory employee with a vesivirus; San Miguel sea lion virus (SMSV). JAM-A has been shown to render non-permissive cells susceptible to Hom-1 infection although the cytoplasmic domain of JAM-A was shown to be dispensable for infection suggesting that it is not involved in triggering the entry of the virus. The same was observed with reovirus although intracellular FCV could not be detected with these JAM-A mutants showing the requirement of the cytoplasmic domain in FCV internalisation and entry. In contrast, β1 integrin has been proposed to enhance the internalisation of reovirus (Sosnovtsev et al., 2017).

1.5 Caliciviridae

Caliciviruses are non-enveloped, single stranded, positive sense RNA viruses. The *Caliciviridae* are sub-divided into the genera: 'Norwalk-like viruses' (Norovirus), 'Saporro-like viruses' (Sapovirus), *Lagovirus, Nebovirus and Vesivirus* (Green et al., 2000).

Both Noroviruses and Sapoviruses are renowned for causing human gastrointestinal disease (with Neboviruses causing bovine enteric disease). The prototypical member of the 'Norwalk-like viruses' is Norwalk virus which was first described following a gastroenteritis outbreak in 1968 in Norwalk, Ohio. The virus was initially classified as a picornavirus due to its appearance in electron microscopy but later classified as a calicivirus based on its use of a single capsid protein. Sapporo virus is the prototype stain of the 'Sapporo-like viruses' and was associated with an outbreak of gastroenteritis in 1982 in infants in Sapporo, Japan (Green et al., 2000).

Lagoviruses infect lagomorphs (for example, rabbits and hares) such as European brown hare syndrome virus (EBHSV) which was found to be the causative agent in a disease outbreak in Denmark in 1982. Liver necrosis and intravascular coagulation were described as a highly fatal consequence of infection with rabbit haemorrhagic disease virus (RHDV) in 1990. The RHDV genome was also the first full length sequence of a calicivirus reported (Green et al., 2000).

Vesiviruses may infect and cause a wide range of symptoms in many animal species (Pesavento et al., 2008). The first calicivirus found to cause disease was the vesicular exanthema of swine virus (VESV) in the United States and was mistaken for foot and mouth disease. VESV in 1968 was shown to be a small virus with icosahedral symmetry with no link to foot and mouth disease. A disease causing vesicular lesions and abortions in sea lions was later shown to be caused by San Miguel sea lion virus (SMSV) and related to VESV. Feline calicivirus (FCV) was first isolated in cell culture in New Zealand in 1957 and had been shown to cause primarily respiratory illness among cats. FCV was also classified as a picornavirus originally (known as feline picornavirus for some time) before amendment and inclusion within the vesivirus genus of the *Caliciviridae*.

The third report of the International Committee on Taxonomy of Viruses (ICTV) in 1979 was when the family *Caliciviridae* were first classified. Their classification was based on their usage of a single capsid protein which assembled to form icosahedral particles with 32 cup shaped depressions on their surface. The name calicivirus derives from the latin word for cup, *calix*. *Caliciviridae* form particles of approximately 30 to 40 nanometres (nm) in diameter. Calicivirus genomes are around 7.5 kilobases (kb) in length and encode a small virion protein g (Vpg) covalently linked to the viral genomic RNA rather than a methylated cap as described for the picornaviruses. Caliciviruses also encode two RNA species during viral replication: one is the full length genome while a shorter, sub-genomic strand of RNA is also produced at the 3' end which serves as a translational template for the capsid proteins, VP1 and VP2. Picornaviruses, however, do not encode a subgenomic RNA species during replication. Another factor where Caliciviruses differ from picornaviruses is the position in the genome where the capsid proteins are encoded. The capsid proteins are encoded at the 5' end of picornavirus genomic RNA but caliciviruses encode them at the 3' end of their RNA genome. While 'Norwalk-like viruses' and vesiviruses encode three open reading frames, lagoviruses and 'Sapporo-like viruses' encode two open reading frames. The first open reading frame (ORF) for all Caliciviruses encodes the non-structural proteins as well as the major capsid protein for the lagoviruses and 'Sapporo-like viruses' although this is encoded on ORF2 for the 'Norwalk-like viruses' and vesiviruses. The minor structural protein is then encoded on a separate ORF for all Caliciviruses (Clarke and Lambden, 1997; Green et al., 2000; Thiel and Konig, 1999).

1.5.1 Feline calicivirus (FCV)

Feline calicivirus was isolated from cats in New Zealand in 1957 and is readily cultured *in vitro* resulting in cell rounding and death within hours of infection. Virus particles are able to survive on surfaces for up to two weeks and are stable within a pH range of around 4 to 8.5 (Pesavento et al., 2008).

Feline calicivirus is a widespread pathogen which primarily causes oral and upper respiratory tract disease in cats, however, some strains have the ability to cause virulent systemic disease. A variety of clinical signs are associated with FCV infection including oral ulceration, ocular and nasal discharge and occasionally

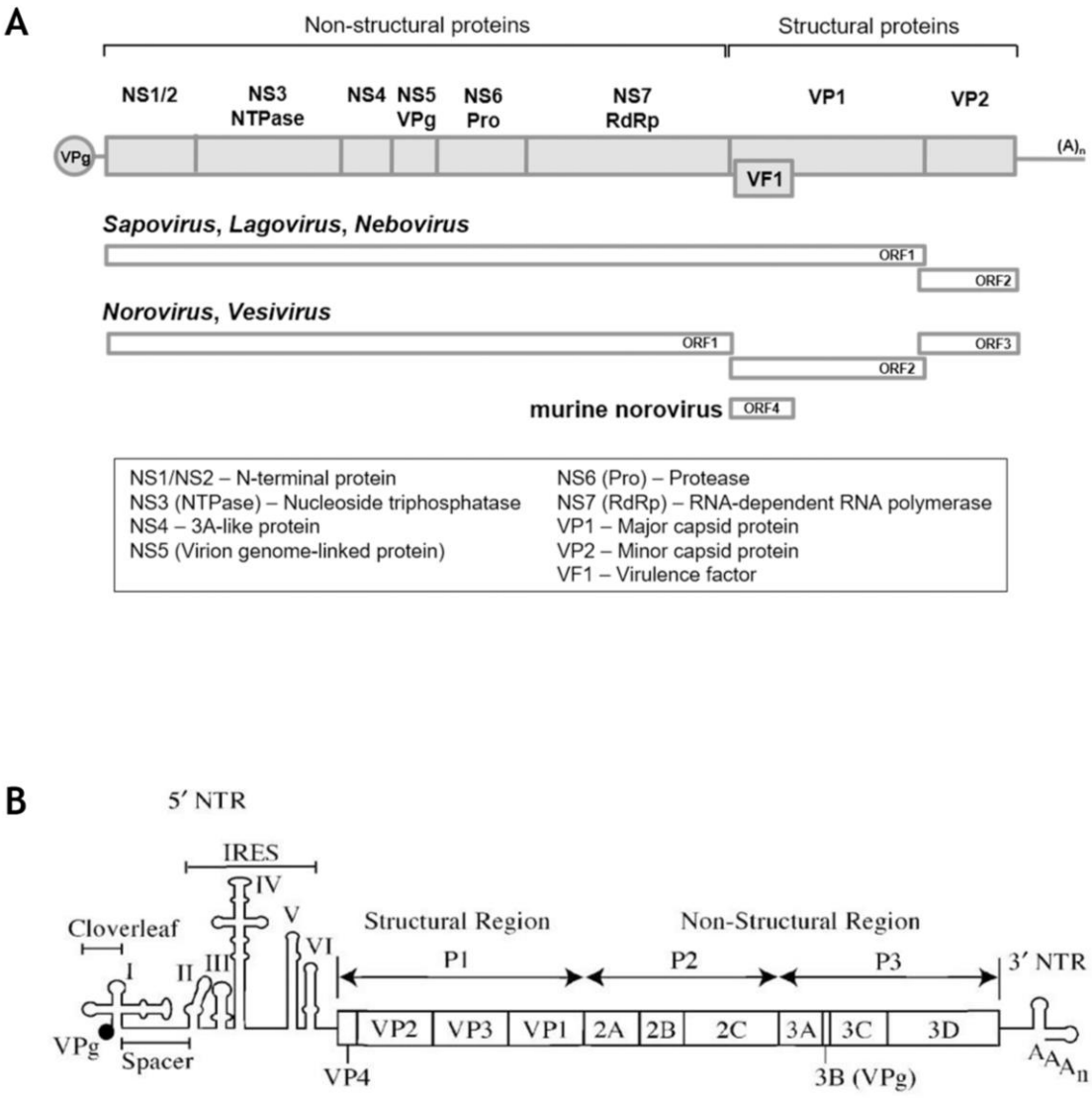

Figure 9- Genome organisation of caliciviruses and picornaviruses

Diagrammatic representation of the open reading frames and proteins encoded by the different caliciviruses as well as picornaviruses (Poliovirus type 1). Taken from Lee et al, 2017 and De Jesus, 2007.

pneumonia. Cats infected with virulent systemic strains of FCV present with varying degrees of pyrexia, ulcerative dermatitis, anorexia, cutaneous oedema and jaundice with a mortality rate of up to 50% (Pesavento et al., 2008). Infection usually occurs via the nasal, oral or conjunctival route with viral replication occurring mainly in the oral and respiratory tract. Mixed infections are not uncommon which provides the possibility for recombination between strains within an infected cell. FCV prevalence among individual households remains relatively low although prevalence among cats in rehoming centres is much higher. Vaccination with the F9 strain, however, only leads to protection against 54% of tested isolates (Coyne et al., 2006; Pesavento et al., 2008; Radford et al., 2007).

FCV encodes a single stranded, positive sense RNA genome of approximately 7.7kb in length with a 5' VPg protein, a 3' polyA tail and three open reading frames (see Figure 9). A smaller RNA species of 2.4kb, known as the subgenomic mRNA, is also observed which encodes the structural proteins of the virus (located at the 3' end of the genome) (Herbert et al., 1997). Open reading frame (ORF) 1 encodes the non-structural proteins of the virus while ORF2 encodes the major capsid protein, VP1, and ORF3 encodes the minor capsid protein, VP2.

Each viral capsid is assembled from 180 VP1 proteins arranged into A/B and C/C capsomeres which form the characteristic arch-like dimers on the capsid surface. Although all members of the *Caliciviridae* show this characteristic capsid morphology, members often differ in the structures of their P2 domains as seen in Figure 10. For example, some form more rounded structures like those seen in RHDV and norovirus GII.10 while others form more rhomboid structures like those seen in FCV (Conley et al., 2017).

Infection with FCV results in the shutdown of cellular protein synthesis via the cleavage of eIF4G (eukaryotic initiation factor 4G), as well as formation of membrane bound vesicular structures via the rearrangement of intracellular membranes (Willcocks et al., 2004). FCV replication has also been shown to induce programmed cell death/apoptosis via the activation of caspases 3, 8 and 9 resulting in the rapid cytopathic effect seen in FCV infected cells *in vitro* (Sosnovtsev et al., 2003).

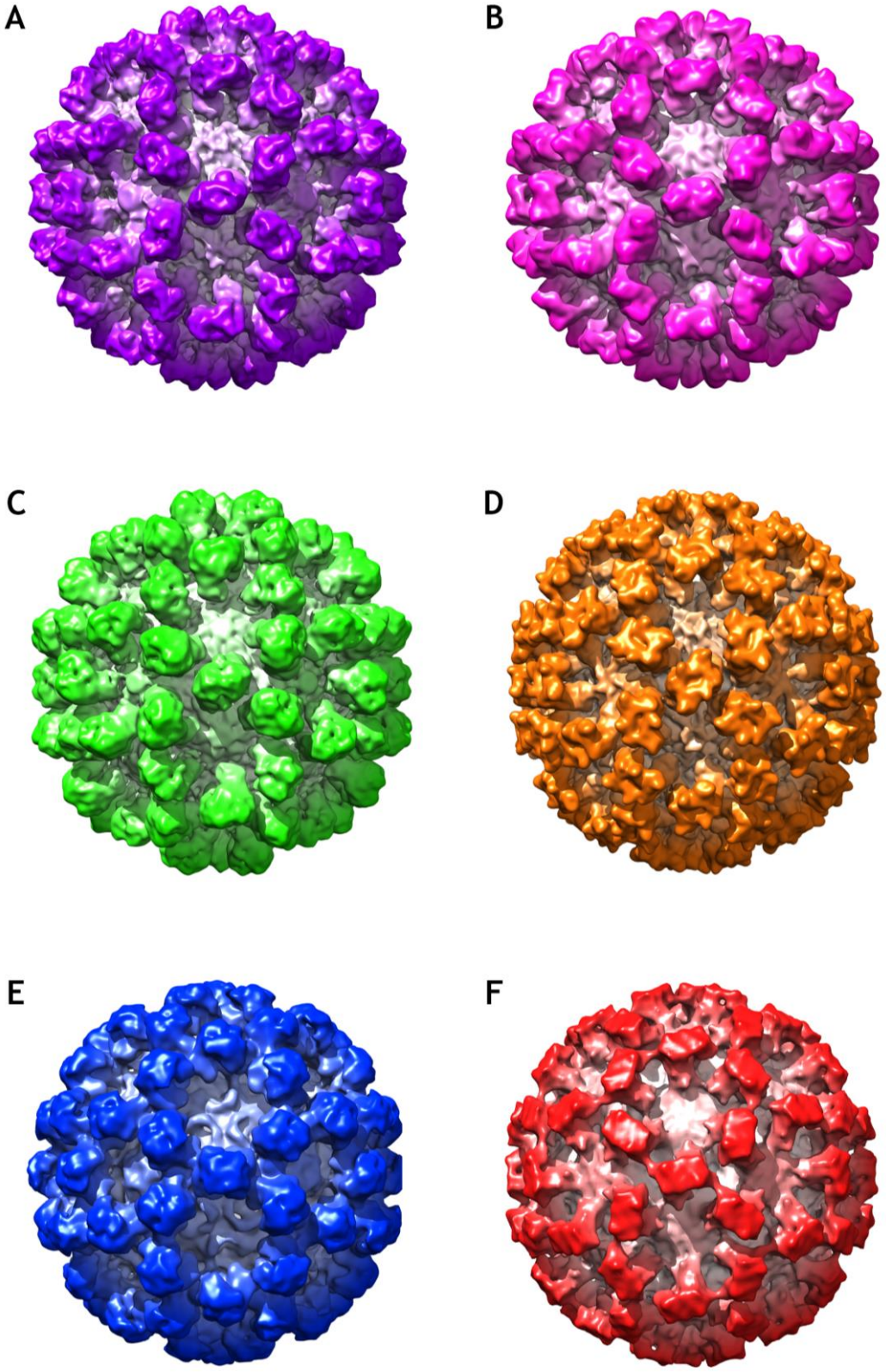

Figure 10- Comparison of calicivirus structures

Side by side comparison of the structures of vesivirus 2117 (A), a chimeric sapovirus (B), RHDV (C), FCV (D), norovirus GII.10 (E) and Norwalk virus (F). Taken from Conley et al, 2017.

Mitochondrial membrane potential is initially lost alongside the translocation of Bax from the cytosol to the mitochondria within 4 to 6 hours post infection. Cytochrome c is then released from mitochondria at 6-8 hours post infection, resulting in the activation of caspases and triggering of apoptosis (Natoni et al., 2006).

1.5.1.1 Non-Structural Proteins

Most of the non-structural proteins of FCV have been found to be associated with membranous replication complexes including p32/NS2, p39/NS3 (helicase) and p76/NS6-7 (protease-RNA dependent RNA polymerase) (Green et al., 2002).

Virion protein g (VPg/p13/NS5) is a small protein that is covalently linked to the 5' end of the viral genome. VPg is not required for FCV infection but must be present (or replaced with a cap structure) for translation of the viral RNA to occur (Sosnovtsev and Green, 1995). Polypyrimidine tract binding protein (PTB) has been shown to redistribute from the nucleus into the cytoplasm (following translation of the viral proteins) where it interacts with the 5' ends of the genomic and subgenomic viral RNAs. PTB partially co-localises with replication complexes and acts as a switch to inhibit translation and promote viral genome replication (Karakasiliotis et al., 2006; Karakasiliotis et al., 2010). VPg is also associated with the p30/NS4 protein within replication complexes, suggesting a role in anchoring VPg near membranous replication complexes ready for RNA replication (Green et al., 2002).

NS2/p32 interacts with p39/NS3, p30/NS4, p76/NS6-7 and also itself in membranous viral replication complexes. NS2/p32, p39/NS3 and p30/NS4 have been identified as potential transmembrane proteins which localise to the endoplasmic reticulum and lead to membranous rearrangements characteristic of FCV infection (Bailey et al., 2010). NS3/p39 has been shown to prevent the activation of interferon response factor-3 (IRF3) and therefore supress factors of the innate immune response during viral infection (Yumiketa et al., 2016).

The FCV protease/polymerase (p76/NS6-7) forms homotypic oligomers and also interacts with the VPg protein (possibly during the replication of progeny viral genomes) as well as ORF2, encoding the major viral capsid protein. A weak

interaction with the minor capsid protein, VP2, has also been described (Kaiser et al., 2006). The viral protease is responsible for the *cis* cleavage of the viral polyprotein to yield the individual viral proteins outlined above, however, it is thought that the full-length protease-polymerase is the active form of the RdRp (Sosnovtseva et al., 1999; Wei et al., 2001). The host protein, nucleolin, has been described as essential for viral replication due to its interactions with both viral RNA and p76/NS6-7 (Cancio-Lonches et al., 2011). The viral protease, NS6, appears to reduce cellular protein synthesis by mediating the cleavage of poly A binding protein (PABP) and recently, NS6 has been shown to impair the formation of stress granules within infected cells, preventing the limitation of energy available for virus replication (Humoud et al., 2016; Kuyumcu-Martinez et al., 2004).

1.5.1.2 Structural Proteins

Caliciviruses encode two structural proteins. The major capsid protein, VP1, forms the majority of the viral capsid with the minor capsid protein, VP2 incorporated to a much lesser extent.

The major capsid protein, VP1, is translated from the subgenomic RNA and forms a 76kDa precursor protein which is cleaved to form the mature capsid protein of 62kDa. This cleavage event is mediated by the viral protease and is critical for the life cycle of the virus (Sosnovtsev et al., 1998). The leader of the capsid protein (LC) which is cleaved post-translationally, has been shown to be responsible for the cytopathic effect seen in infected cells. LC has also been shown to bind to annexin A2, supporting its role in enabling virus spread (Abente et al., 2013). VP1 has been shown to interact with the VPg protein as well as the protease/polymerase, p76/NS6-7, and the minor capsid protein, VP2 (Kaiser et al., 2006). VP1 consists of 2 domains; the S domain forms the shell of the viral capsid with the P domain protruding out from the shell. The P domain can be further divided into P1 and P2 with P2 being an insertion in P1 (see Figure 11) and responsible for receptor binding and therefore tissue tropism (Bhella et al., 2008; Ossiboff et al., 2010).

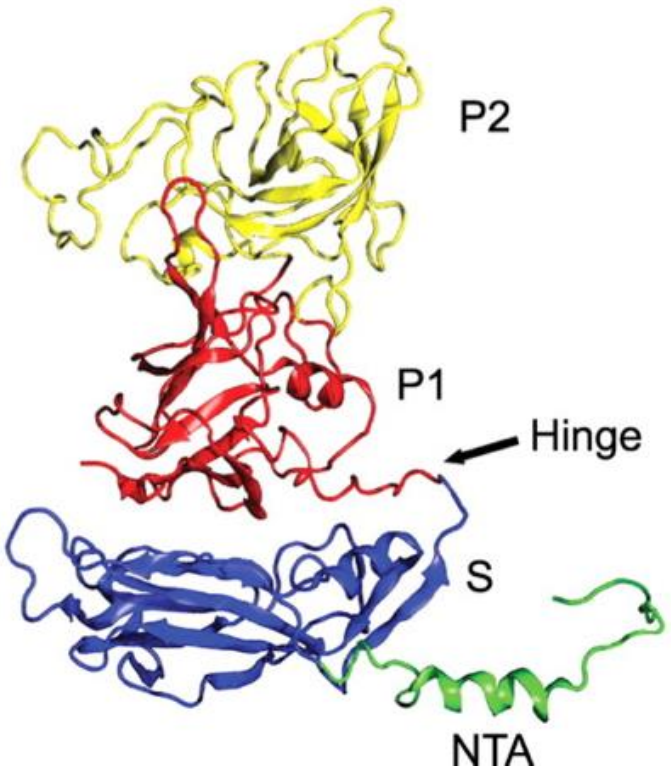

Figure 11- FCV major capsid protein, VP1

Ribbon diagram of FCV strain 5 VP1 capsid protein showing the N-terminal arm (green), S domain (blue), P1 domain (red) and P2 domain (yellow) with the hinge region highlighted. Taken from Ossiboff et al, 2010.

The minor capsid protein, VP2, is essential for FCV replication and release of progeny viral particles (Sosnovtsev et al., 2005). Each virion is predicted to incorporate one or two copies of VP2 and it is involved in the self-assembly of the capsid (Di Martino and Marsilio, 2010; Sosnovtsev and Green, 2000).

1.5.1.3 FCV entry

FCV has a tropism restricted to cells of feline origin although this restriction is overcome when viral RNA is transfected into cells, demonstrating that it is the binding and entry of the virus that is restricted (Kreutz and Seal, 1995). Binding of FCV to cells is most efficient at pH 6.5 with half maximal binding occurring as quickly as after 15 minutes (Kreutz et al., 1994). FCV entry was hypothesised to involve a low pH step during the first 2 hours of infection (Kreutz and Seal, 1995). It has since been shown that acidification of endosomes is required for uncoating of the virus and release of the viral genome into the cell for replication. FCV entry is mediated by clathrin mediated endocytosis and viral genome release may be mediated by permeabilisation of endosomal membranes during virus entry (Stuart and Brown, 2006).

Many viruses have been shown to use carbohydrate moieties such as sialic acid as attachment factors or components of their receptors. Treatment of cells with neuraminidase (which cleaves terminal sialic acid residues) reduces FCV binding to only 23% suggesting a role for sialic acid in FCV binding and entry. It was further demonstrated that FCV binds to α2,6-linked sialic acid that is present on an N-linked glycoprotein on the surface of feline cells. The type of sialic acid linkage may also play a role in tissue specificity and cell tropism (Stuart and Brown, 2007).

A functional receptor for FCV has been identified as feline junctional adhesion molecule A (fJAM-A) which can be found in the tight junctions of epithelial and endothelial cells as well as on platelets and leucocytes as described for the human and murine homologues of the protein. Infection with FCV causes the re-localisation of fJAM-A away from tight junctions and into the cytosol of the cell (Pesavento et al., 2011). Anti-fJAM-A antibodies were shown to decrease FCV binding to feline kidney (CrFK) cells and the expression of fJAM-A in non-permissive cells rendered them susceptible to FCV infection. D1 of the fJAM-A

ectodomain is sufficient for virus binding (Ossiboff and Parker, 2007) and feline JAM-A shares 75.6% amino acid identity with the human form of the protein with a predicted N-glycosylation site at position 185 (Makino et al., 2006).

1.5.1.4 FCV structure

In early electron microscopic studies of FCV, small individual particles of 35nm in diameter were observed within infected cells (Studdert and O'Shea, 1975). Virus particles were also observed in association with smooth membranes (Love and Sabine, 1975).

The major capsid protein, VP1, assembles into arch-like dimers/capsomeres which gives rise to the characteristic calicivirus morphology of cup-shaped depressions on the virus surface (visible in Figure 12). The major capsid proteins differ slightly in their conformations (although not in sequence) to form A, B and C isoforms (see Figure 3). A/B (bent) and C/C (flat) dimers are present at different positions in the viral capsid in order to allow icosahedral symmetry with 180 subunits (*T*=3). A/B capsomeres are located around the five-fold symmetry axes while C/C capsomeres are found at two-fold symmetry axes (resulting in the alternation of A/B and C/C capsomeres around the three-fold symmetry axes). The S domain of VP1 folds into an eight stranded β-barrel structure with each strand designated B to I. These eight strands form two, four stranded β-sheets (BIDG and CHEF) with two alpha helices between strands C and D as well as between E and F. The S domain is linked to the P domain of VP1 via a flexible hinge region, allowing the slightly different conformations adopted by the A, B and C structures. The P domain is subdivided into P1 and P2 with P2 being an insertion into P1 and being responsible for receptor binding. P2 is formed of a six stranded β-barrel (A' to F') with varying lengths and orientations and contains hyper-variable regions which can result in high degrees of variation between strains. These hyper-variable regions often form the neutralising epitopes/antibody binding sites which are targeted by the immune system of the host (Bhella et al., 2008; Ossiboff et al., 2010).

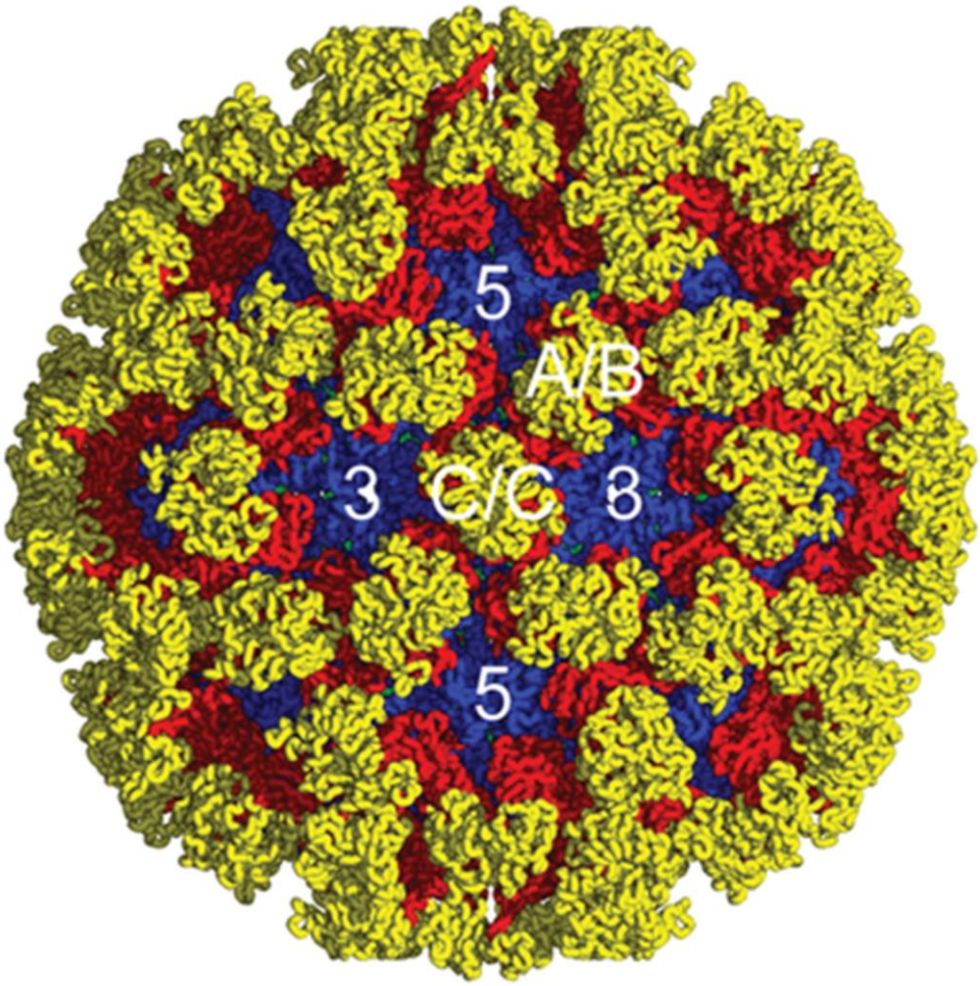

Figure 12- FCV5 structure

Crystal structure of FCV strain 5 at 3.6Å resolution showing the S domains (blue), P1 domains (red) and P2 domains (yellow). Five and three-fold symmetry axes are labelled as well as the positions of the A/B and C/C dimers within the capsid. Taken from Ossiboff et al, 2010.

1.5.1.5 FCV-fJAM-A interaction

Residues D42, K43 and S97 of the D1 subdomain of the fJAM-A ectodomain are involved in the binding of FCV as mutation resulted in decreased binding (shown in pink in Figure 13). In addition, all domains of fJAM-A are necessary for FCV infection although the PDZ-binding motif in the cytoplasmic domain is dispensable for virus entry. FCV interacts with both monomeric and dimeric forms of fJAM-A and this interaction must induce signals through the transmembrane or cytoplasmic domains of fJAM-A to coordinate entry and infection as when these were replaced with a GPI anchor, no infection was seen (Ossiboff and Parker, 2007).

Interestingly, the FCV binding site and fJAM-A dimerisation interface do not overlap, suggesting that FCV does not compete for binding which may be independent of dimerisation. The potential N-linked glycosylation site of fJAM-A (shown in Figure 13) appears to be located close to the transmembrane region of fJAM-A and relatively far away from the FCV binding site and dimerisation interface implying that the glycosylation is not involved in these interactions.

The previous structures of FCV bound to fJAM-A (at 9Å resolution), as solved by cryo-electron microscopy and three-dimensional reconstruction, showed high occupancy binding demonstrating the absence of any steric hindrance between fJAM-A ectodomains. Upon fJAM-A binding, a conformational change is apparent in the capsid. The P domains of the capsid appear to rotate 15° anticlockwise when bound to fJAM-A. The majority of the contacts between FCV and fJAM-A occur in D1 of the ectodomain as shown in pink in Figure 13 (Bhella and Goodfellow, 2011). In support of these observations of conformational changes, Ossiboff et al reported an increase in hydrophobicity upon FCV-fJAM-A incubation consistent with a change in protein structure (Ossiboff et al., 2010). These previous structures were not of sufficient resolution to allow the visualisation of secondary structural elements or precise evaluation of interacting residues and so prompted the study of this interaction at near atomic resolution.

The fJAM-A proteins are bound to the P2 domain of FCV VP1 in a head to tail arrangement, rotated 180° with respect to each other. The density above the

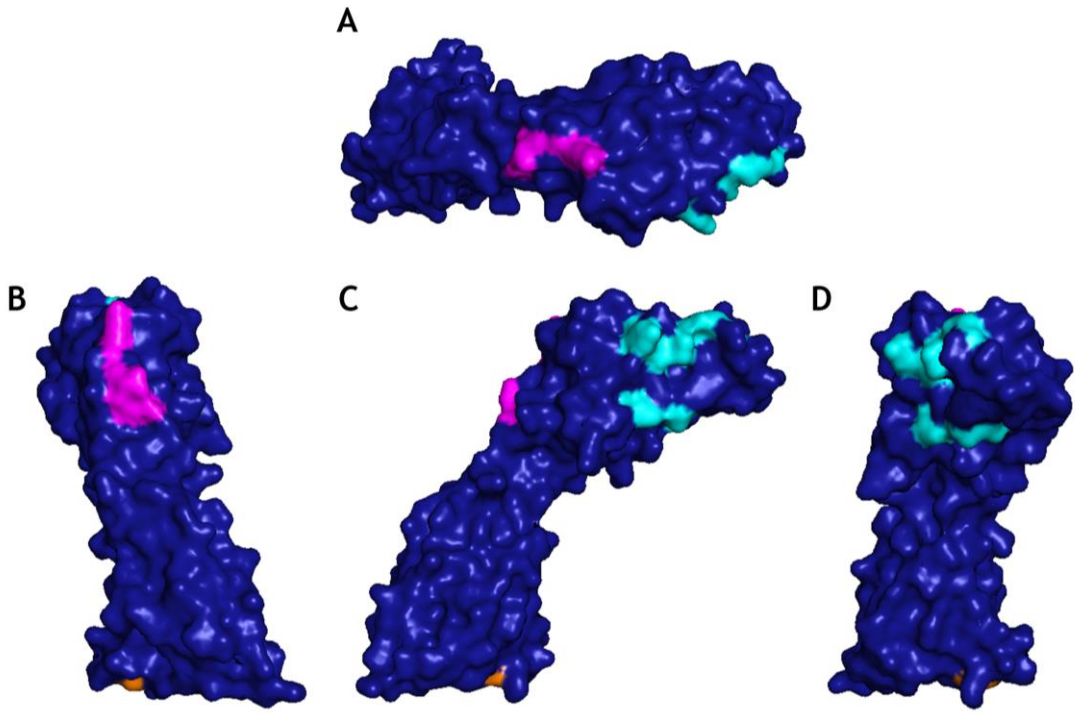

Figure 13- JAM-A monomer highlighting key residues for interactions

Surface representations of human JAM-A with residues involved in dimerisation (turquoise), FCV binding (pink) and N-linked glycosylation (orange) highlighted. Different views of the protein are shown; top view (A), back view (B), side view (C) and underside view (D). PDB ID: 1NBQ.

A/B dimer in the cryo-EM reconstructions is clear and well defined unlike that at the C/C dimer suggesting a higher degree of movement/flexibility limiting the reconstruction. This suggests that the conformational change observed at the A/B dimers is potentially different to that which occurs at the C/C dimers where the icosahedral symmetry may be broken, resulting in difficulty refining the density. Bhella and Goodfellow suggested that this may be caused by the C/C dimer bending away from the two-fold symmetry axis when bound to fJAM-A (Bhella and Goodfellow, 2011). The conformational changes seen in the capsid upon fJAM-A binding are hypothesised to act as a priming step for uncoating of the virus during entry into a host cell via clathrin-mediated endocytosis.

1.6 Aims

The broad aim of this project was to characterise the interaction between FCV and fJAM-A. One aspect of this was to assess the glycosylation state of fJAM-A and also to determine if the previously reported binding to sialic acid on cell surfaces was actually a result of FCV binding to a carbohydrate moiety on glycosylated fJAM-A (Stuart and Brown, 2007).

Another aim of the project was to solve both the undecorated (FCV) and decorated (FCV bound to fJAM-A) virus structures to near-atomic resolution allowing us to determine the mechanism by which fJAM-A induces the previously described conformational changes upon binding, and how FCV disrupts fJAM-A homodimers (Bhella et al., 2008; Bhella and Goodfellow, 2011).

The final aim of the project was to investigate the entry pathway of FCV which has been previously shown to involve clathrin mediated endocytosis (Stuart and Brown, 2006). We aimed to assess the affect of pH on virus structure (both undecorated and decorated) in order to investigate the process of viral entry and uncoating. Another aspect of this aim was to determine the stoichiometry of the virus-receptor interaction as previous studies were performed with fully decorated virus particles which is unlikely to be the case during cell binding and entry (due to the availability of receptor proteins at the cell surface) (Bhella et al., 2008; Bhella and Goodfellow, 2011).

2 Materials and Methods

2.1 Materials

2.1.1 Antibodies

2.1.1.1 Primary Antibodies

Mouse monoclonal anti-feline calicivirus VP1 antibody (Novus Biologicals) was used at a dilution of 1 in 1000 for western blotting.

Goat polyclonal anti-human IgG (Fc specific) antibody (Sigma Aldrich) was used at a dilution of 1 in 20,000 for western blotting.

2.1.1.2 Secondary Antibodies

Goat anti-mouse DyLight 680 antibody (ThermoFisher Scientific) was used at a dilution of 1 in 10,000 for western blotting.

Donkey anti-goat IRDye 800 antibody (LI-COR Biosciences) was used at a dilution of 1 in 10,000 for western blotting.

2.2 Methods

2.2.1 Mammalian cell culture

2.2.1.1 Crandell Rees Feline Kidney cells

Crandell Rees feline kidney (CrFK) cells were cultured in Dulbeccos's modified eagle medium (DMEM, Life Technologies) with 10% foetal bovine serum (FBS, Life Technologies), unless specified otherwise, with 100 units/ml penicillin and 100μg/ml streptomycin (PenStrep, Life technologies) at 37°C in an atmosphere containing 5% carbon dioxide (CO_2).
Cells were passaged by removal of the culture media followed by washing the cells twice with 5ml 1x PBS and incubation with 5ml 0.05% trypsin containing EDTA (Life technologies) for 5 minutes at 37°C in an atmosphere containing 5% CO_2. The cells were then removed from the culture flask and 10% were added to

a new culture flask containing 30ml media and cultured at 37°C in an atmosphere containing 5% CO_2 for 3-4 days.

2.2.1.2 Chinese Hamster Ovary cells

Chinese hamster ovary (CHO) cells stably expressing a secreted form of the fJAM-A ectodomain (amino acid residues 1-237) fused to an Fc tag were cultured in Roswell Park Memorial Institute (RPMI, Life Technologies) medium supplemented with 10% FBS, PenStrep and 200μg/ml hygromycin B (Sigma Aldrich). Cells were cultured at 37°C in an atmosphere containing 5% CO_2 and passaged as described in 2.2.1.1.

2.2.2 Virus Purification

2.2.2.1 Feline Calicivirus

2.2.2.1.1 Infection and virus propagation

FCV (strain F9) was grown and purified from CrFK cells under the conditions outlined in 2.2.1.1. Eight confluent T175cm^3 cell culture flasks containing confluent CrFK cells were trypsinised as outlined in 2.2.1.1. These cells were then added to 16 T850 roller bottles containing 100ml cell culture media and 5% CO_2. The cells were incubated at 37°C for 3 days until confluent. The culture media were removed and the cells infected with FCV at a multiplicity of infection (MOI) of 5 in the presence of 20ml culture medium supplemented with 2% FBS and PenStrep. The cells were then incubated at 37°C for 18 hours and the supernatant collected for FCV purification.

2.2.2.1.2 Virus Purification

The supernatant collected from the infected roller bottles was firstly centrifuged at 420 xg for 10 minutes at 4ºC to remove any cell debris. The supernatant was then centrifuged at 54200 xg for 2 hours at 4 ºC to pellet the virus particles (SureSpin 630 rotor from ThermoFisher Scientific). The supernatant was poured off and the pellets resuspended in 500μl 1x PBS at 4°C overnight. The resuspended material was then layered over a 1.3-1.45 g cm^{-3} caesium chloride gradient and centrifuged at 98700 xg for 16 hours at 12ºC (TH-641 rotor from ThermoFisher Scientific). The band containing virus particles was

then extracted and pelleted by centrifugation at 50400 xg for 2 hours at 4 ºC and the pellet resuspended in approx. 100µl 1x PBS at 4°C overnight.
The protein concentration of the sample was then determined (see 2.2.2.1.3) and the virus titrated (see 2.2.2.1.4).

2.2.2.1.3 **Protein quantification**

Protein quantification was performed using a NanoDrop One (Thermo Scientific) by measuring UV absorbance at 280nm (using the appropriate calculated extinction coefficients to calculate an accurate protein concentration).

2.2.2.1.4 **Titration by plaque assay**

CrFK cells were seeded at 75% confluency in 6 well cell culture plates and incubated at 37°C in an atmosphere containing 5% CO_2 for 24 hours. 10-fold serial dilutions of virus (final volume 1ml) were then made in serum free cell culture medium. The media was removed from the plates and the cells washed with 1x PBS followed by the addition of 400µl of the corresponding serial dilution prior to incubation at 37°C in an atmosphere containing 5% CO_2 for 1.5 hours. Equal volumes of 2x overlay media (14.3g DMEM powder, 3.7g Sodium Bicarbonate and 1.1915g HEPES in 500ml deionised water) and 2% low melting point agarose (LMA) were then combined, with 2ml added to each well after removal of the viral serial dilution. The cell culture plates were then incubated at room temperature for 20 minutes to allow the agarose overlay to solidify. The plates were then inverted and incubated at 37°C in an atmosphere containing 5% CO_2 for 18 hours.
The cells in the 6 well plates were then fixed with 1% formaldehyde in deionised water (ThermoFisher Scientific) for 1 hour at room temperature, after which the fixative was removed and the wells washed with 1x PBS prior to the removal of the agar plugs from the individual wells. Cell monolayers were then stained for 1 hour to detect the presence of plaques using Giemsa stain (Sigma Aldrich). The plates were then washed with water following removal of the stain and left to dry before counting the plaques and calculating the virus titre.

2.2.3 Feline Junctional Adhesion Molecule A expression and purification

2.2.3.1 Expression of fJAM-A ectodomain

CHO cells expressing a secreted form of the fJAM-A ectodomain fused to an Fc tag were provided by Professor Ian Goodfellow (University of Cambridge). The fJAM-A ectodomain was separated from the Fc tag by a factor Xa cleavage site. Cells were grown as described in 2.2.1.2 for 7 days and the supernatant containing secreted Fc-fJAM-A collected.

2.2.3.2 Purification of fJAM-A ectodomain

The supernatant collected from CHO-fJAM-A cells was filtered and degassed at room temperature alongside 1x PBS, 0.1M citrate pH5 and 0.1M glycine pH2.5. The Fc-fJAM-A protein was purified by protein A affinity chromatography using a 1ml HiTrap Protein A column (GE Healthcare Life Sciences) connected to an Äkta pure chromatography system. The system and column were equilibrated with 1x PBS and the filtered cell supernatant passed over the column at a rate of 1ml/min. The column was then washed with 10ml 1x PBS and the contaminating bovine IgG (from FBS in cell culture media) eluted using 10ml 0.1M citrate pH5. The column was subsequently washed with 20ml 1x PBS and the Fc-fJAM-A eluted using 8ml 0.1M glycine pH2.5 in 0.5ml fractions. The pH of each fraction was then neutralised with 75μl 1.5M Tris pH8 and the protein concentration determined as in 2.2.2.1.3.

2.2.3.3 Removal of Fc tag from fJAM-A ectodomain

The Fc tag was removed from the fJAM-A ectodomain by cleavage with Factor Xa (New England Biolabs: NEB). Fc-fJAM-A was incubated at 23°C in the presence of 1x factor Xa cleavage buffer (100mM NaCl, 50mM Tris and 5mM $CaCl_2$) with a 25:1 ratio of protein:factor Xa (μg) for 18 hours.
In order to remove the factor Xa, the sample was then incubated with Xarrest Agarose (Novagen) at a ratio of 1μg factor Xa: 25μl agarose (pre-washed with 10 volumes 1x factor Xa cleavage buffer) for 10 minutes at room temperature. The sample was then centrifuged at 1000 xg for 5 minutes (at room temperature) and the supernatant removed. The agarose pellet was washed with 1ml 1x factor Xa

cleavage buffer and centrifuged as before, repeating the wash once.
The sample was then combined with the two washes and the protein concentration determined as described in 2.2.2.1.3. 240μg protein was then combined with 1ml protein A Dynabeads (Life Technologies) and incubated with rotation for 10 minutes. A magnet was then applied to the sample, the supernatant removed from the beads and the fJAM-A ectodomain protein concentration determined (see 2.2.2.1.3). The beads were then washed in 1x PBS and the Fc portion of the protein eluted from the beads using 50mM glycine pH2.5 following incubation at room temperature for 2 minutes. Purified protein was stored at 4°C until use.

2.2.4 Western Blotting

2.2.4.1 SDS-PAGE

Four 12% resolving gels were made by combining 8ml 30% acrylaminde/bis solution 37.5:1 (BIO-RAD), 6.6ml deionised water, 5ml 1.5M Tris pH8.8, 0.2ml 10% sodium dodecyl sulphate (SDS), 0.2ml 10% ammonium persulfate (APS) and 0.025ml N,N,N',N'-tetramethylethane-1,2-diamine (TEMED) in glass casting plates (BIO-RAD).
Four 5% stacking gels were made by combining 1ml 30% acrylaminde/bis solution 37.5:1 (BIO-RAD), 4.2ml deionised water, 0.76ml 1M Tris pH6.8, 0.06ml 10% SDS, 0.06ml 10% APS and 0.01ml TEMED.
Once the resolving gels had set, the stacking gel could be made, layered on top and a comb inserted while the stacking gel solidified at room temperature.
Protein samples were prepared by the addition of 2x Laemmli loading buffer and incubation at 95°C for 7 minutes. Samples were then loaded into the wells of the gels alongside Precision Plus Protein Kaleidoscope Prestained protein standards (BIO-RAD). Gels were run in the presence of 1x running buffer (3g Tris Base, 14.4g glycine and 1g SDS per litre in deionised water) at 80mA for approximately 1 hour.
If gels were not used for western blotting, the gels were removed from the glass plates, washed in deionised water and stained with Imperial protein stain (ThermoFisher Scientific) for 1 hour followed by destaining in deionised water.

2.2.4.2 Western Blotting

SDS PAGE gels were run as described in 2.2.4.1 and transferred onto nitrocellulose membrane using an Invitrogen Novex mini cell with an XCell II blot module at 25 volts for 1hour. The membranes were blocked for 1 hour with 5% FBS in PBS followed by incubation with the appropriate primary antibody in 0.1% Tween 20 in PBS (PBS-T) containing 5% FBS for 1 hour at room temperature. The membranes were subsequently washed 3 times in PBS-T before incubation with the appropriate secondary antibody in opaque tubes in PBS-T containing 5% FBS for 1 hour at room temperature. The membranes were then washed 3 times in PBS-T, 2 times in PBS and 2 times in deionised water, each wash lasting 5 minutes. Membranes were then stored in deionised water until visualisation on a LI-COR Odyssey CLx.

2.2.5 Deglycosylation of fJAM-A

2.2.5.1 In vitro deglycosylation of fJAM-A

2.2.5.1.1 Alpha2-3,6,8,9 Neuraminidase A

To deglycosylate a protein with Alpha2-3,6,8,9 Neuraminidase A, 1μg protein was incubated in the presence of 1μl 10x Glycobuffer 1 (NEB), 1μl Alpha2-3,6,8,9 Neuraminidase A (NEB) and deionised water to a final volume of 10μl at 37°C for 1 hour.

2.2.5.1.2 Beta1-4 Galactosidase

1μg protein was combined with 1μl 10x Glycobuffer 1 (NEB), 2μl Beta1-4 Galactosidase (NEB) and deionised water to a final volume of 10μl at 37°C for 1 hour.

2.2.5.1.3 Endoglycosidase H

5μg protein was combined with 2μl 10x Glycobuffer 3 (NEB), 5μl Endoglycosidase H (EndoH; NEB) and deionised water to a final volume of 10μl at 37°C for 1 hour.

2.2.5.1.4 **Remove-iT PNGase F**

5μg protein was combined with 2μl 10x Glycobuffer 2 (NEB), 3μl Remove-iT PNGase F (NEB) and deionised water to a final volume of 20μl at 37°C for 1 hour.

To remove the PNGase F enzyme from samples, 1μl of chitin magnetic beads (NEB) per 100U of enzyme were washed in column binding buffer (500mM NaCl, 20mM Tris-HCl, 1mM EDTA and 0.05% Triton-x-100 at pH8) and applied to a magnet before removing the supernatant. The sample is then added to the beads and mixed with rotation for 1 hour at 4°C. The magnet is then applied to the sample and the enzyme free sample removed and stored at 4°C until use.

2.2.5.1.5 **Beta-N-Acetylglucosaminidase**

1μg protein was combined with 1μl 10x Glycobuffer 1 (NEB), 2μl Beta-N-Acetylglucosaminiadse (NEB), 1μl 10x bovine serum albumin (BSA) and deionised water to a final volume of 10μl at 37°C for 1 hour.

2.2.5.1.6 **O-glycosidase**

5μg protein was combined with 2μl 10x Glycobuffer 2 (NEB), 2μl 10% NP-40, 2μl Alpha2-3,6,8,9 Neuraminidase A (NEB) and 5μl O-glycosidase (NEB) and deionised water to a final volume of 20μl at 37°C for 1 hour.

2.2.5.2 Immunoprecipitation of FCV by fJAM-A

5μg Fc-fJAM-A was bound to 50μl Protein A Dynabeads (Life Technologies) by incubation in 200μl PBS-T with rotation at room temperature for 10 minutes. The magnet was then applied to the sample and the supernatant removed. 380μg FCV was then added to the beads and mixed prior to incubation with rotation for 10 minutes at room temperature. The magnet was then reapplied, the supernatant removed and the beads washed 3 times with 200μl PBS-T. The beads were then resuspended in 30μl 2x Laemmli loading buffer and incubated at 95°C for 7 minutes. The magnet was then applied to the sample and the supernatant loaded into SDS-PAGE gels and subsequently blotted for both Fc (Fc-fJAM-A) and FCV VP1 (as described in 2.2.4).

2.2.5.3 Neutralisation assay

Neutralisation assays were performed with an MOI of 3 for FCV in 6 well cell culture plates with confluent CrFK cells. Both Fc-fJAM-A and deglycosylated Fc-fJAM-A (PNGase F treated; see 2.2.5.1.4) were used in a side by side comparison. FCV (0.66μg) was incubated with varying dilutions of Fc-fJAM-A or deglycosylated Fc-fJAM-A (0.66μg, 0.33μg (1 in 2 dilution), 0.22μg (1 in 3 dilution), 0.165μg (1 in 4 dilution) or 0.132μg (1 in 5 dilution)) on ice for 1 hour. The samples were then added to individual wells in the plates and incubated at 37°C for 1.5 hours. The protocol for titration by plaque assay was then followed (as per 2.2.2.1.4) and the plaques counted. Neutralisation assays were performed in triplicate.

2.2.6 Size Exclusion Chromatography

Fc-fJAM-A was purified as described in 2.2.3.2 and the Fc tag removed (if specified) as described in 2.2.3.3. A Superdex 200 Increase 10/300 column (GE Healthcare Life Sciences) was used with an Äkta pure system and the sample loaded onto the column using a 500μl superloop. The sample was passed through the column in 1x PBS at a flow rate of 0.45ml/min and collected in 0.5ml fractions.

2.2.7 pH dependent RNA release assay

2μg FCV was combined with 2μg Fc-fJAM-A in 1x VB buffer (1 litre of 1xVB: 8.75g NaCl, 1.2g Tris base and 2g $MgCl_2$ in deionised water) of the appropriate pH along with 10μl Syto9 nucleic acid binding dye (final concentration 5μM, ThermoFisher Scientific) to a final volume of 100μl in a black 96 well plate (ThermoFisher Scientific). For positive control wells, 550ng FCV RNA (provided by Imogen Herbert) was added in place of the FCV and Fc-fJAM-A samples. A PHERAstar *FS* (BMG Labtech) was used with a 485/520 filter cube to take fluorescence measurements every 5 minutes for 4 hours. The data was then normalised to the corresponding FCV only data in order to eliminate any background signal. All RNA release assays were performed in triplicate.

2.2.8 Small angle x-ray scattering

Small angle x-ray scattering (SAXS) is a structural biology technique used to elucidate the low resolution structures of macromolecules in solution. SAXS offers the advantage that the protein may remain in its native state in solution as opposed to forming a crystal lattice where proteins must all be present in the same orientation, possibly under non-biologically relevant conditions. High pressure liquid chromatography (HPLC) has been added to the SAXS pipeline (HPLC-SAXS) in order to increase the reliability and sensitivity of the data collected. The inclusion of HPLC ensures that any aggregated protein is separated away from the sample prior to the SAXS experiment. As the sample flows off the HPLC, it is directed through the SAXS flow cell where an x-ray beam is passed through the moving sample. As the sample is continuously moving during HPLC-SAXS, the sample receives less radiation damage and so the data recorded is of higher quality. As the x-ray beam passes through the sample, it is scattered by the scattering centres/atoms of the sample. These scattered rays (and their angles of scattering) are recorded on a detector to form a diffraction pattern which contains structural information about the sample. The measured scattering from a sample containing only buffer is then subtracted from the protein data and analysed in order to extract the structural information such as the molecular mass and shape of the protein (Malaby et al., 2015; Mathew et al., 2004).

2.2.8.1 Small angle x-ray scattering experimental methodology

The Fc tag was removed from the Fc-fJAM-A protein as described in 2.2.3.3 and the fJAM-A ectodomain was dialysed into PBS containing 0.01% sodium azide, 1% sucrose and 10mM potassium nitrate at a concentration of 7.47mg/ml. Samples were then taken to the Diamond Light Source where high pressure liquid chromatography (HPLC) small angle x-ray scattering (SAXS) experiments were performed by Professor Olwyn Byron. The HPLC column was equilibrated with the buffer for 1 hour and the sample loaded onto the column from a 96 well plate. After coming off the column, the sample was passed through a capillary where an X-ray beam was passed through the sample and the diffraction data collected. The data was analysed by Professor Olwyn Byron and a three dimensional model produced using DAMMIF (Franke and Svergun, 2009). The

human fJAM-A ectodomain (PDB: 1NBQ) was fitted into the SAXS structure by Prof Olwyn Byron using PyMOL (The PyMOL Molecular Graphics System, Version 1.7.4.5 Schrödinger, LLC).

2.2.9 Isothermal titration calorimetry

Isothermal titration calorimetry is a technique employed to measure the energy associated with a reaction whether it be endothermic or exothermic, for example, protein-protein interactions or ligand binding. The reaction is triggered by changing the chemical composition of the sample by the injection/titration of one of the binding partners being investigated. Two cells are present in the calorimeter, the sample cell and the reference cell. The reference cell contains the relevant buffer while the sample cell contains the macromolecule in the relevant buffer into which the ligand is then titrated by small volume injection. The calorimeter measures the amount of power (microcalories per second) necessary to maintain a constant temperature between the reference and sample cells. These readings are plotted as a function of time with the peaks become progressively smaller as the macromolecule becomes saturated with the injected ligand (Freire et al., 1990; Leavitt and Freire, 2001). This data can then be normalised to a buffer only control to account for any heat produced by the dilution of the macromolecule or by the stirrer during the experiment. This is then used to calculate the association (and dissociation) constant for the macromolecule and ligand, providing a measure of how strongly the two bind to each other.

2.2.9.1 Isothermal titration calorimetry experimental methodology

Isothermal titration calorimetry (iTC) was performed with Dr Sharon Kelly using a MicroCal iTC_{200} (GE Healthcare). All samples and solutions (1x PBS) were degassed at room temperature prior to experiments being performed. 13μM FCV in PBS was added to the chamber and 13μM fJAM-A in PBS was added to the injector of the MicroCal iTC machine at 25°C. Twenty injections of 2μl fJAM-A were performed, each lasting 4 seconds with a spacing of 180 seconds and a stirring speed of 750 rpm. Control experiments were also performed in order to account for any heats of dilution that may be observed. These data were

subtracted from sample data and plotted using Origin (OriginLab, Northampton, MA).

2.2.10 Biacore

Biacore is a surface plasmon resonance (SPR) technique that uses biosensor based technology to investigate the interaction kinetics and affinities of macromolecular complexes. A biacore system is formed of a sensor microchip, a laser light source, a fluid handling system and a position sensitive detector (Raghavan and Bjorkman, 1995). The sensor chip is formed of glass coated in a gold film and a carboxymethylated dextran matrix onto which biomolecules such as proteins of interest or capture antibodies can be bound using amine coupling. Once the capture molecule is bound to the flow cell of the chip, the sample molecule is flowed over the cell and any changes in refractive index measured. Binding of molecules to the capture molecules in the flow cell results in an increased mass and therefore a change of refractive index and also in the SPR angle which is then recorded by the detector. SPR angle changes are measured as response units (RU) and plotted against time in a sensorgram to allow real-time observation of cumulative association/dissociation events (1000RU corresponds to a change in SPR angle of 0.1° and a 1ng mm^{-2} surface mass change) (Raghavan and Bjorkman, 1995). Analysis of the sensorgram allows conclusions to be drawn, for example, on aspects such as comparative dissociation rates if the buffer pH was altered after an equilibrium was reached.

2.2.10.1 Biacore experimental methodology

Biacore experiments were performed with Dr Sharon Kelly.
Cm5 chips were docked into a Biacore 2000 and primed with PBS. The chip was then normalised with 40% glycerol prior to activating the chip with 35µl EDC (1-Ethyl-3-(3-dimethylaminopropyl) carbodiimide hydrochloride) and NHS (N-Hydroxysuccinimide) at a flow rate of 5µl/min.

After activating the chip with EDC and NHS, an antibody was bound to the chip (an anti-herpes virus antibody for the negative control, anti-Fc antibody for experiments). Ethanolamine was then used to block any available sites remaining on the chip. Fc-fJAM-A (either glycosylated or deglycosylated) was then flowed

over until approximately the same amount was bound to all flow cells (measured by response units). Ethanolamine was then used to block any further available sites prior to flowing FCV over all of the flow cells and measuring the change in response units, representing the amount of virus bound to the Fc-fJAM-A.

2.2.11 Electron Microscopy

Transmission electron microscopy (TEM) was first used in the study of biological macromolecules and viruses as early as the 1930's. Samples may be stained directly on grids (known as positive staining) although a more widely adopted method is negative staining which stains around the sample rather than the sample itself and was developed in 1959 (Brenner and Horne, 1959). The field was further revolutionised in 1984 when the imaging of frozen hydrated specimens was described (Adrian et al., 1984).

2.2.11.1 Preparation of samples for electron microscopy

For routine imaging of macromolecular assemblies, negative staining with heavy metal solutions provides high contrast images in the transmission electron microscope. Negative staining EM involves adding a sample onto an EM grid with a carbon support film and embedding it in a thin film of heavy metal salt solution such as uranyl acetate or ammonium molybdate. Uranyl acetate produces the most contrast from all the negative stains although others preserve sample integrity to a higher extent or perform better staining at low pH (Booth et al., 2011). Negative staining with a heavy metal salt solution results in the stain being deposited around the surface of the sample and so macromolecules are visualised by the appearance of a lack of stain rather than the dark contrast produced by the stain itself. Although negative staining EM produces high contrast images, staining causes dehydration, shrinkage and distortion of the biological macromolecules in the sample (Orlova and Saibil, 2011). The resolution of any imaging is also restricted by the size of the heavy metal salt grains (Nogales and Scheres, 2015).

Electron microscopy grids are 3.05mm round metal (usually copper) supports that contain square 'holes' in the metal. The metal strips across the grid are known as grid bars. The grids are coated in a thin layer of carbon to which the

sample adheres during negative stain sample preparation. Grids used for cryo-EM contain regular arrays of circular holes in the carbon within the squares of the grid, such as C-flats or Quantifoils (see Figure 14).

Cryogenic transmission electron microscopy, or CryoEM, involves embedding the sample in a thin layer of vitreous ice such that it is preserved in a frozen-hydrated state, allowing visualisation of the sample in as close to a native state as is possible in the vacuum of the electron microscope. The vitreous ice layer is prepared on a Holey carbon support film on EM grids (often copper). Imaging of the ice embedded material is through the holes, reducing background noise that is produced when imaging through a carbon film.

The carbon around the holes, however, increases stability of the sample and allows the formation of very thin layers of vitrified sample (Adrian et al., 1984). Grids are glow discharged prior to preparation to remove any hydrocarbons and therefore make them hydrophilic, allowing the sample to coat the grid efficiently and evenly (Grassucci et al., 2007). Samples are then added to the grids, blotted with filter paper to produce a thin film of approximately 50-100 nm and plunged into an effective cryogen such as liquid ethane or propane cooled by liquid nitrogen. This process of vitrification is frequently performed using a vitrification robot such as the vitrobot (FEI). This rapid cooling (10^6 ºC/second) results in the sample being trapped in its native state in vitreous ice when cooled to below -140ºC. Between -140ºC and -100ºC, cubic ice is formed which appears as a mosaic of small crystals and above -100ºC, hexagonal ice crystals are formed.

Vitreous ice has no apparent structure, hence its use to preserve and image biological macromolecules (Dubochet et al., 1988). After plunging into a cryogen, such as ethane, grids are transferred into liquid nitrogen prior to either storage or visualisation in the electron microscope. Transfer of the grids into the cryo-specimen holder must also occur under liquid nitrogen (LN_2) once the holder has been cooled to near LN_2 temperature in order to prevent the introduction of contaminating ice crystals and the formation of frost (caused by condensation of atmospheric vapour on the grid). Frost and ice contamination may be introduced at all steps during sample preparation and transfer so these stages must be performed under liquid nitrogen and as quickly as possible.

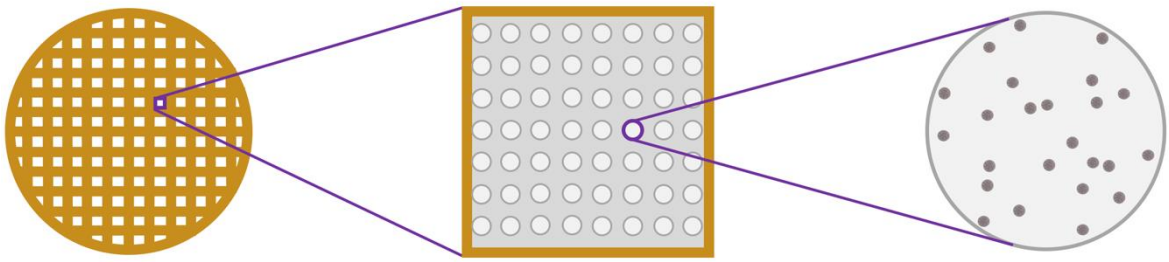

Figure 14- Schematic of a cryo-EM grid

A diagrammatical representation of a cryo-EM grid such as a C-flat showing the relationship between the 3.05mm grid and the grid bars/squares to the holey carbon film and particles suspended in vitreous ice.

Cryo-electron microscopes are equipped with an anti-contaminator which is cooled by an externally mounted dewar containing liquid nitrogen. The anti-contaminator is placed in the area of the specimen (within the microscope column) to ensure that any contaminants present condense on the anti-contaminator as opposed to the specimen. The holder can then be inserted into the electron microscope where high vacuum and the anti-contaminator both reduce the amount of ice contamination on the sample (Dubochet et al., 1988).

Cryo-EM provides many advantages over negative staining EM such as avoiding the dehydration and distortion of the sample although it does present some other challenges. Frozen hydrated specimens must be kept at a temperature near to that of LN_2 to avoid the warming of the sample and the transition to cubic or hexagonal ice. However, as the samples are not stained, they produce substantially lower contrast when imaged in the electron microscope.

2.2.11.2 Imaging in a transmission electron microscope

A typical transmission electron microscope consists of an electron gun, numerous electromagnetic lenses to focus the electrons released from the gun and a detector to record images of the sample (as shown in Figure 15).

The short wavelength of electrons allows high resolution imaging to be performed. However, radiation damage to the sample occurs due to interactions with the electrons from the beam. Three types of interactions can be described between electrons and the sample (see Figure 16). Electrons may pass through the sample without forming any interactions, electrons may be deflected away by the atom nuclei's electrostatic field or electrons may collide directly with the atom nuclei. Elastic scattering of electrons occurs when electrons interact with the specimen but are scattered without losing any energy. Inelastic scattering, conversely, occurs when interacting electrons lose energy/transfer energy to the specimen. This inelastic scattering can cause damage to the specimen in forms such as ionisation, x-ray emission, chemical bond rearrangement or induction of secondary electron scattering.

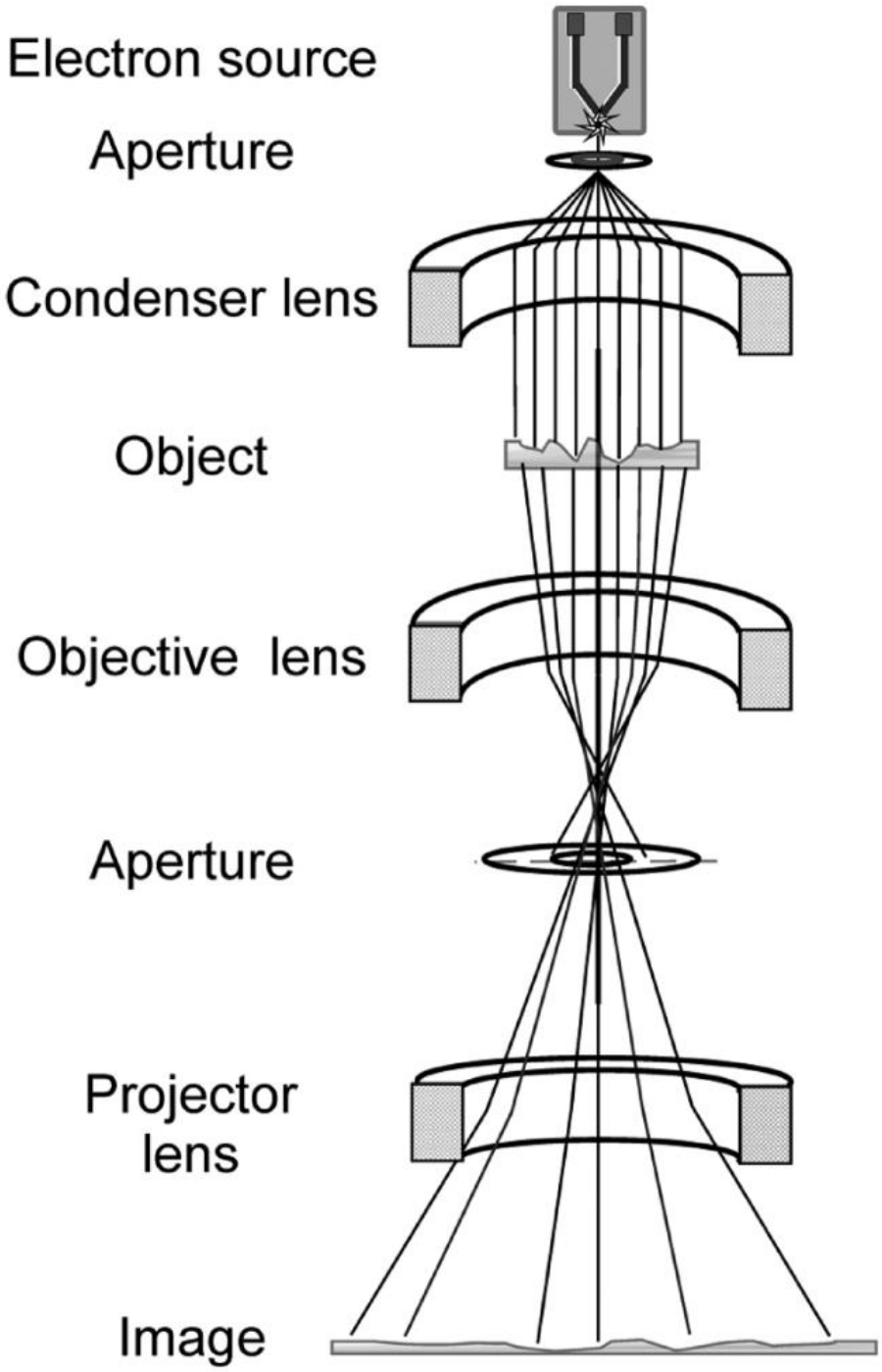

Figure 15- Schematic of a typical electron microscope.

A simplified diagrammatic representation of the major components of a transmission electron microscope. Taken from Orlova and Saibil, 2011.

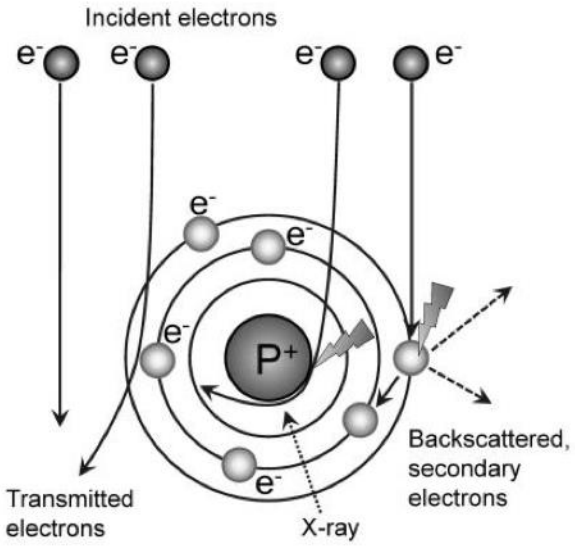

Figure 16- Interactions of electrons with the sample.

Schematic showing the different types of interactions that may occur between electrons and the sample within the electron microscope. Electrons may collide with atoms in the sample, leading to inelastic scattering and energy loss or electrons may be elastically scattered by either not interacting with the sample or by deflection from the electron cloud of the sample. Image taken from Orlova and Saibil, 2011.

Inelastic scattering is one of the main limitations observed when imaging biological macromolecules at high resolution, so sample thickness and beam exposure are reduced to attempt to limit this and the introduction of noise (Orlova and Saibil, 2011).

Electron sources/guns are generally one of three types, a tungsten filament, a Lanthanum hexaboride filament or a field emission gun (FEG). A tungsten filament is heated to 2000-3000ºC (by passing a high voltage through the filament) where the electron energy is higher than the tungsten work function (the amount of energy required to emit electrons). This heating results in the emission of electrons which are then accelerated down the microscope column by an electric field. Lanthanum hexaboride filaments are also thermal filaments although they are more efficient than tungsten filaments due to their lower work function. Field emission electron sources are generally used in high performance microscopes and use a single crystal tungsten with a very small tip radius of 10-25nm which is coated with zirconium oxide to lower the work function (Schottky FEG). Cold FEGs are also available which are considered 'cold' as they emit more electrons than can be emitted using thermal emission alone. Cold FEGs result in increased beam brightness as well as lower energy spread of the electrons which may help to improve resolution. Cold FEGs are, however, less stable than standard/schottky FEGs due to residual gases around the tip although an evacuation procedure has been developed to overcome this. The electrons emitted from FEGs are generally extracted at 200-300kV as opposed to <200kV for tungsten filament electron sources. FEGs also provide a brighter and more coherent beam than that from a tungsten filament (Orlova and Saibil, 2011).

Electron microscopes contain multiple series of lenses, most notably the condenser and objective lenses. The condenser lens system serves to focus the electron beam parallel to the column and onto the specimen. The specimen generally sits within the objective lens system which provides the primary magnification of 20-50x and focuses the beam onto the image plane after passing through the sample. The objective aperture is in the back focal plane of the objective lens and improves contrast by preventing any electrons that have been scattered to a high angle from reaching the image plane. The intermediate and projection lenses then magnify the image further which is then recorded by a

detector. Three main types of lens aberrations have been described: spherical, chromatic and astigmatic. Spherical aberration occurs when the outer edges of the lens focus the beam more strongly than the centre of the lens. Chromatic aberration occurs when a lens focuses longer wavelengths more strongly than shorter ones and is caused by variation in the voltage of the electron source. Astigmatism is a result of a lens being stronger in one direction than in the perpendicular direction and is caused by the lens magnetic field being asymmetric, resulting in an elliptical image (which can be compensated for using stigmator coils) (Orlova and Saibil, 2011).

An energy filter may be added in order to try to improve contrast of the images recorded. Electrons that have been inelastically scattered by the specimen have a lower energy than those that have been elastically scattered which results in them being focussed into different planes (also known as chromatic aberration). These inelastically scattered electrons result in the blurring and increased background noise of the image. Due to this, energy filters have been developed to prevent these electrons from contributing to the final image recorded and can be inserted either within the microscope column or post column (Orlova and Saibil, 2011).

Historically, images/electron micrographs were recorded on photographic film and then scanned/digitised but charge coupled device (CCD) based digital cameras are now the most common detectors in use. The CCD camera uses a phosphor scintillator to detect the incoming electrons and release photons in their place which are then transmitted to a charge coupled device and converted into a digital electronic signal. CCDs are more convenient detectors than recording data on film as it can be immediately inspected and processed. Recently, direct detection devices (DDD) have been developed which can be exposed directly to the electron beam, unlike CCDs which require a scintillator layer, reducing sensitivity. DDDs can be monolithic active pixel sensors (MAPS) or hybrid pixel detectors but MAPS are becoming the more prevalent choice for DDDs. In MAPS, the signal produced is proportional to electron energy detected and the detectors also have a smaller pixel size. As the DDDs do not require a scintillator layer, the signal to noise ratio (SNR) is greatly improved and the devices also show good tolerance to high levels of radiation, allowing their use with 200-300kV electron microscopes. DDDs are being developed to incorporate

aspects of CMOS (complementary metal oxide semi-conductor) which would allow a faster readout rate by permitting the local conversion of charge to voltage. This is possible due to each pixel in the detector containing an amplifier. DDDs/MAPS have a high read-out rate, allowing many frames for one image to be recorded which allows for later frames that received a higher electron dose to be removed if necessary as well as movie processing to correct for any sample movements. These improvements can be adopted during processing of the images (McMullan et al., 2014; Orlova and Saibil, 2011).

2.2.11.3 Image Formation

Contrast is formed in an image due to the interaction of electrons with the specimen. The electron wave is diffracted by regions of the sample and therefore result in its interaction with the undiffracted portion of the electron wave in the image plane. There are 2 different types of contrast: amplitude contrast and phase contrast. Amplitude contrast is caused by the interaction of electrons with the sample and causing them to be scattered beyond the acceptance angle of the objective aperture. Biological molecules produce little amplitude contrast as they are made of light atoms (H, O, N and C) so they do not absorb or highly scatter electrons from the beam, however they do interact so still change the electron properties as it proceeds through the specimen. Phase contrast is caused by the presence of a phase shift between the diffracted and undiffracted waves. The sample contributes to this phase shift as the electron passes through it as well as factors associated with the microscope such as spherical aberration and the level of defocus applied (Orlova and Saibil, 2011).

Imperfections in the microscope and its lens systems results in a modulation of the recorded image by the contrast transfer function (CTF). The CTF is the Fourier transform of the PSF (point spread function) of the microscope which is convoluted with the specimen projection to form the recorded image. Due to the affect of the PSF, CTF correction must be performed on all images prior to processing and three dimensional reconstruction. The CTF is a description of the relationship between the sample and the recorded image. The oscillating CTF is dependent on the accelerating voltage of the microscope, any spherical aberrations as well as the level of defocus applied by the user. At certain spatial

frequencies in the CTF, the oscillations result in zero contrast although this changes for differing levels of defocus (increased defocus results in CTF oscillations with peaks closer together/occurring more rapidly) and so less high resolution information will be recorded). The relationship between defocus and CTF is illustrated in Figure 17. To compensate for this, the phases below zero may be flipped to produce only positive oscillations. Data collected at differing levels of defocus result in overlapping CTFs to compensate for the regions approaching zero in a given CTF.

2.2.11.4 Data Processing/3D reconstruction

Projection theorem states that the Fourier transform of a 2D projection of the sample is a slice through the centre of the 3D Fourier transform of the structure of the sample/object. This means that, once CTF corrected, the Fourier transform of a micrograph represents a central slice through the 3D Fourier transform of the specimen structure (Nogales and Scheres, 2015). In single particle analysis of a sample, objects are assumed to be identical but differently oriented. This means that imaging the sample with its many orientations, provides many central slices through the 3D Fourier transform of the object, allowing the transforms to be combined and a 3D reconstruction computed. High symmetry objects are very efficient in this manor as fewer views/orientations are needed to elucidate the structure owing to repeating subunits and orders of symmetry.

The first steps required in the processing of micrographs are to determine the defocus value using the Thon rings on the Fourier transform by fitting the modelled CTF to the power spectrum (the square of the Fourier transform amplitudes). The simplest method of CTF correction is known as phase correction and involves flipping the phases in the regions where the spectra have negative values. This provides reliable data when micrographs are recorded at differing levels of defocus as the information lost at the zero's is restored from other micrographs. Micrographs can also be corrected for any motion recorded between frames due to factors such as drift at this early stage of image processing.

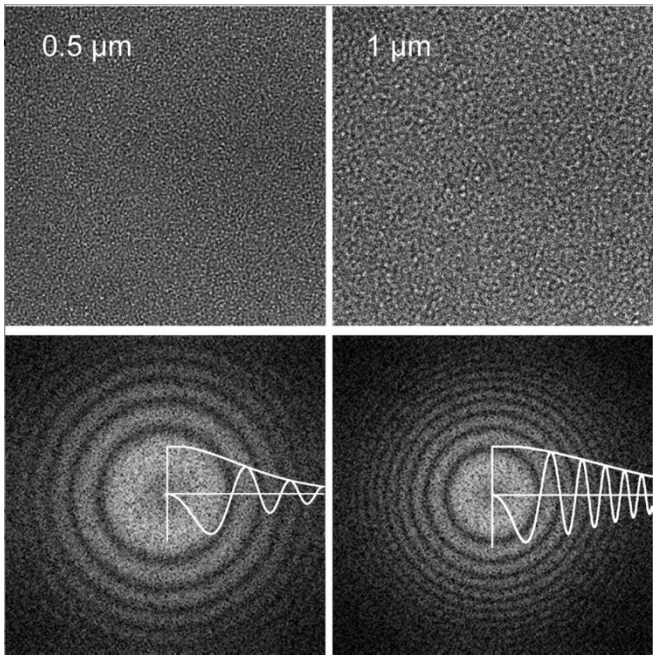

Figure 17- Carbon film images and their diffraction patterns

Images of carbon film at either 0.5 or 1µm defocus showing their diffraction patterns below the respective micrographs. The diffraction patterns show the Thon rings and their CTF curves, illustrating that the CTF oscillations are closer to the origin/occur more rapidly when further away from focus. Taken from Orlova and Saibil, 2011.

Particle coordinates must then be selected either by manual particle picking or automated particle picking. Semi-automated options also exist where the user manually selects particles from a subset of micrographs and these are then used as a template for the automated particle picking such as that in RELION (Scheres, 2015). Manual and semi-automated particle picking results in the introduction of less false positives although it is more time consuming. Individual particles must then be extracted from the micrographs in boxes, the width of which is provided by the user. Differences in image contrast can arise from many factors including specimen particle orientation, sample thickness and SNR so these must be normalised to allow further downstream averaging and processing. Particles are normalised to a common mean and standard deviation to allow efficient subsequent alignment and classification.

RELION implements a maximum likelihood method and iterative classification where images are compared with all references (generated from averages or random subsets in reference free alignment) in all orientations possible and calculates probability weights for each possible orientation. Weighted averages for all orientations are then used to produce class averages which are the input for the next iteration. The only user input here in the 2D classification is the number of classes to generate and the process usually iterates 25 times before producing a final set of class averages where false positives are usually classified separately. This allows the selection of ‘good’ particles/data and the exclusion of ‘bad’ data that would potentially limit the resolution further downstream. 3D classification may also separate out different conformations if a heterogeneous population is present within the sample. The user can select which classes to take forward in different pipelines in order to process data from differing conformations separately if that is desirable. 3D classification is performed with a user defined number of classes and a low resolution starting model. A similar known structure can be used as a starting model although the model must be filtered in order to prevent model bias occurring during the reconstruction process. It has previously been shown that a model can significantly affect the outcome of image processing. Shatsky et al showed that when an image of Einstein was used as the initial model and 1000 images of noise were averaged and processed with the model, the resulting image showed the depiction of Einstein (Shatsky 2009). This illustrates the issue of model bias which must be

overcome in order to generate an accurate structure from data. One way to reduce model bias is to heavily filter the model structure before use (typically to around 60 angstroms) so very few details remain. This ensures that any details present in the final reconstruction have come from the data and not from the model.

Typically, this process is iterated 25 times to maximise accuracy. The user may then select which data they wish to continue processing by selecting the 3D classes containing the 'best' data or selecting different conformations to proceed with in separate processing pipelines. A 3D refinement step is then performed for a number of iterations until the optimal particle orientations and the log-likelihood values no longer change (Scheres, 2010).

The resolution of the reconstructions can then be calculated using 'gold standard' Fourier Shell Correlation (FSC). FSC compares the Fourier transforms of two three dimensional volumes over different shells as a function of spatial frequency. FSC indicates at which spatial frequency (the inverse of which gives a resolution estimate) information above the random noise level is observed.

More traditional methods of FSC calculation have led to overfitting of noise where resolution estimates were not accurate for the given structure. In traditional FSC, the data are divided into two halves and a single model is used to determine the orientations of all the particles. Gold standard FSC, however, avoids model bias by only using the model in the first iteration. The degree of agreement between the FSC curves of the two halves of the data set is then calculated and used to provide a measure of resolution. The spatial frequency where the gold standard FSC passes the 0.143 mark is seen to be a good indicator of resolution (Scheres, 2012; Scheres and Chen, 2012). In RELION, this process is performed at the end of each 3D refinement iteration.

At high resolution, structures may have lost signal due to factors such as beam induced movement, radiation damage or computation inaccuracies. This loss of resolution was traditionally modelled by a Gaussian decay of structure factors with a B-factor (also known as a temperature factor). These 'lost' high resolution features may be rebuilt/sharpened in the map in a process known as B-factor correction. One method of performing B-factor correction involves

estimating the amplitude decay of the structure factors by comparison with an approximate theoretical scattering curve (Fernandez et al., 2008).

Local resolution analysis can also be performed in order to assess whether certain areas of the reconstruction are at higher or lower resolution. Higher resolution may indicate stability when compared to lower resolution components which may be flexible or adopt different conformations and therefore limit the resolution achievable. Known atomic structures can also be docked into the map in order to inspect the secondary structure elements of the sample. This may be needed if the resolution of the map is limited as a resolution of 6-9Å is needed to observe alpha-helices and beta-strands are only visible beyond 4.5Å. The detail of smaller amino acid side chains is only visible in very high resolution structures i.e. below 4Å resolution (Orlova and Saibil, 2011).

Once a high resolution structure has been obtained, molecular modelling may be applied in order to model the amino acid structures into the protein density of the structure. If a homologous structure is already known, this can be computationally fitted into the density of the map. The positions of the amino acids and their side chains can then be optimised to better fit the experimental data/density or even replaced if the sequence differs to that of the homologous model used (using software such as Coot (crystallographic object-orientated toolkit)) (Emsley and Cowtan, 2004).

2.2.11.5 Negative Staining electron microscopy methodology

2.2.11.5.1 Sample preparation

400 Square Mesh Copper 3.05mm electron microscopy grids (Agar Scientific) were formvar and carbon coated then glow discharged prior to negative staining electron microscopy. To formvar coat grids, 0.25g formvar was dissolved with 50ml chloroform to make a 0.5% formvar solution. Standard glass microscope slides were cleaned with alcohol and inserted into the formvar solution for a few seconds. The slides were then removed and allowed to air dry. A diamond marker was then used to score along all 4 edges of the slide. A large vessel was filled with deionised water and the slide slowly inserted into the water while blowing warm air onto the slide-water interface to assist in the floating of the thin formvar layer onto the surface of the water. Electron microscopy grids were

then placed onto the floating formvar film and a large microscope cover slip pressed onto one edge of the film and flipped out of the water. The slide containing the formvar and coated grids was then allowed to dry before carbon coating. A Quorum Q150T turbo pumped carbon coater was then used to deposit a thin layer of carbon onto the formvar coated grids by applying 45 amps through two touching sharpened carbon rods. Grids were glow discharged at 25 mAmps for 1 minute using an EMITECH K100X glow discharger before addition of the sample and staining.

Five microliters of sample was added to each grid and incubated for 2 minutes at room temperature. Excess sample was removed by blotting the side of the grid with filter paper followed by washing 3 times on drops of deionised water, blotting in between each wash. Grids were then washed on 3 drops of 2% uranyl acetate, blotting in between each wash, before a final drop of uranyl acetate was added to each grid and incubated for 5 minutes prior to blotting away any excess stain. Grids were then allowed to dry before visualisation in an electron microscope.

2.2.11.5.2 **Imaging conditions**

Negative staining electron microscopy grids were imaged in a JEOL 1200 EXII Transmission Electron Microscope at a range of magnifications. Images were recorded on a Gatan Orius camera.

2.2.11.6 Cryo-electron microscopy methodology

2.2.11.6.1 **Sample preparation**

Five microlitres of the sample of interest was added to a C-flat Advanced Holey Carbon Film Grid (ProtoChips, glow discharged as previously described) and blotted for 4 seconds (with a blot force of 25) to remove any excess sample. An FEI Mark IV Vitrobot was used (at 100% humidity and 4°C) to plunge the grids into liquid nitrogen cooled liquid ethane. Grids were then transferred to liquid nitrogen for storage prior to imaging.

2.2.11.6.2 Imaging

A JEOL JEM-2200FS Field Emission Electron Microscope was used to image virus particles for cryo-electron microscopy (using liquid nitrogen to ensure a constant temperature of -180°C) under low electron dose conditions. Vitrified samples were imaged in a Gatan 626 cryo-stage with an energy filter slit width of 20eV at 200kV.

Feline calicivirus was imaged as above, with a Direct Electron DE20 direct detection device or on an FEI Titan Krios TEM with a Falcon III detector (as specified). The DE20 direct detection device was used to image virus particles at x50,000 magnification resulting in a pixel size of 1.09Å per pixel. Images were recorded at a defocus of 1.5-2.5μm. Additional acquisition parameters are specified in Table 1.

An FEI Titan Krios with a Falcon III detector was used at 300kV at a magnification of x75,000 resulting in a pixel size of 1.065Å per pixel. Images were taken with defocus values of 1.2-3.5μm (operated by Dr Rebecca Thompson, University of Leeds). Additional acquisition parameters are specified in Table 1.

2.2.11.6.3 Image processing

2.2.11.6.3.1 Icosahedral reconstruction using PFT2

Images of FCV particles at pH4 and pH5 were contrast transfer function (CTF) corrected and the particles extracted from the micrographs using the BSoft program, Bshow (Heymann, 2001). The polar Fourier Transform (PFT2) method was then used to determine the origins and orientations of the particles before the creation of 3D reconstructions using the EM3DR2 program (Baker and Cheng, 1996; Bubeck et al., 2005). The resolution of the maps was estimated by splitting the data set into two and producing 3D reconstructions for each half of the data set. Bresolve was then used to compare the two reconstructions and to calculate the Fourier Shell Correlation (FSC) where a cut off of 0.5 was applied.

Data Set	Microscope	Dose rate (e^-/pix/s)	Dose rate ($e^-/A^2/s$)	No. of frames	Total dose (e^-/A^2)
FCV	FEI Titan Krios	1.26	42	50	63
FCV+fJAM-A	FEI Titan Krios	1.26	42	50	63
FCV+fJAM-A (10:1)	JEOL JEM-2200FS	1.47	25.12	48	70.34
FCV+fJAM-A (11:1)	JEOL JEM-2200FS	1.25	21.24	48	59.48
FCV+fJAM-A (12:1)	JEOL JEM-2200FS	1.36	23.22	48	65.02

Table 1- Electron microscopy data acquisition parameters

The microscopy conditions for each data set are provided alongside the microscope used. Dose rates (electrons per pixel per second as well as electrons per angstrom^2 per second), total doses (electrons per angstrom^2) and the number of frames collected per micrograph are also provided.

2.2.11.6.3.2RELION

MotionCor2 was used to correct micrographs for any drift that may have occurred and the defocus/CTF estimated using Gctf. Relion 2.0.3 was used thereafter for image processing and 3D reconstruction. Particles were picked from the micrographs and reference free 2D class averaging was performed to yield 60 class averages. The classes of interest were then selected and 3D classification was performed followed by 3D refinement (with I2 icosahedral symmetry imposed). Post processing was then performed in order to carry out B-factor correction followed by local resolution estimation using the built in RELION module.

2.2.11.6.4 Visualisation of structures

2.2.11.6.4.1 UCSF Chimera visualisation and calculation of correlation values

UCSF Chimera was used for the visualisation of all three dimensional structures observed (Pettersen et al., 2004). For lower resolution maps, an isosurface threshold of the mean plus 1 standard deviation was used whereas higher resolution maps were rendered to optimally represent visible amino acid side chains. The 'Fit in Map' function of UCSF chimera was used to calculate correlation values between 2 maps and to measure the degrees of rotation of capsid proteins where specified.

2.2.11.6.4.2 Model building

The FCV5 VP1 crystal structure was used alongside the F9 VP1 sequence to generate a model of the FCV VP1 capsid protein (using SWISS-MODEL) which was then fitted into the density map using Coot (Arnold et al., 2006; Emsley and Cowtan, 2004). The density was then used to refine the positions and orientations of the amino acids in the sequence using Phenix (Adams et al., 2010). RMSD values for overlaid structures were calculated in UCSF Chimera (Pettersen et al., 2004).

3 Investigating the influence of fJAM-A glycosylation and oligomerisation on FCV binding

The ectodomain of both human and murine forms of JAM-A have been shown to be dimeric in solution and contain an N-linked glycosylation site. Stuart *et al*. (2007) proposed alpha 2-6 linked sialic acid as a receptor for FCV and so we hypothesised that this sialic acid receptor could be present as a glycosylation of fJAM-A. Here we show that fJAM-A is N-glycosylated and, using a variety of techniques, that deglycosylation of the fJAM-A ectodomain purified from CHO cells does not affect virus binding *in vitro*. Using size exclusion chromatography and SAXS, we also show that fJAM-A is dimeric in solution and forms similar structures to that of its human and murine homologues.

3.1 Purification of bivalent and monovalent forms of fJAM-A

To investigate the nature of the interaction between FCV and fJAM-A, we set out to purify the soluble extracellular domain (ectodomain) of fJAM-A fused to an Fc tag. As previously described, members of Prof Ian Goodfellow's lab (University of Cambridge) generated a mammalian protein expression vector containing the coding sequence for the ectodomain of fJAM-A fused to a C-terminal Fc tag (from human IgG1). A factor Xa cleavage site was engineered between the fJAM-A coding sequence and the Fc tag to allow downstream removal of the tag and purification of the fJAM-A ectodomain. This construct was transfected into CHO cells and a stable cell line expressing the secreted form of the fusion protein (Fc-fJAM-A) established by Prof Ian Goodfellow (University of Cambridge) (Bhella et al., 2008).

Stably transfected CHO cells were incubated for 7 days prior to harvesting the media containing the secreted Fc-fJAM-A protein. Supernatant was filtered through a 0.22µm vacuum system prior to protein A purification (see 2.2.3.2). The chromatogram showing the absorbance at 280nm is shown in Figure 18 where panel A represents the chromatogram as a whole, while B shows a zoomed section highlighting the absorbance peaks visible at the right-hand side of panel A. As cells were grown in the presence of 10% FBS, any contaminating bovine immunoglobulins were removed using a citrate elution with intermediate pH (see

in panel B). Following a PBS wash, the Fc-fJAM-A fusion protein was eluted in 0.1M glycine buffer pH2.5 (see * in panel B) and the fractions neutralised with Tris pH8. Figure 18 (A and B) shows the tight, clean peak produced as the fusion protein is eluted from the column in only three 0.5ml fractions. All eluted fractions, including input controls, were then analysed by SDS-PAGE (C) and western blotting (D) showing the high purity of the samples with very few contaminating proteins visible. By both SDS-PAGE and western blot, a smaller protein of approximately 32kDa is visible in the later stages of purification. This 32kDa band is visible using an anti-Fc antibody for detection by western blotting and so we assumed that this was a population of Fc which was not fused to fJAM-A.

We hypothesise that the Fc-fJAM-A protein will be bivalent in form due to the linkage of Fc regions by disulphide bridges as is seen for antibodies including IgG. For this reason, the Fc tag was cleaved and removed from the samples to yield the monovalent form of fJAM-A. To cleave the Fc domain from the fJAM-A, Fc-fJAM-A was incubated with factor Xa overnight and the enzyme subsequently removed using factor Xa removal resin (see 2.2.3.3).

Fc proteins were removed from the sample using protein A dynabeads, as per manufacturers instructions, resulting in the collection of fJAM-A in the ‘flow through’ and the elution of Fc from the beads, confirming the identity of the contaminating band (see Figure 18E). Using a combination of protein A purification, factor Xa cleavage and protein A dynabead purification, a pure sample of the fJAM-A ectodomain can be produced and used for downstream investigations such as *in vitro* assays as well as cryo-EM.

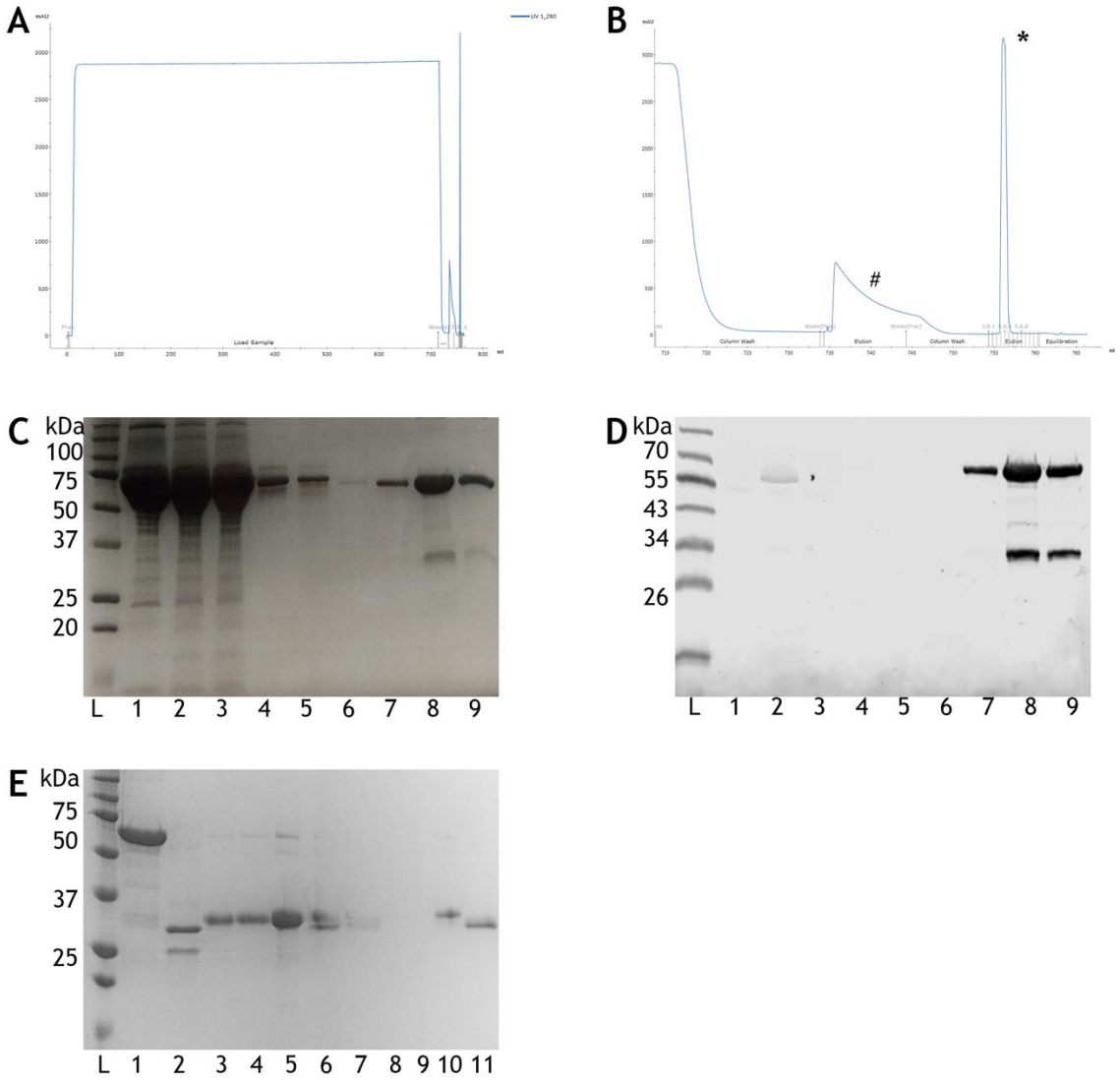

Figure 18- Purification of fJAM-A

Fc-fJAM-A was purified by protein A affinity chromatography followed by factor Xa cleavage to remove the Fc tag. The absorbance during protein purification (A and B (B: zoom of peaks in A)) shows the removal of contaminating bovine immunoglobulins (#) followed by the elution of the Fc-fJAM-A protein (*) into three 0.5ml fractions. All fractions were run on an SDS-PAGE gel (C) and western blotted (D) using an anti-Fc antibody to detect the fusion protein (L: Precision Plus Protein Kaleidoscope ladder (BIO-RAD), 1: negative control cell culture medium, 2: Fc-fJAM-A supernatant (input), 3: flow through, 4: first wash, 5: citrate elution of bovine immunoglobulins, 6: second wash, 7-9: eluted fractions of Fc-fJAM-A). Panels C and D together show the high purity of the Fc-fJAM-A protein although smaller bands corresponding to Fc alone can also be seen of approximately 32kDa. The Fc-fJAM-A fusion protein was cleaved using factor Xa and all fractions run on an SDS-PAGE gel as shown in panel E (L: Precision Plus Protein Kaleidoscope ladder (BIO-RAD), 1: undigested Fc-fJAM-A, 2: Factor Xa, 3: Fc-fJAM-A and factor Xa cleavage reaction, 4: sample post-resin removal of factor Xa, 5: Factor Xa removal resin, 6: protein A purification flow through (containing fJAM-A), 7, 8 and 9: protein A washes, 10: Fc elution, 11: concentrated fJAM-A). A doublet is visible in lane 6 illustrating that some Fc still remained in the sample and so the protein A dynabead step was repeated to successfully remove any residual Fc.

3.2 Deglycosylation of fJAM-A

Sialic acid has previously been identified as a potential receptor for FCV on CrFK cells despite fJAM-A being accepted as the main cellular receptor for the virus (Makino et al., 2006; Stuart and Brown, 2007). We hypothesised that the sialic acid to which FCV binds could perhaps be present as a carbohydrate moiety on fJAM-A rather than being present as a separate entity or receptor. This was a possibility as fJAM-A contains a putative glycosylation site at position 184 (N), which is present in the ectodomain and therefore our purified soluble fragment. This presented a tool for the study of both the glycosylation of fJAM-A but also the effect that receptor glycosylation may have on FCV binding.

3.2.1 fJAM-A is N-glycosylated

To firstly confirm the glycosylation of fJAM-A, and to secondly determine the type of glycosylation present, if any, a panel of six deglycosylation enzymes was screened for their effect on fJAM-A size using SDS-PAGE. fJAM-A was incubated with either alpha 2-3,6,8,9 Neuraminidase A, Beta1-4 galactosidase, Endoglycosidase H (Endo H), PNGase F, Beta-N-Acetylglucosaminidase or O-glycosidase (in combination with alpha 2-3,6,8,9 Neuraminidase A) to determine if the protein contained an N-linked glycosylation (Endo H and PNGase F) or an O-linked glycosylation (O-glycosidase). As shown in Figure 19, the only enzymes which had an effect on the molecular weight of fJAM-A were alpha 2-3,6,8,9 Neuraminidase A and PNGase F. A slight reduction in molecular weight was seen upon treatment with O-glycosidase but this is a result of the required co-incubation with alpha 2-3,6,8,9 Neuraminidase A. These reductions in fJAM-A molecular weight from approximately 32kDa to around 29-30kDa upon incubation with these two enzymes illustrates that fJAM-A is glycosylated and this glycosylation is N-linked. This supports the identification of a predicted N-linked glycosylation site at position 184 of the fJAM-A ectodomain.

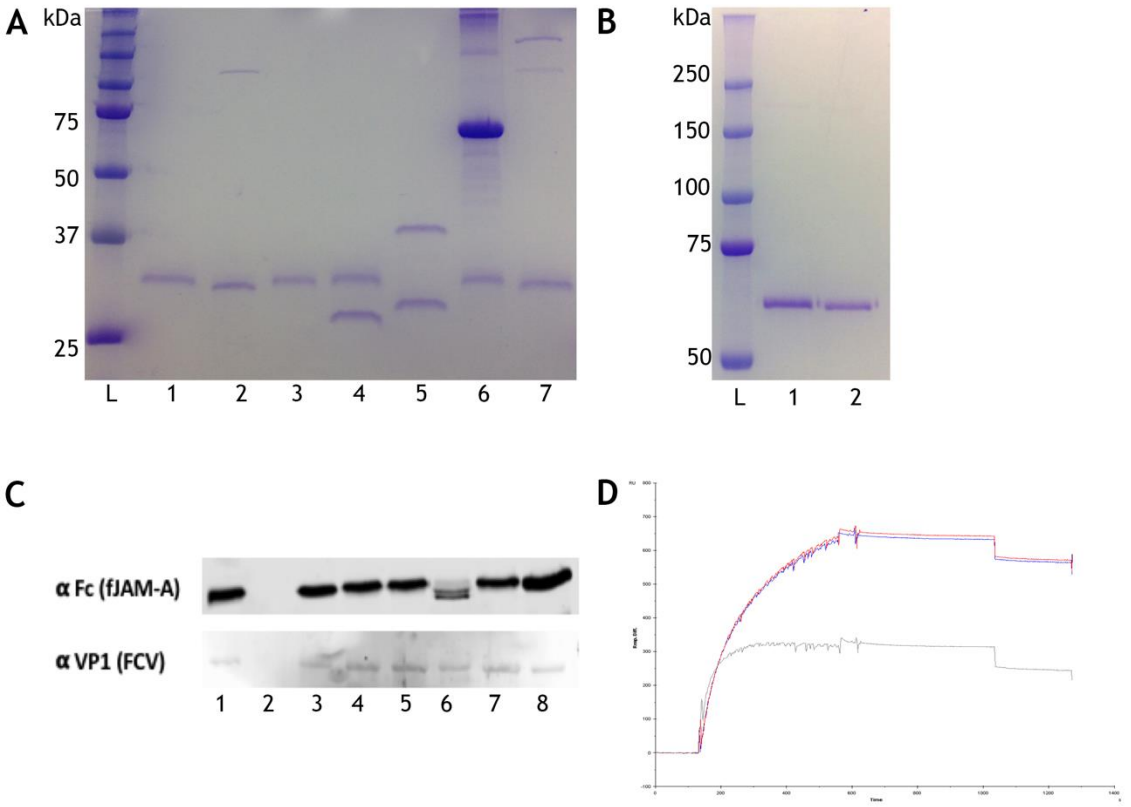

Figure 19- Deglycosylation of fJAM-A and its effect on FCV binding

To determine the glycosylation state of fJAM-A, purified ectodomain was incubated with a panel of six deglycosylation enzymes, as per manufacturer's instructions, and analysed by SDS-PAGE (A). Panel A shows the effect of these enzymes on fJAM-A molecular weight (L: Precision Plus Protein Kaleidoscope ladder (BIO-RAD), 1: untreated fJAM-A and fJAM-A treated with 2: alpha 2-3,6,8,9 neuraminidase A, 3: beta1-4 galactosidase, 4: Endo H, 5: PNGase F, 6: beta-N-acetylglucosaminidase and 7: O-glycosidase (in combination with alpha 2-3,6,8,9 neuraminidase A). Bands above 50kDa represent the corresponding enzymes as well as the bottom band of 29kDa in lane 4 (corresponding to Endo H). Together, these banding patterns reveal that only alpha 2-3,6,8,9 neuraminidase A and PNGase F have the ability to effect the size of fJAM-A and therefore its glycosylation state, indicating the presence of an N-linked glycan on fJAM-A. Panel B shows the effect of alpha 2-3,6,8,9 neuraminidase A on Fc-fJAM-A (L: Precision Plus Protein Kaleidoscope ladder (BIO-RAD), 1: untreated Fc-fJAM-A and 2: alpha 2-3,6,8,9 neuraminidase A treated Fc-fJAM-A) showing the slight decrease in molecular weight upon incubation with the enzymes, demonstrating that the carbohydrate moieties can also be removed from the fusion protein. Panel C shows the outcome of an immunoprecipitation experiment where Fc-fJAM-A was bound to protein A dynabeads following incubation with the aforementioned deglycosylation enzymes. Protein bound beads were then incubated with FCV and analysed by western blotting to assess the extent to which the enzymes affected virus binding (1: untreated Fc-fJAM-A, 2: negative control (no Fc-fJAM-A), Fc-fJAM-A treated with 3: alpha 2-3,6,8,9 neuraminidase A, 4: beta1-4 galactosidase, 5: Endo H, 6: PNGase F, 7: beta-N-acetylglucosaminidase and 8: O-glycosidase (in combination with alpha 2-3,6,8,9 neuraminidase A).

PNGase F treated FcJAM-A (lane 6) was seen to produce multiple bands, likely due to the PNGase F enzyme deglycosylating both fJAM-A and Fc to varying extents. FCV VP1 was detected in all samples except the negative control indicating that the glycosylation of Fc-fJAM-A does not influence FCV binding. Panel D shows a biacore sensorgram illustrating that glycosylated Fc-fJAM-A (blue) is able to bind to flowing FCV to the same extent as alpha 2-3,6,8,9 neuraminidase A treated Fc-fJAM-A (red) with limited non-specific binding seen to a negative control antibody (anti-HSV: grey).

3.2.2 fJAM-A glycosylation does not affect virus binding *in vitro*

To test whether glycosylation of fJAM-A had any effect on virus binding *in vitro* we used a virus pull-down assay. These experiments exploited the presence of an Fc domain on our bivalent Fc-fJAM-A fusion protein. The ability to deglycosylate this fusion protein was therefore evaluated by incubation with alpha 2-3,6,8,9 Neuraminidase A and analysis by SDS-PAGE (see Figure 19B). Following confirmation of our ability to use bivalent Fc-fJAM-A in place of the monovalent ectodomain (fJAM-A), Fc-fJAM-A was incubated with the previously mentioned six deglycosylation enzymes before binding to protein A dynabeads as per manufacturer's instructions. Purified FCV particles were then added to the sample and incubated prior to washing the beads. Any bound protein/virus was then removed from the beads by incubation in laemmli buffer at 95°C and analysed by SDS-PAGE. Separated proteins were then transferred to a nitrocellulose membrane and western blotted to detect FCV VP1 or Fc (Fc-fJAM-A). Figure 19C shows the presence of FCV VP1 in all samples indicating that the deglycosylation of Fc-fJAM-A did not disrupt virus binding.

To confirm that fJAM-A glycosylation status does not affect virus binding we used surface plasmon resonance analysis (Biacore). Three separate experiments were performed in which glycosylated Fc-fJAM-A, alpha 2-3,6,8,9 Neuraminidase A treated Fc-fJAM-A or a negative control ligand (anti-HSV IgG) was bound to a flow cell in a Biacore chip. Purified virus particles were flowed over the cells to assess the amount and rate of analyte binding to each ligand. As shown in Figure 19D, little, if any, virus bound to the negative control (grey), however, virus was

shown to bind to both glycosylated Fc-fJAM-A and desialylated Fc-fJAM-A to very similar extents (blue and red, respectively). This supports the previous immunoprecipitation experiments which suggested that the glycosylation (or rather the deglycosylation) does not affect the ability of FCV to bind to fJAM-A. This does not, however, rule out the possibility that the glycosylation may affect the strength of the virus binding to its receptor or the possibility that the glycosylation is present only to stabilise the protein.

3.2.3 The glycosylation state of soluble fJAM-A does not affect virus neutralisation

Makino *et al*. demonstrated that soluble ectodomain fragments of fJAM-A were able to neutralise FCV (Makino et al., 2006). We sought to test whether glycosylation status influences the ability of soluble fJAM-A fragments to neutralise FCV. FCV was pre-incubated with Fc-fJAM-A or deglycosylated Fc-fJAM-A and then inoculated onto CrFK cells. No significant difference in plaque number was seen between infections with fJAM-A neutralised virus and virus treated with deglycosylated receptor. This shows that the glycosylation state of fJAM-A does not reduce the avidity of the ligand as the glycosylated fJAM-A on cells was not able to compete off the bound deglycosylated fJAM-A. Figure 20 shows a slight reduction in plaque number (incorporating the four normalised Fc-fJAM-A dilutions in triplicate) although the difference between these data was not statistically significant and so no meaningful conclusions can be drawn except the agreement with the previous data suggesting that the glycosylation of fJAM-A does not affect FCV binding.

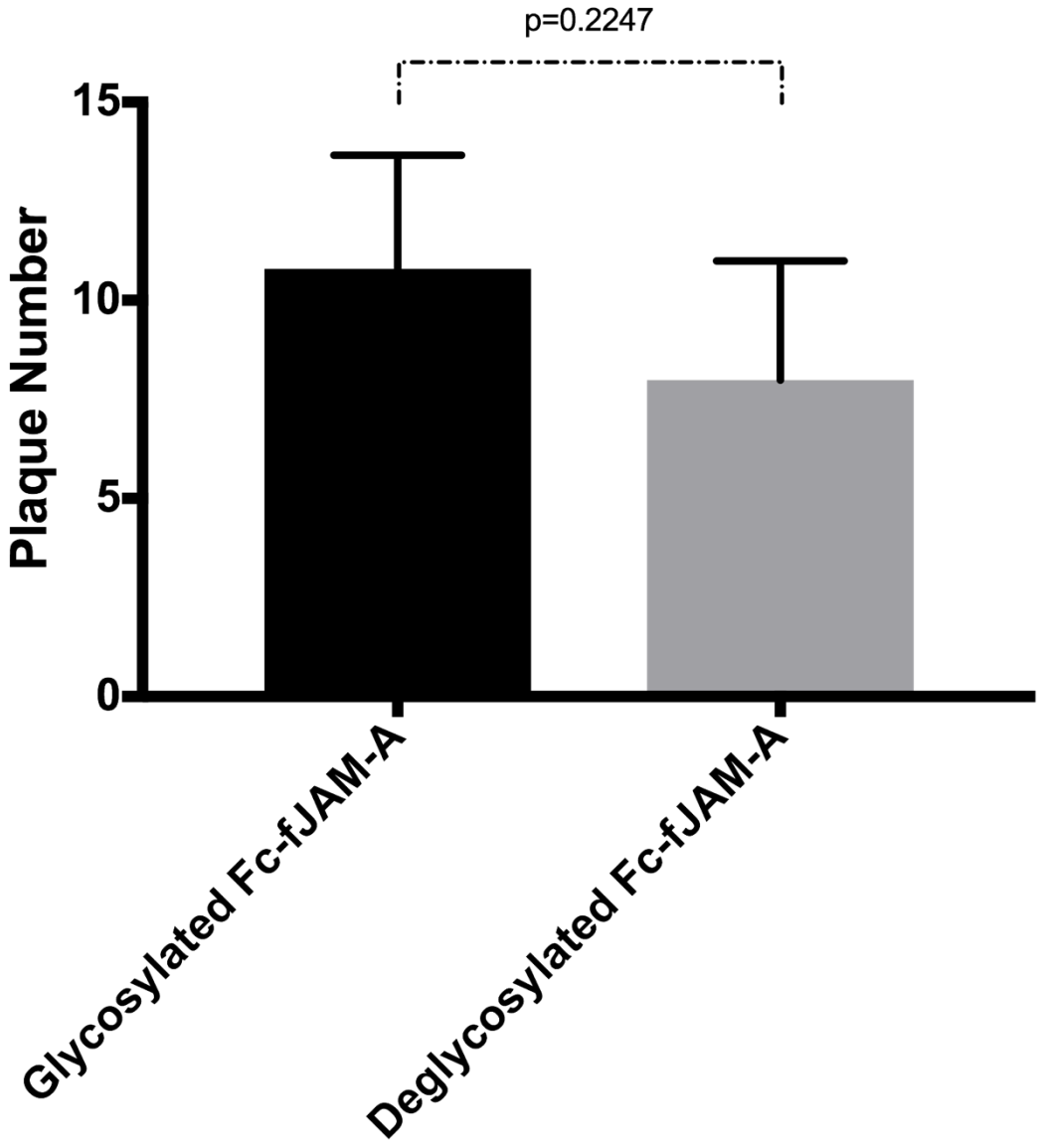

Figure 20- Neutralisation of FCV by Fc-fJAM-A

Fc-fJAM-A was either untreated or PNGase F treated as per manufacturer's instructions prior to incubation at various dilutions with FCV (MOI: 3). FCV with either Fc-fJAM-A or deglycosylated Fc-fJAM-A was incubated for 1hour at 4ºC and added onto a confluent CrFK monolayer in 6-well plates in triplicate. Plates were treated as a plaque assay thereafter. Plaques from each form of Fc-fJAM-A and each dilution were counted and normalised to the corresponding undiluted Fc-fJAM-A sample prior to analysis of the data. No significant (p=0.005) effect on FCV neutralisation was seen with deglycosylated Fc-fJAM-A.

3.3 Oligomerisation state of monovalent and bivalent soluble forms of fJAM-A

Both murine and human JAM-A ectodomains have been shown to be dimeric, by crystallography and size exclusion chromatography (Kostrewa et al., 2001; Prota et al., 2003). We hypothesised that the ectodomain of fJAM-A likely also formed dimers although the bivalent form (Fc-fJAM-A) may form dimers and/or aggregates due to a combination of both fJAM-A dimerisation and Fc dimerisation by disulphide bonds (like that seen with antibodies; see Figure 21). To test the oligomeric state of fJAM-A, size exclusion chromatography was performed on both the glycosylated protein and on deglycosylated protein (PNGase F treated). The Fc-fJAM-A fusion protein and the fJAM-A ectodomain were analysed under both conditions. Figure 22 shows that both Fc-fJAM-A and the fJAM-A ectodomain form dimers in solution (as depicted in Figure 21A and B). Interestingly, the Fc-fJAM-A proteins did not form the aggregates illustrated in Figure 21C as predicted. This may be due to the conformation of fJAM-A linked to an Fc tag or due to steric hindrance caused by the almost equivalent size of the Fc tag. It may also be possible that the fJAM-A from two linked Fc-fJAM-A proteins may dimerise together, similar to that seen with the monovalent form (Figure 21B). Interestingly, treatment of either form of the protein with PNGase F did not alter the oligomeric species observed, with both glycosylated and deglycosylated proteins also forming dimers. Volumes at which the peaks were eluted and the calculated molecular weights (and corresponding number of fJAM-A proteins) are presented in Table 2.

All molecular weights calculated were approximately twice the value of the monomer (62kDa for Fc-fJAM-A and 32kDa for fJAM-A) suggesting that all forms of the protein tested formed dimers in solution. The calculated numbers of fJAM-A proteins for the deglycosylated forms of the protein were slightly reduced compared to the glycosylated fJAM-A proteins due to the apparent reduction in molecular weight following removal of the carbohydrate moiety (as seen in SDS-PAGE: see Figure 19).

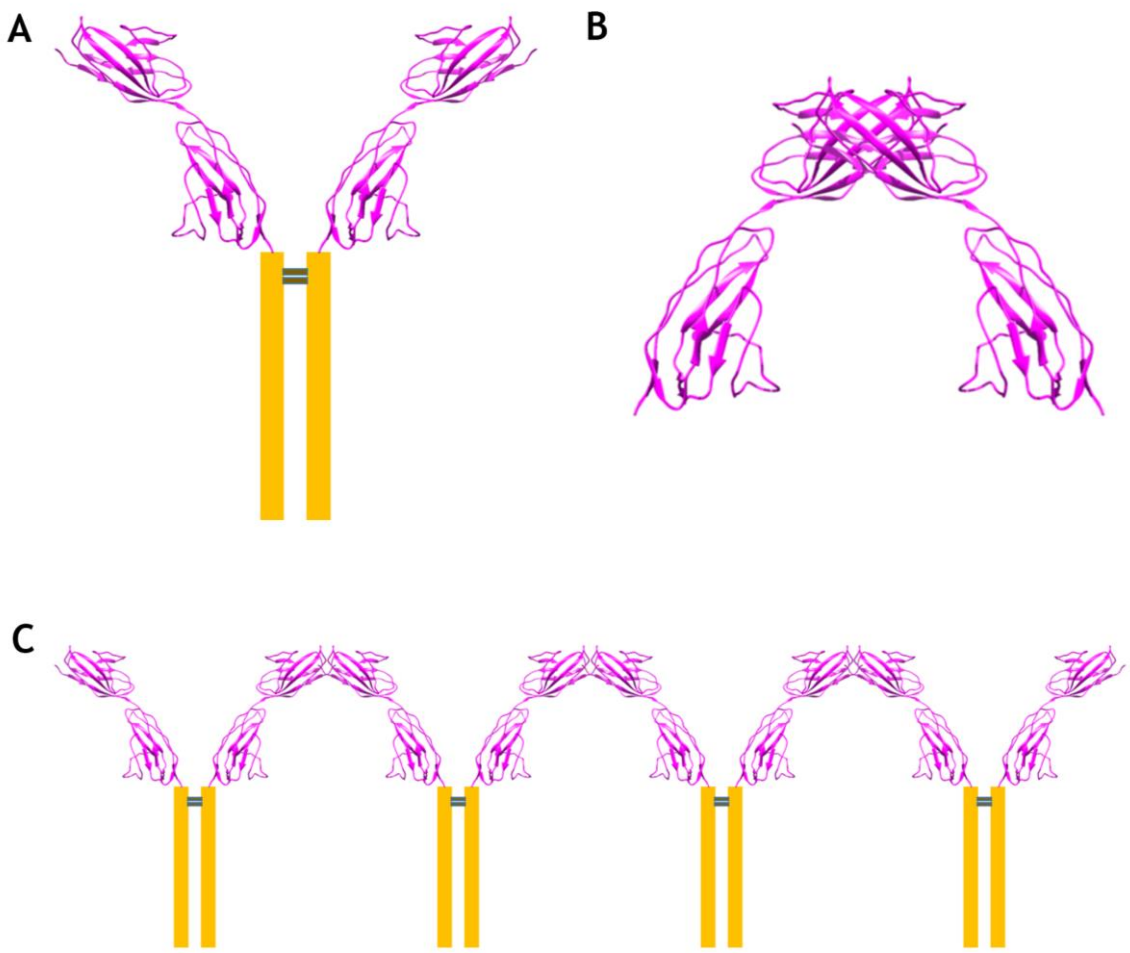

Figure 21- Hypothesised oligomerisation states of bivalent and monovalent fJAM-A

The fJAM-A ectodomain (pink) was expressed with a C-terminal Fc tag (orange) which likely forms dimers due to disulphide bond formation (grey) as seen in antibody production. We therefore hypothesise that the expressed bivalent Fc-fJAM-A will form a dimer (A) and may aggregate due to additional interactions between the fJAM-A ectodomains, resulting in the linkage of many Fc-fJAM-A proteins (C). The monovalent form of JAM-A has been shown to be dimeric (B) in solution and so we hypothesise that fJAM-A will also form these dimeric complexes.

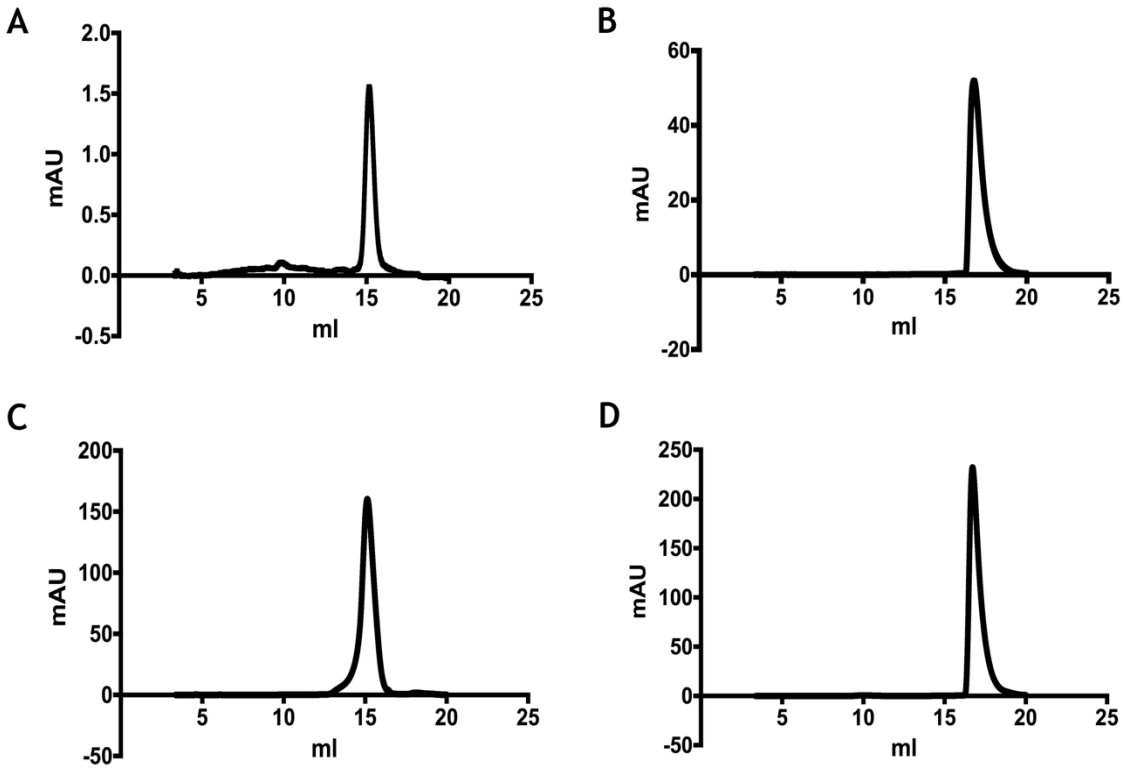

Figure 22- Size exclusion chromatography shows fJAM-A is dimeric

Size exclusion chromatography was performed to determine the oligomeric state of fJAM-A. Previous column calibrations performed by Samuel Stokes (Boutell group - CVR) were used to estimate the molecular weights of the proteins as they formed visible peaks and were eluted from the column at given volumes. Both Fc-fJAM-A (A) and fJAM-A (B) were analysed as well the PNGase F treated Fc-fJAM-A (C) and fJAM-A (D). All samples were eluted at a peak corresponding to the approximate calibrated size expected for a dimer (124kDa for Fc-fJAM-A and 64kDa for fJAM-A: see Table 2).

Sample	Peak elution (ml)	Calibrated MW (kDa)	Number of fJAM-A proteins
Fc-fJAM-A	12.79	138.12	2.22
fJAM-A	14.4	62.8	1.96
Degly Fc-fJAM-A	13.2	113	1.82
Degly fJAM-A	14.35	59.8	1.87

Table 2- Peak elutions in size exclusion chromatography

Volumes at which the protein peaks were visualised during size exclusion chromatography are given for the four samples; Fc-fJAM-A and fJAM-A both glycosylated and deglycosylated by treatment with PNGase F (deglycosylated). The calculated molecular weights corresponding to the calibrated elution volumes are also given along with the number of Fc-fJAM-A or fJAM-A proteins that the molecular weight (MW) corresponds to.

To confirm the oligomerisation state of the fJAM-A ectodomain and evaluate the nature of the dimer, we performed small angle x-ray scattering (SAXS) to calculate a low-resolution solution structure of the protein. The analysis was performed on glycosylated fJAM-A by Prof Olwyn Byron. The shape of the assembly was found to be consistent with that seen in previous X-ray crystallography studies of the mouse and human forms of the protein. The human JAM-A crystal structure (Figure 23C and D) was manually docked into the SAXS envelope as a dimer, confirming the similar arrangement of the human and feline forms of JAM-A (Figure 23). The dimerisation interface of murine JAM-A has been shown to contain two salt bridges formed between Arg58 on one monomer and Glu60 on the other as well as a surrounding hydrophobic stacking interaction (Kostrewa et al., 2001). These interactions were also found in human JAM-A involving Arg59 and Glu61 which can be found in the centre of the cavity/hole which comprises the dimerisation interface between the D1 domains of two JAM-A proteins (see centre of Figure 23D) (Prota et al., 2003).

Both SAXS and size exclusion chromatography confirm that the fJAM-A ectodomain forms dimers in solution as previously reported for related proteins. It is hypothesised that the dimeric form seen in solution represents that seen at the cell surface in tight-junctions. It is further thought that these *cis*-dimers participate in *trans* interactions across tight junctions, contributing to barrier formation (Kostrewa et al., 2001). It is interesting to note however that the interaction that occurs between the monovalent fJAM-A ectodomain fragments leading to the formation of dimers, does not appear to arise in the Fc-fJAM-A form (between fJAM-A ectodomains of separate Fc-fJAM-A dimers). fJAM-A – fJAM-A interactions in the bivalent form might otherwise be expected to lead to the formation of higher-order aggregates.

As we have shown that the fJAM-A ectodomain produced in our expression and purification system is similar to other soluble forms, we can confidently use the protein for structural studies on the fJAM-A binding of FCV as well as in other non-structural *in vitro* assays.

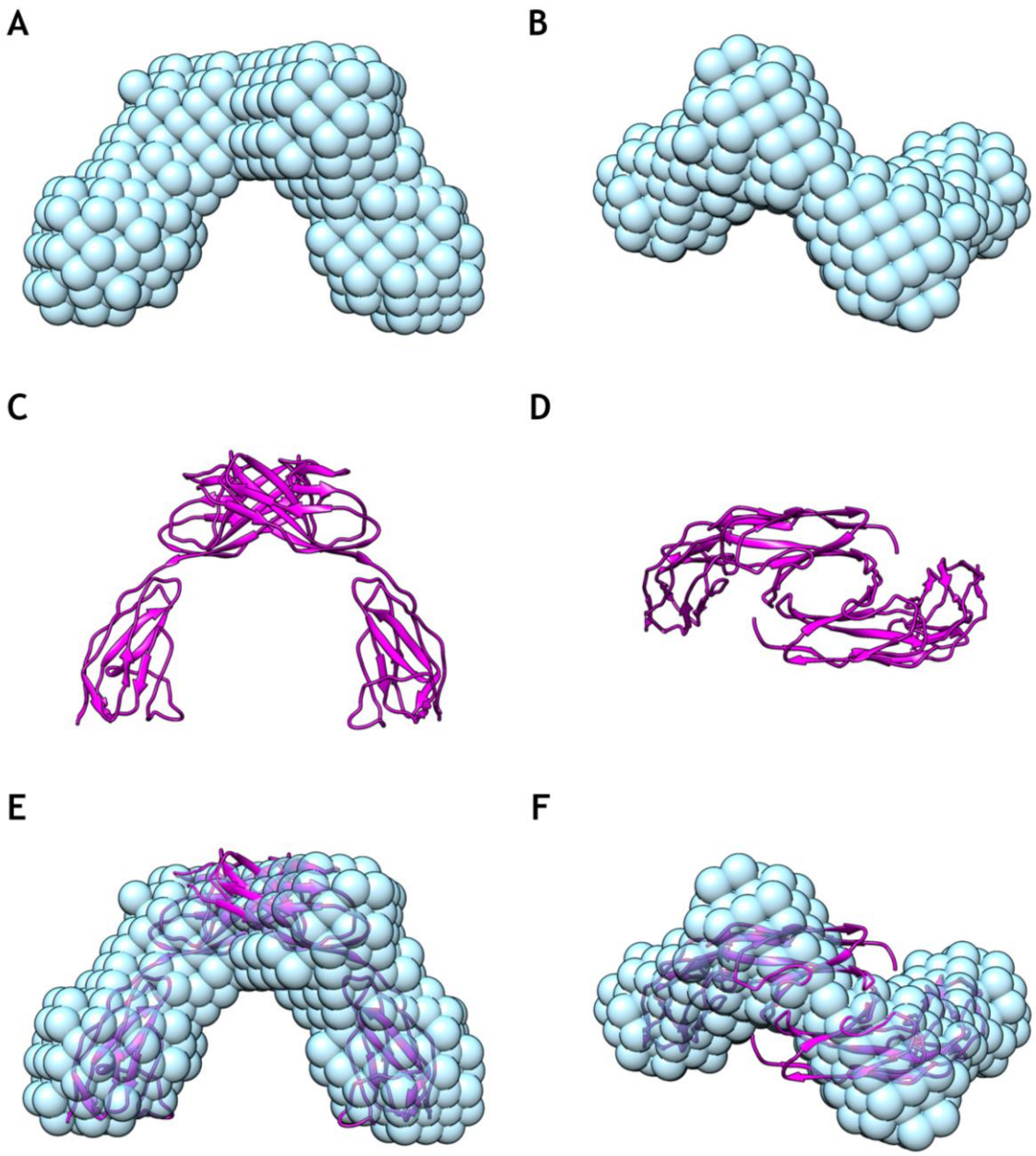

Figure 23- fJAM-A is dimeric in solution by SAXS

Small angle x-ray scattering (SAXS) was performed by Prof Olwyn Byron on soluble fJAM-A ectodomain with the glycosylation present. The fJAM-A structure as elucidated by SAXS is shown in blue spheres (A: side view, B: top view). The human fJAM-A ectodomain (pink; C: side view, D: top view; PDB ID: 1NBQ) was fitted into the SAXS structure of fJAM-A and the side view (E) and top view (F) shown. Panels E and F show that most of the two protein structures overlap, suggesting that they are very similar in structure as well as oligomeric state.

3.4 Thermodynamic properties of the FCV-fJAM-A interaction

Isothermal calorimetry is used to measure the energy required or emitted when two proteins bind/form a complex by holding one protein of interest in a chamber and injecting small volumes of the second protein and observing the heats produced during injections. Control samples of one protein injected into the appropriate buffer are performed and these values subtracted from the final data set produced to determine a dissociation constant which is a measure of how strongly the two proteins bind. For example, a dissociation constant in the single figure nM range is 1000 times stronger than one in the single figure μM range.

To determine the strength and kinetics of the FCV-fJAM-A interaction, isothermal calorimetry was performed with Dr Sharon Kelly at the University of Glasgow. FCV was placed into the chamber of the calorimeter at a concentration of 13μM while 13μM fJAM-A was added into the injector. 20 injections of 2μl were performed at room temperature every 3 minutes and any heats produced from the reaction recorded. The experiments shown in Figure 24 were preliminary due to the small heats observed during the fJAM-A injections (possibly due to sub-optimal protein concentrations) as well as the presence of the Fc tag on the glycosylated fJAM-A which was removed from the deglycosylated form of the protein.

Isothermal calorimetry experiments were performed in the presence and absence of the Fc tag for both glycosylated and deglycosylated proteins although some challenges were encountered which resulted in only two of the samples reliably producing data upon buffer profile extraction. The major challenge encountered during the production of large quantities of samples was the workable scale due to loss of protein during each of the purification steps. Another challenge was the precipitation of the protein upon removal of the Fc tag and/or deglycosylation of the proteins. Removal of the Fc tag and carbohydrate moiety at different stages of the purification process were tested along with different buffers such as Tris-HCl and PBS. After purification and deglycosylation optimisation, two samples were reliably purified; glycosylated Fc-fJAM-A and deglycosylated fJAM-A. It is possible that the deglycosylation of

the Fc region caused precipitation of the protein, allowing only the purification of the untagged form of deglycosylated fJAM-A. The issue affecting the production of glycosylated fJAM-A was likely protein yield or possible contaminating Fc, causing non-linear data points upon subtraction of the buffer negative control data.

Despite these discrepancies, dissociation constants were determined for the interaction of FCV (VP1) with the two forms of fJAM-A. FCV was shown to bind very strongly to glycosylated Fc-fJAM-A, producing a dissociation constant of 12.9nM. The interaction of FCV with deglycosylated fJAM-A was also strong recording a dissociation constant of 128.7nM, 10-fold lower to that observed with the glycosylated form of the protein. It must be noted that the Fc present on the glycosylated fJAM-A likely acted to lower the dissociation constant due to its bivalent form. It is possible that one of the two fJAM-A ectodomains could bind to FCV and then detach, allowing the other fJAM-A ectodomain to bind (i.e., one jumping on while the other detached). Although these two data sets are not directly comparable, both dissociation constants measured are at least 100-fold lower/stronger than that described for the interaction between two D1 domains of human JAM-A and are more comparable to that described for the interaction of the D1 domain with the σ1 reovirus protein (2.4nM) (Guglielmi et al., 2007; Kirchner et al., 2008).

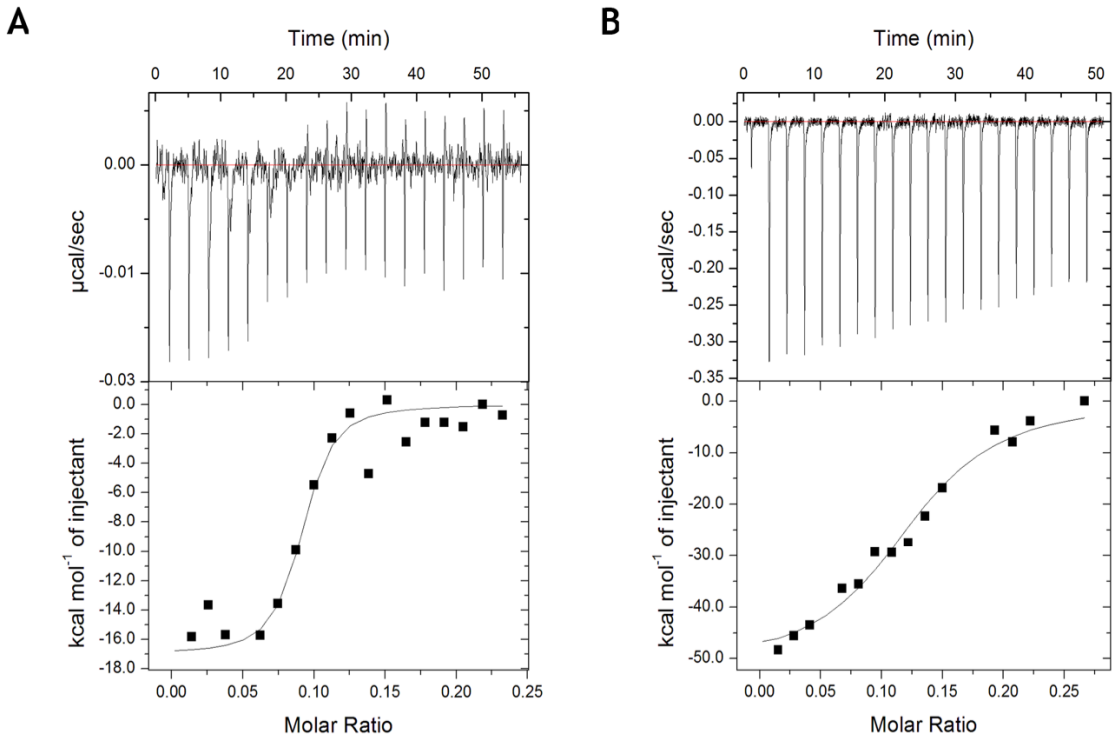

Figure 24- Isothermal calorimetry of FCV and fJAM-A

Isothermal calorimetry was performed by Dr Sharon Kelly in which FCV was added to the chamber of the calorimeter and injections of either glycosylated Fc-fJAM-A or deglycosylated (PNGase F treated) fJAM-A performed at room temperature. The heats produced during fJAM-A injections are shown (top sections) as well as the kinetic rates of the binding (bottom sections). Panel A shows the binding of glycosylated Fc-fJAM-A to FCV resulting in a dissociation constant of 12.9nM, indicating a very strong interaction. Panel B shows the binding of deglycosylated fJAM-A to FCV and, although the reaction did not go to completion/saturate as in panel A, a dissociation constant of 128.7nM was recorded.

3.5 Discussion

Feline junctional adhesion molecule A (fJAM-A) has previously been shown to be a functional receptor for FCV with expression in non-permissive cells rendering them susceptible to FCV infection *in vitro*. fJAM-A has been shown to be present in intracellular tight junctions of epithelial and endothelial cells (as well as on the surface of leucocytes and platelets) (Pesavento et al., 2011). Here, we have described an efficient method for the expression and purification of the fJAM-A ectodomain fused to the Fc region of IgG1 (Fc-fJAM-A) as well as the removal of the Fc tag. We have demonstrated that the fJAM-A ectodomain is dimeric in solution by both size exclusion chromatography as well as small angle x-ray scattering, with the U-shaped structure resembling that of both the human and murine homologues, the latter of which has been shown to form *cis* interactions via an R(VIL)E motif at the dimer interface (Kostrewa et al., 2001). Kirchner *et al*. presented a dissociation constant of 11μM for the D1-D1 human JAM-A dimer interaction, however, the dissociation constant of the reovirus σ1 head domain with the D1 domain of human JAM-A was shown to be 2.4nM (Guglielmi et al., 2007; Kirchner et al., 2008). This dissociation constant showed >1000-fold stronger binding to the reovirus σ1 protein, similar to our preliminary findings of 12.9nM for the interaction of FCV with Fc-fJAM-A. A notable difference, however, is that the reovirus σ1 protein binds to JAM-A via the dimerisation interface whereas FCV binds to the outer surface of the fJAM-A dimer as depicted in Figure 25.

The stronger interaction between JAM-A and viral attachment factors compared to JAM-A homodimer formation in *cis* is of significance with respect to JAM-A dimer disruption upon virus binding. This is further supported by the apparent binding of two monomeric fJAM-A proteins (although added as dimers in solution) to the FCV VP1 capsomeres shown here by cryo-EM and three-dimensional reconstruction. The reovirus σ1 protein has been shown to compete off JAM-A homodimers which may have an effect on triggering endocytosis (Kirchner et al., 2008). This has been shown for the adenovirus knob protein which competes to bind CAR homodimers and induces cellular uptake/viral entry via endocytosis (Salinas et al., 2014).

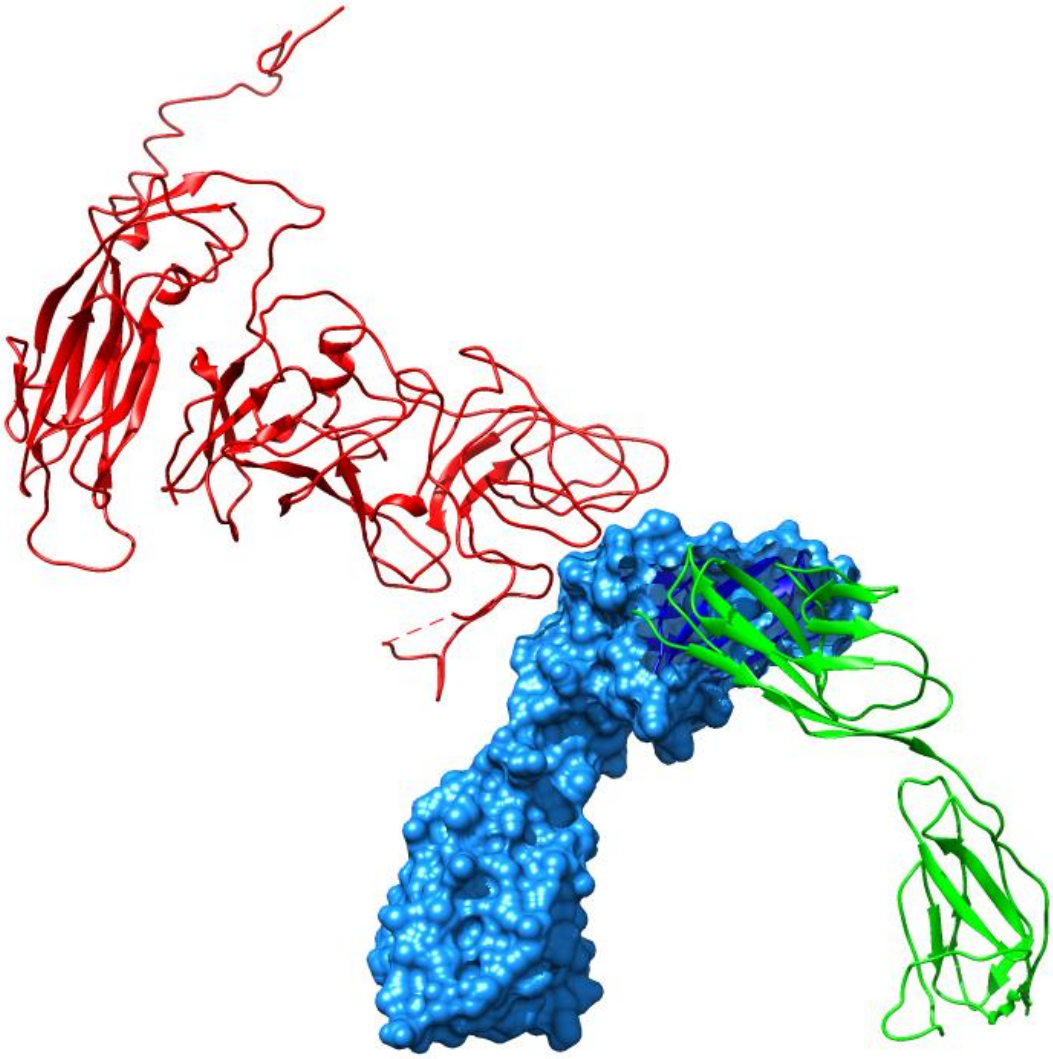

Figure 25- Model of the FCV binding site and D1 dimerisation motif on JAM-A

The dimeric structure of two human JAM-A ectodomains are shown with one monomer represented as blue surfaces and one as a green ribbon diagram, highlighting the location of the dimerisation site between the D1 domains of two JAM-A proteins. The structure of the VP1 capsid protein (chain A) is represented as a red ribbon diagram and highlights the different locations of the FCV binding site and the dimerisation site on JAM-A.

A putative N-linked glycosylation site has been previously identified in fJAM-A at position 184, which we have confirmed (Makino et al., 2006). As sialic acid has been proposed as a cellular receptor for FCV, we proceeded to investigate the possibility that this sialic acid could be present as the glycosylation of fJAM-A (Stuart and Brown, 2007). Here we show via surface plasmon resonance, immunoprecipitation assays and neutralisation assays that removing the glycosylation from fJAM-A *in vitro* does not affect the ability of FCV to bind to fJAM-A. It must be noted, however, that the sialic acid linkage produced in CHO cells (α2,3 linked) differs to that to which FCV has been shown to bind (α2,6 linked) (Lee et al., 1989; Stuart and Brown, 2007).

N-linked glycosylation has been shown to be dispensable for JAM-A transport but is a key regulator of dimerisation, JAM-A stability as well as increased barrier function. Protein homodimerisation has been shown to be regulated by N-linked glycosylation for a number of proteins including E-cadherin, PECAM-1 and N-cadherin. A conserved glycan profile has been suggested for JAM-A including sialic acid as well as fucose on epithelial cells (Scott et al., 2015). Stuart et al presented α2,6 linked sialic acid as a receptor for FCV and found that this sialic acid was not linked to a glycolipid and was present as an N-linked glycosylation of a cellular membrane protein where it may act as an attachment factor for FCV to initially capture the virus and tether it to the membrane (Stuart and Brown, 2007). This may be present on the cell surface and act as an attachment factor to transport FCV to tight junctions where fJAM-A is found or alternatively, the glycoprotein may be found within tight junctions alongside fJAM-A to allow for co-operative and/or sequential binding to occur.

JAM-A has also been identified as the receptor for the newly discovered Hom-1 calicivirus as well as reovirus (Prota et al., 2003; Sosnovtsev et al., 2017). Hom-1 calicivirus has been identified as the first calicivirus to efficiently replicate in human cells in culture following the accidental inoculation of a laboratory employee with purified San Miguel sea lion virus 5 virions (Sosnovtsev et al., 2017). Reovirus has been shown to bind to JAM-A via the viral σ1 protein and some reoviruses use carbohydrate based co-receptors to aid in cell entry, for example, type 3 reoviruses utilise α-linked sialic acid as their co-receptor (Prota et al., 2003). This may be a commonality between reoviruses and FCV in their

binding and entry pathways but more investigation is needed into the sialic acid to which FCV binds. In contrast to FCV, reovirus has been shown to bind to JAM-A at the dimer interface (in the D1 domain) while FCV binds on the outer face of fJAM-A D1 (see Figure 25). Encephalomyocarditis virus (a picornavirus) also binds to sialic acid prior to engagement of its receptor VCAM-1 (vascular cell adhesion molecule 1) and other viruses such as hepatitis C virus (HCV) also utilise carbohydrate receptors such as heparin sulphate as well as many other cellular receptors during virus entry (Bhella, 2015). The use of an additional receptor or attachment factor to deliver the virus from the cell surface to tight junctions where other receptors are located was first proposed for group B coxsackie viruses (CVBs). CVBs bind to DAF (decay-accelerating factor/CD55) on the apical cell surface resulting in remodelling of the actin cytoskeleton which delivers the virus to the tight junctions of cells where it engages the coxsackie and adenovirus receptor (CAR) prior to virus entry by caveolin-mediated endocytosis (Coyne and Bergelson, 2006). FCV may utilise a similar mechanism by binding to an as yet unknown glycoprotein receptor (containing sialic acid) at the cell surface, possibly inducing cellular rearrangements resulting in the delivery of FCV to tight junctions where it binds to fJAM-A prior to entry via clathrin-mediated endocytosis.

4 Structural characterisation of undecorated FCV and fJAM-A decorated FCV by cryo-electron microscopy

The receptor for feline calicivirus (FCV) has been identified as feline junctional adhesion molecule A. Previous work on FCV has shown that upon binding to the soluble ectodomain of fJAM-A, a conformational change is seen in the capsid which may be important during viral entry. A rotation in the P domains of the capsid proteins was identified as well as a tilting of the C/C dimer P-domains away from the 2-fold symmetry axes. We aimed to solve the structure of FCV both undecorated and decorated with the fJAM-A ectodomain to near atomic resolution. Model-based classification has previously allowed the separation of images of fJAM-A decorated FCV into classes reflecting intermediate stages of the conformational change, leading to the calculation of a series of low resolution 3D reconstructions. Here we present near atomic-resolution three-dimensional reconstructions of undecorated and decorated FCV alongside the modelled protein structure of the VP1 major capsid protein. Using cryo-EM and three-dimensional reconstruction, the FCV capsid structure was solved to 3.0Å resolution while the decorated capsid was resolved at 3.55Å although movement in the P domains limited the resolution of the spike and receptor density. We were also able to resolve both the pre and post conformational change states of the decorated structure which allowed us to measure the P domain rotation as 19°. The high resolutions achieved allowed us to perform modelling of the protein structure as well as comparison of the S domains under the two conditions. The undecorated structure was also compared with that of FCV-5, a virulent systemic strain, although only variations in the NTA and the P2 domain were seen.

4.1 Structure of FCV

The structure of FCV strain 5 was determined to 3.6Å resolution by x-ray crystallography revealing similar morphology to the F9 strain (Ossiboff et al., 2010). The structure of the feline calicivirus vaccine strain (F9) has previously been solved to 7Å resolution by cryo-electron microscopy and shows the characteristic calicivirus morphology with cup-shaped depressions on the surface

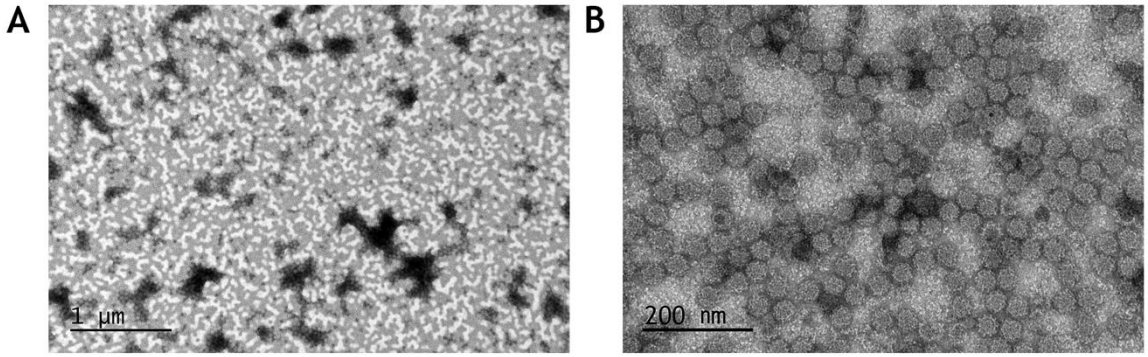

Figure 26- Negative staining electron microscopy of feline calicivirus particles

Virus samples were incubated on formvar-carbon coated, glow discharged grids for two minutes prior to removal of the sample by blotting, washing of the grid with deionised water droplets and staining with droplets of uranyl acetate for five minutes (see 2.2.11.5.1). Grids were imaged in a JEOL 1200 EXII TEM with a Gatan Orius camera. Virus samples were imaged at 40,000 x magnification (A) and 100,000 x magnification (B) to assess the purity and integrity of the virus particles, determining their suitability for downstream applications such as cryo-EM.

of the capsid (formed by the protruding P domains of the VP1 capsid proteins) (Conley et al., 2017).

FCV is the type member of the Vesivirus genus within the *Caliciviridae* and is often used to represent the genus when comparing different viruses, either by sequence or by structure. To characterise the structure of FCV bound to its cellular receptor fJAM-A, we first set out to solve the structure of undecorated strain F9 virions. As well as informing our study of the receptor bound structure, this would allow direct comparison with the X-ray structure of FCV-5.

Feline calicivirus (F9) particles were purified (see 2.2.2.1.2) from CrFK cells. Cells were infected at an MOI of 5 and incubated at 37°C with 5% CO_2 for 16 hours, by which point most of the cells appeared lysed with no remaining adherent cells. The supernatant was collected and centrifuged to remove cellular debris prior to ultracentrifugation. The pellet (containing virus particles) was then resuspended and centrifuged through a caesium chloride gradient for 8 hours. The virus containing band was extracted from the gradient and concentrated by ultracentrifugation. The resultant pellet was resuspended and assessed by negative staining electron microscopy for purity and particle concentration (see Figure 26).

Once a pure and concentrated virus sample had been confirmed by negative staining EM, vitrification for cryo-EM was performed. As described in 2.2.11.6.1, virus particles were added to a glow-discharged C-flat Holey Carbon Film Grid (Protochips) and plunged into liquid ethane cooled by liquid nitrogen. This rapid freezing of the sample prevents the formation of cubic or hexagonal ice and preserves the sample in a close to native state for imaging by cryo-EM.

Feline calicivirus particles were imaged in an FEI Titan Krios equipped with a Falcon III detector at 75,000 x magnification (resulting in a pixel size of 1.065Å). 5198 micrographs of FCV were collected at a range of defocus values (see 2.2.11.6.2). A representative micrograph is shown in Figure 27A and shows the high purity, integrity and concentration of the purified virus particles. The respective power spectrum for the presented micrograph is shown in Figure 27B and demonstrates clearly visible Thon rings. The plots shown in Figure 27C

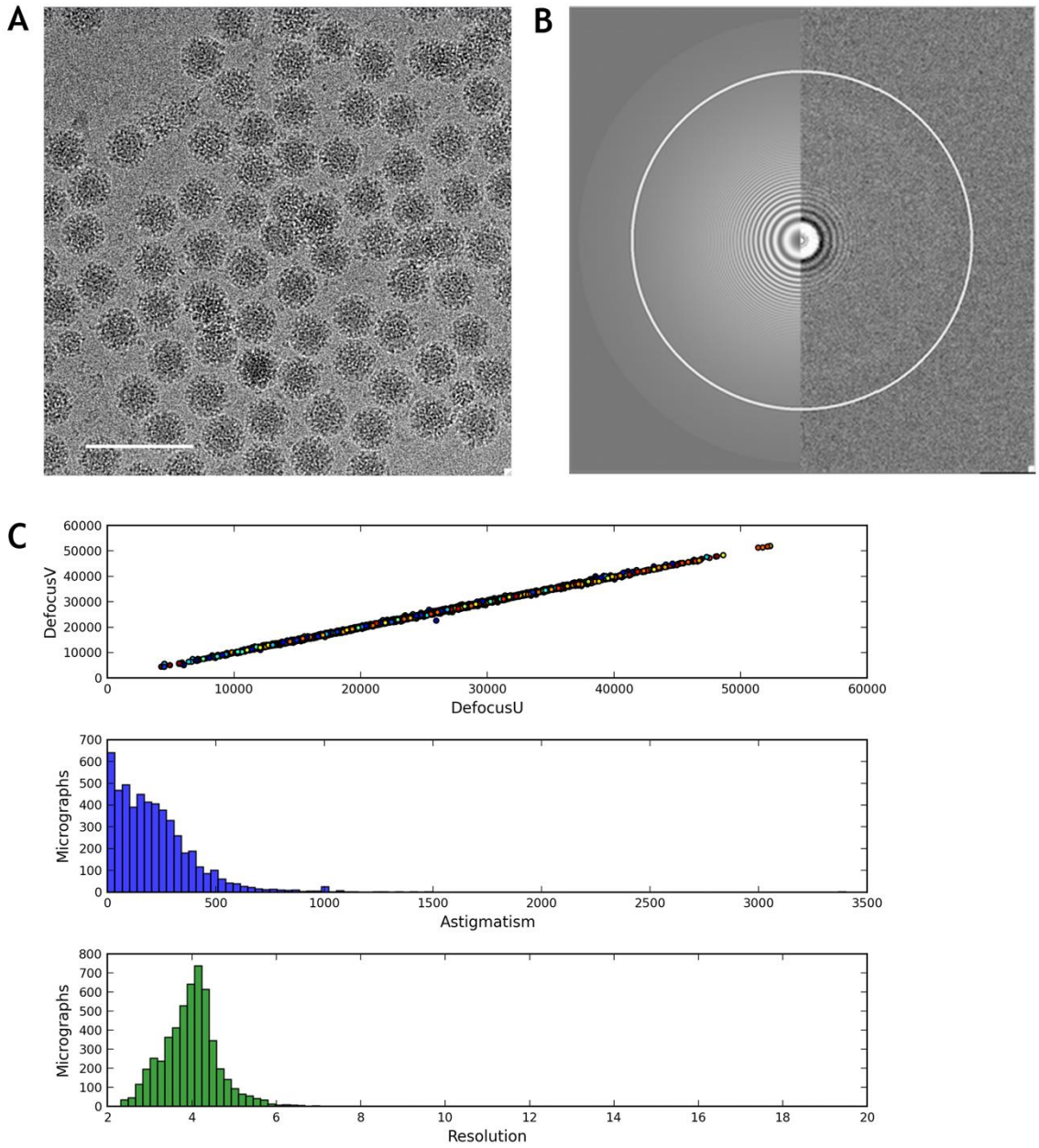

Figure 27- Validation of FCV data set quality

A representative micrograph for the data set is shown (A) with a scale bar measuring 100nm. The power spectrum of the micrograph is shown (B) with the white circle representing the maximum extent of measured Thon rings and hence the likely resolution that can be achieved with data from this micrograph. These values for the whole data set are presented (C: green bars) alongside the measures of astigmatism from the Fourier transforms (C: multi-coloured dots and blue bars). Script written by Astbury Biostructure Laboratory (University of Leeds).

represent the quality of the data set by demonstrating the low levels of astigmatism and the maximum estimated resolution of each micrograph determined by measuring the extent of Thon rings from the power spectra (white circle in Figure 27B). These data show that a near-atomic resolution structure was possible from the acquired data set. Data were analysed using the RELION package. Each micrograph was first motion-corrected using MotionCor 2, followed by defocus estimation using GCTF. To generate a template for automated particle picking a small subset of particles were manually picked and processed to calculate a set of 2D class-averages. The best class averages were used for automated particle picking of the entire dataset.

59,531 particles were extracted from the 5198 micrographs recorded and used as the input for 2D classification where the data was split into 60 self-similar classes. Figure 28 shows the clarity of the class averages calculated in both the 2D (A) and 3D (B) classification steps, with distinct features of the viral capsid visible even at the early stages of data processing. Those 2D classes that showed clear high-resolution features were selected (see Figure 28A: 55,945 particles) as input for 3D classification, which required a reference map of a similar structure. We used a previous intermediate resolution structure of FCV solved on a JEOL JEM-2200FS TEM as the reference map and applied a 60Å filter to eliminate any model bias (Conley et al., 2017). Following 3D classification, the class containing the most data (41,436 particles) was selected and is shown in Figure 28B. The central section through the density map produced by 3D classification appears very detailed, particularly in the S domain of the capsid proteins, illustrating the high resolution that was achieved.

3D refinement was then performed with the same reference map as for 3D classification. The output map from the 3D refinement was visualised using UCSF chimera and the lowest threshold that did not result in the appearance of ‘dust’ used to create a mask of the map (Pettersen et al., 2004). This mask was then used in a post-processing step to provide a final resolution estimate of 3.0Å based on the gold-standard FSC criterion with a cut-off of 0.143 (see Figure 29B). Post-processing also produces an estimate of the most appropriate sharpening factor (B-factor). Local resolution estimation was performed using RELION to filter parts of the map to their estimated resolution (Scheres, 2012).

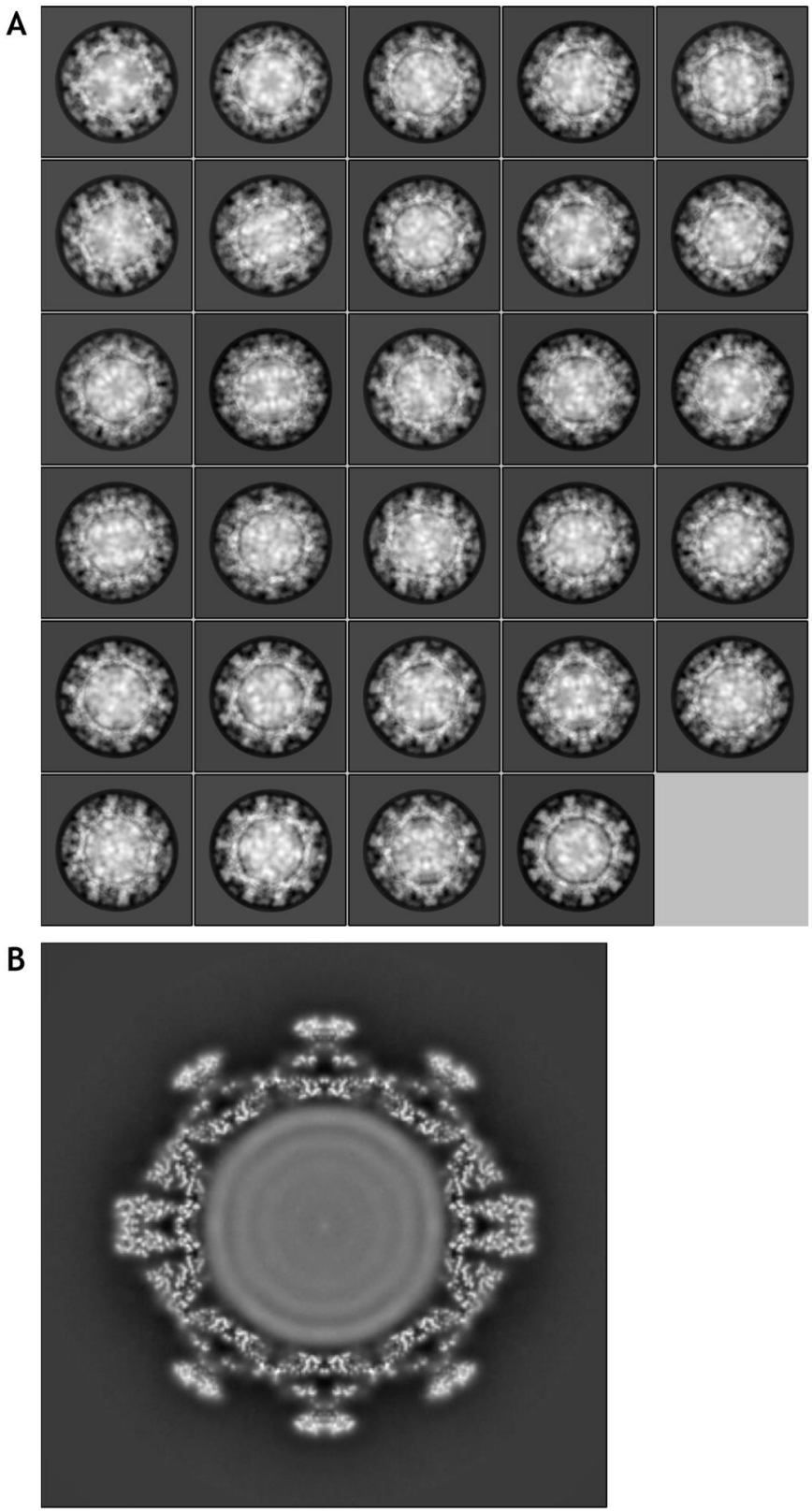

Figure 28- Class averages produced during FCV icosahedral reconstruction

RELION was used to calculate (A) 2D and (B) 3D class averages of feline calicivirus particles. Panel A shows representative 2D class averages, showing that there was a good distribution of views of the FCV virion. Panel B shows a central section through the 3D reconstruction following 25 iterations of classification. Data from this reconstruction were taken forward for further refinement.

This local resolution processing of the structure prevents over-sharpening of the lower resolution elements of the structure avoiding the possible inaccurate representation of poorly resolved regions of the reconstruction.

The 3.0Å structure of FCV (in stereo view (C) and a cross-section (A)) is shown in Figure 29. FCV exhibits *T=3* icosahedral symmetry with the stereo images shown viewed along the 2-fold symmetry axis (Figure 29C). The P2 dimers of the capsid proteins are known to form rhomboid structures at the outer face of the virus particles, shown in Figure 29C, with approximately 2 loop regions on each capsid protein (4 per capsomere) protruding above the rest of the P domain. These protrusions appear to be less well resolved, indicated by an estimated resolution of 3.4Å compared to 3.1Å for most of the P domain. The outer surface of the capsomeres (P2) forms the receptor binding site for fJAM-A and so it is likely that these protruding residues may contribute to receptor and/or attachment factor binding. These surfaces correspond to the hyper-variable regions of the capsid proteins which are responsible for receptor binding and are likely involved in antibody neutralisation by an infected host. At the centre of each of the 5 and 3-fold icosahedral symmetry axes, a slightly raised circular region can also be seen.

The S domain of the FCV capsid appears to resolve to higher resolution (approximately 2.85Å) than the P domains (3.2-3.4Å), shown in red and turquoise/blue, respectively, in Figure 29C. This implies that the shell of the capsid forms a more rigid structure with some degree of flexibility seen in the P domains. This scope for flexibility is supported by previous work which has shown that the P domains of the capsid proteins undergo a rotation when engaged with their receptor, fJAM-A (Bhella et al., 2008; Bhella and Goodfellow, 2011).

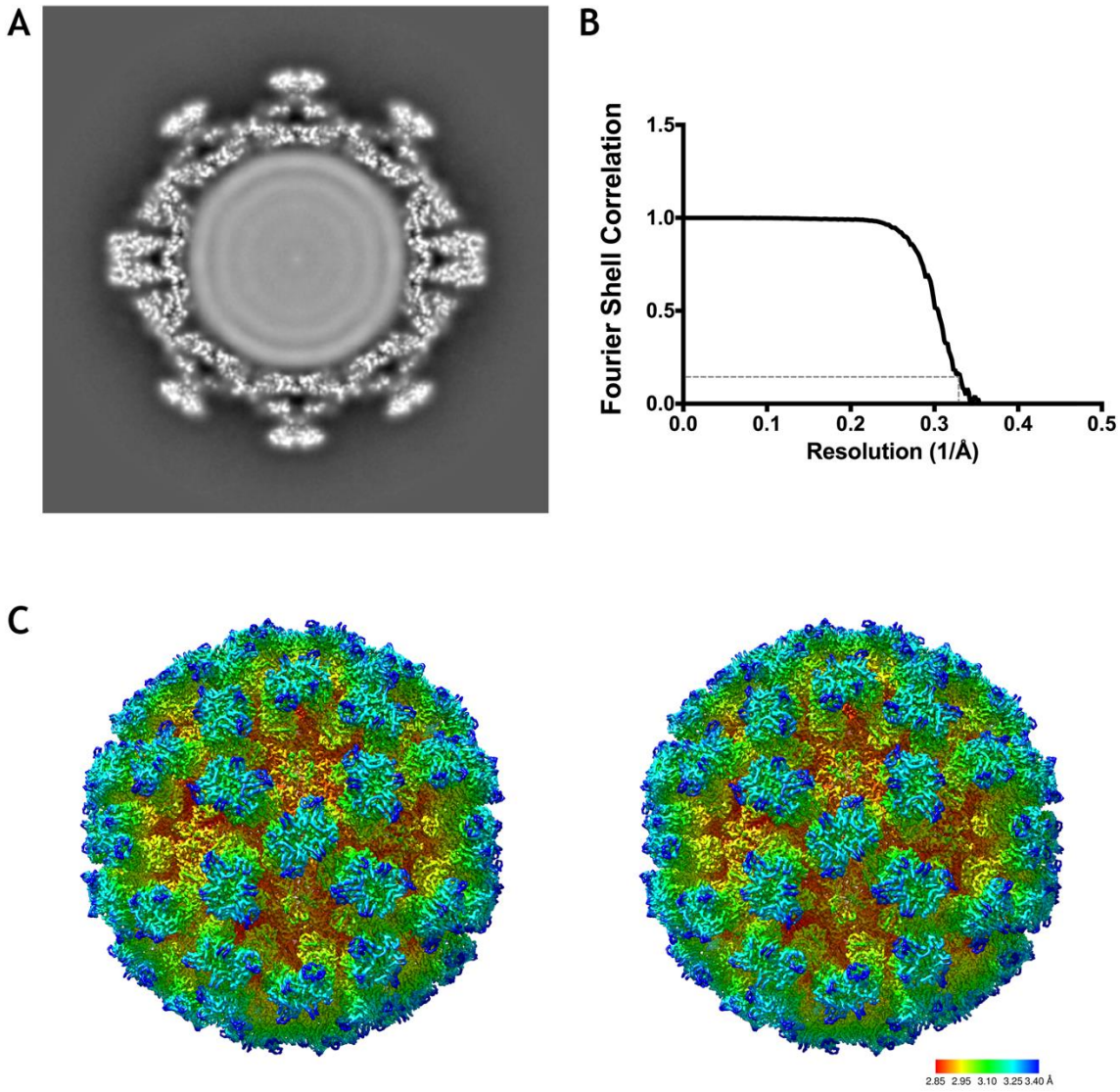

Figure 29- 3.0Å resolution structure of feline calicivirus by cryo-EM

Feline calicivirus particles were imaged using an FEI Titan Krios with a Falcon III detector at 75,000 x magnification with a range of defocus values. A cross section of the three-dimensional reconstruction is shown in panel A with the Fourier shell correlation plot shown in panel B. The 3.0Å structure of FCV is shown in stereo view looking down the 2-fold symmetry axis (C/C dimer) in panel C. The structure is coloured by resolution following local resolution analysis performed in RELION from red (2.85Å) through to blue (3.4Å) showing that the S domain of the VP1 capsid protein was solved to higher resolution than the P (particularly P2) domain of the capsid.

4.2 Modelling of protein structure into the cryo-EM density map of FCV

Solving the structure of a protein or capsid to near atomic resolution allows the fitting/modelling of the amino acid sequence into the resolved density. As the undecorated FCV structure presented here was solved to a resolution of 3.0Å, we aimed to use protein modelling to determine the structure of the major capsid protein VP1.

To determine the protein structure of the FCV F9 major capsid protein, VP1, the known structure of FCV-5 VP1 was used alongside the F9 VP1 amino acid sequence (UniProtKB: P27406) to generate a homology model of the protein structure using SWISS-MODEL (Arnold et al., 2006). This model was then fitted into the density map solved by cryo-EM and refined using Coot and Phenix to yield the protein structure of FCV F9 VP1 (Adams et al., 2010; Emsley and Cowtan, 2004).

The structures of the A, B and C conformations of VP1 are presented in Figure 30A revealing modest differences in the N-terminal arm (NTA) as well as the previously established slight variations causing the bent A/B and flat C/C dimers (B and C). Example slices through the S and P domains of chain B are shown in grey in Figure 30F and G, respectively, with the modelled protein structure represented in pink to illustrate the goodness of fit in the model. The slices illustrate that the protein backbone fits within the density well with aromatic side chains clearly visible. The structure of the asymmetric unit (chains A, B and C) presented contains 0% outliers with a map correlation coefficient around atoms of 0.858, describing the high probable accuracy of the structure modelled into the cryo-EM density.

The NTA's of the three different chains of VP1 show some slight variations in the lengths of the alpha helices and at the N-terminus of the protein where the structure is less well-ordered. The S domains of the VP1 capsid proteins show the previously identified eight-stranded ß-barrel structure which is formed of two, four-stranded ß-sheets (termed BIDG and CHEF).

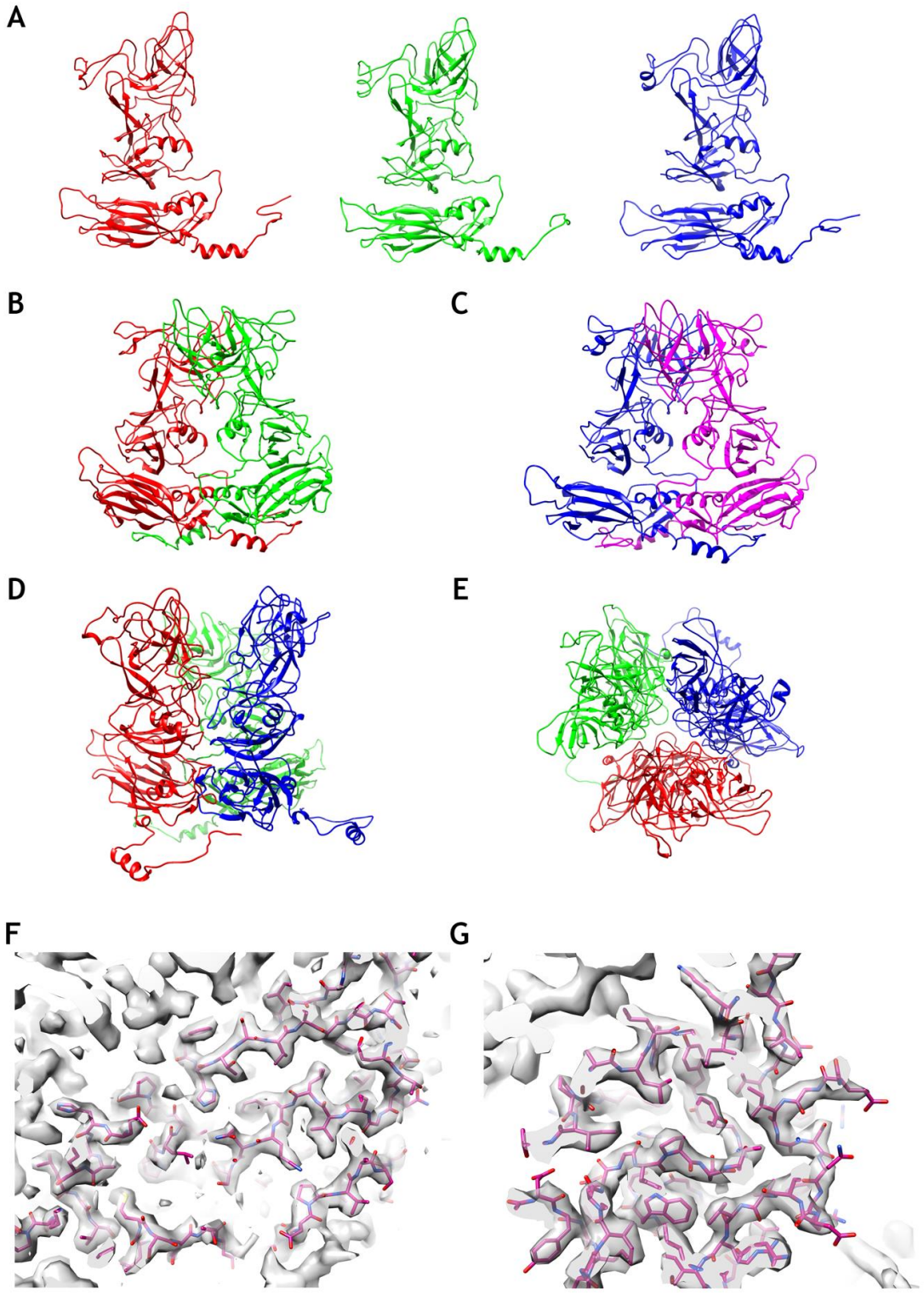

Figure 30- FCV VP1 protein structure determined by amino acid modelling

The FCV VP1 capsid protein structure was determined by modelling into the cryo-EM density map using Coot and Phenix. The structures of VP1 chains A, B and C are shown (A: red, green and blue, respectively) alongside the A/B (B) and C/C (C) capsomeres. A side view (D) and top view (E) of the asymmetric unit are shown, illustrating the interactions between the 3 conformations of VP1. Representative sections through the density map in the S domain (F) and the P domain (G) are shown in grey with the protein structure shown in pink, illustrating the accuracy of the protein structures determined.

The two alpha helices between strands C and D and stands E and F have also been resolved. The P1 domains appear to be formed predominantly of ß-strands with 2 alpha helices visible. The previously described six stranded ß-barrel in the P2 domain is also visible although this region has been described to vary in orientation and strand length.

4.3 Structural comparison of FCV F9 and FCV-5

FCV-5 is known to be a strain of the virus capable of causing virulent systemic disease in cats while F9 is a vaccine strain. Structures of the two FCV strains have previously been resolved although that of the F9 strain was of intermediate resolution. The structure of F9 decorated with the soluble ectodomain of fJAM-A has also been solved (Bhella and Goodfellow, 2011; Conley et al., 2017; Ossiboff et al., 2010).

After determining the structure of FCV F9 VP1 by modelling of the protein structure into our cryo-EM density map, we aimed to perform a structural comparison of the VP1 capsid proteins from each strain. To aid in this comparison, the structures of VP1 chains A, B and C from F9 and FCV-5 were overlaid in UCSF Chimera as shown in Figure 31A. The RMSD values of the two maps were then calculated for each chain and the F9 structure coloured by RMSD value as a visualisation tool for comparing the two structures (see Figure 31B).

Figure 31 shows that the S domains and P1 domains of the VP1 capsid proteins from F9 and FCV-5 are very similar with most of the major structural variations occurring within the P2 domain. Some slight variations are seen within the NTA's of the proteins with chain A of F9 (Figure 31A: red) resolving an alpha helix while the corresponding structure of FCV-5 did not contain any secondary structural elements. The NTA's of chains B and C form alpha helices in both structures although of slightly differing conformations.

The S domains of the two proteins appear very similar with slight variations seen in the outer loop regions of chains A and C (between ß-strands H and I). The flexible hinge region connecting the S domain to the P1 domain appears to be highly conserved between the two strains of FCV.

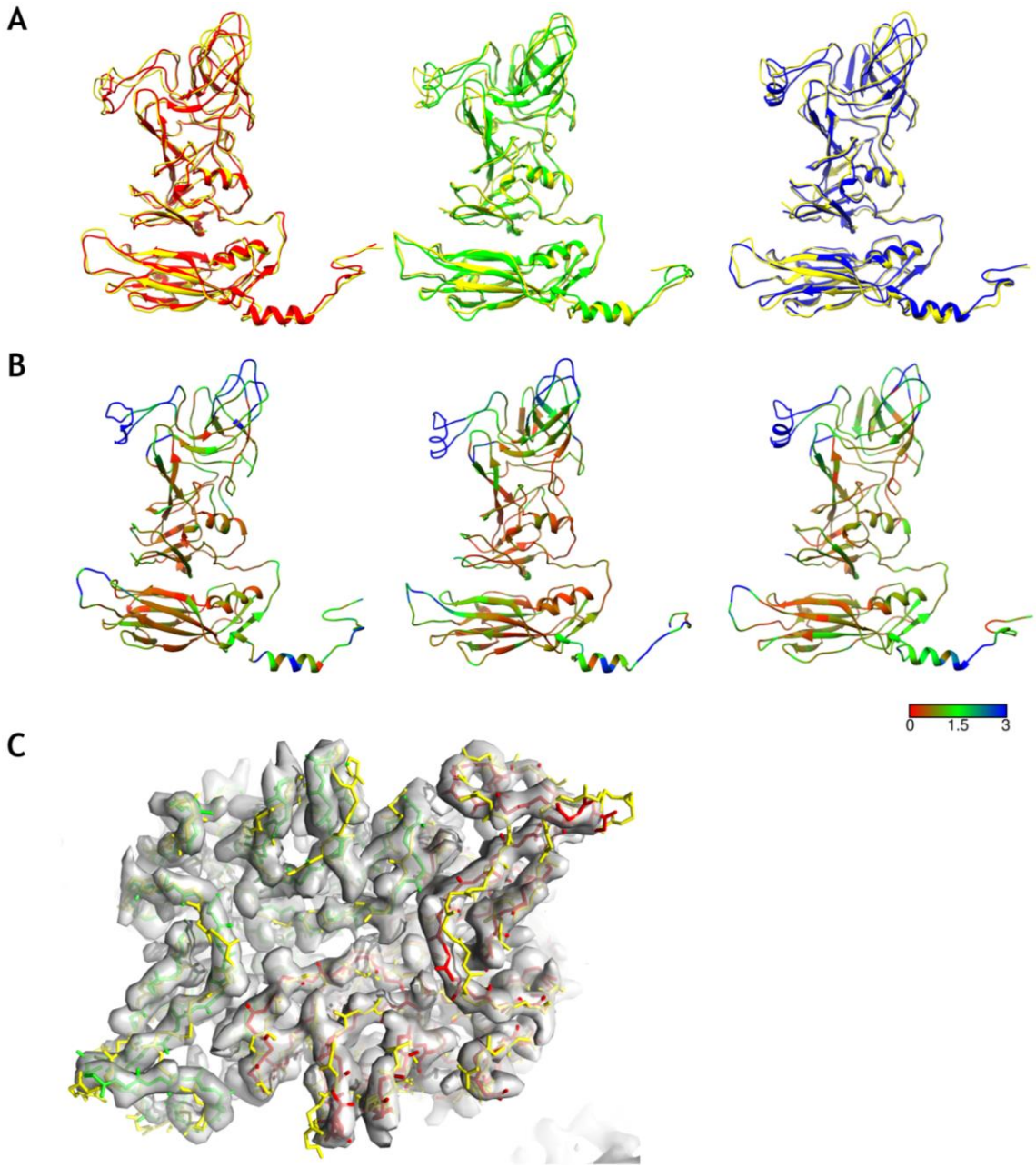

Figure 31- Comparison of FCV F9 against FCV-5

Structures of the FCV F9 VP1 capsid protein were overlaid with the structure of the corresponding chains of FCV strain 5 (PDB ID: 3M8L). VP1 chains A, B and C are shown (A; F9: red, green and blue, respectively. FCV-5: yellow). The RMSD of the two overlaid structures was determined and the F9 VP1 structure coloured by RMSD using UCSF Chimera (B: Chains A, B and C respectively). The colour key represents RMSD values of 0 (red), 1.5 (green) and 3 (blue). Chains A and B of FCV F9 and FCV-5 were fitted into the cryo-EM density to illustrate the most varied regions with the top of the capsomere (P2) shown (red and green: FCV F9 A and B, respectively and FCV-5 shown in yellow).

The P1 domains of the two strains appear to adopt very similar conformations with the secondary structure conserved within all three chains. The P2 domain shows the most variation between the two strains although this is expected as it is the site of receptor binding and antibody neutralisation. The bottom portion of P2 does not appear to differ significantly between F9 and FCV-5, however the loop regions at the top of P2 appear quite different in their conformations, likely due to the presence of a hyper-variable region (see Figure 31C).

The colouring of the F9 strain VP1 structure by RMSD (see Figure 31B) allows the easy visualisation of the most variable regions when comparing it to that of FCV-5. Regions shown in red are highly conserved while green are moderately conserved and blue are less conserved (RMSD values of 0, 1.5 and 3.0 respectively). Colouring of the structure in this way confirms the observations made by eye when overlaying the structures (see Figure 31A) and re-iterates that the most conserved regions of the proteins are the S domain, particularly the ß-barrel motif, and the P1 domain. The most variable regions are confirmed as parts of the NTA as well as the areas within the top of the P2 domain.

This structural comparison shows that the vaccine strain, F9 and a virulent systemic strain, FCV-5, are very similar in structure. Most of the two proteins adopt the same structure and conformations with the main variability seen in the NTA's and in the top of the P2 domains. This variability in the P2 domains is expected due to the presence of a hyper-variable region responsible for receptor binding and antibody neutralisation.

4.4 Structure of FCV decorated with fJAM-A

Feline junctional adhesion molecule A (fJAM-A) has been demonstrated to be an essential cellular receptor for FCV with expression in non-permissive cells rendering them susceptible to FCV infection (Makino et al., 2006). The cryo-electron microscopy structure of FCV decorated with the soluble ectodomain of fJAM-A has previously been determined to 9Å resolution and a conformational change identified in the capsid proteins when bound to fJAM-A. An anticlockwise rotation of 15° in the VP1 P domains of FCV F9 was determined as well as the tilting of the C/C dimer resulting in the breaking of icosahedral symmetry and limiting the resolvable density in these regions of the map. Stages of the conformational change/rotation were separated computationally although remained at intermediate resolution, limiting the interpretation of the data (Bhella and Goodfellow, 2011).

We aimed to determine the structure of FCV decorated with the soluble ectodomain of fJAM-A to near atomic resolution. Moreover, we sought to calculate separate reconstructions for each of the stages of the conformational change and to characterise the conformational changes that take place as a prelude to uncoating at the atomic level.

To elucidate the structure of FCV decorated with fJAM-A, the soluble ectodomain of fJAM-A was purified as described in 2.2.3 and combined with FCV for 1 hour at 4°C. Samples were then plunge frozen and imaged in an FEI Titan Krios equipped with a Falcon III detector (see 2.2.11.6.2) at a magnification of 75,000 x yielding a pixel size of 1.065Å/pixel. Micrographs were collected at a range of defocus values from 1.2 to 3.5µm. A representative micrograph is shown in Figure 32A alongside the corresponding power spectrum (B) showing the maximum resolution achievable from the micrograph (white circle). The virus particles in the micrograph appear to be ‘spiky’ around their perimeter, confirming their decoration with the soluble fJAM-A ectodomain and clear, sharp Thon rings are visible in the power spectrum. The maximum resolution of each micrograph and the levels of astigmatism observed, as calculated by GCTF, are shown in Figure 32C (green and multi-coloured/blue, respectively).

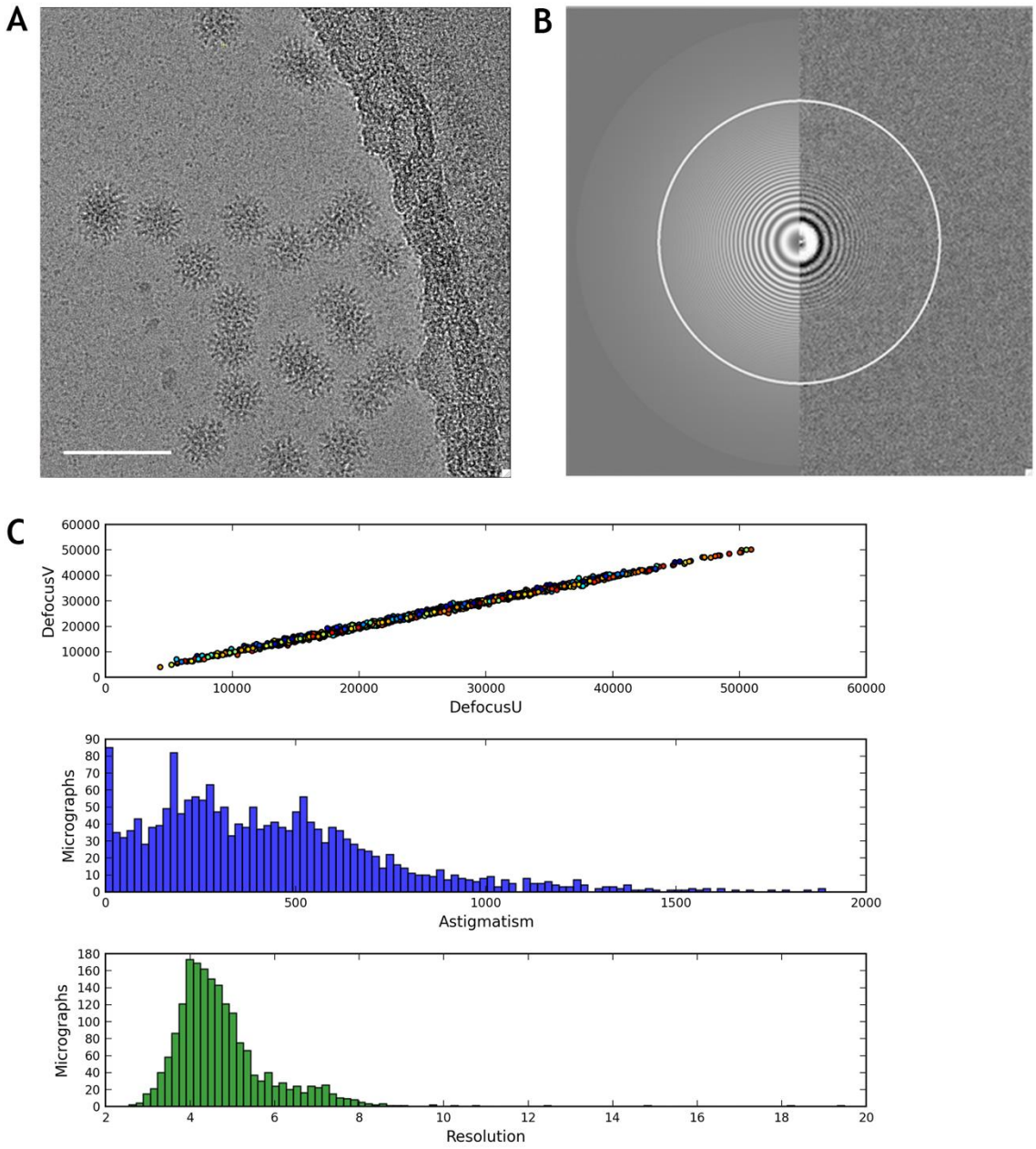

Figure 32- Validation of FCV-fJAM-A data set quality

A representative micrograph for the data set is shown (A) with a scale bar measuring 100nm. The power spectrum of the micrograph is shown (B) with the white circle representing the maximum resolution that can be achieved from this micrograph. These values for the whole data set are presented (C: green bars) alongside the measures of astigmatism from the Fourier transforms (C: multi-coloured dots and blue bars). Script written by Astbury Biostructure Laboratory (University of Leeds).

60,137 particles were extracted from 6673 micrographs as described previously for FCV (see 4.1) using RELION following the motion correction and defocus estimation of the recorded micrographs (Scheres, 2012). Particles were submitted to 2D classification and the sharply resolved classes were selected (40,580 particles: Figure 33A) and 3D classification performed to separate out the data into self-similar classes. Initially, we specified the number of classes as 6, although not all classes contained particles. Additionally, of those classes that did contain data, most were not highly detailed or 'FCV-like' apart from one class which contained 88% of the input data from the 2D classification and was used for further downstream processing (35,843 particles: Figure 33B). It is clear from the 3D classification cross section (Figure 33B) that extra density is present on the outer surface of all of the visible capsid proteins (bound to the P2 domains). The bound fJAM-A appears as a V-shaped density in the outer portions of the cross section where two fJAM-A proteins have bound to each VP1 dimeric capsomere. The S domain density appears to be much more detailed and sharply resolved than that of the P domains or fJAM-A, suggesting a degree of rigidity in the viral capsid shell and the movement/flexibility induced in the P domains upon receptor binding.

Following 3D refinement against a previously determined intermediate resolution structure of FCV decorated with fJAM-A, a mask was created and post-processing used to yield a final resolution of 3.55Å for the fJAM-A decorated FCV structure (see Figure 34) (Bhella and Goodfellow, 2011). The cross section through the 3D reconstruction (shown in Figure 34A) shows the additional density above each of the P domains of the capsid proteins as also illustrated in Figure 33B. Density attributed to the P-domain and fJAM-A is blurred compared to the S-domain density, strongly suggesting that this feature is incoherently averaged, possibly due to movement or a mixed population of conformations. Figure 34B shows the reconstruction calculated following 3D refinement prior to sharpening, allowing better visualisation of the blurred features. Sharpening emphasises the high resolution features of the S-domain (Figure 34C), however the P-domain and fJAM-A density are now less well represented. Local resolution estimation was performed in RELION and a low-pass filter applied to the lower resolution regions of the density map (Scheres, 2012). Figure 34C shows the stereo-paired view of the 3.55Å resolution structure of FCV decorated with fJAM-A (coloured by

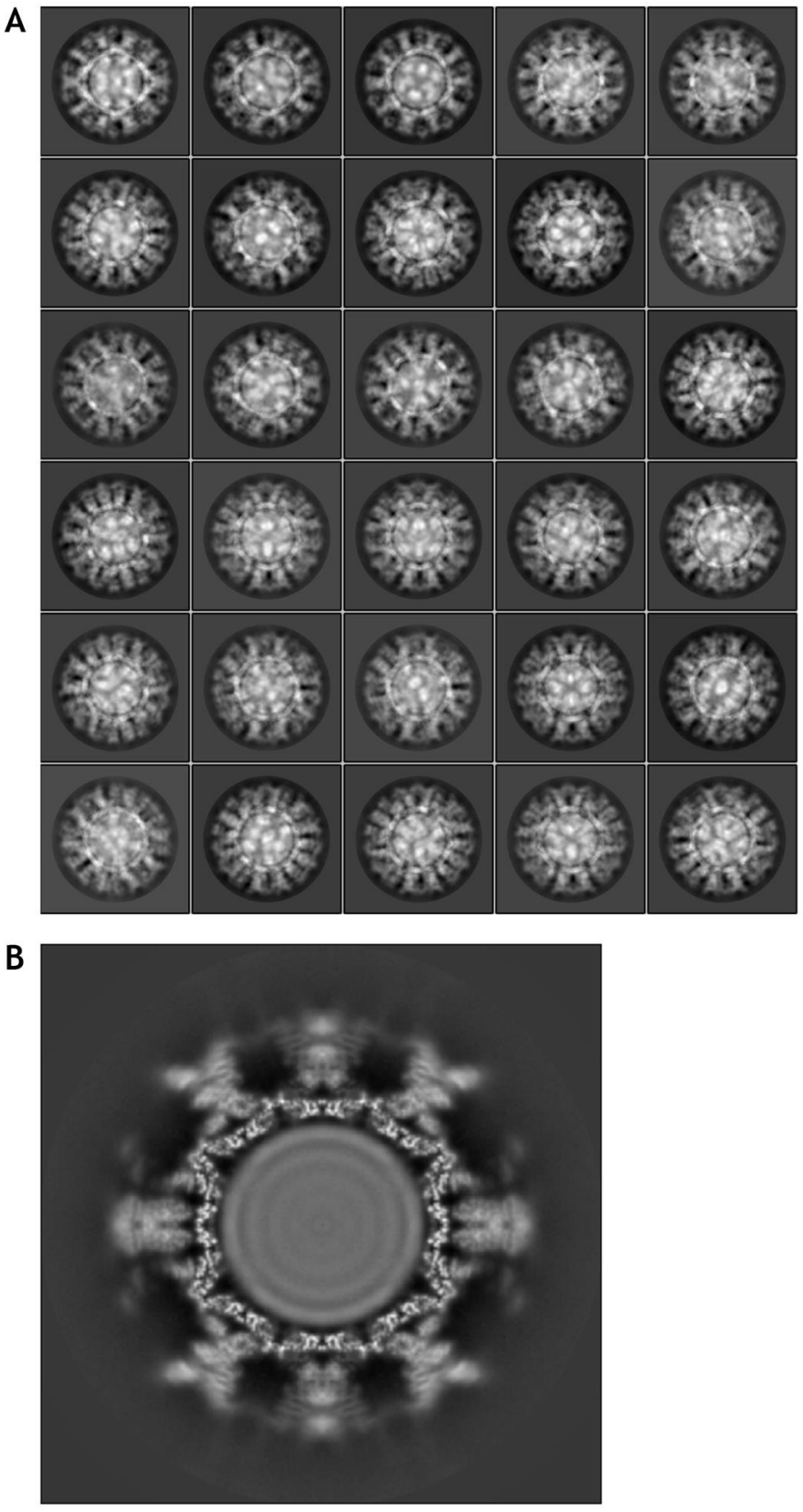

Figure 33- Class averages of fJAM-A decorated FCV particles

RELION was used to classify fJAM-A decorated feline calicivirus particles in two dimensions (A) and, following selection of certain classes, three dimensions (B). Panel A shows the different views of the decorated FCV particles imaged while panel B shows a cross section of the final three dimensional class of data used for further processing of fJAM-A decorated FCV.

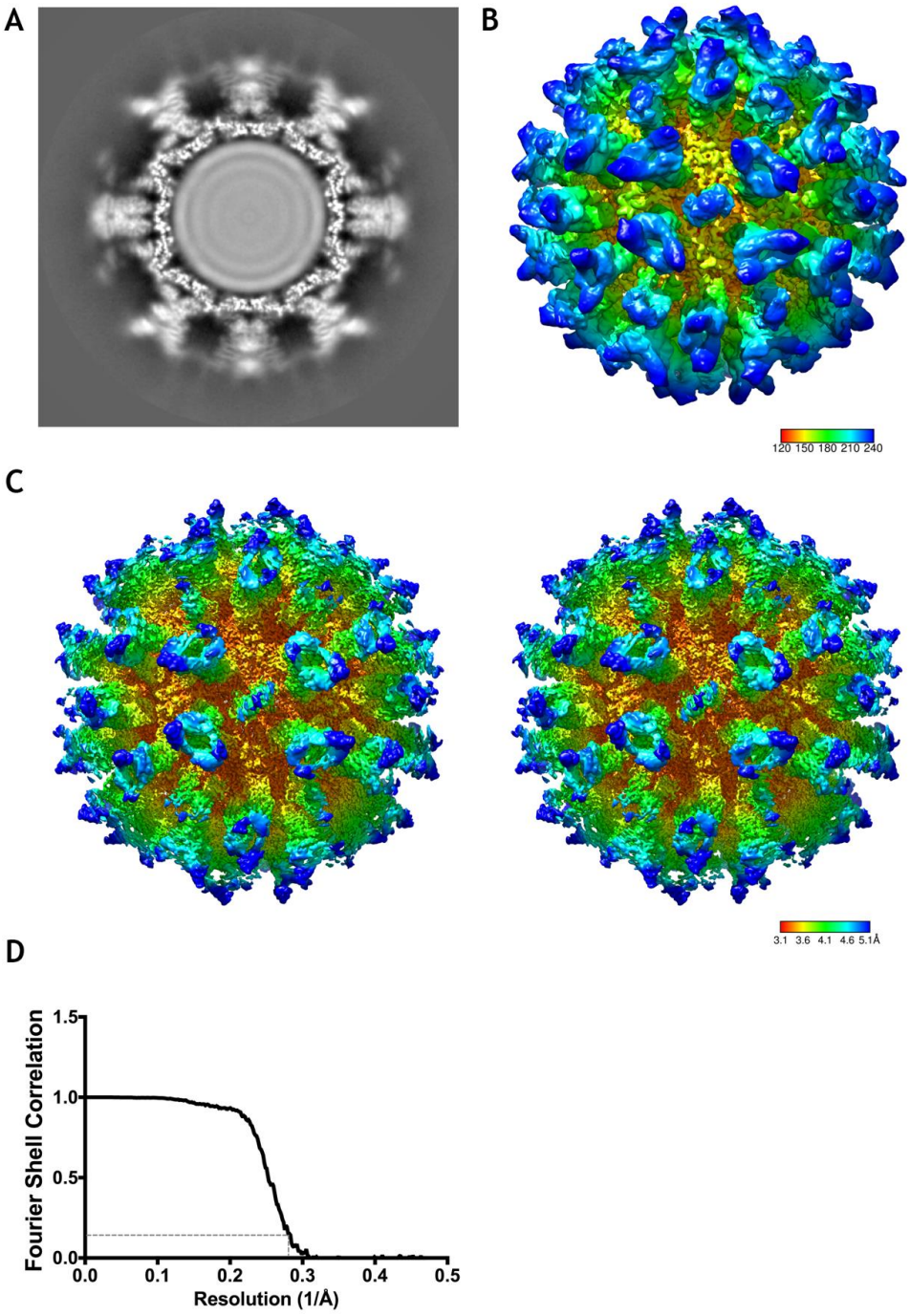

Figure 34- 3.55Å structure of fJAM-A decorated FCV solved by cryo-EM

Decorated FCV particles were imaged using an FEI Titan Krios equipped with a Falcon III detector at 75,000 x magnification and at a range of defocus values. A cross section of the three-dimensional reconstruction is shown in panel A. Panel B shows the 3D refined structure of fJAM-A decorated FCV to allow the visualisation of the lower resolution features (e.g. fJAM-A: coloured by radius). The 3.55Å structure of FCV decorated with the soluble fJAM-A ectodomain (B factor sharpened) is shown in stereo view looking down the 2-fold symmetry axis (C/C dimer) in panel C. The structure is coloured by resolution following local resolution analysis performed in RELION from red (3.1Å) through to blue (5.1Å) showing that the viral capsid was solved to higher resolution than fJAM-A, possibly due to the previously described conformational change. The FSC plot of the structure is shown in panel D.

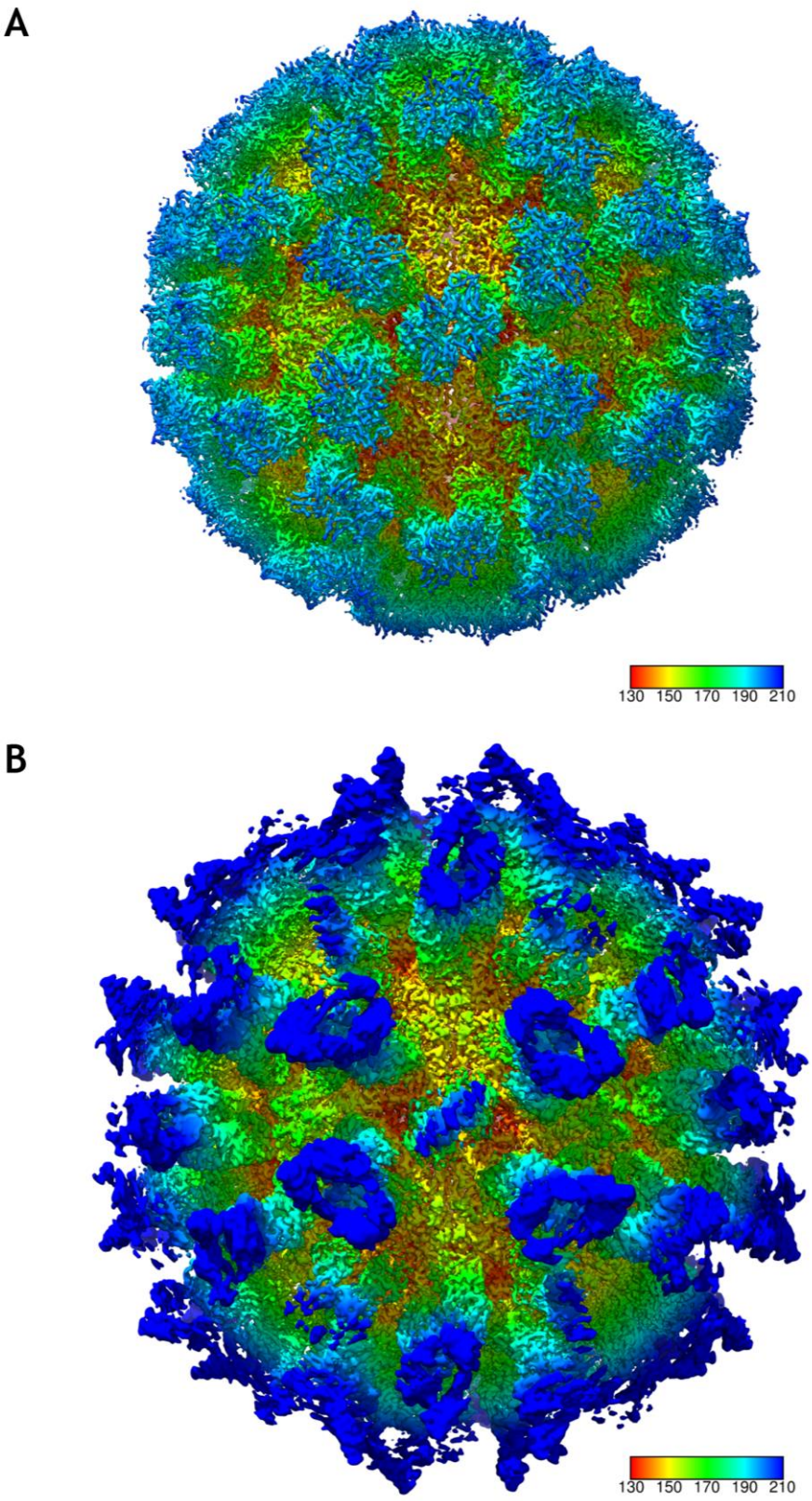

Figure 35- Side by side comparison of undecorated and decorated FCV structures.

A side by side comparison of the 3.0Å undecorated FCV structure (A) and the 3.55Å fJAM-A decorated FCV structure (B) coloured by radial density.

resolution). It is immediately clear that the resolution of the decorated structure is lower than that of the undecorated virus structure shown in the side by side comparison presented in Figure 35Figure 29. This is due to the presence of a conformational change that has been previously reported to occur in the capsid upon fJAM-A binding (Bhella et al., 2008; Bhella and Goodfellow, 2011). The fJAM-A structure appears to be of much lower resolution (5.1Å) than that of the S domain of the capsid (3.1Å) although the P domain was resolved to a resolution intermediate between the two (4.1Å), suggesting an increase in flexibility/movement as you move further out from the S domain. Less density was resolved above the C/C dimers than the A/B dimers suggesting an additional movement in these capsomeres that does not occur in the A/B capsomeres. Bhella et al proposed a tilting of the C/C capsomere resulting in the breaking of icosahedral symmetry in this region, accounting for the loss in resolvable density (Bhella and Goodfellow, 2011).

Overlaying of the undecorated FCV structure with the fJAM-A decorated FCV structure allows the visualisation of not only the fJAM-A density but also the conformational change induced upon fJAM-A binding (see Figure 36). The stereo-paired view of the overlaid structures in Figure 36A shows the predominant fJAM-A decorated FCV density (purple) although clear patches of undecorated FCV (yellow) are visible, showing the regions affected by the conformational change on a scale of the whole viral capsid. Figure 36B and C shows two different views of an A/B capsomere with the V-shaped fJAM-A density clear when looking from one end of the dimer (C) rather than looking side on at the dimer (B). The side view shown in panel B, however, more effectively illustrates the movement of the P domains as a lot of the density appears only in the undecorated structure (yellow) when visualised in this way. Likewise, the side view of the C/C capsomere (D) demonstrates the movement or lack of resolved density upon fJAM-A binding with mostly undecorated FCV P domain structure visible and little visible fJAM-A density bound to the outer face of the P2 domain.

A solid sphere was applied (with a diameter of 18nm, using UCSF Chimera) to the centre of the structure to obscure the details in the S domain and allow easier visualisation of details in the P domains and fJAM-A as seen in Figure 36E. When viewing the top of the A/B capsomere it is less easy to distinguish the

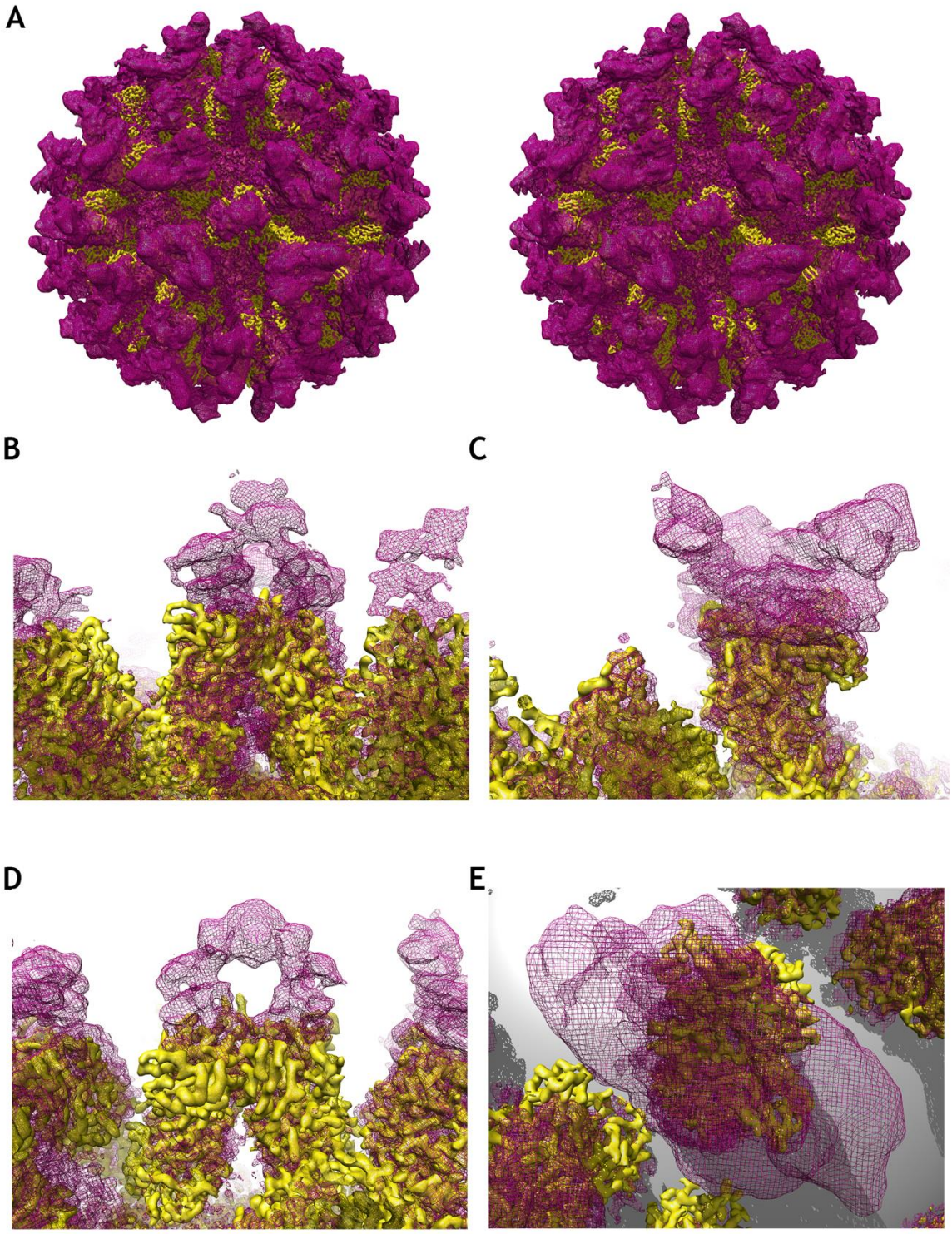

Figure 36- Comparison of undecorated and fJAM-A decorated FCV structures

Both undecorated (yellow) and fJAM-A decorated (purple) structures were visualised in UCSF Chimera and overlaid to illustrate the effect of fJAM-A binding on capsid structure. The Stereo view of the two overlaid structures is presented in panel A with the side view (B) and end view (C) of an A/B dimer shown as well as the side view of a C/C dimer (D). Panel E shows the top view of an A/B dimer with an icosahedral surface of 18nm applied to allow clear visualisation of the conformational change induced upon fJAM-A binding.

fJAM-A binding orientation on the P2 domain, although it is clear upon inspection of different views of the capsomeres that a conformational change occurs in the P domains of the capsid proteins upon fJAM-A binding.

Upon fitting of the modelled FCV P domain A/B dimer into the undecorated and decorated virus structures, it was possible to determine the degree of rotation that occurs in the P domains upon fJAM-A binding. Overlaying of the two structures reveals an anti-clockwise rotation of the P domains of the VP1 capsid proteins. This anti-clockwise rotation from the undecorated FCV structure to the fJAM-A decorated FCV structure was determined to be of 19° using UCSF Chimera (Pettersen et al., 2004). This rotation is clearly visible when spherical sections of the two structures are compared as in Figure 37. Changes are seen in both the P1 and P2 domains which appear to rotate anti-clockwise upon fJAM-A engagement (Figure 37A to D).

Bhella et al have previously resolved the structure of fJAM-A decorated FCV at several stages during the conformational change. As we did not achieve this with unsupervised 3D classification of the data, 3D classification was attempted again on the selected 3D class containing 88% of the data (35,843 particles), to try to separate these data into the 5 or 6 classes shown previously (Bhella and Goodfellow, 2011). Repeated iterations of unsupervised classification did not yield classes of differing conformations however. To separate labelled virion images, the previously resolved structures were used in a multi-reference 3D classification. This produced only two classes of differing conformations which were further processed in RELION (Scheres, 2012). To ensure that the differing conformations were not due to model bias introduced in the 3D classification, an undecorated FCV structure was used as the reference map for a final round of 3D refinement of the two classes. Using this method, the pre- and post-conformational change structures of fJAM-A decorated FCV were determined. While the post-conformational change structure was resolved to 3.65Å (25,984 particles), the pre-conformational change data set was very small, consisting of only 258 particles, resulting in a lower resolution of 6Å. This shows that under these experimental conditions, only a small subset of virus particles did not undergo the conformational change upon fJAM-A binding.

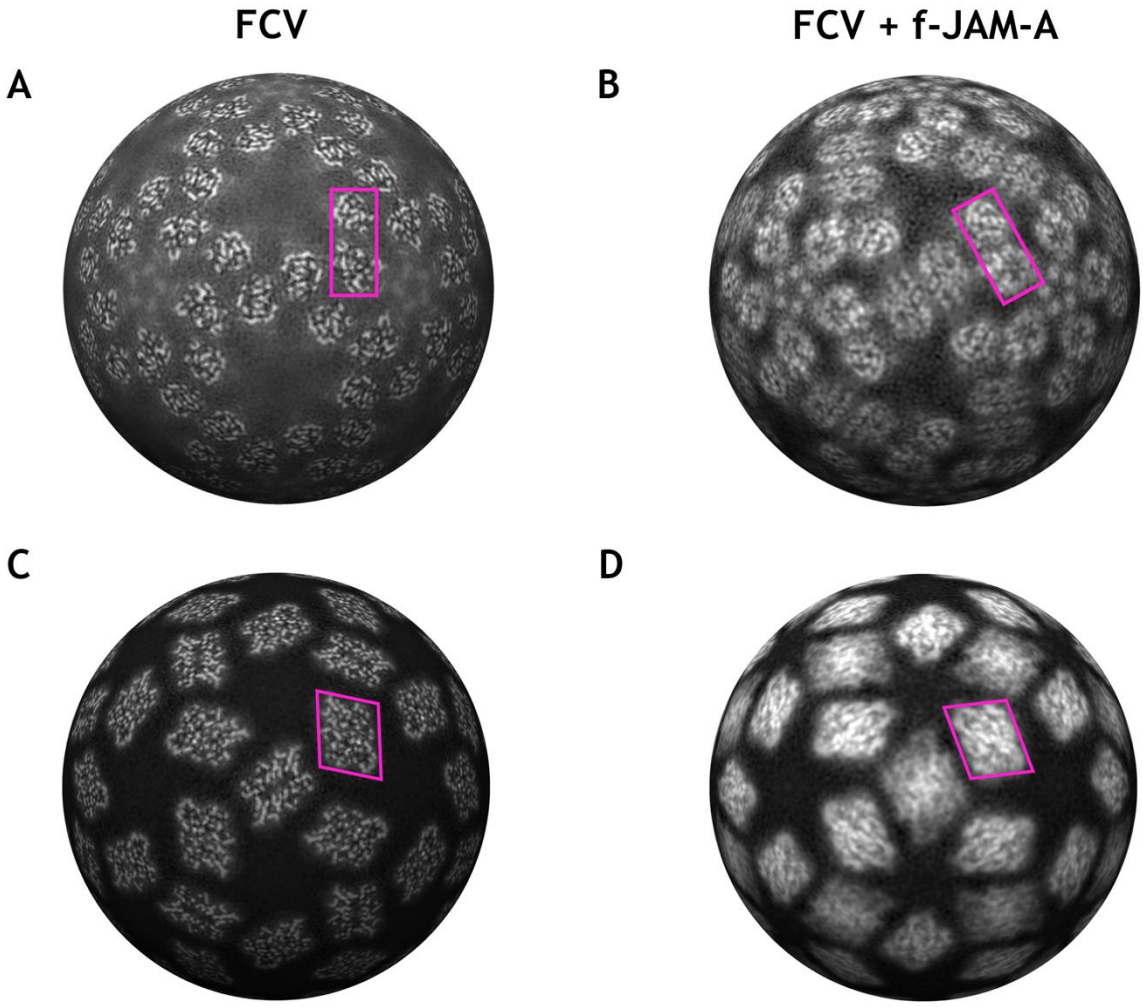

Figure 37- Spherical sections to compare undecorated FCV against fJAM-A decorated FCV

Spherical sectioning was performed in UCSF chimera with varying radii to allow the visualisation of the P1 domains (A and B) and P2 domains (C and D) for the undecorated and fJAM-A decorated structures respectively. Pink boxes highlight changes between the two structures with the 19° rotation visible in both the P1 and P2 domains of the capsid proteins (A to D).

Figure 38A shows the pre-conformational change structure coloured by resolution, indicating the lower resolution of the P domains and fJAM-A even in the pre-conformational change state. The pre-conformational change structure (gold) was overlaid with the post-conformational change structure (pink) and shown in stereo view (B) as well as the top views of an A/B capsomere (C) and a C/C capsomere (D). The anti-clockwise rotation of 19° from the pre to post-conformational change structure is clearly visible in panel C when observing the top of an A/B dimer. The lack of resolved density at the C/C dimer for the post-conformational change structure is obvious in panel D. This structural overlay allows us to hypothesise that fJAM-A binds to the P2 domains of the C/C capsomeres in the same orientation as the A/B dimers prior to induction of movement in the C/C dimers, breaking the icosahedral symmetry, and resulting in weaker density due to this movement/flexibility.

Overlaying of the pre-conformational change structure onto the undecorated FCV structure (Figure 38, panels E and F: purple and yellow, respectively) allows the visualisation of how fJAM-A binds to the P2 domains of both the A/B (E) and C/C (F) capsomeres. Despite fJAM-A being predicted to form *cis* (and *trans*) dimers at the tight junctions between cells, fJAM-A appears to bind to FCV VP1 in a monomeric form. Figure 38, panels E and F, show that 2 fJAM-A proteins bind to each VP1 dimer/capsomere in a head to tail arrangement i.e. with D1 of one fJAM-A monomer laying adjacent to D2 of another fJAM-A monomer and vice versa. It is interesting that in all previous experiments described here, fJAM-A was present in a dimeric form, however, in electron microscopy experiments, it appears to bind to FCV in a monomeric form (2 fJAM-A proteins bind to 2 VP1 capsid proteins).

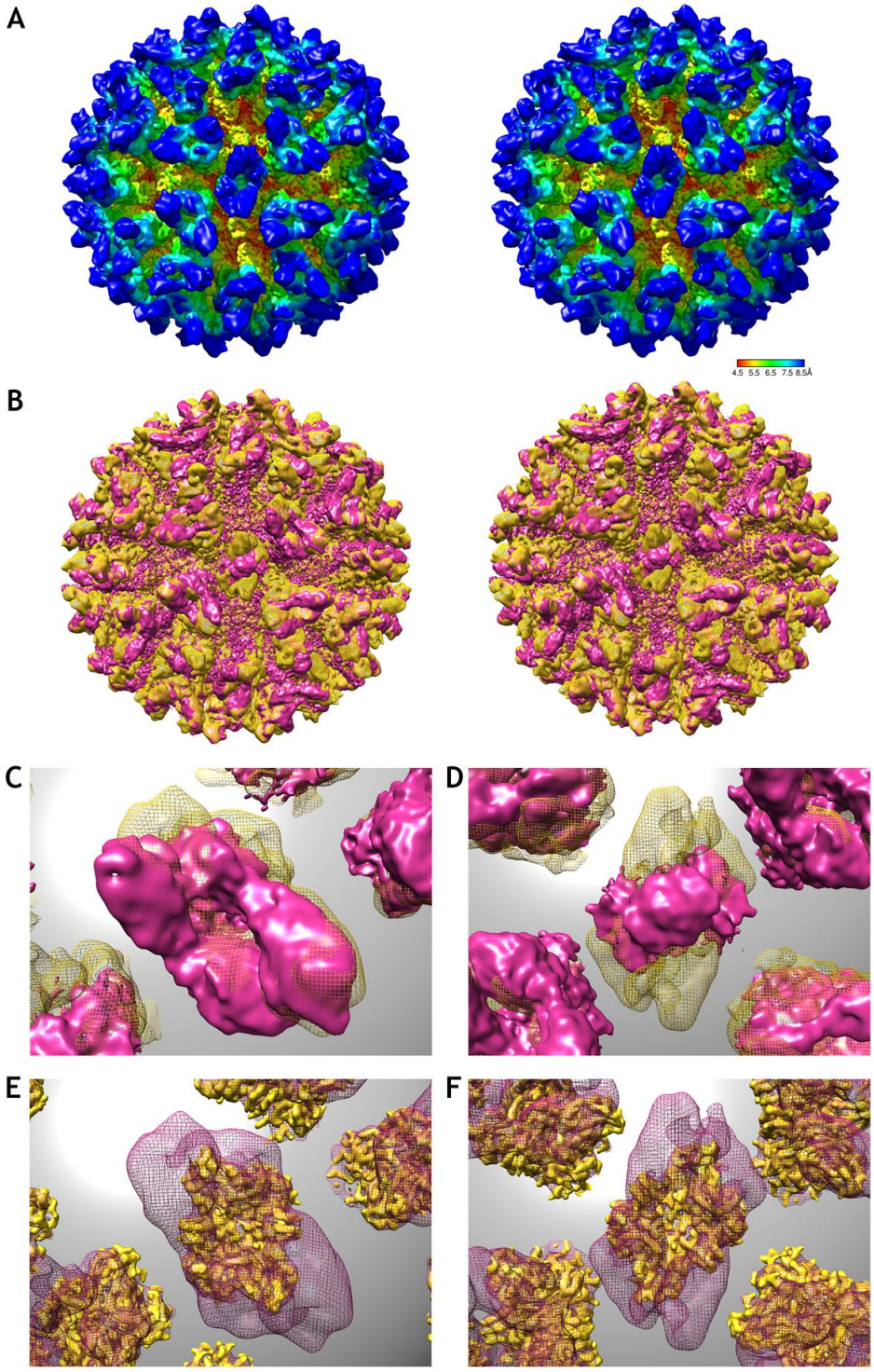

Figure 38- A comparison of the pre and post-conformational change structures of fJAM-A decorated FCV

The pre-conformational change structure is shown in stereo (A: coloured by resolution, B: gold) as well as overlaid with the post-conformational change structure of fJAM-A decorated FCV (pink), also presented in stereo view (B). The top view of an A/B dimer (C) and C/C dimer (D) in the overlaid structures are also shown. The A/B (E) and C/C dimers (F) of the undecorated FCV structure (yellow) overlaid with the pre-conformational change structure (purple in E and F) effectively illustrates the orientation in which fJAM-A binds to the P2 domains of the FCV VP1 capsomeres (panels C-F are shown with an icosahedron surface of 18nm).

The VP1 protein structure modelled here (see 4.5) was docked into both the pre and post-conformational change structures alongside an fJAM-A homology model previously produced using the structure of human JAM-A (Bhella 2011). Chain A of VP1 is shown bound to fJAM-A in Figure 39 for both the pre (A) and post-conformational change states (B). UCSF Chimera was used to find contacts between the two proteins in both stages of the conformational change. Contact residues identified in VP1 are shown in Figure 39 (C: pre and D: post-conformational change structures). Although chain C of VP1 was not resolved in the post-conformational change structure (shown in white), many of the contact residues remain consistent between the structures. Fewer contacts were determined in the post-conformational change state although this may reflect the lower resolution in these regions of the map.

As most contact residues appear to be the same between the two stages of the conformational change, it is likely that the fJAM-A does not move once bound to VP1 and that the P domain and fJAM-A rotate together on the virus capsid. The contact residues on the fJAM-A proteins were also identified and are shown in Figure 39 (E: pre and F: post-conformational change). Again, the contact residues between the two structures/stages of the conformational change appear to be very similar and support the rigidity of the P-fJAM-A complex upon the virus-receptor interaction.

The contact residues identified are shown in Figure 40 for the 3 VP1 chains (A) as well as fJAM-A (B) in both the pre and post-conformational change structures. Some variation is apparent although certain residues are clearly important for the virus receptor interaction such as 434D and 495N in VP1 and 33S in fJAM-A. Some differences are evident in the fJAM-A contact residues although the region spanning 43K to 48S appears to be important with very few differences between the pre and post-conformational change states.

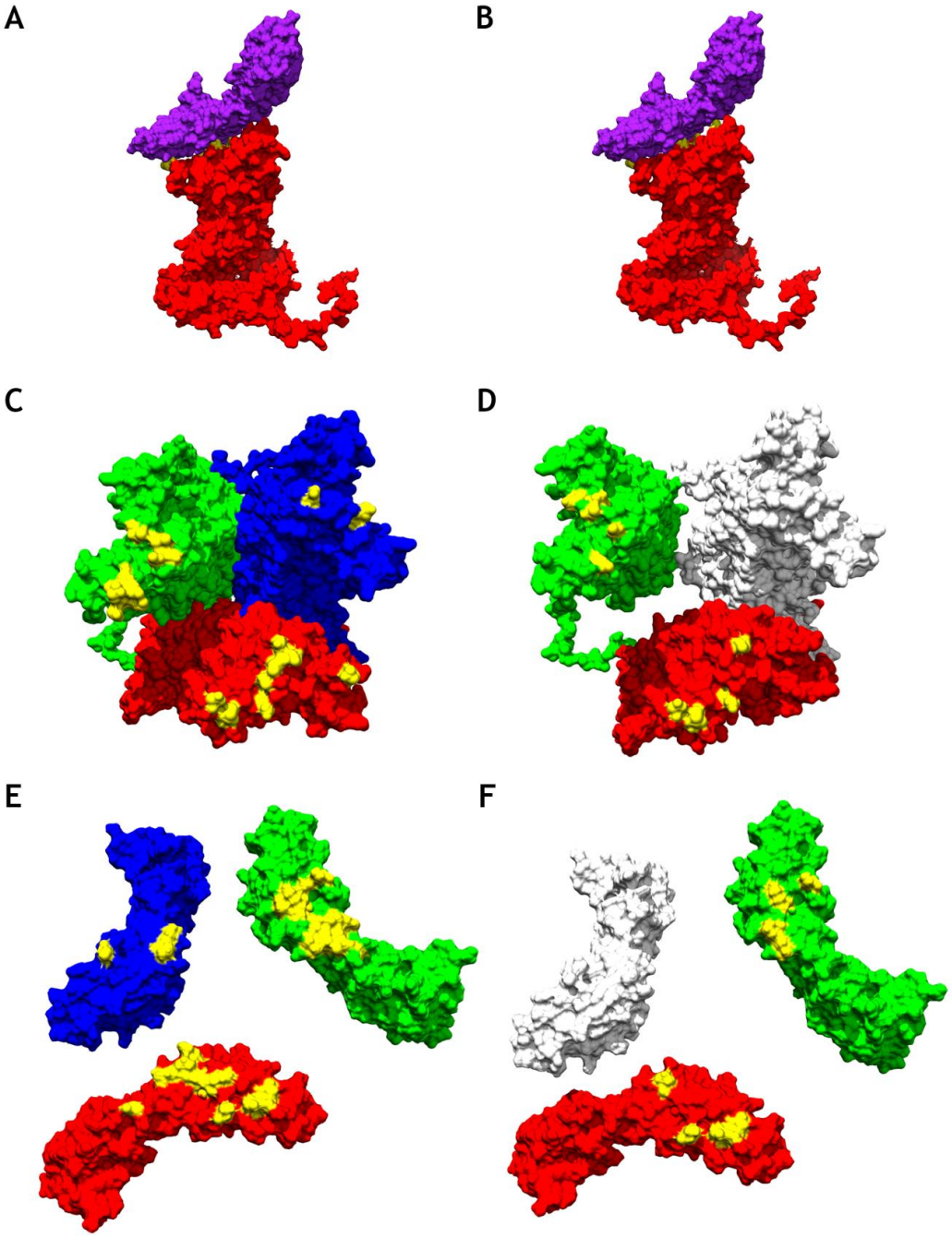

Figure 39- Determination of contact residues between FCV VP1 and fJAM-A

Modelled VP1 protein structures (see 4.5) and an fJAM-A homology model (Bhella 2011) were docked into both the pre-conformational change structure (A, C and E) and the post-conformational change structure (B, D and F; P domains only fitted due to rotation in relation to the S domain). VP1 chain A is shown bound to fJAM-A for the pre (A) and post (B) conformational change states. Contact residues were calculated using UCSF Chimera and coloured yellow on both the VP1 asymmetric units (C: pre-conformational change and D: post-conformational change, top view shown) and the fJAM-A proteins (E: pre-conformational change and F: post-conformational change, underside/interacting face shown). VP1 proteins and their interacting fJAM-A proteins were coloured by chain (chain A: red, chain B: green, chain C: blue) with chain C in the post-conformational change state coloured white as these positions could not be determined due to the movement and therefore loss of resolution/density in the map.

A

Pre Conf Change	Chain A	351	GNRYWTDITD	FVIRPFVFQA	NRHFDFNQET	AGWSTPRFRP	ITITISEKNG	SKLGIGVATD	420
Pre Conf Change	Chain B	351	GNRYWTDITD	FVIRPFVFQA	NRHFDFNQET	AGWSTPRFRP	ITITISEKNG	SKLGIGVATD	420
Pre Conf Change	Chain C	351	GNRYWTDITD	FVIRPFVFQA	NRHFDFNQET	AGWSTPRFRP	ITITISEKNG	SKLGIGVATD	420
Post Conf Change	Chain A	351	GNRYWTDITD	FVIRPFVFQA	NRHFDFNQET	AGWSTPRFRP	ITITISEKNG	SKLGIGVATD	420
Post Conf Change	Chain B	351	GNRYWTDITD	FVIRPFVFQA	NRHFDFNQET	AGWSTPRFRP	ITITISEKNG	SKLGIGVATD	420
Pre Conf Change	Chain A	411	YIIPGIPDGW	PDTTIPDKLI	PAGDYSITTG	EGNDIKTAQA	YDTAAVVKNT	TNFRGMYICG	480
Pre Conf Change	Chain B	411	YIIPGIPDGW	PDTTIPDKLI	PAGDYSITTG	EGNDIKTAQA	YDTAAVVKNT	TNFRGMYICG	480
Pre Conf Change	Chain C	411	YIIPGIPDGW	PDTTIPDKLI	PAGDYSITTG	EGNDIKTAQA	YDTAAVVKNT	TNFRGMYICG	480
Post Conf Change	Chain A	411	YIIPGIPDGW	PDTTIPDKLI	PAGDYSITTG	EGNDIKTAQA	YDTAAVVKNT	TNFRGMYICG	480
Post Conf Change	Chain B	411	YIIPGIPDGW	PDTTIPDKLI	PAGDYSITTG	EGNDIKTAQA	YDTAAVVKNT	TNFRGMYICG	480
Pre Conf Change	Chain A	471	SLQRAWGDKK	ISNTAFITTA	IRDGNEIKPS	NTIDMTKLAV	YQDTHVGQEV	QTSDDTLALL	540
Pre Conf Change	Chain B	471	SLQRAWGDKK	ISNTAFITTA	IRDGNEIKPS	NTIDMTKLAV	YQDTHVGQEV	QTSDDTLALL	540
Pre Conf Change	Chain C	471	SLQRAWGDKK	ISNTAFITTA	IRDGNEIKPS	NTIDMTKLAV	YQDTHVGQEV	QTSDDTLALL	540
Post Conf Change	Chain A	471	SLQRAWGDKK	ISNTAFITTA	IRDGNEIKPS	NTIDMTKLAV	YQDTHVGQEV	QTSDDTLALL	540
Post Conf Change	Chain B	471	SLQRAWGDKK	ISNTAFITTA	IRDGNEIKPS	NTIDMTKLAV	YQDTHVGQEV	QTSDDTLALL	540

B

Pre Conf Change	Chain A	1	MGTEARAGRR	QLLVFTSVVL	SSLALGRGAV	YTSEPDVRVP	EDKPAKLSCS	YSGFSNPRVE	60
Pre Conf Change	Chain B	1	MGTEARAGRR	QLLVFTSVVL	SSLALGRGAV	YTSEPDVRVP	EDKPAKLSCS	YSGFSNPRVE	60
Pre Conf Change	Chain C	1	MGTEARAGRR	QLLVFTSVVL	SSLALGRGAV	YTSEPDVRVP	EDKPAKLSCS	YSGFSNPRVE	60
Post Conf Change	Chain A	1	MGTEARAGRR	QLLVFTSVVL	SSLALGRGAV	YTSEPDVRVP	EDKPAKLSCS	YSGFSNPRVE	60
Post Conf Change	Chain B	1	MGTEARAGRR	QLLVFTSVVL	SSLALGRGAV	YTSEPDVRVP	EDKPAKLSCS	YSGFSNPRVE	60
Pre Conf Change	Chain A	61	WKFAHGDITS	LVCYKNKITA	SYADRVTFSH	SGITFHSVTR	KDTGTYTCMV	SDDGGNTYGE	120
Pre Conf Change	Chain B	61	WKFAHGDITS	LVCYKNKITA	SYADRVTFSH	SGITFHSVTR	KDTGTYTCMV	SDDGGNTYGE	120
Pre Conf Change	Chain C	61	WKFAHGDITS	LVCYKNKITA	SYADRVTFSH	SGITFHSVTR	KDTGTYTCMV	SDDGGNTYGE	120
Post Conf Change	Chain A	61	WKFAHGDITS	LVCYKNKITA	SYADRVTFSH	SGITFHSVTR	KDTGTYTCMV	SDDGGNTYGE	120
Post Conf Change	Chain B	61	WKFAHGDITS	LVCYKNKITA	SYADRVTFSH	SGITFHSVTR	KDTGTYTCMV	SDDGGNTYGE	120
Pre Conf Change	Chain A	121	VSVQLTVLVP	PSKPTVHIPS	SATIGSRAVL	TCSEKDGSPP	SEYYWFKDGV	RMPLEPKGNR	180
Pre Conf Change	Chain B	121	VSVQLTVLVP	PSKPTVHIPS	SATIGSRAVL	TCSEKDGSPP	SEYYWFKDGV	RMPLEPKGNR	180
Pre Conf Change	Chain C	121	VSVQLTVLVP	PSKPTVHIPS	SATIGSRAVL	TCSEKDGSPP	SEYYWFKDGV	RMPLEPKGNR	180
Post Conf Change	Chain A	121	VSVQLTVLVP	PSKPTVHIPS	SATIGSRAVL	TCSEKDGSPP	SEYYWFKDGV	RMPLEPKGNR	180
Post Conf Change	Chain B	121	VSVQLTVLVP	PSKPTVHIPS	SATIGSRAVL	TCSEKDGSPP	SEYYWFKDGV	RMPLEPKGNR	180
Pre Conf Change	Chain A	181	AFSNSSYSLN	EKTGELVFDP	VSAWDTGEYT	CEAQNGYGMP	MRSEAVRMEA	AELNVGGIVA	240
Pre Conf Change	Chain B	181	AFSNSSYSLN	EKTGELVFDP	VSAWDTGEYT	CEAQNGYGMP	MRSEAVRMEA	AELNVGGIVA	240
Pre Conf Change	Chain C	181	AFSNSSYSLN	EKTGELVFDP	VSAWDTGEYT	CEAQNGYGMP	MRSEAVRMEA	AELNVGGIVA	240
Post Conf Change	Chain A	181	AFSNSSYSLN	EKTGELVFDP	VSAWDTGEYT	CEAQNGYGMP	MRSEAVRMEA	AELNVGGIVA	240
Post Conf Change	Chain B	181	AFSNSSYSLN	EKTGELVFDP	VSAWDTGEYT	CEAQNGYGMP	MRSEAVRMEA	AELNVGGIVA	240

Figure 40- Contact residues identified on both VP1 and fJAM-A

Sequences of FCV VP1 (A) and fJAM-A (B) are presented with the determined contact residues highlighted in red. The residues are shown separately for each VP1 chain (A, B or C) as well as for the pre and post-conformational change states. Chain C in the post-conformational change structure could not be resolved sufficiently to allow docking of the protein structures and so has been omitted here.

4.5 Protein structure modelling into the fJAM-A decorated FCV cryo-EM density map

As the structure of FCV decorated with the soluble ectodomain of fJAM-A was resolved to 3.55Å resolution, we aimed to model the protein structure of VP1 when bound to fJAM-A in order to further characterise the conformational change in the P domains and to map the interaction between the two proteins.

Following the determination of the FCV F9 VP1 structure by modelling, we aimed to also model the structure of VP1 when decorated/bound to the soluble ectodomain of fJAM-A. The cryo-EM structure of decorated FCV was resolved to a slightly lower overall resolution of 3.55Å although the S domain appeared to be around 3.3Å. However, the P domains were only resolved to approximately 4.0Å with the fJAM-A ectodomain resolving to around 4.6-5.1Å. The high resolution of the S domains supported modelling in these regions, however, the lower resolution of the P domains and fJAM-A was more challenging.

The previously determined structure of the FCV F9 VP1 asymmetric unit was fitted into the cryo-EM density map and modelled as previously described using Coot and Phenix. Unfortunately, the P domains and fJAM-A density were of too low resolution to allow for protein modelling. Some ß-strand density was visible in the P domains although no distinguishable side chains or nearby density was resolved in order to build in the amino acid structure for those regions. However, the density of the S domains for the asymmetric unit (decorated with fJAM-A) were sufficiently resolved to allow modelling of the protein structure in these domains.

Figure 41 shows the structure of the S domains of the asymmetric unit determined by modelling of the protein structure into the fJAM-A decorated FCV VP1 density. The S domains of the decorated capsid proteins show the eight-stranded ß-barrel structure previously described which is formed of two, four-stranded ß-sheets (formed of strands: BIDG and CHEF). The two alpha helices between strands are also clearly visible.

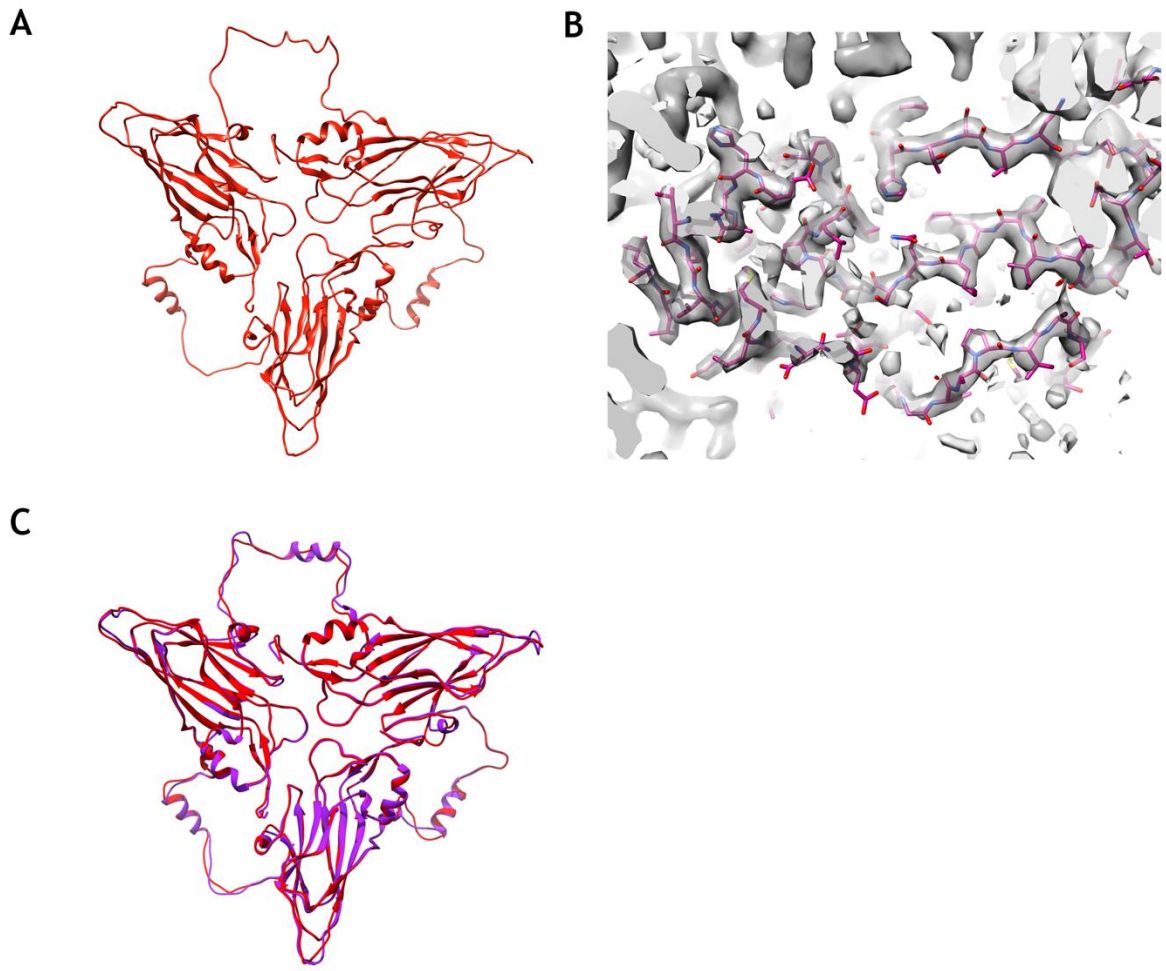

Figure 41- Modelling of the S domain in the fJAM-A decorated FCV structure

The S domain of the VP1 capsid protein when bound to the soluble ectodomain of fJAM-A was determined by modelling into the cryo-EM density map using Coot and Phenix. The structure of the S domains of the asymmetric unit (decorated with fJAM-A) are shown in red (A). A representative slice through the density (grey) showing the modelled structure of the S domain (pink) is shown in panel B. The S domains determined by modelling into the decorated structure of FCV VP1 (red) were overlaid with those modelled into the undecorated structure (purple) and are shown in panel C.

Figure 41B shows a representative slice through the density (grey) illustrating the accuracy of the modelled amino acid structure (pink). The high accuracy of the modelled structure is further supported by a map correlation coefficient around atoms of 0.845 with 0.0% outliers. Figure 41C shows the determined S domain structures from the decorated virus (red) overlaid with those from the undecorated virus (purple). The structures of the S domains of the two asymmetric units are almost identical with an RMSD (root-mean-square deviation) of 0.47 and the only slight changes being in the NTA and the outer loop of the S domains. These slight variations were visualised in both density maps and no significant variations were identified, suggesting that the slight differences seen are due to the modelling and are of no structural significance. The similarity of these structures suggests that the binding of the soluble ectodomain of fJAM-A to FCV does not result in a conformational change in the S domains of VP1 and that the rotation of the P domains as well as the possible tilting of the C/C dimers must be limited to only the P domains themselves. The observation that no change is seen in the S domain even upon the 19° rotation of the P domains suggests that the flexible hinge region between the two domains likely allows for this movement while retaining S domain structure and capsid integrity.

4.6 Discussion

The structure of FCV F9 has previously been presented at intermediate resolution showing the characteristic calicivirus morphology of the capsid proteins (Bhella et al., 2008; Bhella and Goodfellow, 2011; Conley et al., 2017). The structure of FCV (F9) decorated with the soluble ectodomain of its cellular receptor, fJAM-A, has also been presented at intermediate resolution showing an anti-clockwise rotation of the P domains of the capsid proteins as well as a possible tilting of the C/C dimers away from the icosahedral axis (Bhella and Goodfellow, 2011).

Here, we present the structure of FCV at 3.0Å resolution as well as the structure of FCV decorated with the soluble ectodomain of fJAM-A at 3.55Å resolution. Although we were unable to separate out the stages of the conformational change, a pre-conformational change state was solved to 6Å, allowing further characterisation of the FCV-fJAM-A interaction. Key residues in VP1 were identified as 434D and 495N with fJAM-A residues 33S and between 43K to 48S also being important in the virus-receptor interaction. The conformational change was determined as an anti-clockwise rotation of 19° in the P domains of the capsid proteins. This was previously identified as an anti-clockwise rotation of 15° although that structure was of intermediate resolution and so our near atomic resolution structure provides a more accurate model for calculating the extent of rotation that occurred in the P domains upon engagement by fJAM-A (Bhella and Goodfellow, 2011). The C/C dimer also appears to be less well resolved in the structures solved by us and others in the post-conformational change state suggesting that the movement/tilting of the capsomere results in the breaking of the icosahedral symmetry which is why those regions are poorly resolved (Bhella and Goodfellow, 2011). This is supported by our findings that in the pre-conformational change state, the C/C dimers appear similar to the A/B dimers with the fJAM-A visible bound to the P2 domains.

The structure of FCV decorated with the soluble ectodomain of fJAM-A shows that 2 fJAM-A proteins bind to each VP1 dimer in a head to tail arrangement (Bhella and Goodfellow, 2011). This is different to that seen in solution (and predicted in the tight junctions between cells) where the fJAM-A ectodomain forms homodimers as shown in Figure 23 (Kostrewa et al., 2001; Prota et al.,

2003). When dimeric, the D1 domains of the two fJAM-A proteins interact while the D2 domains remain separated. However, upon FCV binding, the D1-D1 interaction is abolished and each monomer binds to each VP1 capsid protein, rotated 180º from the neighbouring fJAM-A monomer. Interestingly, the region of fJAM-A to which FCV binds is located on a different face/area of the protein to the dimerisation domain (see Figure 13 and Figure 25). The affinity of the D1-D1 interaction (11μM) has been shown to be much higher than that between hJAM-A and reovirus σ1 protein (2.4nM) (Guglielmi et al., 2007; Kirchner et al., 2008). Likewise, our findings suggest a dissociation constant in the nM range for FCV and fJAM-A. Together, these findings suggest that the lower affinity between two fJAM-A proteins may result in the breakage of the dimer upon engagement in a stronger interaction with a viral protein which may explain the monomeric form of fJAM-A found on decorated FCV particles. Dimeric CAR (coxsackievirus and adenovirus receptor) has also been shown to be disrupted upon binding of the adenovirus fibre knob protein which, interestingly, triggered endocytosis (Salinas et al., 2014). More investigation is needed, however, to determine if this mechanism also plays a role in FCV internalisation/entry.

Upon comparison of the VP1 capsid protein structures of FCV F9 and FCV-5, they appear very similar, particularly in the S domain and the P1 domain. Some slight variations exist in the N-terminal arm of the protein although the major variations are seen in the top most region of the P2 domain which is responsible for receptor engagement and antibody neutralisation. It is not unreasonable to speculate that these variations in the P2 domains of the VP1 capsid proteins may affect the dissemination of FCV-5, allowing the infection of non-respiratory cells/tissues and therefore causing the described virulent systemic disease associated with this strain. In contrast, F9 is a vaccine strain of FCV and so the highly similar nature of the two proteins is both expected (as they are related strains of FCV) and unexpected (due to highly differing disease outcomes for the two strains).

A conformational change in the FCV-5 capsid upon fJAM-A binding has been proposed by Ossiboff et al who showed an increase in bis-ANS fluorescence upon incubation of the virus and fJAM-A. Interestingly, it was reported that this increase in fluorescence, signifying a conformational change and the exposure of

hydrophobic regions, was not seen for the F9 vaccine strain upon incubation with fJAM-A (Ossiboff et al., 2010). The exposure of hydrophobic regions could come from either VP1 or fJAM-A although our data suggests that a conformational change in the capsid is more likely than movement of the fJAM-A on the virus. It is worth noting, however, that the bis-ANS experiments were performed with bacterially expressed fJAM-A and so any post-translational modifications such as glycosylation would not be present on the receptor. The structure of FCV-5 decorated with the soluble ectodomain of fJAM-A would be interesting to investigate the presence and degree of any conformational change seen in a virulent systemic strain and to compare it with that presented here from the vaccine strain, F9.

5 Characterisation of FCV attachment and uncoating

The entry pathway of FCV has previously been shown to involve viral uptake by clathrin-mediated endocytosis (Stuart and Brown, 2006). We have shown that upon receptor engagement, FCV undergoes a conformational change (Bhella et al., 2008; Bhella and Goodfellow, 2011). This finding led us to hypothesise that receptor engagement may prime the virus for uncoating in the endosome. We therefore set out to investigate the effect of pH on FCV virion integrity, in the presence or absence of fJAM-A. We also aimed to determine the number of fJAM-A proteins required to cause the conformational change seen in the virus.

5.1 Effect of pH on capsid structure and integrity

To investigate the effect of pH on FCV capsid structure, both FCV and FCV with Fc-fJAM-A were incubated at pH values of 4, 5, 6 and 7 for 1 hour at 4°C. Samples were then plunge frozen into liquid ethane cooled by liquid nitrogen and imaged in a JEOL JEM-2200FS Field emission electron microscope equipped with a Gatan Ultrascan US4000 CCD camera. Samples were imaged at 100,000 x magnification at a range of defocus values with a resulting pixel size of 1.05Å/pixel. We found that undecorated virions could be seen at all pH values down to 4, while the FCV-fJAM-A virions appeared to be disrupted at pH 4. To test whether undecorated FCV or FCV-fJAM-A had undergone structural changes at the different acidity levels, we calculated 3D reconstructions of both the undecorated and decorated virus structures.

The structure of FCV at pH4 was determined from 934 particles (extracted from 141 micrographs) and solved to 10Å resolution. Our findings when FCV was incubated alone at pH4, showed that the viral capsid resembled that at pH7 with no structural changes visible as shown in Figure 42. Interestingly, when FCV was incubated with Fc-fJAM-A at pH4, no intact virus particles could be seen by cryo-EM. A representative cryo-micrograph is presented in Figure 42, showing the presence of small globular objects which we hypothesise to be capsid proteins (purple arrow) as well as long strands of what we hypothesise to be viral RNA (pink arrow). This suggested that upon incubation with Fc-fJAM-A at pH4, FCV particles disassemble into their component parts. As FCV seemed to

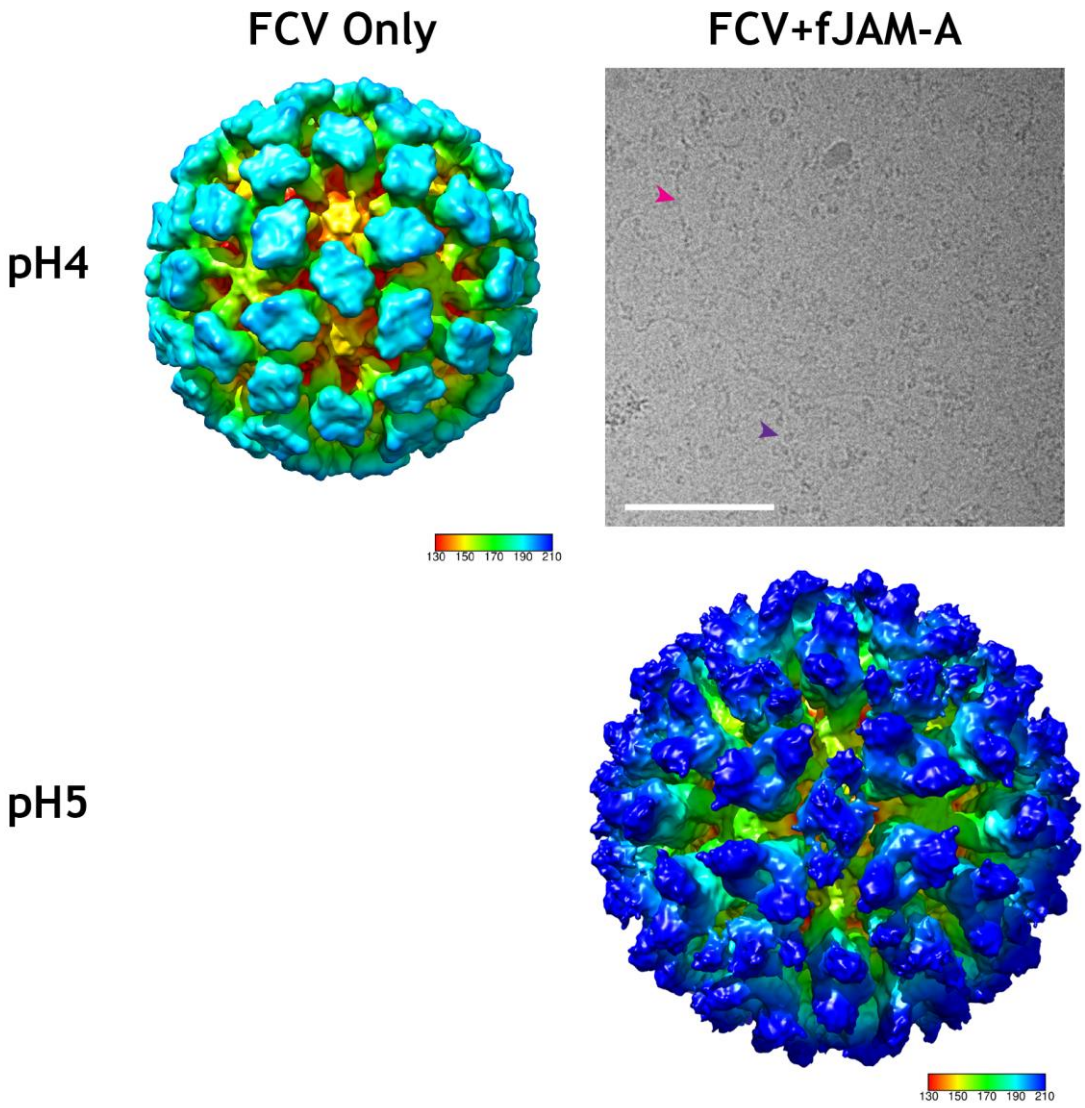

Figure 42- Effect of pH on FCV capsid structure by cryo-EM

FCV was either aliquoted alone or combined with Fc-fJAM-A for investigating the effect of pH on capsid integrity. Samples were reduced in pH by the addition of the appropriate volume of pH2 buffer and incubated for 1 hour at 4°C prior to plunge freezing and imaging. FCV particles remained intact at pH4 although when incubated with Fc-fJAM-A, no intact viral particles were visible. The presence of proteins and strands of RNA can be seen (purple and pink arrows, respectively) in the cryo-EM micrographs. FCV when incubated with Fc-fJAM-A at pH5, however, remains intact and adopts the same structure as that previously determined at pH7.

fall apart in the presence of Fc-fJAM-A at pH4, we proceeded to investigate the structure at pH5. The structure of FCV with Fc-fJAM-A at pH5 was solved to 14Å from 643 particles (extracted from 184 micrographs) and shows no difference at this resolution to the previously solved structure of the virus-receptor complex at neutral pH.

To confirm our finding that fJAM-A decorated FCV, but not undecorated FCV, uncoated at low pH and to further investigate the effect of pH on receptor mediated uncoating, we adapted an *in vitro* assay of virion stability known as PaSTRy (Particle Stability Thermal Release assay). The PaSTRy assay was developed to measure RNA released from virions following heating, and uses a nucleic acid binding dye (Syto9). Syto9 is one of a family of fluorescent molecules that undergo enhancement of fluorescence when bound to nucleic acids, possibly upon intercalation into the minor groove (personal communication with ThermoFisher Scientific). The absorption/emission spectra (nm) of the Syto9 nucleic acid binding dye are 486/501. Thus in PaSTRy assays, the temperature at which capsid integrity is lost may be determined by measuring fluorescence induced by the dye binding to the viral genome. We modified this assay to examine the effect of pH rather than temperature such that when the pH was sufficiently reduced to cause disassembly of fJAM-A bound FCV, the viral RNA released would be bound by the Syto9 reagent, leading to enhanced fluorescence. No change in fluorescence intensity would indicate that virions had remained intact.

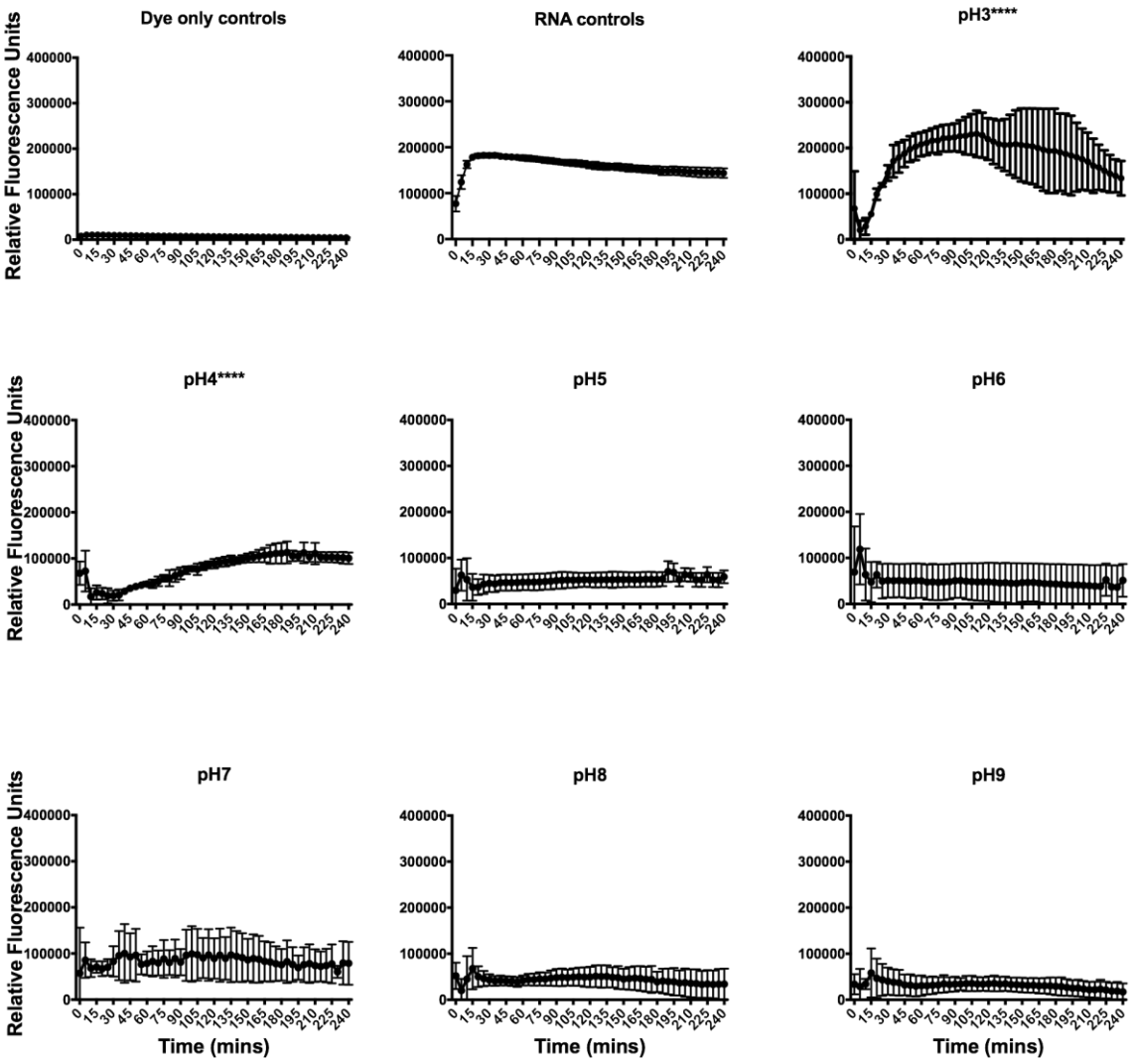

Figure 43- RNA release assay to determine the pH at which FCV uncoats

RNA release assays were performed in triplicate at a range of pH values from 3 to 9. Dye (negative) and RNA (positive) controls are averages of all pH values investigated. Equal concentrations of FCV and Fc-fJAM-A were combined with Syto9 nucleic acid binding dye in a Tris-HCl buffer of appropriate pH and fluorescence measured every 5 minutes over a period of 4 hours. Fluorescence readings were normalised to an equivalent sample containing FCV and nucleic acid binding dye (no Fc-fJAM-A) prior to plotting of the data. P values of <0.0001 upon comparison to pH7 data are represented by ****.

We had previously established that disassembly occurred up to 1 hour following the addition of Fc-fJAM-A to FCV (at pH4). We therefore added one of these two critical components of the reaction mixture last and then immediately took fluorescence measurements over a period of 4 hours to establish the time taken for virion disassembly to occur.

The RNA release assay was used to test pH values ranging from 3 to 9, examining the pH at which viral disassembly occurs. Negative control samples were tested that comprised the dye in buffer, while positive controls were tested that contained purified FCV RNA. The control data presented represent averages of the data collected at all tested pH values due to little variation observed between the samples. All samples of FCV and Fc-fJAM-A were normalised to controls containing only FCV and nucleic acid binding dye to remove any non-specific/background fluorescence.

Figure 43 shows a very low signal for the dye only negative control alongside a high fluorescence signal for the positive RNA control confirming the principle of the assay. As shown in Figure 43, no increase in fluorescence can be seen when FCV and Fc-fJAM-A were combined at pH values of 5, 6, 7, 8 or 9, confirming our previous findings by EM that the virus-receptor complex remains intact at pH5 and at neutral pH (see Figure 42). At pH4, a steady increase in fluorescence intensity is observed signifying the previously hypothesised disassembly of the virus-receptor complex with maximal uncoating occurring 180 minutes post incubation. Only a slight increase in fluorescence is seen 60-90 minutes post incubation although, by electron microscopy, this was sufficient time for uncoating of most FCV particles to occur. Interestingly, the uncoating seen at pH3 appears to occur much more rapidly with maximal uncoating occurring after approximately 105 minutes. This confirms our hypothesis that upon incubation with Fc-fJAM-A, FCV undergoes disassembly at pH values of 4 and lower which may be significant in fully understanding the entry mechanism utilised by caliciviruses.

5.2 Stoichiometry of FCV-fJAM-A interaction

To determine the ratio of virus to receptor that would be sufficient to prime virions for uncoating at low pH, virion disassembly at pH3 was assessed by RNA release assay. As the virus disassembles when incubated at low pH with fJAM-A but not at pH5 (although the conformational change is present), we can assume that the receptor induced conformational change occurs prior to viral disassembly. We can, therefore, use the rapid disassembly we observe at pH3 as a measure of the extent of virion destabilisation as a consequence of the conformational change induced by differing ratios of receptor to capsid protein. To confirm the results of our RNA release assay, we also used negative stain TEM to directly visualise virion disassembly at low pH.

To estimate the minimum ratio of receptor to capsid protein that is necessary to induce destabilisation of virions, the RNA release assay previously described was adopted. Ratios of VP1 (62kDa) to Fc-fJAM-A (62kDa monovalent or 124kDa bivalent) were calculated and virions combined with varying amounts of receptor in the presence of pH3 buffer. We hypothesised that virion disassembly would occur if sufficient Fc-fJAM-A was present to induce the conformational changes previously seen. We also hypothesised that only one fJAM-A ectodomain (of the two bivalently linked proteins) would bind to the capsid as we have seen no evidence of bivalent binding in our reconstructions. Each sample contained an equal concentration of FCV with reducing Fc-fJAM-A concentrations, starting from an estimated 1:1 ratio of VP1 to Fc-fJAM-A and ranging to a 22:1 ratio of VP1 to Fc-fJAM-A. As previously described, fluorescence was read every 5 minutes over a period of 4 hours and normalised to a virus only control sample.

Figure 44 shows the low signal in the dye negative control and the substantial increase in fluorescence in samples containing an equal concentration of Fc-fJAM-A to FCV (1:1) down to, and including, a VP1 to Fc-fJAM-A ratio of approximately 7:1. This increase in fluorescence signifies the increase in viral RNA released as the virus disassembles and indirectly represents the presence of the conformation change in FCV. No increase in fluorescence, and therefore disassembly, can be seen with VP1 to Fc-fJAM-A ratios from 16:1 onwards. Figure 44, therefore, demonstrates that the minimum amount of Fc-fJAM-A needed to

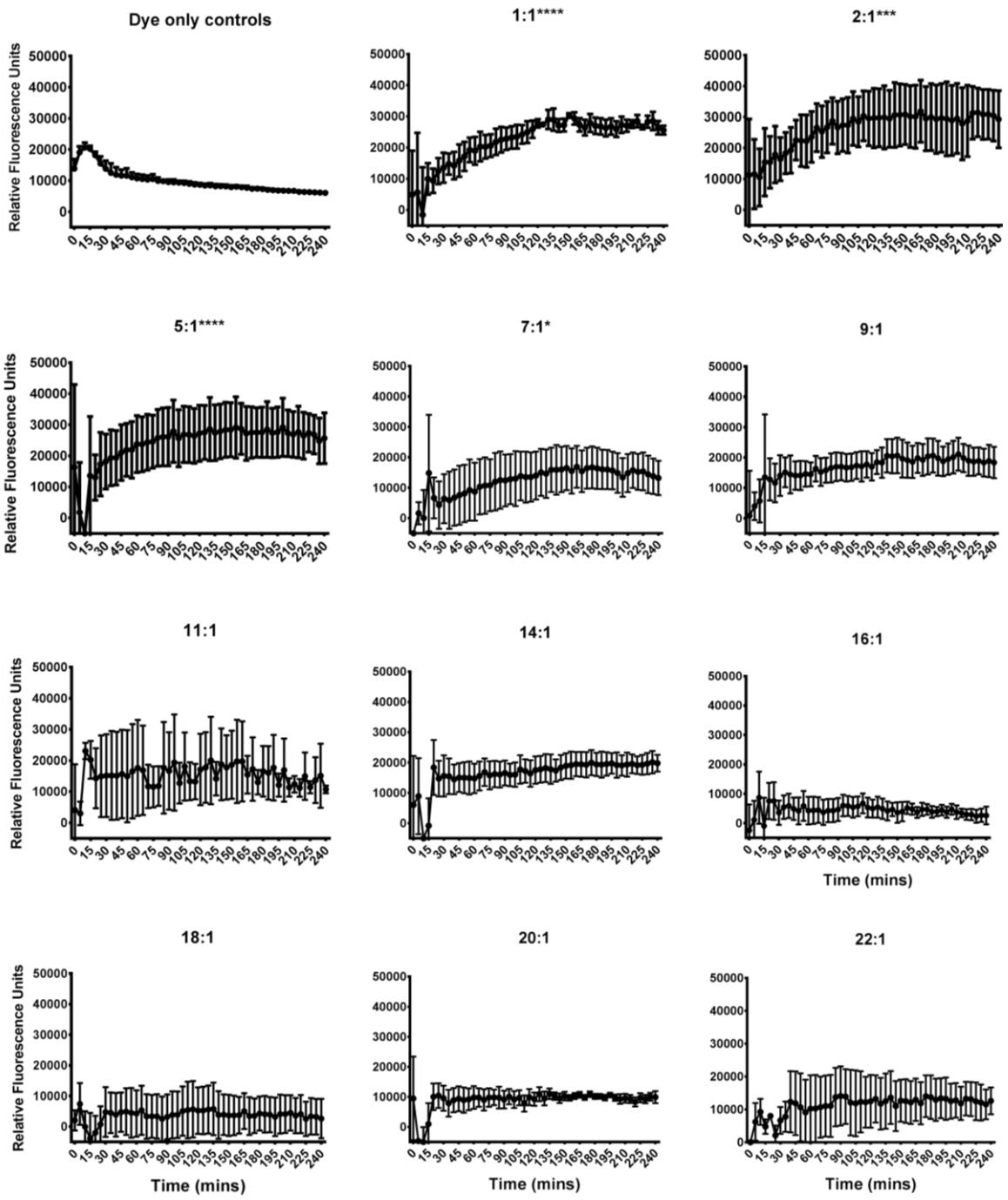

Figure 44- RNA release assay to determine the limiting molar ratio of receptor induced virion uncoating at low pH.

RNA release assays were performed in triplicate in the presence of pH3 buffer in order to force the virus to disassemble if sufficient Fc-fJAM-A was present (signifying the presence of the conformational change in the capsid). All samples contained an equal concentration of FCV while Fc-fJAM-A concentration was reduced from a 1:1 down to 22:1 ratio of VP1 to Fc-fJAM-A in PBS. Fluorescence of samples was read every 5 minutes for 4 hours and data normalised to an FCV only control. P values (when compared to the dye only negative control) are shown with asterisks (****: p=<0.0001, ***:p=<0.005 and *:p=<0.05).

cause the disassembly (and conformational change) of FCV is a VP1 to Fc-fJAM-A ratio of between 9:1 and 14:1. This was then investigated by negative staining electron microscopy to further elucidate the lowest ratio of receptor to virus that was sufficient to destabilise the virion. Without performing three-dimensional reconstruction, the conformational change in the capsid (present from pH5 upwards) cannot be seen with negative staining EM and so virus disassembly at pH3 (but not at pH7) was used as an indicator of the presence of the receptor mediated priming event. The presence of the conformational change (signified by viral disassembly at pH3) indicated that enough Fc-fJAM-A was present and so the stoichiometry of the virus-receptor interaction can be taken as the lowest ratio of Fc-fJAM-A that is able to cause the conformational change/destabilisation (and disassembly at pH3). Negative staining electron microscopy samples of VP1 to Fc-fJAM-A ratios of between 9:1 and 14:1 were incubated for 1 hour at 4°C at both pH7 and pH3 to allow the comparison of the two pH values.

Figure 45A shows that FCV particles remain intact when incubated at both pH3 and pH7, however, when incubated with an equal concentration of Fc-fJAM-A (1:1), intact viral particles can only be seen at pH7 with no visible particles when incubated at pH3. This demonstrates the occurrence of viral disassembly at low pH as well as the presence of the conformational change in the capsid when incubated with an equal concentration of Fc-fJAM-A. Likewise, when FCV was incubated with a VP1 to Fc-fJAM-A ratio of 9:1 (see Figure 45B), no intact viral particles could be seen at pH3 unlike at pH7 where all particles appeared undamaged. Interestingly, alongside some broken particles at pH3, smaller particles are visible that we hypothesise could be compacted viral RNA, possibly in complex with viral proteins such as VP2. Figure 45B demonstrates that a ratio of 9:1 of VP1 to Fc-fJAM-A (corresponding to 20 fJAM-A proteins per virion) results in viral disassembly at low pH and therefore we hypothesise the associated conformational change.

As shown in Figure 45C, a VP1 to Fc-fJAM-A ratio of 10:1 (corresponding to 18 proteins per virus particle) was enough to cause viral disassembly at low pH with intact viral particles visible at pH7, again indicating the likely presence of the conformational change. The previously observed small particles are also visible

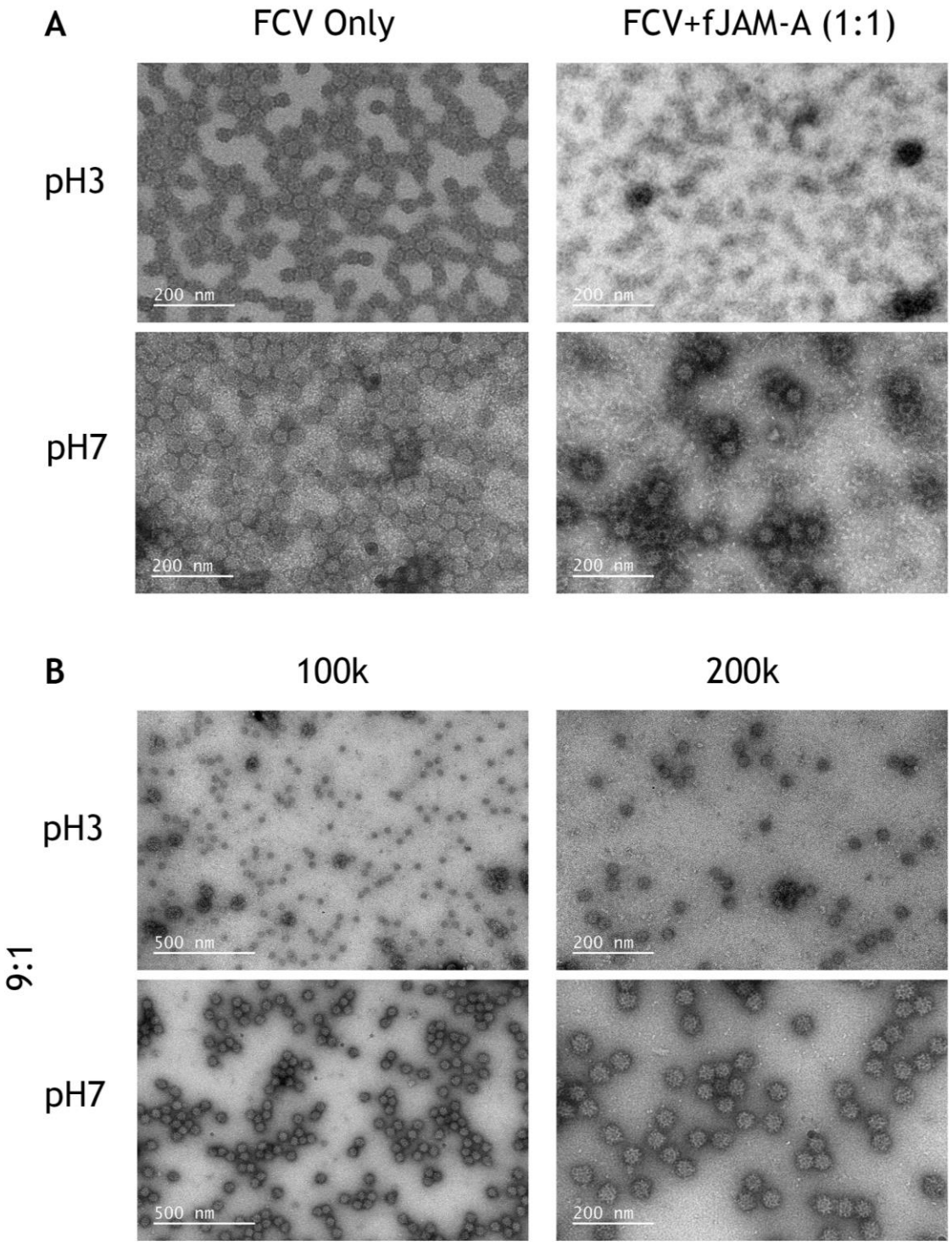

Figure 45- Negative staining EM to determine the stoichiometry of the virus-receptor interaction part 1/3

FCV was incubated with the appropriate dilution of Fc-fJAM-A at 4°C for 1 hour at either pH3 or pH7 prior to preparation of the negative staining EM grids and visualisation at both 100,000 and 200,000 x magnification. Panel A shows FCV only and FCV incubated with an equal concentration of Fc-fJAM-A (1:1) at both pH3 and pH7 (all images taken at 200,000x magnification). Panel B shows data collected with a ratio of 9:1 of VP1 to Fc-fJAM-A.

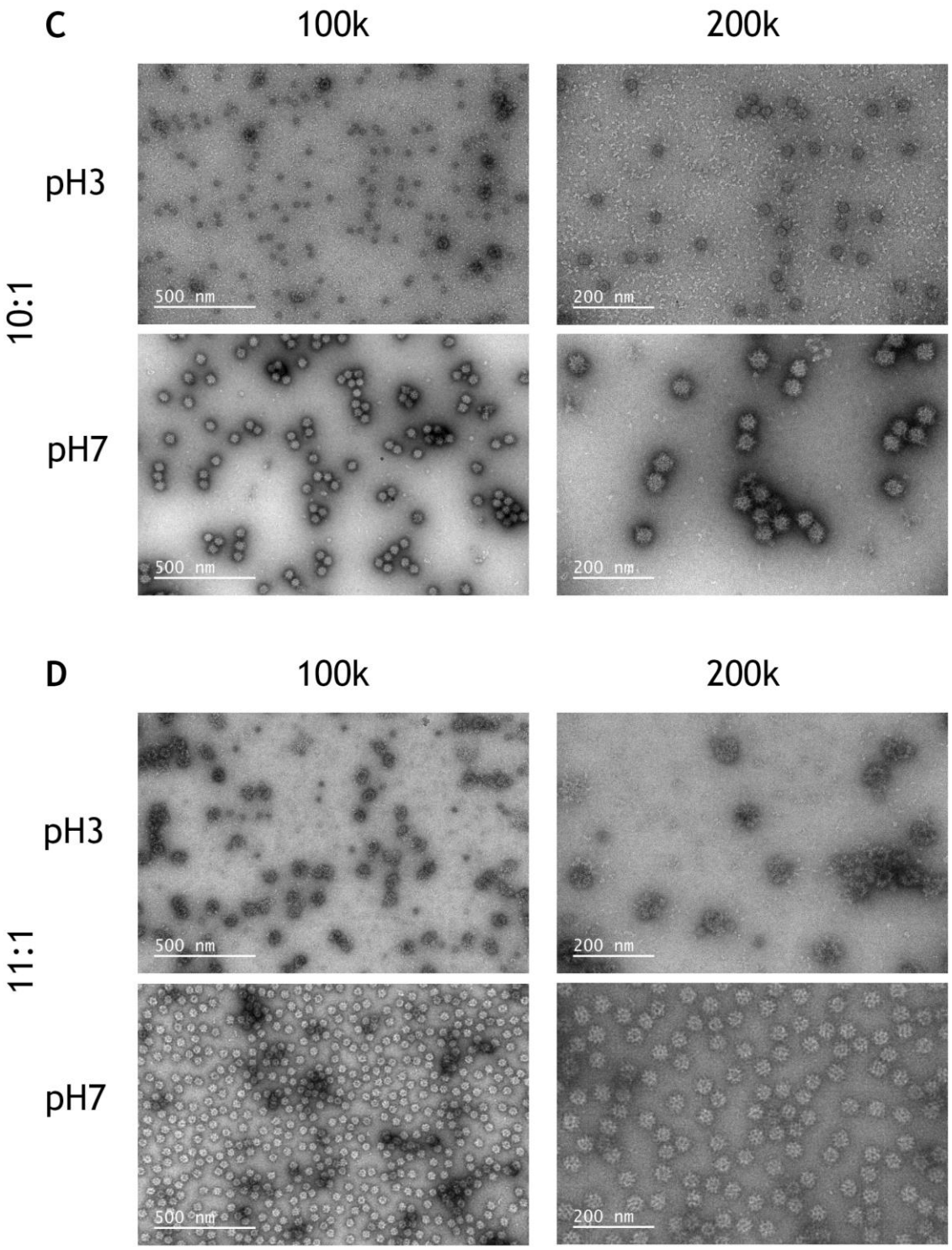

Figure 45-Negative staining EM to determine the stoichiometry of the virus-receptor interaction part 2/3

FCV was incubated with the appropriate dilution of Fc-fJAM-A at 4°C for 1 hour at either pH3 or pH7 prior to preparation of the negative staining EM grids and visualisation at both 100,000 and 200,000 x magnification. Panel C shows FCV incubated with a VP1 to Fc-fJAM-A ratio of 10:1 and panel D shows data collected with a ratio of 11:1 of VP1 to Fc-fJAM-A.

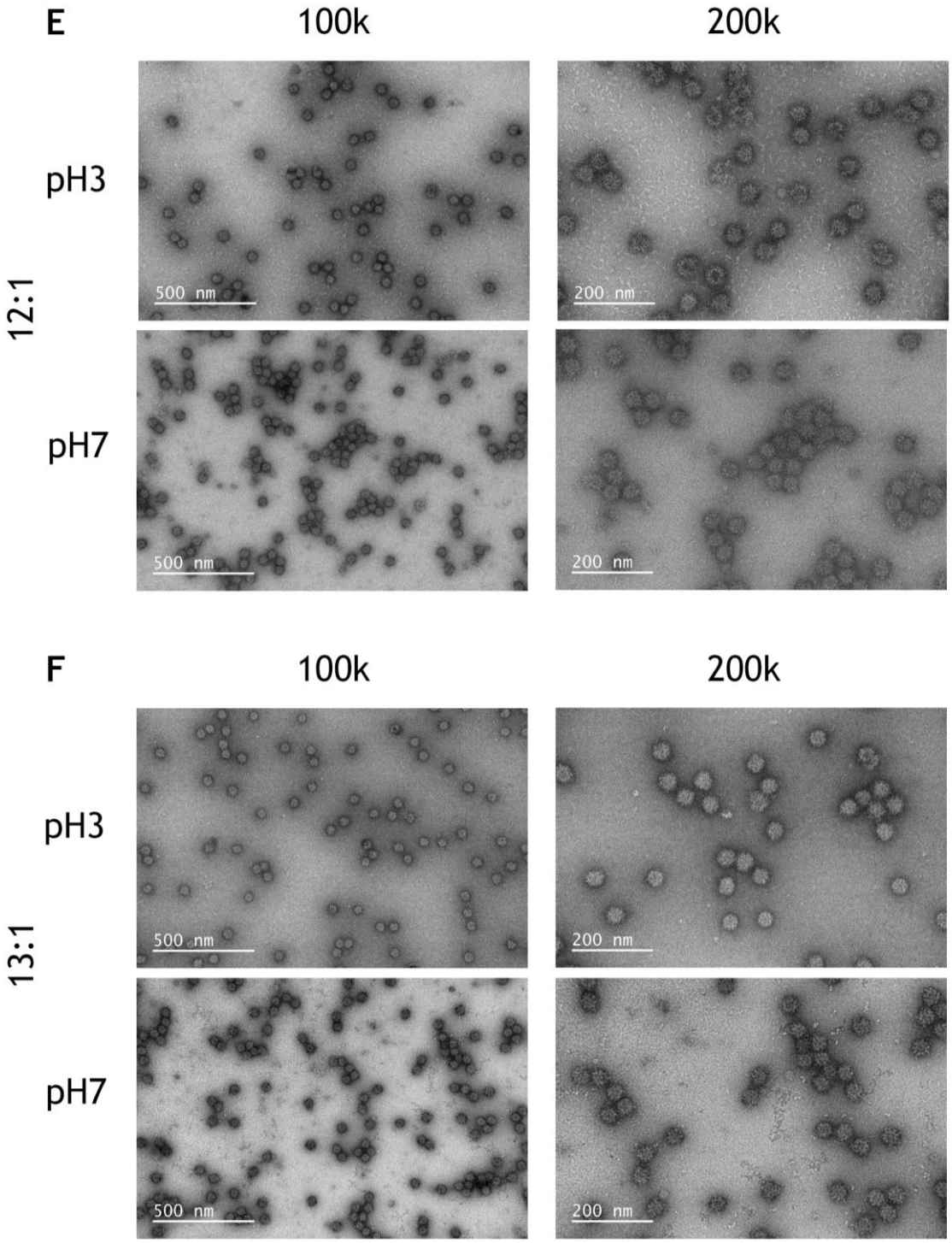

Figure 45- Negative staining EM to determine the stoichiometry of the virus-receptor interaction part 3/3

FCV was incubated with the appropriate dilution of Fc-fJAM-A at 4°C for 1 hour at either pH3 or pH7 prior to preparation of the negative staining EM grids and visualisation at both 100,000 and 200,000 x magnification. Panel E shows FCV incubated with a VP1 to Fc-fJAM-A ratio of 12:1 and panel F shows data collected with a 13:1 ratio of VP1 to Fc-fJAM-A.

as well as what appears to be protein debris following disassembly of the virus. Figure 45D shows FCV incubated with a ratio of approximately 11:1 of VP1 to Fc-fJAM-A. At pH7, intact viral particles can be seen, however, at pH3 the particles appear to be irregular in shape and broken as if they are in the process of falling apart. None of the smaller particles previously observed at low pH are visible, suggesting that they are produced during the disassembly of the virus. The presence of broken and irregular particles with a VP1 to Fc-fJAM-A ratio of 11:1 (corresponding to 16 proteins per virion) suggests that this is a crucial dilution for determining the stoichiometry of the virus-receptor interaction.

Figure 45E shows the presence of intact viral particles at both pH3 and pH7 when FCV was incubated with a VP1 to Fc-fJAM-A ratio of 12:1. However, at low pH some proteinaceous debris can be seen as well as a small proportion of particles appearing broken as seen for all visible particles in Figure 45D. When FCV was combined with a 13:1 ratio of VP1 to Fc-fJAM-A (see Figure 45F) only intact viral particles can be seen at both pH3 and pH7 suggesting that this amount of Fc-fJAM-A was not enough to trigger the conformational change in the capsid and uncoating of the virus at low pH.

Together, Figure 45 suggests that the stoichiometric limit of the virus-receptor interaction that primes for uncoating at low-pH lies between a ratio of VP1 to Fc-fJAM-A of 10:1 and 12:1. As broken and irregular particles were observed with an 11:1 ratio, we therefore suggest that this was the minimum concentration of Fc-fJAM-A needed to prime the capsid and therefore might represent the minimum number of fJAM-A proteins required to be bound by the virus during entry into a host cell.

To further investigate the presence or absence of the conformational change in the FCV capsid when incubated with these Fc-fJAM-A ratios, samples were prepared as previously described at pH7 and plunge frozen for cryo-EM imaging and three-dimensional reconstruction to visualise the extent of any conformational change. We determined the stoichiometry to be the minimum ratio/number of Fc-fJAM-A proteins needed to prime the capsid for uncoating.

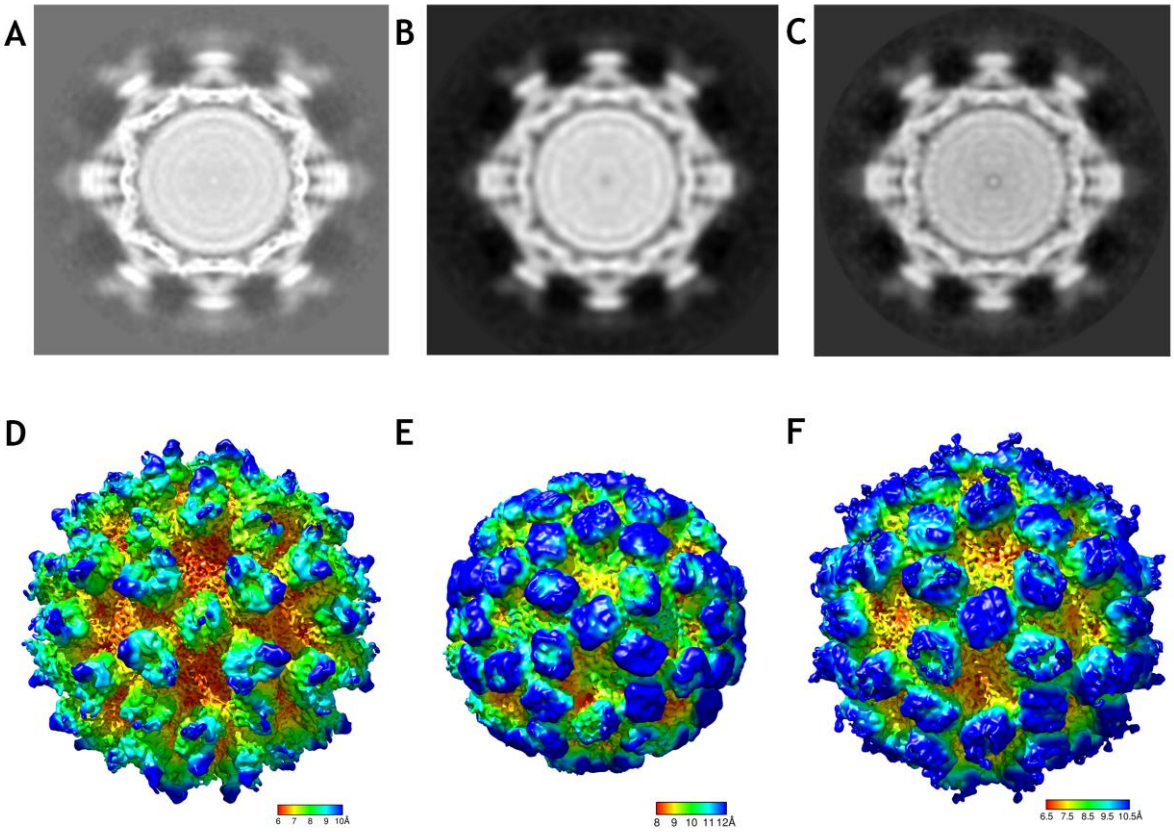

Figure 46- Cryo-EM structures of FCV decorated with varying Fc-fJAM-A concentrations

FCV particles were incubated with either a VP1 to Fc-fJAM-A ratio of 10:1 (A and D), 11:1 (B and E) or 12:1 (C and F) dilution of Fc-fJAM-A for 1 hour at 4°C prior to plunge freezing grids for cryo-EM. Samples were imaged in a JEOL JEM-2200FS field emission electron microscope equipped with a DE20 direct detection device. Data was processed and reconstructed using RELION. Central slices through the reconstructions are shown in A-C while the corresponding reconstructed maps are shown in D-F. Maps were visualised in UCSF Chimera with a threshold of the mean density plus one standard deviation.

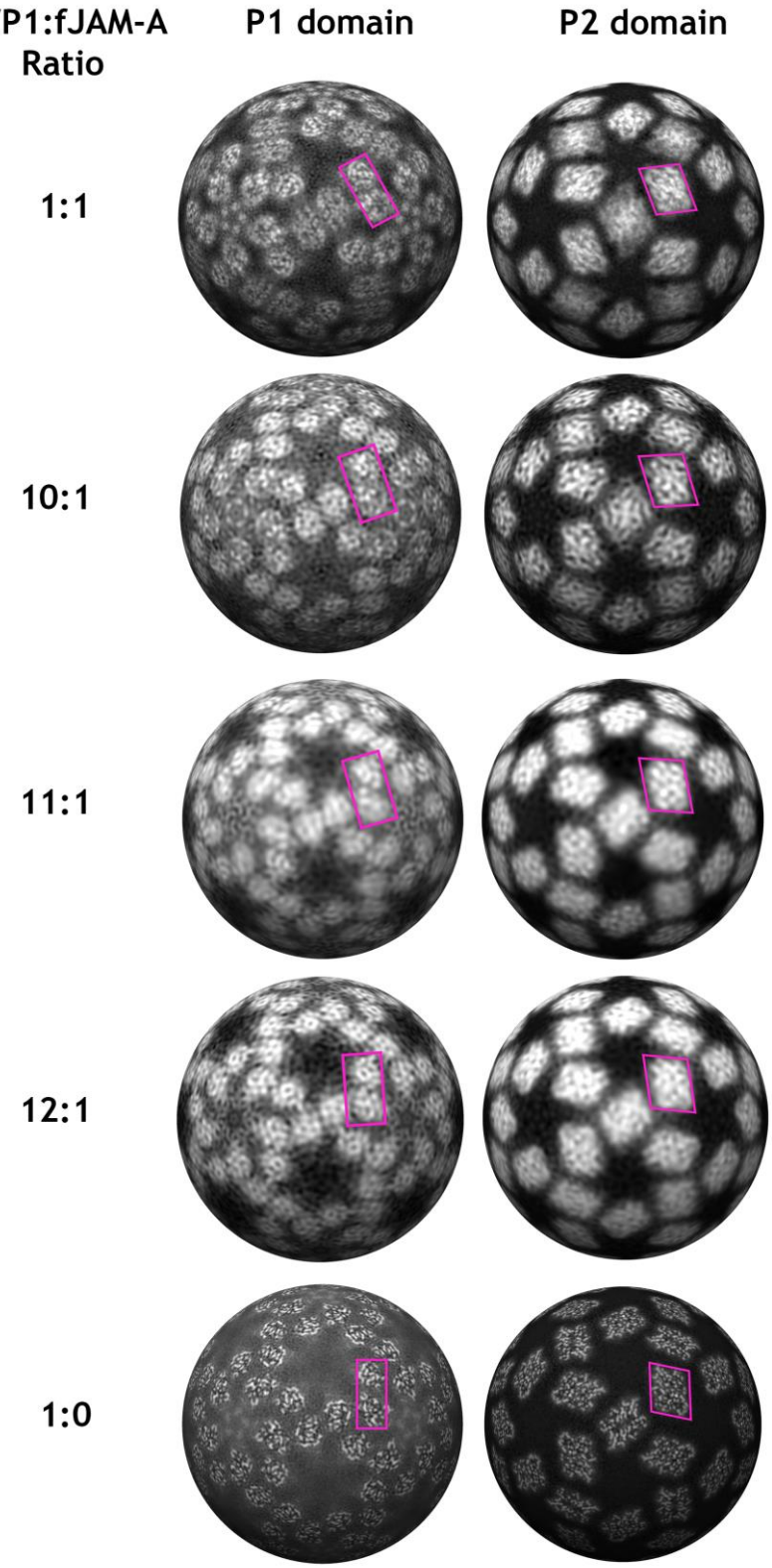

Figure 47- Spherical sections of FCV reconstructions incubated with varying ratios of VP1 to Fc-fJAM-A

Spherical sections were rendered in UCSF chimera for the VP1 to Fc-fJAM-A ratios of 10:1, 11:1 and 12:1 and compared to the undecorated (1:0) and decorated (1:1) structures presented in the previous chapter). Visualisation of the P1 domain and P2 domains is aided by the addition of pink shapes outlining an area of interest.

Figure 46A and D show the structure of the Fc-fJAM-A decorated FCV capsid calculated from 2298 particles extracted from 209 micrographs using RELION as previously described following motion and CTF correction. After 2D classification, relevant data classes were selected (2285 particles) and 3D classification performed. The detailed classes were selected (1606 particles) and used to refine the structure to 6.5Å. The structure illustrates the presence of the conformational change when FCV was incubated with a 10:1 ratio of Fc-fJAM-A (18 proteins per virus particle). The presence of the conformational change is visible in Figure 47, highlighting the rotation of the both the P1 and P2 domains upon incubation with Fc-fJAM-A.

For FCV incubated with an 11:1 ratio of VP1 to Fc-fJAM-A (16 proteins per virus particle), 1175 particles were extracted from 384 micrographs. Following 2D and 3D classification, 699 and 438 particles, respectively, were selected and refined to a resolution of 9Å using RELION. Figure 46B and E suggest a lack of a conformational change in the capsid upon incubation with an 11:1 ratio of VP1 to Fc-fJAM-A indicating that 16 fJAM-A proteins are sufficient to cause viral uncoating at low pH but not a conformational change in the capsid.

When FCV was incubated with a VP1 to Fc-fJAM-A ratio of 12:1, 885 particles were extracted from 111 micrographs and post classification, 568 particles were used for refinement of the structure against the undecorated reference map. The resulting structure, shown in Figure 46C and F, was resolved to 7.5Å using RELION. The structure suggests the absence of a conformational change in the capsid when incubated with a 12:1 ratio of VP1 to Fc-fJAM-A (14 proteins per virus particle) predicted by the lack of viral uncoating seen at pH3 (see Figure 45E).

The spherical sections presented in Figure 47 possibly show hybrid density arising from capsomeres in different conformations, resulting in blurring of the density. This suggests that the conformational changes previously seen may be formed of local changes/destabilisation rather than a concerted, capsid wide conformational change. The lack of structural change seen in the S domains of the undecorated and decorated virus structures (see 4.5) supports the hypothesis of local changes as opposed to a concerted conformational change.

VP1:Fc-fJAM-A ratio	S domain	P domain	Fc-fJAM-A
1:1	1	0.783	0.744
10:1	1	0.850	0.501
11:1	1	0.928	0.453
12:1	1	0.938	0.456
1:0	1	0.980	-

Table 3- Fc-fJAM-A occupancy in three-dimensional reconstructions

Structures were re-scaled to allocate density values between 0 (least intense) and 1 (most intense) and masks applied to separate out the S domains, P domains and Fc-fJAM-A. All S domains showed an occupancy of 1 as they contained the highest density values. Structures of decorated FCV (1:1, see previous chapter), FCV incubated with VP1 to Fc-fJAM-A ratios of 10:1, 11:1 and 12:1 as well as undecorated FCV (1:0, see previous chapter) were investigated.

Co-operative binding of the Fc-fJAM-A proteins could have been possible and so to test for this, 3D classifications of the data sets were performed with 2 starting models, the undecorated virus structure and the decorated virus structure (see previous chapter). If co-operative binding were occurring, we would expect to classify the data into two classes; one containing FCV with no Fc-fJAM-A bound and one class containing decorated particles. Upon 3D classification of all 3 data sets (10:1, 11:1 and 12:1 ratios of VP1 to Fc-fJAM-A) no subsets of undecorated particles were classified indicating that no co-operative binding was occurring in these experiments.

The central sections of the reconstructions (shown in Figure 46A-C) show the reduced occupancy of fJAM-A in each population. The fJAM-A density in the central sections appears as weaker density than the VP1 density, showing that the virus particles were not saturated with fJAM-A as in previous experiments (see previous chapter). The fJAM-A density also appears to fade upon each dilution of the receptor, confirming that each of the three reconstructions contained less fJAM-A and that the virus particles were not saturated with the receptor. To approximate the Fc-fJAM-A occupancy in each of the reconstructions, the structures were re-scaled to between 1 and 0. Masks were applied to separate out the S domains, P domains and the Fc-fJAM-A density and then the maximum density in each region of the map determined as previously described (Kandiah 2012) (see Table 3). As the S domains in all of the structures contained the highest density values, occupancy levels of 1 were assigned. Interestingly, increasing P domain density values were recorded with decreasing Fc-fJAM-A occupancy suggesting that the binding of Fc-fJAM-A and the induction of the conformational change resulted in a decrease of P domain density likely due to the movement incurred causing blurring of the density. The levels of Fc-fJAM-A occupancy support the addition of less Fc-fJAM-A to each subsequent sample in Table 3 although reductions were not in line with the calculated ratios of VP1 to Fc-fJAM-A. This could be due to the saturation of the virus particle upon incubation with a calculated 1:1 VP1 to Fc-fJAM-A ratio. The occupancy levels calculated for the 11:1 and 12:1 VP1 to Fc-fJAM-A ratios are very similar suggesting that the experiment may not have been accurate when combining the FCV and Fc-fJAM-A. A significant difference between these ratios, however, is

notable from Figure 45 showing the partial disassembly of particles with an 11:1 ratio but no disassembly with a 12:1 ratio of VP1 to Fc-fJAM-A.

To conclude, Figure 45 shows that no viral disassembly seems to occur when FCV is incubated with a VP1 to Fc-fJAM-A ratio of 13:1, however broken particles are seen with an 11:1 ratio and some particle irregularity is observed with a 12:1 ratio of VP1 to Fc-fJAM-A. The presence of a receptor mediated priming event of the capsid upon incubation of FCV with Fc-fJAM-A ratios of 10:1, 11:1 and 12:1 was confirmed by cryo-electron microscopy and three dimensional reconstruction as shown in Figure 46. Taken together, these data suggest that the minimum number of fJAM-A proteins required to bind to FCV to induce viral uncoating is approximately 16 (an 11:1 ratio of VP1 to Fc-fJAM-A) although local conformational changes in the capsid can be seen with lower ratios of VP1 to Fc-fJAM-A.

We hypothesise that during entry into a host cell, FCV attaches to the cell surface at tight junctions (possibly mediated by an attachment factor containing sialic acid) where it binds to approximately 16 fJAM-A proteins. The virus may initially bind to fewer fJAM-A proteins on the cell surface and engage more during endocytosis due to the induction of membrane curvature. This binding to fJAM-A destabilises the capsid and induces a local conformational change which, upon endocytosis and a reduction in pH, may contribute to the delivery of the viral genome into the cytoplasm of the host cell, possibly by the formation of a pore.

5.3 Discussion

Here, we show that FCV particles remain intact at low pH (pH4) by cryo-EM, however upon incubation with fJAM-A at pH4, no intact viral particles were seen in cryo-micrographs. The observation of proteins and strands of RNA in the micrographs (see Figure 42) together with no visible virus particles suggests viral disassembly upon incubation with fJAM-A at low pH. Interestingly, upon incubation of FCV with fJAM-A at pH5, intact decorated virus particles were observed and the structure elucidated by three-dimensional reconstruction shows a structure resembling that at neutral pH with the conformational change in the capsid visible. An RNA release assay was developed to test this effect of pH on capsid integrity which confirmed the release of viral RNA from the capsid (likely during viral disassembly) upon incubation with fJAM-A below pH5 (pH values of 3 and 4 were tested). The stability of the virus-receptor complex from pH5 to neutral pH was also confirmed as well as showing that the virus-receptor complex remains intact at pH values above 7 (values up to pH9 were tested). These pH values below 5 could represent the pH encountered by the virus-receptor complex upon entry into host cells via clathrin-mediated endocytosis. It has previously been shown that endosomal acidification is necessary for viral uncoating and release of the viral genome into the cytoplasm (Stuart and Brown, 2006). However, there appears to be some discrepancy in the pH values of the endocytic pathway reported by different authors although a consensus seems to suggest a pH value of around 6 for early endosomes, 5-6 for late endosomes and <5 for endo/lysosomes (Cossart and Helenius, 2014; Lozach et al., 2011). This suggests that FCV uncoating may occur in the endo-lysosome although a narrower pH range must be tested to elucidate the exact pH at which the virus uncoats.

The entry of FCV into CrFK cells results in their permeabilisation as previously reported for poliovirus and reovirus (Stuart and Brown, 2006). Feline JAM-A has been shown to be partially redistributed throughout the cytoplasm of cells at early time points of FCV infection with some expression remaining at cellular tight junctions (Pesavento et al., 2011). This redistribution may represent the internalisation of fJAM-A bound to FCV during clathrin-mediated endocytosis. This hypothesis is supported by our observation that fJAM-A bound to FCV

appears to be monomeric in form and that fJAM-A dimers have been shown to be disrupted at pH values below 6 (Monteiro et al., 2014).

As an indirect method of visualising the presence of the conformational change, the RNA release assay was adopted at pH3 with varying VP1 to fJAM-A ratios to force the virus to disassemble if enough fJAM-A was present. Negative staining and cryo electron microscopy were also used to look at virus structure upon incubation with a range of fJAM-A ratios at either pH3 (negative staining EM) or pH7 (cryo-EM) to observe the presence or absence of the conformational change. Together, these findings suggest that a VP1 to Fc-fJAM-A ratio of 11:1, corresponding to 16 fJAM-A proteins per virus particle, is the minimum required to cause the local destabilisation/conformational changes of the P domains of the FCV capsid proteins and viral uncoating at low pH.

We propose a model of FCV entry where FCV binds to fJAM-A within tight junctions, inducing a conformational change in the capsid. Clathrin mediated endocytosis is then triggered and, if not previously bound, additional fJAM-A proteins may bind to the virus during the curvature/internalisation of the membrane resulting in approximately 16 fJAM-A proteins bound to each virus particle. Upon movement through the endocytic pathway, the environment in which the decorated virus particles are held will reduce in pH. This reduction in pH to below 5 induces the release of the viral genome into the cytoplasm (possibly by pore formation and/or by inducing the permeabilisation of the endosomal membrane).

6 Discussion

This thesis presents the results of a biophysical characterisation of the attachment and entry process of an important member of the *Caliciviridae* – feline calicivirus. This virus was selected as it is a tractable model for calicivirus biology owing to it being readily propagated in cell culture and having a known protein cellular receptor. Virus entry is the critical first step of the infectious process and is therefore an important area of study. The attachment of FCV to its cellular receptor, fJAM-A, is followed by uptake via clathrin mediated endocytosis. The mechanism of viral uncoating and endosome escape is poorly understood. Previous structural studies on FCV bound to fJAM-A have revealed the presence of a conformational change thought to prime the virion for genome release. Here, we present the results of a high-resolution structural characterisation of purified FCV virions, both undecorated and labelled with the soluble ectodomain fragment of fJAM-A. These data allowed us to build an atomic model of the FCV major capsid protein VP1 and confirmed the presence of conformational changes upon receptor engagement. These included an anti-clockwise rotation of 19º in the P domains of the capsid proteins at the A and B quasi equivalent positions. This conformational change is also apparent at pH5 although upon lowering the pH further, viral disassembly was observed. This phenomenon was further explored to estimate the number of fJAM-A proteins required to prime the virion for uncoating. Receptor binding was shown to occur via the monomeric form of fJAM-A although we have shown it to be dimeric in solution. This led us to propose a mechanism by which FCV may induce endocytosis to initiate the infectious process. Finally, we have identified a carbohydrate moiety on fJAM-A produced in CHO cells and shown that it does not affect the virus-receptor interaction *in vitro*.

6.1 Investigating the influence of fJAM-A glycosylation and oligomerisation on feline calicivirus binding

Feline junctional adhesion molecule A (fJAM-A) has previously been shown to be a functional receptor for FCV with expression in non-fJAM-A cells rendering them susceptible to FCV infection *in vitro*. Feline JAM-A was shown to be present in intracellular tight junctions of epithelial and endothelial cells (as well as on the surface of leucocytes and platelets) (Pesavento et al., 2011). We have shown

that the fJAM-A ectodomain is dimeric in solution by both size exclusion chromatography as well as small angle x-ray scattering. The U-shaped structure resembles that of both the human and murine homologues, the latter of which has been shown to form *cis* interactions via an R(VIL)E motif at the dimer interface (Kostrewa et al., 2001). Kirchner et al presented a dissociation constant of 11μM for the D1-D1 human JAM-A dimer interaction (Kirchner et al., 2008), however, the dissociation constant of the reovirus σ1 head domain with D1 domain of human JAM-A was shown to be 2.4nM (Guglielmi et al., 2007). This dissociation constant of >1000-fold stronger binding to the reovirus σ1 protein represents a similar phenomenon as seen here with a dissociation constant of 12.9nM for the interaction of FCV with Fc-fJAM-A. A similar occurrence is seen with a μM dissociation constant for homophillic CAR interactions while both coxsackie virus and adenovirus have both been shown to bind to CAR with nM affinity (Coyne and Bergelson, 2005; Goodfellow et al., 2005; van Raaij et al., 2000). This appears to be a common feature among viruses that utilise tight junctional proteins as receptors.

The stronger binding of these viral proteins to JAM-A compared to homo-dimer formation in *cis* suggests a mechanism for JAM-A dimer disruption upon virus binding. This is evidenced by the binding of the monomeric form of fJAM-A to VP1 shown here by cryo-EM and three-dimensional reconstruction. Adenovirus knob fibre protein has also been shown to disrupt homodimers of the tight-junction protein CAR, leading to the induction of endocytosis (Salinas et al., 2014). We therefore hypothesise that dimer disruption upon FCV binding may provide the mechanism by which FCV gains entry to the cell. Further investigation of this disruption of fJAM-A dimerisation is therefore warranted to elucidate its role, if any, in the induction of viral uptake by clathrin mediated endocytosis.

Another receptor, α2,6 linked sialic acid, was proposed for FCV although it is unknown whether this is present as part of fJAM-A or not. To investigate this, we proceeded to purify fJAM-A from CHO cells and enzymatically remove the carbohydrate moiety on the protein. It must be noted, however, that CHO cells reportedly cannot produce α2,6 linked sialic acid and produce α2,3 linked instead. Although this was not optimal, it allowed us to elucidate that the

glycosylation present on the fJAM-A was not needed for virus binding and did not affect the oligomerisation state of the proteins. A dissociation constant of 128.7nM was determined for the deglycosylated protein and FCV although the dissociation constant calculated for glycosylated protein was done so in the presence of the Fc tag (12.9nM) and so these cannot be directly compared (as the bivalent form of Fc-fJAM-A may lead to one fJAM-A protein dissociating while its bivalent 'partner' binds). Both of these values, however, are significantly lower than that of the D1-D1 interaction in human JAM-A (11μM) supporting the hypothesis that FCV may have the ability to compete off fJAM-A homodimers as seen for both reovirus (with JAM-A) and adenovirus (CAR) (Kirchner et al., 2008; Salinas et al., 2014).

It is possible that the presence of α2,6 linked sialic acid on fJAM-A may behave differently although we are able to conclude that it is not essential for FCV binding due to our interaction studies lacking this sialic acid linkage. Furthermore, previous investigations have utilised fJAM-A expressed in bacteria which would contain no carbohydrate moieties, also suggesting that the sialic acid on fJAM-A is not required for FCV binding and may function as a regulator of fJAM-A half-life among other roles (Ossiboff et al., 2010; Scott et al., 2015). Together, data suggest that an α2,6 linked sialic acid moiety may be present on the surface of cells that aids in the entry of FCV into host cells. It is possible that this moiety may be present on a different, as yet unidentified cellular protein receptor. Another possibility, other than a separate receptor, is that the carbohydrate moiety may act as an attachment factor for FCV and aid in the delivery of virus particles from the cell surface into tight junctions where they can engage with fJAM-A. Reovirus entry has also been shown to involve binding to sialic acid, facilitating the delivery of the virus to the tight junction where it can encounter JAM-A (Bergelson, 2009). Additionally, Coxsackie B virus has been shown to initially bind to DAF (complement decay accelerating factor) on the apical surface of cells resulting in the movement of the DAF bound virus to tight junctions where it engages CAR (Bergelson et al., 1995; Coyne and Bergelson, 2006).

6.2 Structural characterisation of undecorated FCV and fJAM-A decorated FCV by cryo-electron microscopy

Bhella et al (2008, 2011) have previously shown the intermediate resolution structures of FCV and FCV decorated with fJAM-A demonstrating a conformational change in the VP1 capsid proteins upon fJAM-A engagement. An anti-clockwise rotation of 15° was reported in the A/B capsomeres as well as the possibly tilting of the C/C capsomeres resulting in the breakage of icosahedral symmetry and a less well defined structure (Bhella et al., 2008; Bhella and Goodfellow, 2011). Here we present near-atomic resolution structures for both the undecorated and decorated virus particles allowing the determination of the rotation as 19° anti-clockwise. The high resolution structure of undecorated FCV permitted the modelling of atomic coordinates for the capsid protein VP1 into the reconstructed density. Unfortunately, the P domains and fJAM-A in the decorated virus structure were not of sufficient resolution to allow their modelling, however, the S domains were well defined. Comparison of the two reconstructions as well as the modelled protein structures showed no apparent changes in the S domains of the VP1 capsid proteins upon fJAM-A engagement. This may not be expected if the virus fully uncoats as a genome delivery mechanism although the combination of the conformational change and low pH environment is likely needed to cause such structural changes and allow the formation of a pore, disruption of the endosomal membrane and/or complete uncoating of the virus.

Both our findings and previous studies have demonstrated that 2 fJAM-A proteins appear to bind to each VP1 capsomere in a head to tail arrangement (Bhella and Goodfellow, 2011). This is different to the oligomerisation state and protein structure determined for feline, human and murine JAM-A in solution where homodimers are formed via the dimerisation interface which is located away from the FCV binding site (Kostrewa et al., 2001; Prota et al., 2003). Human JAM-A dimers have been shown to dissociate upon incubation at low pH which may represent what occurs during viral entry via clathrin-mediated endocytosis although our experiments were conducted at neutral pH (Kirchner et al., 2008). It is more plausible that the higher affinity of FCV for fJAM-A than homotypic interactions between fJAM-A proteins allows the dissociation of the fJAM-A dimers upon virus binding. Tight junction proteins demonstrating a higher

affinity for certain viral proteins than their dimeric counterparts have been described previously and may allude to a common binding and/or entry mechanism. This has also been demonstrated for reovirus with JAM-A and for coxsackie virus and adenovirus interactions with CAR (Coyne and Bergelson, 2005; Goodfellow et al., 2005; Guglielmi et al., 2007; van Raaij et al., 2000). As our data suggest FCV binding to approximately 16 fJAM-A proteins, this would involve the disruption of 8-16 fJAM-A *cis*-dimers and the binding to 8-16 VP1 capsomeres during viral entry. However, these experiments were performed in solution and so differing amounts of membrane anchored fJAM-A may be required to trigger capsid destabilisation and uncoating.

Docking of our modelled VP1 structure as well as a previously described fJAM-A ectodomain homology model allowed the prediction of contact residues between the two proteins (Bhella and Goodfellow, 2011). We identified 434D and 495N as important residues in VP1 as well as fJAM-A residue 33S and an area encompassing 43K to 48S although differential binding was seen at these residues between VP1 chains and/or stages of the conformational change. Many additional contact residues between the two proteins were proposed previously although they were calculated by docking a homology model into a lower resolution map of fJAM-A decorated FCV (Bhella and Goodfellow, 2011). Structure guided mutations have previously been introduced into the fJAM-A ectodomain that resulted in a decreased binding to FCV-5. Key residues that upon mutation resulted in reduced virus binding were identified as 42D, 43K and 97S (Ossiboff and Parker, 2007). In our docking investigations, only 33S was commonly identified as a contact residue although neighbouring residues between 43K and 48S were routinely identified. FCV-5 VP1 capsid proteins that became resistant to fJAM-A neutralisation *in vitro* have also been characterised with the main recurring mutated residues being identified as G329, T438, K480, V516 and K572 (Ossiboff et al., 2010). Residue G329 forms part of the flexible hinge region between the S and P1 domain while K572 is located at the VP1 dimer interface. Residues T438, K480 and V516 are located in the P2 domain although were not identified in our contact residue screen. This suggests that a different conformational change may occur in FCV-5 than in the F9 vaccine strain used here although neutralisation mutants may differ from conformational change mutants and so these data sets must be compared with caution. It was

also proposed that upon fJAM-A binding, FCV-5 underwent a conformational change resulting in the exposure of hydrophobic regions which was not seen for FCV F9. Personal communication has also suggested uncoating of FCV-5 in the presence of fJAM-A at neutral pH. These investigations, however, were performed with bacterially expressed fJAM-A ectodomain resulting in the lack of any post-translational modifications. It is also noteworthy that the fJAM-A used to select the neutralisation mutants contained an N-terminal GST tag (located at the D1/virus binding and dimerisation domain) which may have impacted the dimerisation of fJAM-A proposed here and for the human and mouse homologues of the protein (Kostrewa et al., 2001; Ossiboff et al., 2010; Prota et al., 2003). Interestingly, when the same method of docking was used for FCV-5 as was utilised here, similar residues were identified to those predicted here (Bhella and Goodfellow, 2011). Near-atomic resolution structures of the P2-fJAM-A interactions, however, are needed to reliably determine the contact residues between the virus and receptor.

Upon comparison of the FCV F9 VP1 protein structure with that of FCV-5, few structural differences are apparent with the most unique portions mapping to the upper P2 domain. This is as expected as this is the region responsible for receptor binding and antibody neutralisation and is therefore the location of the hypervariable region. As the vaccine strain (F9) and the virulent systemic strain (FCV-5) are quite different in the disease (or lack of) that they cause, it is not surprising that the region responsible for receptor binding and neutralisation is varied. It may, however, be surprising how similar the remaining areas of the proteins appear to be with very little variation seen, particularly in the S domain. These variations in P2 may fully or partially reflect the different contact residues proposed in this region between the two strains although more investigation is needed to accurately determine the contacts for both VP1 proteins with fJAM-A.

6.3 Characterisation of FCV attachment and uncoating

Feline calicivirus entry into host cells has been shown to be facilitated by clathrin-mediated endocytosis followed by endosomal acidification (Stuart and Brown, 2006). Due to this finding, we proceeded to investigate whether a reduction in pH would affect the structure of FCV. We have shown here that

upon incubation at pH4, FCV remains intact with no structural changes seen from the pH7 counterpart at the resolutions achieved. However, upon incubation of FCV with Fc-fJAM-A at pH4, the virus receptor complex disassembles with no intact viral particles visible by negative staining or cryo-EM. An RNA release assay demonstrated that the virus receptor complex remains intact upon incubation at pH values between 5 and 9 although under conditions of pH3 or 4, the release of viral RNA was observed, signifying viral disassembly as seen by EM. Interestingly, human JAM-A dimers have been shown to dissociate at low pH (below 5) although it is unknown whether fJAM-A remains bound to FCV during uptake by endocytosis (Kirchner et al., 2008). Many viruses utilise endocytosis as a means to enter host cells although they can vary in the stage at which they escape the compartment. For example, foot and mouth disease virus (FMDV) escapes from the early endosome while human papillomavirus-16 (HPV-16) escapes from the late endosome where the pH will be even lower (~5-6) (Cossart and Helenius, 2014). The estimated pH value in endo-lysosomes/lysosomes is thought to be below 5 suggesting that FCV may remain in the endosome until the pH is sufficiently reduced before delivering the viral genome into the cytoplasm of the host cell. FCV has been shown to have the ability to permeabilise cells and so the genome delivery mechanism may involve the formation of a pore in the endosomal membrane although this requires further investigation (Stuart and Brown, 2006). We hypothesise that binding of FCV to fJAM-A destabilises the capsid and induces the conformational change described here and previously (Bhella et al., 2008; Bhella and Goodfellow, 2011). This conformational change likely primes the capsid for genome uncoating/delivery upon lowering of the endosomal pH.

The mechanism of FCV genome delivery from endosomes into the cytoplasm of cells is not yet known although 3 models are generally proposed for non-enveloped, RNA viruses that enter via endocytosis. One model is that the viral genome is released into the endosome and is then transported into the cytoplasm either across the membrane or via membrane disruption. Another model involves the insertion of viral peptides into the endosomal membrane resulting in its disruption and release of the intact viral particle into the cytoplasm where the genome is released from the capsid. Rhinovirus-14 (HRV-14) has been shown to undergo receptor mediated structural changes and cause

disruption of endosomal membranes (Schober et al., 1998). A third entry model involves viral peptides forming pores in the endosomal membrane allowing passage of the viral genome into the cytoplasm. Poliovirus (PV) appears to promote the translocation of the viral genome across the endosomal membrane through a virally encoded pore/channel (Groppelli et al., 2017). An increase in empty viral particles upon lowering of the pH has been reported for slow bee paralysis virus (SBPV) as well as rotation of the capsid proteins resulting in the formation of a pore at the 3-fold axis of the capsid (Kalynych et al., 2017). FCV has previously been shown to permeabilise membranes (Stuart and Brown, 2006). This, together with our findings may suggest the uncoating of the virus-receptor complex upon lowering of the pH and simultaneous permeabilisation of the endosomal membrane to allow delivery of the viral genome into the cytoplasm. It is also possible that FCV may form a pore in the endosomal membrane to allow delivery of the viral genome although no mechanism/potential viral protein has been proposed for this so more investigation into the genome delivery mechanism is needed.

As previous studies of the virus receptor complex involved the saturation of FCV with fJAM-A (something unlikely to occur in natural infections) we set out to determine the minimum amount of fJAM-A required to cause the conformational change observed as well as the uncoating at low pH. Electron microscopy (negative staining and cryo-EM) was adopted alongside an RNA release assay where FCV was incubated with varying ratios of FCV VP1 capsid proteins to Fc-fJAM-A proteins. To allow the indirect evaluation of capsid destabilisation, samples were incubated at pH3 (alongside pH7 controls) in order to force the virus to uncoat if enough fJAM-A was present. This method suggested a VP1 to Fc-fJAM-A ratio of between 9:1 and 13:1. Negative staining electron microscopy then confirmed the uncoating of the virus-receptor complex upon incubation with a 9:1 and 10:1 ratio of VP1 to Fc-fJAM-A. Interestingly, upon incubation of FCV with a Fc-fJAM-A ratio of 11:1, irregular particles were observed suggesting that they were in the process of uncoating. No uncoating was seen with any lower ratios of VP1 to Fc-fJAM-A. An 11:1 ratio of VP1 to Fc-fJAM-A corresponds to 16 Fc-fJAM-A proteins per virus particle. It is possible that FCV would bind to some receptor proteins at the cell surface with the membrane curvature induced upon the induction of endocytosis resulting in more fJAM-A binding to FCV within

the endosome. This would trigger the destabilisation of the virus particle inducing the conformational change and priming the capsid for uncoating/genome delivery at low pH.

To conclude, here we show that the fJAM-A ectodomain forms dimers in solution although it appears to bind to the VP1 capsomeres of FCV in a monomeric form (in a head to tail arrangement). The FCV binding site on fJAM-A is distinct from the dimerisation site although the binding affinities between these proteins may play a role in dimer disruption. The deglycosylation of fJAM-A produced in CHO cells does not appear to affect its oligomerisation state or the binding and neutralisation of FCV.

We, therefore, present an entry model for FCV (illustrated in Figure 48) where the virus binds to sialic acid (or a glycoprotein containing sialic acid) on the surface of cells resulting in the delivery of the virus to tight junctions where it can encounter fJAM-A. Upon the induction of endocytosis, brought about by the disruption of receptor homodimers, FCV may bind approximately 16 fJAM-A proteins resulting in priming of the capsid. Upon lowering of the pH within the endosome, the virus either uncoats and disrupts the endosomal membrane or forms a pore in order to deliver the viral genome into the cytoplasm. Further investigation is required to test these hypotheses and provide a detailed mechanistic view of calicivirus entry.

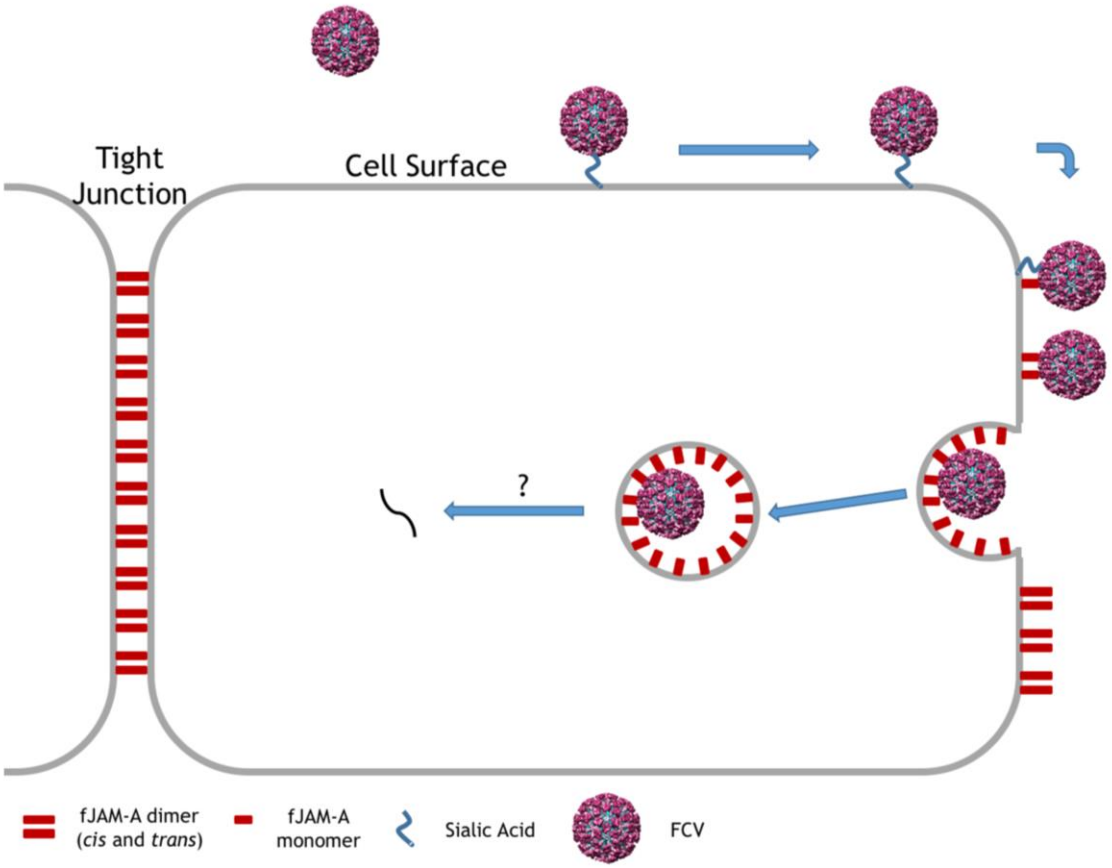

Figure 48- Schematic of FCV entry

An illustrative representation of our model for FCV entry involving the binding of FCV to sialic acid (blue) at the cell surface which is then transported to tight junctions where it can engage with fJAM-A (red), causing disruption of the *cis* and *trans* fJAM-A dimers. Clathrin mediated endocytosis is then triggered which may result in more fJAM-A binding to FCV, causing a conformational change in the capsid and, upon lowering of the luminal pH, release of the viral genome into the cytoplasm of the cell by an as yet unknown mechanism, possibly involving pore formation.

List of References

Abente, E.J., S.V. Sosnovtsev, C. Sandoval-Jaime, G.I. Parra, K. Bok, and K.Y. Green. 2013. The feline calicivirus leader of the capsid protein is associated with cytopathic effect. *J Virol*. 87:3003-3017.

Adams, P.D., P.V. Afonine, G. Bunkoczi, V.B. Chen, I.W. Davis, N. Echols, J.J. Headd, L.W. Hung, G.J. Kapral, R.W. Grosse-Kunstleve, A.J. McCoy, N.W. Moriarty, R. Oeffner, R.J. Read, D.C. Richardson, J.S. Richardson, T.C. Terwilliger, and P.H. Zwart. 2010. PHENIX: a comprehensive Python-based system for macromolecular structure solution. *Acta Crystallogr D Biol Crystallogr*. 66:213-221.

Adrian, M., J. Dubochet, J. Lepault, and A.W. McDowall. 1984. Cryo-electron microscopy of viruses. *Nature*. 308:32-36.

Arnold, K., L. Bordoli, J. Kopp, and T. Schwede. 2006. The SWISS-MODEL workspace: a web-based environment for protein structure homology modelling. *Bioinformatics*. 22:195-201.

Bailey, D., W.J. Kaiser, M. Hollinshead, K. Moffat, Y. Chaudhry, T. Wileman, S.V. Sosnovtsev, and I.G. Goodfellow. 2010. Feline calicivirus p32, p39 and p30 proteins localize to the endoplasmic reticulum to initiate replication complex formation. *J Gen Virol*. 91:739-749.

Baker, T.S., and R.H. Cheng. 1996. A model-based approach for determining orientations of biological macromolecules imaged by cryoelectron microscopy. *J Struct Biol*. 116:120-130.

Bauer, H., J. Zweimueller-Mayer, P. Steinbacher, A. Lametschwandtner, and H.C. Bauer. 2010. The dual role of zonula occludens (ZO) proteins. *J Biomed Biotechnol*. 2010:402593.

Bergelson, J.M. 2009. Intercellular junctional proteins as receptors and barriers to virus infection and spread. *Cell Host Microbe*. 5:517-521.

Bergelson, J.M., J.G. Mohanty, R.L. Crowell, N.F. St John, D.M. Lublin, and R.W. Finberg. 1995. Coxsackievirus B3 adapted to growth in RD cells binds to decay-accelerating factor (CD55). *J Virol*. 69:1903-1906.

Bhella, D. 2015. The role of cellular adhesion molecules in virus attachment and entry. *Philos Trans R Soc Lond B Biol Sci*. 370:20140035.

Bhella, D., D. Gatherer, Y. Chaudhry, R. Pink, and I.G. Goodfellow. 2008. Structural insights into calicivirus attachment and uncoating. *J Virol*. 82:8051-8058.

Bhella, D., and I.G. Goodfellow. 2011. The cryo-electron microscopy structure of feline calicivirus bound to junctional adhesion molecule A at 9-angstrom resolution reveals receptor-induced flexibility and two distinct conformational changes in the capsid protein VP1. *J Virol*. 85:11381-11390.

Booth, D.S., A. Avila-Sakar, and Y. Cheng. 2011. Visualizing proteins and macromolecular complexes by negative stain EM: from grid preparation to image acquisition. *J Vis Exp*.

Brenner, S., and R.W. Horne. 1959. A negative staining method for high resolution electron microscopy of viruses. *Biochim Biophys Acta*. 34:103-110.

Bubeck, D., D.J. Filman, and J.M. Hogle. 2005. Cryo-electron microscopy reconstruction of a poliovirus-receptor-membrane complex. *Nat Struct Mol Biol*. 12:615-618.

Cancio-Lonches, C., M. Yocupicio-Monroy, C. Sandoval-Jaime, I. Galvan-Mendoza, L. Urena, S. Vashist, I. Goodfellow, J. Salas-Benito, and A.L. Gutierrez-Escolano. 2011. Nucleolin interacts with the feline calicivirus 3' untranslated region and the protease-polymerase NS6 and NS7 proteins, playing a role in virus replication. *J Virol*. 85:8056-8068.

Caspar, D.L. 1956. Structure of bushy stunt virus. *Nature*. 177:475-476.

Caspar, D.L., and A. Klug. 1962. Physical principles in the construction of regular viruses. *Cold Spring Harb Symp Quant Biol*. 27:1-24.

Chiba, H., M. Osanai, M. Murata, T. Kojima, and N. Sawada. 2008. Transmembrane proteins of tight junctions. *Biochim Biophys Acta*. 1778:588-600.

Clarke, I.N., and P.R. Lambden. 1997. The molecular biology of caliciviruses. *J Gen Virol*. 78 (Pt 2):291-301.

Conley, M., E. Emmott, R. Orton, D. Taylor, D.G. Carneiro, K. Murata, I.G. Goodfellow, G.S. Hansman, and D. Bhella. 2017. Vesivirus 2117 capsids more closely resemble sapovirus and lagovirus particles than other known vesivirus structures. *J Gen Virol*. 98:68-76.

Cossart, P., and A. Helenius. 2014. Endocytosis of viruses and bacteria. *Cold Spring Harb Perspect Biol*. 6.

Coyne, C.B., and J.M. Bergelson. 2005. CAR: a virus receptor within the tight junction. *Adv Drug Deliv Rev*. 57:869-882.

Coyne, C.B., and J.M. Bergelson. 2006. Virus-induced Abl and Fyn kinase signals permit coxsackievirus entry through epithelial tight junctions. *Cell*. 124:119-131.

Coyne, K.P., F.C. Reed, C.J. Porter, S. Dawson, R.M. Gaskell, and A.D. Radford. 2006. Recombination of Feline calicivirus within an endemically infected cat colony. *J Gen Virol*. 87:921-926.

Crick, F.H., and J.D. Watson. 1956. Structure of small viruses. *Nature*. 177:473-475.

Devadas, D., T. Koithan, R. Diestel, U. Prank, B. Sodeik, and K. Dohner. 2014. Herpes simplex virus internalization into epithelial cells requires Na+/H+ exchangers and p21-activated kinases but neither clathrin- nor caveolin-mediated endocytosis. *J Virol*. 88:13378-13395.

Di Martino, B., and F. Marsilio. 2010. Feline calicivirus VP2 is involved in the self-assembly of the capsid protein into virus-like particles. *Res Vet Sci*. 89:279-281.

Dubochet, J., M. Adrian, J.J. Chang, J.C. Homo, J. Lepault, A.W. McDowall, and P. Schultz. 1988. Cryo-electron microscopy of vitrified specimens. *Q Rev Biophys*. 21:129-228.

Ebnet, K., A. Suzuki, S. Ohno, and D. Vestweber. 2004. Junctional adhesion molecules (JAMs): more molecules with dual functions? *J Cell Sci*. 117:19-29.

Emsley, P., and K. Cowtan. 2004. Coot: model-building tools for molecular graphics. *Acta Crystallogr D Biol Crystallogr*. 60:2126-2132.

Fernandez, J.J., D. Luque, J.R. Caston, and J.L. Carrascosa. 2008. Sharpening high resolution information in single particle electron cryomicroscopy. *J Struct Biol*. 164:170-175.

Franke, D., and D.I. Svergun. 2009. DAMMIF, a program for rapid ab-initio shape determination in small-angle scattering. *J Appl Crystallogr*. 42:342-346.

Franklin, R.E., and A. Klug. 1956. The Nature of the Helical Groove on the Tobacco Mosaic Virus Particle - X-Ray Diffraction Studies. *Biochimica Et Biophysica Acta*. 19:403-416.

Freire, E., O.L. Mayorga, and M. Straume. 1990. Isothermal Titration Calorimetry. *Anal Chem*. 62:A950-A959.

Gonzalez-Mariscal, L., A. Dominguez-Calderon, A. Raya-Sandino, J.M. Ortega-Olvera, O. Vargas-Sierra, and G. Martinez-Revollar. 2014. Tight junctions and the regulation of gene expression. *Semin Cell Dev Biol*. 36:213-223.

Gonzalez-Mariscal, L., R. Tapia, and D. Chamorro. 2008. Crosstalk of tight junction components with signaling pathways. *Biochim Biophys Acta*. 1778:729-756.

Goodfellow, I.G., D.J. Evans, A.M. Blom, D. Kerrigan, J.S. Miners, B.P. Morgan, and O.B. Spiller. 2005. Inhibition of coxsackie B virus infection by soluble forms of its receptors: binding affinities, altered particle formation, and competition with cellular receptors. *J Virol*. 79:12016-12024.

Grassucci, R.A., D.J. Taylor, and J. Frank. 2007. Preparation of macromolecular complexes for cryo-electron microscopy. *Nat Protoc*. 2:3239-3246.

Green, K.Y., T. Ando, M.S. Balayan, T. Berke, I.N. Clarke, M.K. Estes, D.O. Matson, S. Nakata, J.D. Neill, M.J. Studdert, and H.J. Thiel. 2000. Taxonomy of the caliciviruses. *J Infect Dis*. 181 Suppl 2:S322-330.

Green, K.Y., A. Mory, M.H. Fogg, A. Weisberg, G. Belliot, M. Wagner, T. Mitra, E. Ehrenfeld, C.E. Cameron, and S.V. Sosnovtsev. 2002. Isolation of Enzymatically Active Replication Complexes from Feline Calicivirus-Infected Cells. *Journal of Virology*. 76:8582-8595.

Groppelli, E., H.C. Levy, E. Sun, M. Strauss, C. Nicol, S. Gold, X. Zhuang, T.J. Tuthill, J.M. Hogle, and D.J. Rowlands. 2017. Picornavirus RNA is protected from cleavage by ribonuclease during virion uncoating and transfer across cellular and model membranes. *PLoS Pathog*. 13:e1006197.

Guglielmi, K.M., E. Kirchner, G.H. Holm, T. Stehle, and T.S. Dermody. 2007. Reovirus binding determinants in junctional adhesion molecule-A. *J Biol Chem*. 282:17930-17940.

Helenius, A. 2013. Virus entry: what has pH got to do with it? *Nat Cell Biol*. 15:125.

Herbert, T.P., I. Brierley, and T.D. Brown. 1997. Identification of a protein linked to the genomic and subgenomic mRNAs of feline calicivirus and its role in translation. *J Gen Virol*. 78 (Pt 5):1033-1040.

Heymann, J.B. 2001. Bsoft: image and molecular processing in electron microscopy. *J Struct Biol*. 133:156-169.

Ho, K.L., C.L. Kueh, P.L. Beh, W.S. Tan, and D. Bhella. 2017. Cryo-Electron Microscopy Structure of the Macrobrachium rosenbergii Nodavirus Capsid at 7 Angstroms Resolution. *Sci Rep*. 7:2083.

Hossler, P., S.F. Khattak, and Z.J. Li. 2009. Optimal and consistent protein glycosylation in mammalian cell culture. *Glycobiology*. 19:936-949.

Humoud, M.N., N. Doyle, E. Royall, M.M. Willcocks, F. Sorgeloos, F. van Kuppeveld, L.O. Roberts, I.G. Goodfellow, M.A. Langereis, and N. Locker. 2016. Feline Calicivirus Infection Disrupts Assembly of Cytoplasmic Stress Granules and Induces G3BP1 Cleavage. *J Virol*. 90:6489-6501.

Huotari, J., and A. Helenius. 2011. Endosome maturation. *EMBO J*. 30:3481-3500.

Kaiser, W.J., Y. Chaudhry, S.V. Sosnovtsev, and I.G. Goodfellow. 2006. Analysis of protein-protein interactions in the feline calicivirus replication complex. *J Gen Virol*. 87:363-368.

Kalynych, S., T. Fuzik, A. Pridal, J. de Miranda, and P. Plevka. 2017. Cryo-EM study of slow bee paralysis virus at low pH reveals iflavirus genome release mechanism. *Proc Natl Acad Sci U S A*. 114:598-603.

Karakasiliotis, I., Y. Chaudhry, L.O. Roberts, and I.G. Goodfellow. 2006. Feline calicivirus replication: requirement for polypyrimidine tract-binding protein is temperature-dependent. *J Gen Virol*. 87:3339-3347.

Karakasiliotis, I., S. Vashist, D. Bailey, E.J. Abente, K.Y. Green, L.O. Roberts, S.V. Sosnovtsev, and I.G. Goodfellow. 2010. Polypyrimidine tract binding protein functions as a negative regulator of feline calicivirus translation. *PLoS One*. 5:e9562.

Kirchner, E., K.M. Guglielmi, H.M. Strauss, T.S. Dermody, and T. Stehle. 2008. Structure of reovirus sigma1 in complex with its receptor junctional adhesion molecule-A. *PLoS Pathog*. 4:e1000235.

Klug, A., J.T. Finch, and R.E. Franklin. 1957. The structure of turnip yellow mosaic virus; x-ray diffraction studies. *Biochim Biophys Acta*. 25:242-252.

Kostrewa, D., M. Brockhaus, A. D'Arcy, G.E. Dale, P. Nelboeck, G. Schmid, F. Mueller, G. Bazzoni, E. Dejana, T. Bartfai, F.K. Winkler, and M. Hennig. 2001. X-ray structure of junctional adhesion molecule: structural basis for homophilic adhesion via a novel dimerization motif. *EMBO J*. 20:4391-4398.

Kreutz, L.C., and B.S. Seal. 1995. The pathway of feline calicivirus entry. *Virus Res*. 35:63-70.

Kreutz, L.C., B.S. Seal, and W.L. Mengeling. 1994. Early interaction of feline calicivirus with cells in culture. *Arch Virol*. 136:19-34.

Kruger, D.H., P. Schneck, and H.R. Gelderblom. 2000. Helmut Ruska and the visualisation of viruses. *Lancet*. 355:1713-1717.

Kuyumcu-Martinez, M., G. Belliot, S.V. Sosnovtsev, K.O. Chang, K.Y. Green, and R.E. Lloyd. 2004. Calicivirus 3C-like proteinase inhibits cellular translation by cleavage of poly(A)-binding protein. *J Virol*. 78:8172-8182.

Leavitt, S., and E. Freire. 2001. Direct measurement of protein binding energetics by isothermal titration calorimetry. *Curr Opin Struct Biol*. 11:560-566.

Lee, E.U., J. Roth, and J.C. Paulson. 1989. Alteration of terminal glycosylation sequences on N-linked oligosaccharides of Chinese hamster ovary cells by expression of beta-galactoside alpha 2,6-sialyltransferase. *J Biol Chem*. 264:13848-13855.

Love, D.N., and M. Sabine. 1975. Electron microscopic observation of feline kidney cells infected with a feline calicivirus. *Arch Virol*. 48:213-228.

Lozach, P.Y., J. Huotari, and A. Helenius. 2011. Late-penetrating viruses. *Curr Opin Virol*. 1:35-43.

Makino, A., M. Shimojima, T. Miyazawa, K. Kato, Y. Tohya, and H. Akashi. 2006. Junctional adhesion molecule 1 is a functional receptor for feline calicivirus. *J Virol*. 80:4482-4490.

Malaby, A.W., S. Chakravarthy, T.C. Irving, S.V. Kathuria, O. Bilsel, and D.G. Lambright. 2015. Methods for analysis of size-exclusion chromatography-small-angle X-ray scattering and reconstruction of protein scattering. *J Appl Crystallogr*. 48:1102-1113.

Mandell, K.J., I.C. McCall, and C.A. Parkos. 2004. Involvement of the junctional adhesion molecule-1 (JAM1) homodimer interface in regulation of epithelial barrier function. *J Biol Chem*. 279:16254-16262.

Marsh, M., and A. Helenius. 2006. Virus entry: open sesame. *Cell*. 124:729-740.

Mathew, E., A. Mirza, and N. Menhart. 2004. Liquid-chromatography-coupled SAXS for accurate sizing of aggregating proteins. *J Synchrotron Radiat*. 11:314-318.

McMullan, G., A.R. Faruqi, D. Clare, and R. Henderson. 2014. Comparison of optimal performance at 300keV of three direct electron detectors for use in low dose electron microscopy. *Ultramicroscopy*. 147:156-163.

Monteiro, A.C., A.C. Luissint, R. Sumagin, C. Lai, F. Vielmuth, M.F. Wolf, O. Laur, K. Reiss, V. Spindler, T. Stehle, T.S. Dermody, A. Nusrat, and C.A. Parkos. 2014. Trans-dimerization of JAM-A regulates Rap2 and is mediated by a domain that is distinct from the cis-dimerization interface. *Mol Biol Cell*. 25:1574-1585.

Monteiro, A.C., and C.A. Parkos. 2012. Intracellular mediators of JAM-A-dependent epithelial barrier function. *Ann N Y Acad Sci*. 1257:115-124.

Namba, K., and G. Stubbs. 1986. Structure of tobacco mosaic virus at 3.6 A resolution: implications for assembly. *Science*. 231:1401-1406.

Natoni, A., G.E. Kass, M.J. Carter, and L.O. Roberts. 2006. The mitochondrial pathway of apoptosis is triggered during feline calicivirus infection. *J Gen Virol*. 87:357-361.

Nava, P., C.T. Capaldo, S. Koch, K. Kolegraff, C.R. Rankin, A.E. Farkas, M.E. Feasel, L. Li, C. Addis, C.A. Parkos, and A. Nusrat. 2011. JAM-A regulates epithelial proliferation through Akt/beta-catenin signalling. *EMBO Rep*. 12:314-320.

Nogales, E., and S.H. Scheres. 2015. Cryo-EM: A Unique Tool for the Visualization of Macromolecular Complexity. *Mol Cell*. 58:677-689.

Orlova, E.V., and H.R. Saibil. 2011. Structural analysis of macromolecular assemblies by electron microscopy. *Chem Rev*. 111:7710-7748.

Ossiboff, R.J., and J.S. Parker. 2007. Identification of regions and residues in feline junctional adhesion molecule required for feline calicivirus binding and infection. *J Virol*. 81:13608-13621.

Ossiboff, R.J., Y. Zhou, P.J. Lightfoot, B.V. Prasad, and J.S. Parker. 2010. Conformational changes in the capsid of a calicivirus upon interaction with its functional receptor. *J Virol*. 84:5550-5564.

Paris, L., L. Tonutti, C. Vannini, and G. Bazzoni. 2008. Structural organization of the tight junctions. *Biochim Biophys Acta*. 1778:646-659.

Pelkmans, L. 2005. Secrets of caveolae- and lipid raft-mediated endocytosis revealed by mammalian viruses. *Biochim Biophys Acta*. 1746:295-304.

Pesavento, P.A., K.O. Chang, and J.S. Parker. 2008. Molecular virology of feline calicivirus. *Vet Clin North Am Small Anim Pract*. 38:775-786, vii.

Pesavento, P.A., T. Stokol, H. Liu, D.A. van der List, P.M. Gaffney, and J.S. Parker. 2011. Distribution of the feline calicivirus receptor junctional adhesion molecule a in feline tissues. *Vet Pathol*. 48:361-368.

Pettersen, E.F., T.D. Goddard, C.C. Huang, G.S. Couch, D.M. Greenblatt, E.C. Meng, and T.E. Ferrin. 2004. UCSF Chimera--a visualization system for exploratory research and analysis. *J Comput Chem*. 25:1605-1612.

Prasad, B.V., and M.F. Schmid. 2012. Principles of virus structural organization. *Adv Exp Med Biol*. 726:17-47.

Prota, A.E., J.A. Campbell, P. Schelling, J.C. Forrest, M.J. Watson, T.R. Peters, M. Aurrand-Lions, B.A. Imhof, T.S. Dermody, and T. Stehle. 2003. Crystal structure of human junctional adhesion molecule 1: implications for reovirus binding. *Proc Natl Acad Sci U S A*. 100:5366-5371.

Radford, A.D., K.P. Coyne, S. Dawson, C.J. Porter, and R.M. Gaskell. 2007. Feline calicivirus. *Vet Res*. 38:319-335.

Raghavan, M., and P.J. Bjorkman. 1995. BIAcore: a microchip-based system for analyzing the formation of macromolecular complexes. *Structure*. 3:331-333.

Reglero-Real, N., B. Colom, J.V. Bodkin, and S. Nourshargh. 2016. Endothelial Cell Junctional Adhesion Molecules: Role and Regulation of Expression in Inflammation. *Arterioscler Thromb Vasc Biol*. 36:2048-2057.

Rossmann, M.G., E. Arnold, J.W. Erickson, E.A. Frankenberger, J.P. Griffith, H.J. Hecht, J.E. Johnson, G. Kamer, M. Luo, G. Vriend, A.G. Mosser, A.C. Palmenberg, R.R. Rueckert, and B. Sherry. 1986. The Structure of a Human Common Cold Virus (Rhinovirus 14) and Its Evolutionary Relations to Other Viruses. *Chem Scripta*. 26b:313-323.

Roth, Z., G. Yehezkel, and I. Khalaila. 2012. Identification and Quantification of Protein Glycosylation. *International Journal of Carbohydrate Chemistry*. 2012:1-10.

Rybicki, E., and R. Kightley. 2015. A Short History of the Discovery of Viruses.

Salinas, S., C. Zussy, F. Loustalot, D. Henaff, G. Menendez, P.E. Morton, M. Parsons, G. Schiavo, and E.J. Kremer. 2014. Disruption of the coxsackievirus and adenovirus receptor-homodimeric interaction triggers lipid microdomain- and dynamin-dependent endocytosis and lysosomal targeting. *J Biol Chem*. 289:680-695.

Scheres, S.H. 2010. Classification of structural heterogeneity by maximum-likelihood methods. *Methods Enzymol*. 482:295-320.

Scheres, S.H. 2012. RELION: implementation of a Bayesian approach to cryo-EM structure determination. *J Struct Biol*. 180:519-530.

Scheres, S.H. 2015. Semi-automated selection of cryo-EM particles in RELION-1.3. *J Struct Biol*. 189:114-122.

Scheres, S.H., and S. Chen. 2012. Prevention of overfitting in cryo-EM structure determination. *Nat Methods*. 9:853-854.

Schober, D., P. Kronenberger, E. Prchla, D. Blaas, and R. Fuchs. 1998. Major and minor receptor group human rhinoviruses penetrate from endosomes by different mechanisms. *J Virol*. 72:1354-1364.

Schwarz, F., and M. Aebi. 2011. Mechanisms and principles of N-linked protein glycosylation. *Curr Opin Struct Biol*. 21:576-582.

Scott, D.W., C.E. Tolbert, D.M. Graham, E. Wittchen, J.E. Bear, and K. Burridge. 2015. N-glycosylation controls the function of junctional adhesion molecule-A. *Mol Biol Cell*. 26:3205-3214.

Severson, E.A., and C.A. Parkos. 2009. Structural determinants of Junctional Adhesion Molecule A (JAM-A) function and mechanisms of intracellular signaling. *Curr Opin Cell Biol*. 21:701-707.

Snyers, L., H. Zwickl, and D. Blaas. 2003. Human rhinovirus type 2 is internalized by clathrin-mediated endocytosis. *J Virol*. 77:5360-5369.

Sosnovtsev, S., and K.Y. Green. 1995. RNA transcripts derived from a cloned full-length copy of the feline calicivirus genome do not require VpG for infectivity. *Virology*. 210:383-390.

Sosnovtsev, S.V., G. Belliot, K.O. Chang, O. Onwudiwe, and K.Y. Green. 2005. Feline calicivirus VP2 is essential for the production of infectious virions. *J Virol*. 79:4012-4024.

Sosnovtsev, S.V., and K.Y. Green. 2000. Identification and genomic mapping of the ORF3 and VPg proteins in feline calicivirus virions. *Virology*. 277:193-203.

Sosnovtsev, S.V., E.A. Prikhod'ko, G. Belliot, J.I. Cohen, and K.Y. Green. 2003. Feline calicivirus replication induces apoptosis in cultured cells. *Virus Res*. 94:1-10.

Sosnovtsev, S.V., C. Sandoval-Jaime, G.I. Parra, C.M. Tin, R.W. Jones, J. Soden, D. Barnes, J. Freeth, A.W. Smith, and K.Y. Green. 2017. Identification of

Human Junctional Adhesion Molecule 1 as a Functional Receptor for the Hom-1 Calicivirus on Human Cells. *MBio*. 8.

Sosnovtsev, S.V., S.A. Sosnovtseva, and K.Y. Green. 1998. Cleavage of the feline calicivirus capsid precursor is mediated by a virus-encoded proteinase. *J Virol*. 72:3051-3059.

Sosnovtseva, S.A., S.V. Sosnovtsev, and K.Y. Green. 1999. Mapping of the feline calicivirus proteinase responsible for autocatalytic processing of the nonstructural polyprotein and identification of a stable proteinase-polymerase precursor protein. *J Virol*. 73:6626-6633.

Stuart, A.D., and T.D. Brown. 2006. Entry of feline calicivirus is dependent on clathrin-mediated endocytosis and acidification in endosomes. *J Virol*. 80:7500-7509.

Stuart, A.D., and T.D. Brown. 2007. Alpha2,6-linked sialic acid acts as a receptor for Feline calicivirus. *J Gen Virol*. 88:177-186.

Studdert, M.J., and J.D. O'Shea. 1975. Ultrastructural studies of the development of feline calicivirus in a feline embryo cell line. *Arch Virol*. 48:317-325.

Thiel, H.J., and M. Konig. 1999. Caliciviruses: an overview. *Vet Microbiol*. 69:55-62.

van Raaij, M.J., E. Chouin, H. van der Zandt, J.M. Bergelson, and S. Cusack. 2000. Dimeric structure of the coxsackievirus and adenovirus receptor D1 domain at 1.7 A resolution. *Structure*. 8:1147-1155.

Wei, L., J.S. Huhn, A. Mory, H.B. Pathak, S.V. Sosnovtsev, K.Y. Green, and C.E. Cameron. 2001. Proteinase-polymerase precursor as the active form of feline calicivirus RNA-dependent RNA polymerase. *J Virol*. 75:1211-1219.

Willcocks, M.M., M.J. Carter, and L.O. Roberts. 2004. Cleavage of eukaryotic initiation factor eIF4G and inhibition of host-cell protein synthesis during feline calicivirus infection. *J Gen Virol*. 85:1125-1130.

Xu, C., and D.T. Ng. 2015. Glycosylation-directed quality control of protein folding. *Nat Rev Mol Cell Biol*. 16:742-752.

Yumiketa, Y., T. Narita, Y. Inoue, G. Sato, W. Kamitani, T. Oka, K. Katayama, T. Sakaguchi, and Y. Tohya. 2016. Nonstructural protein p39 of feline calicivirus suppresses host innate immune response by preventing IRF-3 activation. *Vet Microbiol*. 185:62-67.

Appendices

JOURNAL OF GENERAL VIROLOGY

RESEARCH ARTICLE
Conley *et al.*, *Journal of General Virology* 2017;98:68–76
DOI 10.1099/jgv.0.000658

MICROBIOLOGY SOCIETY
OPEN MICROBIOLOGY

Vesivirus 2117 capsids more closely resemble sapovirus and lagovirus particles than other known vesivirus structures

Michaela Conley,[1] Edward Emmott,[2] Richard Orton,[1] David Taylor,[3]† Daniel G. Carneiro,[1]‡ Kazuyoshi Murata,[3] Ian G. Goodfellow,[2] Grant S. Hansman[3]§ and David Bhella[1,*]

Abstract

Vesivirus 2117 is an adventitious agent that, in 2009, was identified as a contaminant of Chinese hamster ovary cells propagated in bioreactors at a pharmaceutical manufacturing plant belonging to Genzyme. The consequent interruption in supply of Fabrazyme and Cerezyme (drugs used to treat Fabry and Gaucher diseases, respectively) caused significant economic losses. Vesivirus 2117 is a member of the *Caliciviridae*, a family of small icosahedral viruses encoding a positive-sense RNA genome. We have used cryo-electron microscopy and three-dimensional image reconstruction to calculate a structure of vesivirus 2117 virus-like particles as well as feline calicivirus and a chimeric sapovirus. We present a structural comparison of several members of the *Caliciviridae*, showing that the distal P domain of vesivirus 2117 is morphologically distinct from that seen in other known vesivirus structures. Furthermore, at intermediate resolutions, we found a high level of structural similarity between vesivirus 2117 and *Caliciviridae* from other genera: sapovirus and rabbit hemorrhagic disease virus. Phylogenetic analysis confirms vesivirus 2117 as a vesivirus closely related to canine vesiviruses. We postulate that morphological differences in virion structure seen between vesivirus clades may reflect differences in receptor usage.

INTRODUCTION

Caliciviruses are non-enveloped icosahedral viruses that have single-stranded, positive-sense RNA genomes. The *Caliciviridae* are divided into five genera, namely, *Norovirus*, *Sapovirus*, *Vesivirus*, *Lagovirus* and *Nebovirus*. The representative viruses of these genera are Norwalk virus (NoV), sapporovirus (SV), feline calicivirus (FCV), rabbit hemorrhagic disease virus (RHDV) and Newbury-1 virus, respectively. The noroviruses and sapoviruses cause gastroenteritis in humans, while neboviruses have been shown to cause gastroenteritis in cattle. Vesiviruses and lagoviruses cause a range of symptoms in different animal species including stomatitis, conjunctivitis, respiratory illness and hemorrhagic disease [1–3].

Calicivirus genomes are around 7.5 kb in length, encode up to four ORFs and are polyadenylated. The first ORF encodes the non-structural proteins and in the lagoviruses and sapoviruses the major capsid protein, VP1. In the genera *Norovirus* and *Vesivirus*, the VP1 protein is encoded by a second ORF and the minor structural protein, VP2, is encoded by ORF3, which is translated following ribosomal termination–reinitiation [4]. The ORF1 polyprotein is post-translationally cleaved by the autocatalytic viral protease to yield several non-structural proteins [5]. The major capsid protein, VP1, is also post-translationally processed, resulting in the removal of the N-terminal 124 amino acids to produce the mature form of the protein (62 kDa) [6]. Murine norovirus (MuNV) is the only member of the *Caliciviridae* that encodes a fourth ORF, the product of which, referred to as

Received 11 July 2016; Accepted 11 November 2016
Author affiliations: [1]Medical Research Council – University of Glasgow Centre for Virus Research, Sir Michael Stoker Building, Garscube Campus, 464 Bearsden Road, Glasgow G61 1QH, UK; [2]Department of Pathology, Division of Virology, University of Cambridge, Addenbrooke's Hospital, Hills Road, Cambridge CB2 2QQ, UK; [3]National Institute for Physiological Sciences (NIPS), 38 Nishigonaka, Myodaiji, Okazaki, Aichi 444-8585, Japan.
***Correspondence:** David Bhella, david.bhella@glasgow.ac.uk
Keywords: calicivirus; capsid; virus structure; cryo-EM.
Abbreviations: 3D, three-dimensional; CHO, Chinese hamster ovary; cryo-EM, cryogenic electron microscopy; EM, electron microscopy; FCV, feline calicivirus; NoV, Norwalk virus; RHDV, rabbit hemorrhagic disease virus; SMSV, San Miguel sea lion virus; SV, sapporovirus; VESV, vesicular exanthema of swine virus; VLP, virus-like particle.
†Present address: Howard Hughes Medical Institute, 742 Stanley Hall, MS 3220 University of California, Berkeley, CA 94720-3220, USA.
‡Present address: School of Immunity and Infection, Institute of Biomedical Research, University of Birmingham, Edgbaston, Birmingham B15 2TT, UK.
§Present address: Centre for Infectious Diseases, Department of Virology, University Hospital Heidelberg, Im Neuenheimer Feld 324, Heidelberg 69120, Germany.
One supplementary figure is available with the online Supplementary Material.

VF1, is involved in the regulation of the innate response to infection [7].

Members of the *Caliciviridae* exhibit a characteristic virion morphology of 32 cup-shaped depressions on their outer surface. The *T*=3 capsid is composed of three quasi-equivalent forms of the VP1 protein, termed A, B and C. These give rise to two classes of dimeric capsomere: A/B and C/C. Ninety dimers/capsomeres assemble to form a 35–40 nm spherical capsid that encloses the viral genome. A/B and C/C capsomeres differ only slightly in their conformations. An atomic model of RHDV shows the A/B capsomeres (described as bent) arranged around the fivefold symmetry axis, while the C/C capsomere, which adopts a flatter conformation, is located at the twofold symmetry axis [8–11]. The VP1 protein has been divided into three domains: the N-terminal arm, the shell domain (S) and the protruding domain (P). The N-terminal arm is hypothesized to be involved in the switch between the A/B and C/C conformations. The S domain contains a β-barrel motif and forms the floor of the viral capsid. Sequences within the S domain have been shown to interact with the viral RNA-dependent RNA polymerase to promote *de novo* RNA synthesis [12]. The P domain is further divided into two subdomains, P1 and P2, with the P2 domain containing the antigenic and receptor-binding sites [13–15].

Recently, vesivirus 2117 was identified as a contaminant of bioreactors containing Chinese hamster ovary (CHO) cells at Genzyme in both their Allston Landing and Geel sites. This led to an interruption in production of Cerezyme and Fabrazyme biopharmaceuticals for the treatment of patients suffering from Gaucher disease and Fabry disease, respectively. Vesivirus 2117 was first described as an adventitious agent from an unknown source following observations of cytopathic changes in CHO cells grown in culture [16]. Electron microscopy (EM) showed the presence of viral particles measuring approximately 40 nm in diameter and exhibiting the typical morphology of caliciviruses. Upon infection of CHO cells with vesivirus 2117, cells become rounded and detach from cell culture plastic within 24 h, which accounts for the loss of cell viability seen at Genzyme. It is thought that the viral contamination at Genzyme was introduced from reagents used in the manufacturing process. It was estimated that approximately 5×10^9 virus particles were present in each millilitre of bioreactor fluid. Subsequently, the bioreactors were closed for decontamination, causing a significant delay in the production of Cerezyme and Fabrazyme, which affected around 8000 patients. Stock analysts estimate that the contamination and interruption in manufacturing may have cost Genzyme in the region of $200–300 million [17].

Adventitious agent testing is mandated for the prevention of contamination by viruses able to replicate in CHO cells and has led to the detection of five incidents in the past 20 years caused by murine minute virus, reovirus, Cache Valley virus, epizootic hemorrhagic disease virus and vesivirus 2117 [18–23]. Currently, three processes are adopted to minimize the risk of introducing contaminants into cell culture: control and testing of raw materials, testing at key stages during manufacturing and the use of virus inactivation techniques. These steps are necessary owing to the extent to which CHO cells in particular are used for the production of therapeutic agents. Although these cells are less permissive to infection than, for example, baby hamster kidney cells, episodes of contamination have been documented. In each case, the source of the contaminants was suspected to be input raw materials. Since 1998, the Food and Drug Administration has made it a regulatory requirement in the production of biopharmaceuticals to demonstrate the lack of adventitious agents [18, 20, 24, 25].

Another calicivirus, SV (the type member of the genus *Sapovirus*), was first identified by EM in 1976 from stool samples of infants presenting with gastroenteritis. Sapovirus strains are classified into five genogroups (GI–GV) based on their capsid protein sequences. Currently, only GIII viruses can be propagated in cell culture; however, members of this genogroup cause porcine infections, while the other genogroups cause gastroenteritis in humans. As is the case for many members of the *Caliciviridae*, expression of a recombinant form of the major capsid protein is sufficient for the assembly of virus-like particles (VLPs), which exhibit the same morphology as virions [26–29].

Here we describe the structures of VLPs formed by recombinant expression of vesivirus 2117 VP1 and a chimeric sapovirus VP1, alongside an improved structure for FCV strain F9, all solved by cryogenic EM (cryo-EM) and three-dimensional (3D) image reconstruction. These data reveal that the vesivirus 2117 capsid structure more closely resembles that of sapoviruses, and surprisingly a lagovirus, than it does other known vesivirus structures. Phylogenetic analysis of capsid protein sequences supports the classification of vesivirus 2117 as a member of the genus *Vesivirus*, although it resides in a clade distinct from FCV and the vesicular exanthema of swine virus (VESV) and San Miguel sea lion virus (SMSV) groups. It has recently been proposed that structural similarities may be used to infer common heritage of diverse virus groups in the absence of genetic similarity [30]. Here we see substantial differences in virion morphology between clades of the genus *Vesivirus* and, albeit at comparatively low resolution, similarities between vesivirus 2117 and structures for both sapoviruses and lagoviruses. The striking differences in P domain morphology within vesiviruses may indicate functional differences, perhaps related to receptor usage and entry mechanisms.

RESULTS

Vesivirus 2117 VLPs are structurally distinct from known vesivirus capsid structures

Vesivirus 2117 VLPs were prepared by baculovirus expression of VP1 in Hi5 insect cells and purified by differential centrifugation. VLP preparations were vitrified by plunge freezing in liquid ethane and imaged in a frozen-hydrated state by cryogenic transmission electron microscopy

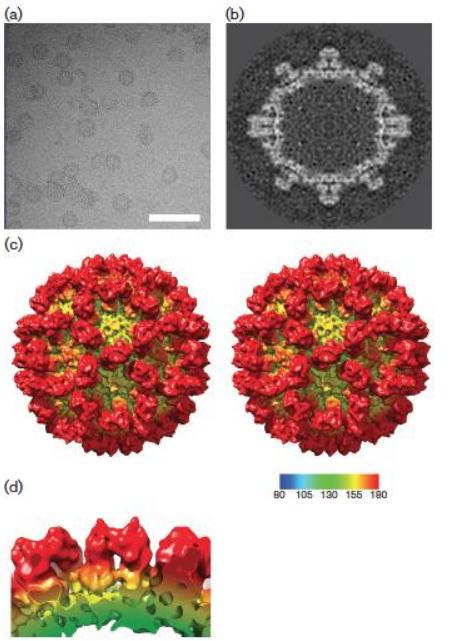

Fig. 1. Cryo-EM structure of vesivirus 2117 at 10 Å resolution. (a) Cryo-electron micrograph of vesivirus 2117 VLPs imaged in a frozen-hydrated state. Bar, 100 nm. (b) A central slice through the 3D reconstruction of vesivirus 2117 shows the compact structure of the P domain. (c) Stereo pair images of the reconstruction, calculated at 10 Å resolution, viewed along the twofold symmetry axis. (d) A side view of the 2117 VP1 dimer viewed parallel to the capsid surface highlights the pronounced horn-shaped structures on the outer faces of the P domains.

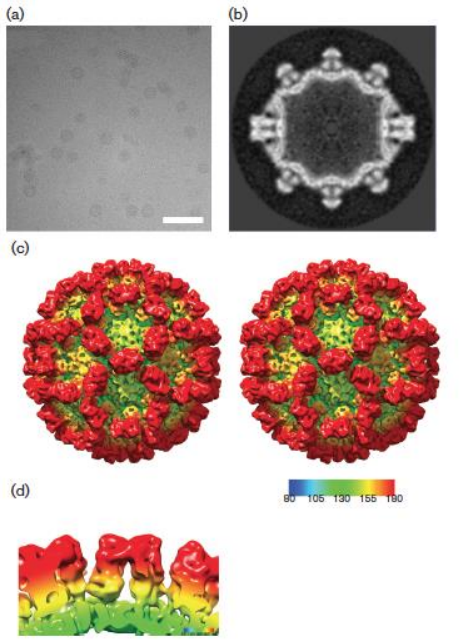

Fig. 2. 3D reconstruction of a chimeric sapovirus VLP. (a) Cryo-electron micrograph of chimeric sapovirus-like particles. Bar, 100 nm. (b) A central slice through the sapovirus VLP structure reveals a compact P domain structure, similar to that seen in 2117. (c) Stereo pair images of the reconstruction calculated at 10 Å resolution, viewed along the two-fold symmetry axis. (d) Side view of the sapovirus VP1 dimer.

(Fig. 1a). Nine hundred and sixty particle images were extracted from 242 micrographs and processed to calculate a 3D icosahedral reconstruction of the VLP at a resolution of 10 Å (Fig. 1b, c). Vesivirus 2117 VLPs were seen to exhibit the characteristic calicivirus morphology: a *T*=3 icosahedral capsid composed of VP1 dimers, giving rise to arch-like capsomeres. The VP1 dimers also appear to form intradimeric interactions between P2 domains and interdimeric interactions between P1 domains, similar to those seen in FCV and as previously described for SMSV [31]. Viewed perpendicular to the capsid floor, a side view of the VP1 dimeric capsomere (Fig. 1d) shows that the outer surface of the P2 domain has pronounced horn-like structures at either end. This is quite distinct from the morphology seen in previously solved vesivirus capsid structures [13, 14, 32]. This morphological divergence from known vesivirus capsid structures led us to hypothesize that 2117 might represent an intermediate between classical vesiviruses and other genera. We therefore set out to compare 2117 VLPs to other calicivirus capsid structures.

Comparison of vesivirus 2117 VLP structure to that of a chimeric sapovirus

We observed that our 2117 structure closely resembled a published low-resolution structure of Parkville virus (a sapovirus) [31]. To draw a comparison between vesivirus 2117 capsids and those of the genus *Sapovirus* at higher resolution, we calculated a 3D structure from images of VLPs produced by a chimeric VP1 construct that has been shown to yield high levels of expression [28]. Briefly, a construct consisting of amino acids 1–289 of the Yokote strain VP1 and amino acids 290–560 of the Mc114 sapovirus strain was used to produce VLPs. The chimera consisted of the N-terminal arm, S domain and P1.1 domain of the Yokote strain and the P2 domain, P1.2 domain and VP2 of the Mc114 strain [28]. These particles were imaged in a frozen-hydrated state (Fig. 2a). A total of 2943 particles were picked

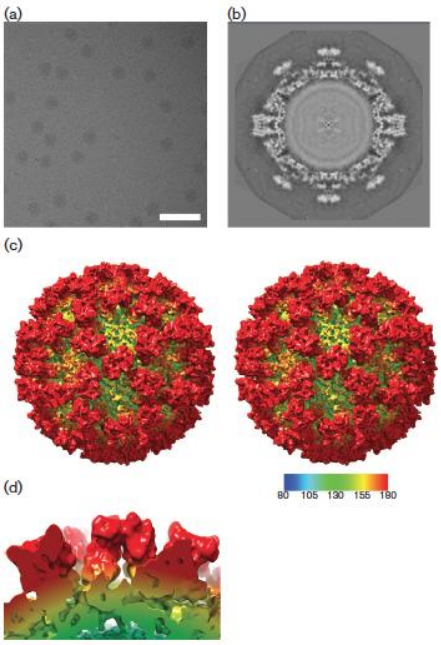

Fig. 3. Structure of FCV. (a) Cryo-microscopy of native FCV virions. Bar, 100 nm. (b) The central section shows a broader P domain structure that presents a flatter outer face. (c) Stereo pair images of the reconstruction, calculated at 7 Å resolution, viewed along the twofold symmetry axis. (d) A side view of a dimeric FCV VP1 capsomere.

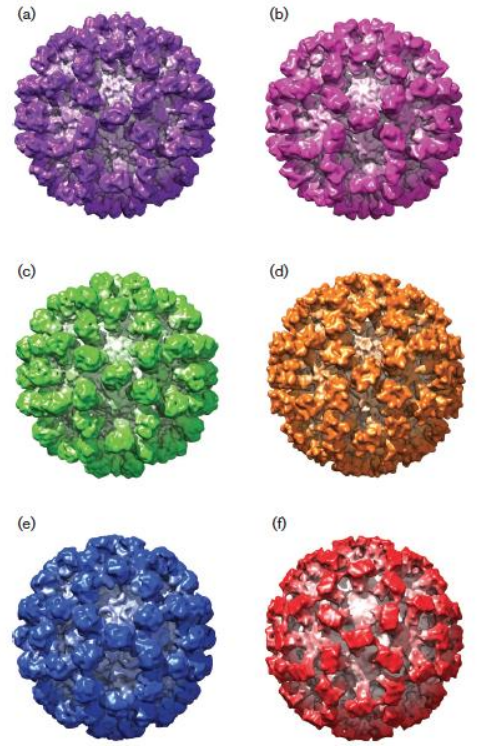

Fig. 4. Side-by-side comparison of (a) vesivirus 2117, (b) a chimeric sapovirus, (c) RHDV, (d) FCV, (e) norovirus GII.10 and (f) NoV at 10 Å resolution, viewed along the twofold symmetry axis.

from 222 micrographs and used to calculate a 3D reconstruction of the chimeric sapovirus VLP at 10 Å resolution (Fig. 2b, c). The sapovirus structure also exhibits typical calicivirus morphology, with notable similarities to that of vesivirus 2117. In particular, the P2 region of the dimeric capsomeres is compact and rounded. The outermost surface of the P2 domain of vesivirus 2117 shows horn-like protrusions at either end, whereas the P2 domains of the sapovirus VLPs appear to have a more curved structure without such large protuberances (Fig. 2d). The S and P1 domains of the two structures appear quite similar at this resolution.

Structure of FCV at 7 Å resolution

We have extended the resolution of our structure for the vesivirus FCV strain F9 to 7 Å resolution using a new dataset. A total of 6965 particles were picked from 241 micrographs (Fig. 3a) and used to calculate the 3D reconstruction shown in Fig. 3(b, c). This structure exhibits striking differences from the vesivirus 2117 and sapovirus structures set out above; the FCV P2 region forms a flattened, rhombus-shaped outer face (Fig. 3c, d). Central sections through each reconstruction (Figs 1b, 2b and 3b) show that this region of the P domain of FCV has a broader conformation than that of either 2117 or sapovirus.

Structural comparison of members of the *Caliciviridae*

Given the clear differences in capsomere morphology between these three structures, we sought to extend our comparison to include a capsid structure from each genus of the *Caliciviridae*. The structures of a lagovirus (RHDV: EMDB 1933; Fig. 4c) and two noroviruses (EMDB 5374 and PDB 1IHM; Fig. 4e, f, respectively) were used to calculate density maps filtered to 10 Å resolution. Likewise, the sapovirus (Fig. 4b) and FCV (Fig. 4d) structures presented above were filtered to 10 Å (the resolution attained for vesivirus 2117; Fig. 4a). Fig. 4 shows a side-by-side comparison of the six 3D structures viewed along the twofold symmetry axis. The similarities (and differences) between the maps are

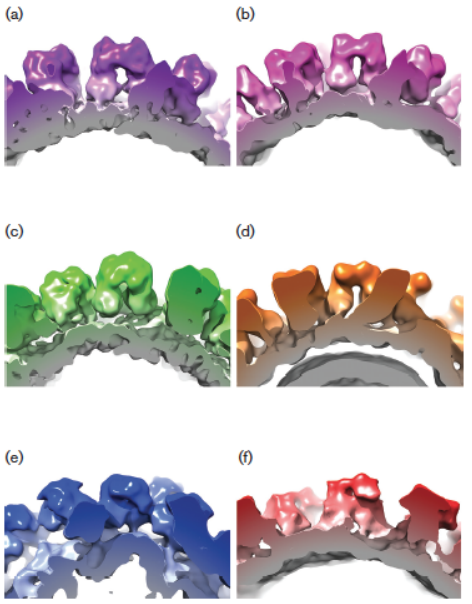

Fig. 5. Side-by-side comparison of the P domains of (a) vesivirus 2117, (b) a chimeric sapovirus, (c) RHDV, (d) FCV, (e) norovirus GII.10 and (f) NoV at 10 Å resolution.

clearly recognized at this resolution. Fig. 5 shows a side-by-side comparison of the P domains of each of the viruses compared in Fig. 4. The P domains of vesivirus 2117, sapovirus and RHDV (Fig. 5a–c, respectively) appear rather similar, showing a compact morphology. The capsomeres of FCV, norovirus GII.10 and NoV (Fig. 5d–f, respectively), however, appear to be quite distinct in conformation; indeed, there are notable differences between the two norovirus structures GII.10 and Norwalk. The P domains of vesivirus 2117, sapovirus and FCV appear to be raised off the S domain, as previously observed for RHDV and MuNV-1, in contrast to the P domains of NoV, which form a more collapsed conformation in relation to the S domain [33, 34].

Table 1. Correlation values calculated by docking structures of several calicivirus capsids into that of vesivirus 2117

A correlation value of 1.0 indicates perfect agreement.

Virus structure fitted into vesivirus 2117	Correlation value
A chimeric sapovirus	0.9214
RHDV	0.9007
FCV (P9)	0.8478
NoV	0.8117
Norovirus GII.10	0.8498

To provide a quantitative index of similarity between the maps under investigation, the maps were brought to a common alignment, resolution and scale. Cross-correlation coefficients between vesivirus 2117 and each of the other five structures were calculated (Table 1). In such analyses, identical maps would give a correlation of 1.0. The structure that produced the highest correlation value when aligned to the vesivirus 2117 structure was the chimeric sapovirus described here, giving a correlation value of 0.9214. This might be expected given the apparent similarities in the maps when visualized by isosurface rendering as in Fig. 4. It is immediately apparent that the sapovirus structure is the most comparable to that of vesivirus 2117, in both the S domains and the P domains of the VP1 proteins. When fitting the structure of RHDV into that of vesivirus 2117, a correlation value of 0.9007 was recorded, signifying a high degree of similarity between the two capsids, again in both the S and P domains of VP1. These results are unexpected given that all three viruses (vesivirus 2117, sapovirus and RHDV) are classified into different genera of the *Caliciviridae*. When the structure of FCV is fitted into the vesivirus 2117 structure, the correlation value obtained is comparatively low at 0.8478. While this value still indicates reasonable similarity, consistent with a common architecture, we might have expected these two viruses to exhibit a higher degree of correlation, as both FCV and vesivirus 2117 are classified in the same genus, *Vesivirus*. While the NoV structure produced a correlation value of 0.8117, the norovirus GII.10 structure produced a correlation value of 0.8498. This suggests that the structures of FCV and norovirus GII.10 are equally similar to that of vesivirus 2117. When observing the structures in Fig. 4, the P2 domains of norovirus GII.10 seem similar to those of vesivirus 2117, whereas the S domains and P1 domains of FCV seem to resemble those of vesivirus 2117. When comparing the structures side by side, it is likely that different domains of the capsid proteins of the two viruses have contributed to the close correlation values recorded. When the norovirus GII.10 structure is fitted into the FCV structure, a correlation value of only 0.6261 is produced, supporting this hypothesis of different components of the capsids contributing to the similar correlation values.

Phylogenetic analysis of vesivirus 2117

Fifty-one sequences of the VP1 capsid protein from the three genera highlighted as being structurally similar to that of vesivirus 2117 (*Vesivirus*, *Lagovirus* and *Sapovirus*) were aligned and analysed to compute a phylogenetic tree (Fig. 6). As expected, this analysis placed vesivirus 2117 firmly within the *Vesivirus* genus and showed that the sapoviruses are more closely related to the vesiviruses than the *Lagovirus* genus. Vesivirus 2117 isolates and canine vesivirus are clearly closely related and occupy their own clade. These viruses along with the canine caliciviruses, SMSV8 and mink calicivirus are distinct from the FCV and VESV clades. Cross-correlation data indicated a high degree of similarity between vesivirus 2117 and both sapovirus and RHDV but a lesser

degree when compared with FCV. At 10 Å resolution, gross morphological similarities or differences may not indicate common tertiary structures; therefore, such comparisons should be interpreted with care. However, the P2 domain plays a critical role in the viral infection cycle as it contains both the major immunodominant epitopes and the receptor-binding site [32, 35]. Thus, differences in capsid morphology between the vesivirus clades and similarities between vesivirus 2117 and viruses in different genera within the *Caliciviridae* may allude to important functional differences and similarities, respectively.

DISCUSSION

Vesivirus 2117 has caused significant financial losses owing to the contamination of bioreactors at Genzyme (Allston Landing and Geel facilities) where CHO cells were used for the production of biopharmaceuticals. The contamination necessitated the shutdown and decontamination of bioreactors, causing a significant delay in the delivery of drugs to patients with Gaucher or Fabry disease (17). The substantial impact of this contamination highlights the need for effective adventitious agent testing.

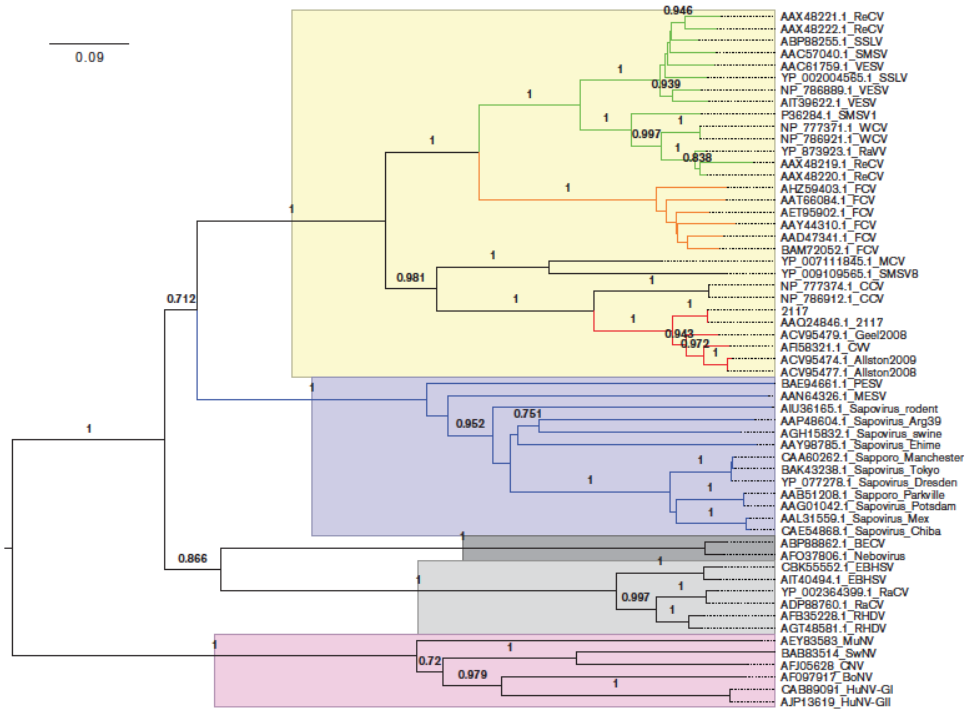

Fig. 6. Vesivirus 2117 neighbour-joining tree. The evolutionary history of the VP1 capsid of 2117 was inferred using the neighbour-joining method. The vesivirus 2117 cluster is highlighted in red; FCV cluster, in orange; VESV cluster (includes walrus, reptile and sea lion viruses), in green; and the sapovirus cluster, in blue. The proportions of replicate trees in which the associated taxa clustered together in the bootstrap test (1000 replicates) are shown next to the branches. The tree is drawn to scale, with branch lengths in the same units as those of the evolutionary distances used to infer the phylogenetic tree. The genus *Vesivirus* is highlighted in yellow; the genus *Sapovirus*, in blue; the genus *Nebovirus*, in dark grey; the genus *Lagovirus*, in light grey; and the genus *Norovirus*, in pink. BECV, bovine enteric calicivirus; BoNV, bovine norovirus; CCV, canine calicivirus; CNV, canine norovirus; CVV, canine vesivirus; EBHSV, European brown hare syndrome virus; FCV, feline calicivirus; HuCV, human calicivirus; HuNV-GI, human norovirus GI; HuNV-GII, human norovirus GII; MCV, mink calicivirus; MuNV, murine norovirus; PESV, porcine enteric sapovirus; RaCV, rabbit calicivirus; RaVV, rabbit vesivirus; ReCV, reptile calicivirus; ReVV, reptile vesivirus; RHDV, rabbit hemorrhagic disease virus; SMSV, San Miguel sea lion virus; SMSV1, San Miguel sea lion virus 1; SSLV, Steller sea lion vesivirus; SwNV, swine norovirus; VESV, vesicular exanthema of swine virus; WCV, walrus calicivirus.

We have determined the structure of vesivirus 2117 at 10 Å resolution by cryo-EM and 3D reconstruction. We also determined the structure of a chimeric sapovirus at 10 Å resolution and showed the high degree of morphological similarity between the two. Indeed, vesivirus 2117 appeared to be structurally closer to sapovirus and RHDV (a lagovirus) than other vesiviruses, including FCV. However, phylogenetic analysis based on VP1 sequences confirmed that vesivirus 2117 is correctly classified as a vesivirus, also showing that it resides in a clade distinct from FCV and VESV.

The dimeric capsomeres formed of vesivirus 2117 capsid protein present two horn-like structures on the outer surface of the P2 domains. Similar structures are present on the outer faces of P domains of sapovirus VP1, although they are less pronounced. MuNV also exhibits prominent horn-like protrusions on the outer surface of the P2 domain of VP1 [34]. Conversely, the P2 domains of FCV form a rhombus-shaped structure with a flatter outer surface (similar to that of SMSV and Tulane virus [36, 37]). Despite this obvious morphological difference, sequence analysis suggests that FCV is indeed the calicivirus most closely related to vesivirus 2117 for which we have a capsid structure.

The outer face of the FCV capsomere incorporates the receptor-binding site. Two molecules of feline junctional adhesion molecule-A bind to the flat surface in a head-to-tail arrangement [13, 32]. Receptor binding induces conformational changes in the capsid that are hypothesized to prime the virion for genome uncoating in the late endosome. FCV is the only calicivirus that has been shown to enter via attachment to a protein receptor. Sapoviruses and MuNV are thought to bind sialic acid moieties to mediate attachment [38, 39], while RHDV and human noroviruses bind histo-blood group antigens – complex carbohydrates linked to glycoproteins or glycolipids on the surface of erythrocytes and mucosal epithelial cells [40–42]. Our morphological comparison of vesivirus 2117 and sapovirus may therefore provide clues to entry pathways exploited by the 2117 and CCV clades of the genus *Vesivirus*.

There is a paucity of data concerning pathology caused by vesiviruses in the CCV and 2117 clades. Reports of enteritis associated with CCV suggest the possibility of sapovirus-like disease [43], whereas for 2117, the natural host and pathology remain unknown.

Interestingly, the first and second ORFs of vesivirus 2117 are separated by a stop codon, which is typical of the noroviruses and vesiviruses. However, the capsid protein is encoded within the first ORF along with the viral non-structural proteins, typical of the sapoviruses and lagoviruses [16]. This has, to date, only been described for canine calicivirus [44], which is possibly the closest related virus to vesivirus 2117.

While phylogenetic analysis indicated a close genetic relatedness between vesivirus 2117 and canine vesivirus, the striking morphological similarities with sapoviruses led us to question the taxonomic classification of vesivirus 2117 as a vesivirus. However, based on sequence data alone, vesivirus 2117 is undoubtedly more closely related to FCV than it is to the genus *Sapovirus*. Structural analysis has been proposed to provide insights into the common ancestry of distantly related viruses following the discovery of fold conservation between viruses that infect highly divergent branches on the tree of life [30]. Within the *Caliciviridae*, VP1 proteins share a common topology. The fact that the outer face of the P domain presents the receptor-binding site and major immunodominant epitopes means that it is subject to significant evolutionary pressure from immune surveillance. Typically, receptor-binding sites of viruses are embedded in hyper-variable regions of capsid proteins. Thus, morphological differences/similarities in the P domain may be uncoupled from genetic relatedness but may provide important clues concerning critical aspects of virus biology, such as entry pathway.

METHODS

Virus culture and purification

Vesivirus 2117 VLPs were produced by baculovirus expression of the VP1 gene (lacking the predicted leader sequence) in Hi5 cells. Six days post-infection, cells were freeze–thawed and the lysate was clarified by centrifugation at 14 000 ***g*** for 30 min. The supernatant was filtered (0.45 µm vacuum filter) and protein was precipitated by addition of polyethylene glycol to a final concentration of 10 % followed by incubation at 4 °C. The precipitate was centrifuged at 8000 ***g*** and 4 °C for 30 min. The VLP-containing pellet was then resuspended in boric acid buffer (0.2 M boric acid, 0.5 M NaCl, pH 7.5). VLPs were then centrifuged through a sucrose cushion (30 %, 150 000 ***g*** at 4 °C). The VLP pellets were subsequently resuspended in boric acid buffer, centrifuged (8000 ***g***, 4 °C for 10 min) and mixed with an equal volume of PBS containing 0.5 M NaCl and 4.51 M CsCl for ultracentrifugation using a Sw55 Ti rotor at 40 000 r.p.m. for 20 h at 4 °C. Purified VLPs were then collected and dialysed against PBS.

FCV strain F9 was propagated in Crandell Rees feline kidney cells for 8 h. The virus-infected cells were pelleted from the culture medium by centrifugation (1500 ***g***, 10 min at 4 °C). The pellet was resuspended in TBS (250 mM NaCl and 85 mM Tris/HCl, pH 7.2) and freeze–thawed at −80 °C prior to sonication with an equal volume of Vertrel XF (Sigma-Aldrich). The cell suspension was then clarified by low-speed centrifugation (7000 ***g***, 10 min at 4 °C), and the aqueous phase was subjected to repeated sonication. Virus was then purified from the aqueous phase by centrifugation through a caesium chloride gradient (1.31–1.45 g ml^{-1}) using a SW-41 Ti rotor at 28 000 r.p.m. for 8 h at 12 °C. The purified virus was collected from the gradient and dialysed into virion buffer (10 mM Tris, 150 mM NaCl and 20 mM $MgCl_2$, pH 7.2).

Sapovirus particles were made using a baculovirus expression system in Tn5 cells as previously described [27].

Electron microscopy

Vesivirus 2117 VLPs and FCV virions (4 µl) were loaded on-to glow discharged C-flat holey carbon support films (R2/2 ProtoChips), blotted at 4 °C for 4 s at 100 % humidity and plunged into liquid-nitrogen-cooled liquid ethane using an FEI Mark IV Vitrobot. Vitrified samples were imaged in a JEOL 2200 FS cryo-microscope equipped with a Gatan 626 cryo-stage. Energy-filtered images were recorded (with a 20 eV slit width) on a Gatan Ultrascan US4000 charge-coupled device camera at a magnification of ×100 000, corresponding to a pixel size of 1.05 Å per pixel (vesivirus 2117) or a Direct Electron DE20 direct detection device at a magnification of ×40 000 with a pixel size of 1.39 Å per pixel (FCV). Sapovirus VLPs were plunged using the same method but using R1.2/1.3 Mo 200 mesh holey carbon grids (Quantifoil), imaging was performed in a JEOL 2200FS at a magnification of ×80 000 and micrographs were recorded on a TVIPS 4k×4k CCD camera, giving a pixel size of 1.6 Å per pixel.

3D image reconstruction

Two hundred and forty-two micrographs of vesivirus 2117 VLPs, 241 micrographs of FCV and 222 micrographs of SV VLPs were processed to calculate 3D reconstructions. Images of particles were contrast transfer function corrected and extracted from micrographs using the BSoft program Bshow [45]. The vesivirus 2117 and SV particles were masked and sorted by size into five classes by cross-correlation against fuzzy ring models using SPIDER [46]. The most populous class for each was selected for use in further processing. The origins and orientations of the particles were then determined using the polar Fourier transform method (PFT2), and the EM3DR2 program was used to create 3D reconstructions [47, 48]. Resolution estimates for each map were determined by dividing the data set into two and calculating 3D reconstructions from each half. The paired reconstructions were compared in Bresolve to compute a number of indices of similarity including the Fourier shell correlation (FSC). A FSC cut-off value of 0.5 was taken (Fig. S1, available in the online Supplementary Material). To draw comparisons between different calicivirus capsids, additional structures were downloaded from the Protein Data Bank and Electron Microscopy Data Bank public databases. Density maps were calculated from Protein Data Bank files using the EMAN program pdb2mrc. All density maps were then low pass filtered to a common resolution of 10 Å using EMAN [49]. UCSF Chimera was used for visualizing cryo-EM reconstructions (using an isosurface threshold of the mean plus 1 SD) and for calculation of correlation values between pairs of maps. Correlation values were calculated in UCSF Chimera using the 'Fit in Map' function [50].

Phylogenetic analysis

Our 2117 capsid amino acid sequence was used as a query sequence in a BLASTP search against the GenBank non-redundant database. The top hit was to an existing 2117 sequence (AAQ24846; 99 % identity), followed by three hits to other suspected 2117 sequences sampled in Geel, Belgium (ACV95479; 85 % identity) and Allston, USA (ACV95474, ACV95477; 84 % identity). The next most similar hits were canine vesivirus (AFI58321; 84 % identity) and canine calicivirus (NP_786912, NP_777374; 68 % identity) sequences. All of the above sequences had an *E* value of 0 and were selected for inclusion in the phylogenetic analysis. Representative sequences from other species within the genera *Vesivirus*, *Sapovirus*, *Lagovirus* and *Norovirus* of the family *Caliciviridae* were also selected from the BLAST hits for inclusion in the phylogenetic analysis. In total, 57 protein sequences were selected (including our 2117 capsid sequence) and aligned using CLUSTALW within the MEGA software [51]. The evolutionary history of the 2117 capsid sequence was inferred using the neighbour-joining method (1000 bootstrap replicates) to generate a phylogenetic tree, evolutionary distances were computed using the JTT-matrix-based method and all positions in the alignment containing gaps and missing data were eliminated, leaving a total of 402 positions in the final dataset.

Funding information
M. C. was funded by a PhD studentship from the UK Biotechnology and Biological Sciences Research Council (BBSRC WestBIO DTP; grant number BB/J013854/1). D. G. C. was supported by an Erasmus scholarship. G. S. H. was funded by the Chica and Heinz Schaller Foundation, Heidelberg, Grant-in-Aid for Scientific Research, a grant from the Ministry of Health, Labor, and Welfare of Japan. K. M. was funded by a grant from the Ministry of Education, Culture, Sports, Science and Technology (MEXT) of Japan and the Collaborative Study Program of the National Institute for Physiological Sciences. D. T. performed this work in Japan as a Japan Society for the Promotion of Science/National Science Foundation East Asia and Pacific Summer Institute Fellow. I. G. G. was supported by a Wellcome Trust senior fellowship in basic biomedical science. R. O. and D. B. were supported by the UK Medical Research Council (MC_UU_12014/3 and MC_UU_12014/7 respectively).

Conflicts of interest
The authors declare there are no conflicts of interest.

References

1. **Etherington GJ, Ring SM, Charleston MA, Dicks J, Rayward-Smith VJ *et al.*** Tracing the origin and co-phylogeny of the caliciviruses. *J Gen Virol* 2006;87:1229–1235.
2. **Green KY, Ando T, Balayan MS, Berke T, Clarke IN *et al.*** Taxonomy of the caliciviruses. *J Infect Dis* 2000;181:S322–S330.
3. **Radford AD, Gaskell RM, Hart CA.** Human norovirus infection and the lessons from animal caliciviruses. *Curr Opin Infect Dis* 2004;17:471–478.
4. **Sosnovtsev SV, Belliot G, Chang KO, Onwudiwe O, Green KY.** Feline calicivirus VP2 is essential for the production of infectious virions. *J Virol* 2005;79:4012–4024.
5. **Oka T, Yamamoto M, Yokoyama M, Ogawa S, Hansman GS *et al.*** Highly conserved configuration of catalytic amino acid residues among calicivirus-encoded proteases. *J Virol* 2007;81:6798–6806.
6. **Al-Molawi N, Beardmore VA, Carter MJ, Kass GE, Roberts LO.** Caspase-mediated cleavage of the feline calicivirus capsid protein. *J Gen Virol* 2003;84:1237–1244.
7. **Mcfadden N, Bailey D, Carrara G, Benson A, Chaudhry Y *et al.*** Norovirus regulation of the innate immune response and apoptosis occurs via the product of the alternative open reading frame 4. *PLoS Pathog* 2011;7:e1002413.
8. **Caspar DL, Klug A.** Physical principles in the construction of regular viruses. *Cold Spring Harb Symp Quant Biol* 1962;27:1–24.

9. **Harrison SC.** The familiar and the unexpected in structures of icosahedral viruses. *Curr Opin Struct Biol* 2001;11:195–199.
10. **Rossmann MG, Johnson JE.** Icosahedral RNA virus structure. *Annu Rev Biochem* 1989;58:533–569.
11. **Wang X, Xu F, Liu J, Gao B, Liu Y *et al.*** Atomic model of rabbit hemorrhagic disease virus by cryo-electron microscopy and crystallography. *PLoS Pathog* 2013;9:e1003132.
12. **Subba-Reddy CV, Yunus MA, Goodfellow IG, Kao CC.** Norovirus RNA synthesis is modulated by an interaction between the viral RNA-dependent RNA polymerase and the major capsid protein, VP1. *J Virol* 2012;86:10138–10149.
13. **Bhella D, Gatherer D, Chaudhry Y, Pink R, Goodfellow IG.** Structural insights into calicivirus attachment and uncoating. *J Virol* 2008;82:8051–8058.
14. **Chen R, Neill JD, Estes MK, Prasad BV.** X-ray structure of a native calicivirus: structural insights into antigenic diversity and host specificity. *Proc Natl Acad Sci USA* 2006;103:8048–8053.
15. **Prasad BV, Rothnagel R, Jiang X, Estes MK.** Three-dimensional structure of baculovirus-expressed Norwalk virus capsids. *J Virol* 1994;68:5117–5125.
16. **Oehmig A, Büttner M, Weiland F, Werz W, Bergemann K *et al.*** Identification of a calicivirus isolate of unknown origin. *J Gen Virol* 2003;84:2837–2845.
17. **Qiu Y, Jones N, Busch M, Pan P, Keegan J *et al.*** Identification and quantitation of vesivirus 2117 particles in bioreactor fluids from infected Chinese hamster ovary cell cultures. *Biotechnol Bioeng* 2013;110:1342–1353.
18. **Berting A, Farcet MR, Kreil TR.** Virus susceptibility of Chinese hamster ovary (CHO) cells and detection of viral contaminations by adventitious agent testing. *Biotechnol Bioeng* 2010;106:598–607.
19. **Burstyn DG.** Contamination of genetically engineered Chinese hamster ovary cells. *Dev Biol Stand* 1995;88:199–203.
20. **Garnick RL.** Raw materials as a source of contamination in large-scale cell culture. *Dev Biol Stand* 1998;93:21–29.
21. **Kerr A, Nims R.** Adventitious viruses detected in biopharmaceutical bulk harvest samples over a 10 year period. *PDA J Pharm Sci Technol* 2010;64:481–485.
22. **Plavsic M, Qiu Y, Jones N, Keegan J, Woodcock D *et al.*** *Caliciviridae* and vesivirus 2117. *Bioprocessing (Williamsbg Va)* 2011;9:6–12.
23. **Rabenau H, Ohlinger V, Anderson J, Selb B, Cinatl J *et al.*** Contamination of genetically engineered CHO-cells by epizootic haemorrhagic disease virus (EHDV). *Biologicals* 1993;21:207–214.
24. **Onions D.** Animal virus contaminants of biotechnology products. *Dev Biol* 2004;118:155–163.
25. **Wurm FM.** Production of recombinant protein therapeutics in cultivated mammalian cells. *Nat Biotechnol* 2004;22:1393–1398.
26. **Han MG, Wang Q, Smiley JR, Chang KO, Saif LJ.** Self-assembly of the recombinant capsid protein of a bovine norovirus (BoNV) into virus-like particles and evaluation of cross-reactivity of BoNV with human noroviruses. *J Clin Microbiol* 2005;43:778–785.
27. **Hansman GS, Oka T, Katayama K, Takeda N.** Enhancement of sapovirus recombinant capsid protein expression in insect cells. *FEBS Lett* 2006;580:4047–4050.
28. **Miyazaki N, Taylor DW, Hansman GS, Murata K.** Antigenic and cryo-electron microscopy structure analysis of a chimeric sapovirus capsid. *J Virol* 2016;90:2664–2675.
29. **Oka T, Hansman GS, Katayama K, Ogawa S, Nagata N *et al.*** Expression of sapovirus virus-like particles in mammalian cells. *Arch Virol* 2006;151:399–404.
30. **Bamford DH, Grimes JM, Stuart DI.** What does structure tell us about virus evolution? *Curr Opin Struct Biol* 2005;15:655–663.
31. **Chen R, Neill JD, Noel JS, Hutson AM, Glass RI *et al.*** Inter- and intragenus structural variations in caliciviruses and their functional implications. *J Virol* 2004;78:6469–6479.
32. **Bhella D, Goodfellow IG.** The cryo-electron microscopy structure of feline calicivirus bound to junctional adhesion molecule A at 9-angstrom resolution reveals receptor-induced flexibility and two distinct conformational changes in the capsid protein VP1. *J Virol* 2011;85:11381–11390.
33. **Katpally U, Wobus CE, Dryden K, Virgin HW, Smith TJ.** Structure of antibody-neutralized murine norovirus and unexpected differences from viruslike particles. *J Virol* 2008;82:2079–2088.
34. **Katpally U, Voss NR, Cavazza T, Taube S, Rubin JR *et al.*** High-resolution cryo-electron microscopy structures of murine norovirus 1 and rabbit hemorrhagic disease virus reveal marked flexibility in the receptor binding domains. *J Virol* 2010;84:5836–5841.
35. **Radford AD, Willoughby K, Dawson S, Mccracken C, Gaskell RM.** The capsid gene of feline calicivirus contains linear B-cell epitopes in both variable and conserved regions. *J Virol* 1999;73:8496–8502.
36. **Chen R, Neill JD, Prasad BV.** Crystallization and preliminary crystallographic analysis of San Miguel sea lion virus: an animal calicivirus. *J Struct Biol* 2003;141:143–148.
37. **Yu G, Zhang D, Guo F, Tan M, Jiang X *et al.*** Cryo-EM structure of a novel calicivirus, Tulane virus. *PLoS One* 2013;8:e59817.
38. **Kim DS, Hosmillo M, Alfajaro MM, Kim JY, Park JG *et al.*** Both α2,3- and α2,6-linked sialic acids on O-linked glycoproteins act as functional receptors for porcine sapovirus. *PLoS Pathog* 2014;10:e1004172.
39. **Taube S, Perry JW, Mcgreevy E, Yetming K, Perkins C *et al.*** Murine noroviruses bind glycolipid and glycoprotein attachment receptors in a strain-dependent manner. *J Virol* 2012;86:5584–5593.
40. **Marionneau S, Ruvoën N, Le Moullac-Vaidye B, Clement M, Cailleau-Thomas A *et al.*** Norwalk virus binds to histo-blood group antigens present on gastroduodenal epithelial cells of secretor individuals. *Gastroenterology* 2002;122:1967–1977.
41. **Nyström K, Le Gall-Reculé G, Grassi P, Abrantes J, Ruvoën-Clouet N *et al.*** Histo-blood group antigens act as attachment factors of rabbit hemorrhagic disease virus infection in a virus strain-dependent manner. *PLoS Pathog* 2011;7:e1002188.
42. **Ruvoën-Clouet N, Ganière JP, André-Fontaine G, Blanchard D, Le Pendu J.** Binding of rabbit hemorrhagic disease virus to antigens of the ABH histo-blood group family. *J Virol* 2000;74:11950–11954.
43. **Schaffer FL, Soergel ME, Black JW, Skilling DE, Smith AW *et al.*** Characterization of a new calicivirus isolated from feces of a dog. *Arch Virol* 1985;84:181–195.
44. **Roerink F, Hashimoto M, Tohya Y, Mochizuki M.** Genetic analysis of a canine calicivirus: evidence for a new clade of animal caliciviruses. *Vet Microbiol* 1999;69:69–72.
45. **Heymann JB.** Bsoft: image and molecular processing in electron microscopy. *J Struct Biol* 2001;133:156–169.
46. **Frank J, Radermacher M, Penczek P, Zhu J, Li Y *et al.*** SPIDER and WEB: processing and visualization of images in 3D electron microscopy and related fields. *J Struct Biol* 1996;116:190–199.
47. **Baker TS, Cheng RH.** A model-based approach for determining orientations of biological macromolecules imaged by cryoelectron microscopy. *J Struct Biol* 1996;116:120–130.
48. **Bubeck D, Filman DJ, Cheng N, Steven AC, Hogle JM *et al.*** The structure of the poliovirus 135S cell entry intermediate at 10-angstrom resolution reveals the location of an externalized polypeptide that binds to membranes. *J Virol* 2005;79:7745–7755.
49. **Ludtke SJ, Baldwin PR, Chiu W.** EMAN: semiautomated software for high-resolution single-particle reconstructions. *J Struct Biol* 1999;128:82–97.
50. **Pettersen EF, Goddard TD, Huang CC, Couch GS, Greenblatt DM *et al.*** UCSF Chimera—a visualization system for exploratory research and analysis. *J Comput Chem* 2004;25:1605–1612.
51. **Tamura K, Stecher G, Peterson D, Filipski A, Kumar S.** MEGA6: Molecular Evolutionary Genetics Analysis version 6.0. *Mol Biol Evol* 2013;30:2725–2729.